First Principles Based Design of Bimetallic Catalysts for Benzene Hydrogenation

Ab initio gebaseerd ontwerp van bimetaalkatalysatoren voor benzeenhydrogenering

Gonzalo Canduela Rodriguez

Promotoren: prof. dr. M.-F. Reyniers, dr. ir. M. Sabbe
Proefschrift ingediend tot het behalen van de graad van
Doctor in de Ingenieurswetenschappen: Chemische Technologie

Vakgroep Chemische Proceskunde en Technische Chemie
Voorzitter: prof. dr. ir. G. B. Marin
Faculteit Ingenieurswetenschappen en Architectuur
Academiejaar 2014 - 2015

UNIVERSITEIT
GENT

ISBN 978-90-8578-775-4
NUR 952
Wettelijk depot: D/2015/10.500/19

Promotoren

Prof. dr. Marie-Françoise Reyniers

Dr. ir. Maarten K. Sabbe

Universiteit Gent
Vakgroep Chemische proceskunde en Technische Chemie (EA12)
Laboratorium voor Chemische Technologie
Technologiepark 914
9052 Gent
België

Decaan: Prof. dr. ir. Rik Van de Walle

Rector: Prof. dr. Anne De Paepe

Internal promoter IFP Energies nouvelles

Dr. Ir. Jean-François Joly
Expert Director
IFP Energies nouvelles

Onderzoek verricht met financiering door het IFP Energies nouvelles in Solaize, Lyon.
Research performed with funding from the IFP Energies nouvelles in Solaize, Lyon.

EXAMENCOMMISSIE

Leescommissie

Dr. ir. Maarten K. Sabbe [promotor]
Vakgroep Chemische proceskunde en Technische Chemie
Faculteit Ingenieurswetenschappen en Architectuur (EA12)
Universiteit Gent

Prof. dr. Patrick Bultinck
Vakgroep Anorganische en Fysische Chemie (WE06)
Universiteit Gent

Prof. dr. Philippe Sautet
Membre de l'académie des Sciences
Université de Lyon, CNRS, ENS Lyon
Directeur de recherche au CNRS

Dr. Jean-Marc Schweitzer
Direction Conception Modélisation Procédés
IFP Energies nouvelles

Andere leden van de examencommissie

Prof. dr. Marie-Françoise Reyniers [promotor]
Vakgroep Chemische proceskunde en Technische Chemie
Faculteit Ingenieurswetenschappen en Architectuur (EA12)
Universiteit Gent

Prof. dr. ir. Guy B. Marin
Vakgroep Chemische proceskunde en Technische Chemie
Faculteit Ingenieurswetenschappen en Architectuur (EA12)
Universiteit Gent

Prof. dr. ir. Joris Thybaut
Vakgroep Chemische proceskunde en Technische Chemie
Faculteit Ingenieurswetenschappen en Architectuur (EA12)
Universiteit Gent

Prof. dr. ir. Mark Saeys
Vakgroep Chemische proceskunde en Technische Chemie
Faculteit Ingenieurswetenschappen en Architectuur (EA12)
Universiteit Gent

Prof. dr. ir. Rik Van de Walle [voorzitter]
Vakgroep Elektronica en Informatiesystemen
Faculteit Ingenieurswetenschappen en Architectuur
Universiteit Gent

A Sagrario y Oliva…

Acknowledgements

First, I want to thank **Prof. Guy B. Marin** and my promoter **Prof. Marie-Françoise Reyniers** for this great opportunity to do doctoral research in the Laboratory for Chemical Technology at Ghent University. I also want to thank **IFP Energies nouvelles** for financial support, and in particular Dr. Jean-François Joly and Dr. Christophe Boyer for their help.

My most sincere gratitude goes to my promoter **Dr. Maarten Sabbe**. Maarten, since I was an Erasmus student five years ago you have guided me and helped me along this difficult path. Clearly, you have been a catalyst for this work.

Esta tesis está dedicada a mis padres, mi hermano y a Carlota. Estar lejos de casa ya es difícil de por sí. Estar lejos de vosotros ha sido una gran prueba que me ha hecho más fuerte. **Papá, mamá**, **Pablo**, sois la mejor familia que jamar podría pedir. No puedo estar más agradecido de teneros, os doy las gracias por estar siempre ahí, os quiero muchísimo. También quiero dedicar este trabajo a mis abuelas, que no pudieron verme acabar pero sé que estarían muy orgullosas. Os echo muchísimo de menos.

Car, no hay palabras que puedan explicar lo que ha sido estar lejos de ti estos cuatro años. Una grandísima parte de este trabajo es también tuyo. Te agradezco infinitamente el apoyo que me has dado. La distancia no ha sido nada fácil, pero lo hemos conseguido y ahora nos merecemos lo mejor. Te quiero.

Chavales, no me olvido de vosotros. Nunca podría haber hecho nada de esto sin la gente con la que crecí y me formé como persona. Jaime y Miguel, nenes, sois los mejores. Ceci, Mario, Giorgio… y tantísimos otros, no puedo tener mejores amigos que vosotros, bien sabéis lo muchísimo que os he echado de menos a todos.

During these years I had great experiences and I have met amazing people that will never be forgotten. The list of their names would have the same pages as this Ph.D. However, I want to highlight some names. **Jokin**, chiquitín!, en este tiempo te has convertido en mi hermano, te voy a echar muchísimo de menos. **Isa**, **Lucio**, **Quique, Mirella, Marko, Andrés, Peter**... que grandes sois cabrones. **Panos** and **Maria**, you cannot imagine how much I will miss you. **Mahesh**, thanks for being such an amazing flat mate. A great thank goes to my good colleagues, and even better friends: **Marita**, **Jelena**, **Pieter**, **Gilles**, **Aditya**, **Chetan**, **Kaustav**, **Kostas**, **Ezgi**…too many names, so much fun in these years. I am going to miss so much this lab and everyone there.

Finally, I am indebted to you, **Gent**. You have been my home for the last five years, and thanks to you I have felt just like I was born here. Your charm, your streets, your beer… You are the perfect city!
I will miss you.

Gonzalo Canduela Rodríguez

February, 2015

Contents

Contents i
Notation v
Summary xi
Samenvatting xv

Chapter 1: Introduction 1
- 1.1 Catalytic hydrogenation of benzene 2
  - 1.1.1 Adsorption on metal catalysts 4
  - 1.1.2 Mechanism for benzene hydrogenation 8
- 1.2 Catalyst design for benzene hydrogenation 9
- 1.3 Objectives and outline of this work 12
- 1.4 References 13

Chapter 2: Thermodynamic study of benzene and hydrogen coadsorption on Pd(111) 19
- 2.1 Introduction 21
- 2.2 Methodology 24
  - 2.2.1 Electronic energy calculations 24
  - 2.2.2 Thermodynamic calculations 26
- 2.3 Results 30
  - 2.3.1 Hydrogen adsorption as a function of coverage 30

2.3.1.a Adsorption geometries and energies 30
2.3.1.b Thermodynamic phase diagrams...................................... 32
2.3.2 Benzene adsorption as a function of coverage 38
2.3.2.a Adsorption geometries and energies 38
2.3.2.b Thermodynamic phase diagrams...................................... 42
2.3.3 Benzene and hydrogen coadsorption as a function of coverage 46
2.3.3.a Adsorption geometries and energies 46
2.3.3.b Thermodynamic phase diagrams...................................... 53
2.3 Conclusions 57
2.4 References 58

Chapter 3: Ab initio coverage-dependent microkinetic modelling of benzene hydrogenation on Pd(111) 61
3.1 Introduction 63
3.2 Methodology 66
3.2.1 Electronic energy calculations 66
3.2.2 Construction of the microkinetic model 69
3.2.3 Microkinetic modeling 74
3.3 Results 77
3.3.1 Kinetic analysis at low coverage 77
3.3.2 Kinetic analysis as a function of coverage 84
3.3.2.a Thermodynamics and kinetics from DFT calculations 84
3.3.2.b Construction of the microkinetic model........................... 89
3.3.2.c Validations of the microkinetic model 92
3.4 Conclusions 97
3.5 References 98

Chapter 4: Periodic DFT study of benzene adsorption on Pd(100) and Pd(110) as a function of coverage 103
4.1 Introduction 105
4.2 Methodology 108
4.3 Benzene adsorption on Pd(100) at medium and saturation coverage 111
4.3.1 Adsorption energies.. 112
4.3.2 Vibrational properties.. 118

4.3.3 Electronic properties 120
4.4 Benzene adsorption on Pd(110) at medium and saturation coverage 129
4.4.1 Adsorption energies 129
4.4.2 Vibrational properties 137
4.4.3 Electronic properties 138
4.5 Conclusions 145
4.6 References 146

Chapter 5: First principles based design of bimetallic catalysts for benzene hydrogenation 151
5.1 Introduction 153
5.2 Methodology 156
5.2.1 Electronic energy calculations 156
5.2.2 Modeling the catalytic surface 158
5.2.3 Implementing catalyst descriptors in a microkinetic model 159
5.3 Results 162
5.3.1 Surface segregation 162
5.3.2 Benzene adsorption on Pd_3M bulk alloys 165
5.3.3 Benzene adsorption on Ni_3M bulk alloys 170
5.3.4 Catalysts descriptors for benzene adsorption 172
5.3.5 Screening the reactivity for benzene hydrogenation 175
5.4 Conclusions 180
5.5 References 181

Chapter 6: Conclusions and perspectives 185
6.1 Conclusions 185
6.2 Perspectives 188

Appendices 191
List of publications 249
Glossary 251

Notation

Roman symbols

$\ddagger$	transition state	-
A	pre-exponential factor	s^{-1}
A	surface area	m^2
C_t	concentration of active sites	m^{-2}
d	distance between two atoms	pm
E_a	activation energy	kJ mol^{-1}
$E_{adsorbate}$	electronic energy of the adsorbate complex	kJ mol^{-1}
ΔE_{ads}	adsorption energy	kJ mol^{-1}
$\Delta\Delta E_{ads}$	difference in adsorption energy relative to that on Pd(111)	kJ mol^{-1}
$\Delta E_{antiseg}$	antisegregation energy	kJ mol^{-1}
E_{el}	electronic energy	kJ mol^{-1}
$E_{el.segregated}$	electronic energy of the slab of an alloy X_3M in the segregated state	kJ mol^{-1}
$E_{el.antisegregated}$	electronic energy of the slab of an alloy X_3M in the antisegregated state	kJ mol^{-1}
$E_{el.X3M}$	electronic energy of the slab of an alloy X_3M in the non-segregated state	kJ mol^{-1}
E_f	energy of the Fermi level	eV
E_{gas}	electronic energy of the gas phase species	kJ mol^{-1}
$E_{interaction}$	interaction energy between adsorbate and slab	kJ mol^{-1}
$E_{molecule}^{dist}$	energy difference between the relaxed and distorted geometry (constrained to the adsorbed geometry) in gas phase	kJ mol^{-1}

E_{slab}	electronic energy of the clean slab	kJ mol^{-1}
$E_{surface}^{dist}$	energy difference between the slab with the relaxed and with the distorted geometry (constrained to the adsorbed geometry)	kJ mol^{-1}
ΔE_{seg}	segregation energy	kJ mol^{-1}
E_{vac}	energy of the vacuum level	eV
F	molar flow	mol s^{-1}
F	flux of incident gas phase molecules on a surface	molecules m^{-2} s^{-1}
G	Gibbs free energy	kJ mol^{-1}
$\Delta^{\ddagger}G$	Gibbs activation energy	kJ mol^{-1}
$\Delta_r G^o$	standard reaction Gibbs free energy	kJ mol^{-1}
$\Delta_r G_{gas}{}^o$	gas-phase standard reaction Gibbs free energy	kJ mol^{-1}
ΔG_{ads}	Gibbs adsorption energy	kJ mol^{-1}
H	enthalpy	kJ mol^{-1}
h	Planck's constant	6.62 10^{-34} J s^{-1}
$\Delta^{\ddagger}H$	activation enthalpy	kJ mol^{-1}
$\Delta_r H^0$	standard reaction enthalpy	kJ mol^{-1}
$\Delta_r H_{gas}{}^o$	gas-phase standard reaction enthalpy	kJ mol^{-1}
ΔH_{ads}	adsorption enthalpy	kJ mol^{-1}
I	reduced moment of inertia for internal rotation	kg m^2
k_B	Boltzmann constant	1.38 10^{-23} J K^{-1}
k	reaction rate coefficient	s^{-1} or Pa^{-1}s^{-1}
K	equilibrium coefficient	Pa^{-1} or -
m	mass of one molecule	kg
m	partial reaction order of hydrogen	-
n	partial reaction order of benzene	-
N_A	Avogadro constant	6.022 10^{23} mol^{-1}

n_i	number of gas phase molecules	-
n_{Pd}	number of Pd atoms in a unit cell	-
p	pressure	bar
p^o	standard pressure	bar
Q	molar partition function	-
q	molecular partition function	-
r	net reaction rate of an elementary step	mol $\text{mol}_{\text{activesite}}^{-1}\text{s}^{-1}$
R	universal gas constant	J mol^{-1} K^{-1}
R	global rate of production per active site	mol $\text{mol}_{\text{activesite}}^{-1}\text{s}^{-1}$
S	entropy	J mol^{-1} K^{-1}
S_0	sticking probability on a clean surface	-
$S_{trans+rot}$	entropy contribution from translational and rotational modes	J mol^{-1} K^{-1}
S_{vib}	entropy contribution from vibrational frequencies	J mol^{-1} K^{-1}
T	temperature	K
$U_{trans+rot}$	enthalpy contribution from translational and rotational modes	kJ mol^{-1}
U_{vib}	thermal correction to the enthalpy from vibrational contributions	kJ mol^{-1}
$\Delta_r S^o$	standard reaction entropy	J mol^{-1} K^{-1}
$\Delta_r S_{gas}{}^o$	gas-phase standard reaction entropy	J mol^{-1} K^{-1}
ΔS_{ads}	adsorption entropy	J mol^{-1} K^{-1}
X_{ROP}	rate of production coefficient	-
X_{SA}	sensitivity coefficient	-
W	catalyst mass	kg

Greek symbols

Δ	Increment	-

Γ	Surface Gibbs free energy	J m^{-2}
γ	Out-of-plane bending vibrational mode	-
δ	In-plane bending mode	-
ε_d	d-band centre	eV
θ	Tilting angle of adsorbate relative to the surface plane	°
θ	Fractional surface coverage	-
ν	vibrational frequency	cm^{-1}
ν	Stretching vibrational mode	-
π	type of bond	-
σ	type of bond	-
Φ	Work function	eV
ϕ	Azimuthal angle of adsorbate relative to the surface normal direction	°

Acronyms

ARUPS	Angle-Resolved Ultraviolet Photoemission Spectroscopy
CBS-QB3	Complete Basis Set - Quadratic Becke3
DOS	Density of States
DFT	Density Functional Theory
ESQC	Elastic Scattering Quantum Chemistry
GGA	Generalized Gradient Approximation
GPAW	Grid-based Projector-Augmented Wave method
HO	Harmonic Oscillator
HOMO	Highest Occupied Molecular Orbital
HREELS	High-Resolution Electron Energy Loss Spectroscopy
IPES	Inverse Photo-Emission Spectroscopy
LDH	Layered Double Hydroxides

LDA	Local Density Approximation
LEED	Low-Energy Electron Diffraction
LSODA	Livermore Solver for Ordinary Differential Equations
LUMO	Lowest Unoccupied Molecular Orbital
NEXAFS	Near-Edge X-ray Absorption Fine Structure spectroscopy
optPBE-vdW	Optimized Perdew-Burke-Ernzerhof van der Waals exchange and correlation functional
PHVA	Partial Hessian vibration analysis
PBE	Perdew, Burke and Ernzerhof's 1996 exchange and correlation functional
PW91	Perdew and Wang's 1991 exchange and correlation functional
PAW	Projector Augmented Wave method
PDOS	Projected Density of States
QM	Quantum Mechanics
RMM-DIIS	Residual Minimization Method with Direct Inversion in Iterative Subspace
ROP	Rate of Production Analysis
SA	Sensitivity Analysis
STM	Scanning Tunneling Microscopy
TPD	Thermal Desorption Spectroscopy
TOF	Turn-Over Frequency
UPS	Ultraviolet Photoemission Spectroscopy
vdW	van der Waals
vdW-DF	van der Waals Density Functional method
VASP	Vienna Ab initio Simulation Package
ZPVE	Zero-Point Vibrational Energy

Summary

Since catalytic reactions are essential in the chemical industry, the development of catalysts with optimal characteristics is of prime importance. The catalytic hydrogenation of benzene is an important industrial reaction for several reasons: it is used to improve the quality of diesel fuels, to obtain monomers for nylon production, and in the production of cleaner fuels. Benzene hydrogenation has a complex reaction network with multiple reactions paths and surface species. Quantum chemistry theoretical methods, such as density functional theory, can provide accurate detailed information at the molecular level for this reaction. These methods can be used to obtain a better understanding of the reaction mechanism and to predict the catalytic performance as a function of the conditions. Furthermore, these methods can also elucidate the essential differences between catalysts allowing to search for cheaper catalysts with optimal properties for benzene hydrogenation.

The present work first aims to obtain a detailed molecular level understanding of benzene hydrogenation on Pd as a function of surface coverage. Theoretical studies typically pertain to low, fixed surface coverages to reduce the computational cost related to larger systems and also to avoid the difficult geometry convergence that is often present at higher coverages due to repulsive lateral interactions. However, high coverages can be expected on the catalyst surface under reactions conditions. Therefore, inclusion of the effect of coverage on the

adsorption equilibria and reaction rate coefficients is possibly decisive to obtain theoretical results that are comparable to experimental observations.

Secondly, this work applies the knowledge acquired on Pd to screen different Pd-based bimetallic alloys for benzene hydrogenation, aiming to find optimal catalysts as a function of the conditions. Furthermore, given that the noble metal Pd is an expensive material and Ni is an active and much cheaper catalyst, this works evaluates Ni-based catalysts as well.

Aim. The present first principles based modeling work aims (i) to acquire a detailed molecular level description of benzene hydrogenation on Pd, and (ii) to develop a predictive model to search for optimal bimetallic catalysts for benzene hydrogenation as function of the reaction conditions.

Chapter 1 presents the catalytic hydrogenation of benzene from a general point of view and focuses on the adsorption and reactions steps on metal catalysts. This chapter introduces the approach that can be followed to design optimal catalysts based on theoretical calculations as a function of the conditions. Finally, a short literature overview of possible bimetallic catalysts for benzene hydrogenation is given.

Chapter 2 discusses the coadsorption of benzene and hydrogen on Pd(111) as a function of coverage. First the adsorption of the separate species is studied in detail, and the results are used to investigate their coadsorption as a function of hydrogen coverage. Surface Gibbs free energies are calculated and used to construct thermodynamic phase diagrams, which predict the preferred coverage on the surface as a function of the reaction conditions. Different approaches are considered in this chapter to calculate the surface Gibbs free energies. Comparison of the results to experimental observations suggests that thermodynamic phase diagram should be constructed accounting for both (i) vibrational contributions and (ii) a proper description of van der Waals interactions (vdW), in contrast to what is usually considered in theoretical studies

In **Chapter 3** an extensive study is performed on the effect of surface coverages on the catalytic hydrogenation of benzene on Pd(111). Adsorption equilibrium coefficients and surface (de)hydrogenation rate coefficients are evaluated at different surface coverages. With increasing surface coverage, a decrease in adsorption equilibrium coefficients and an increase in surface hydrogenation rate coefficients is observed. For surface reactions, an excellent correlation is observed between activation and reaction energies. The results are used to construct a coverage-dependent microkinetic model, which is solved as a function of the reaction conditions. In contrast to the results at low coverage or without a proper description of vdW interactions, the catalytic activity obtained from the coverage-dependent model with a proper description of van der Waals interactions is comparable with that from experimental observations.

Chapter 4 deals with the adsorption of benzene on Pd(100) and Pd(110) as a function of the coverage. Since Pd nanoparticles on industrial catalysts are composed of different surfaces, the knowledge of the preferred adsorption sites of benzene and their behavior with coverage on these surfaces is important for modeling benzene hydrogenation on Pd multifaceted particles.

A large decrease in stability is predicted for benzene adsorption at saturation as compared to medium coverage on the two surfaces, particularly on Pd(110). The comparison of these results to experimental data allows to propose preferred adsorption sites for benzene on both surfaces, reducing the number of possible adsorption sites to a large extent.

Chapter 5 investigates several Pd-based and Ni-based bimetallic catalysts for benzene hydrogenation. First, the most stable segregation state is studied for the clean surface of these alloys. For the most stable state, the different adsorption sites of benzene are studied, evaluating changes in the segregation state upon benzene adsorption as well. Since the calculation of benzene adsorption is computationally expensive, correlations between benzene

adsorption energy and carbon adsorption energy, and also with the occupied d-band centre of the surface atoms are evaluated. The reactivity of selected alloys for benzene hydrogenation is predicted based on the reactivity of the first hydrogenation step. A good correlation is observed between activation barrier of this step and the adsorption energy of benzene and, hence, the latter can be used as a catalyst descriptor that represents the essential differences between catalysts. The results, expressed relative to those on Pd(111), are implemented in the constructed microkinetic model for benzene hydrogenation on Pd(111). The activity for a broad range of catalyst descriptor values and reactions conditions indicate that, for temperatures between 400 and 500 K, maxima in activity are predicted for catalysts that bind benzene 10 – 20 kJ mol^{-1} stronger than Pd(111), e.g. the Ni_3Ru and Ni_3Os alloys.

Finally, in **Chapter 6**, the most important conclusions of this Ph.D. are highlighted together with perspectives for future research. This work confirms the usefulness of first principles theoretical calculations for acquiring molecular level insights for catalytic reactions. The work stresses the importance of two effects on the rate coefficients that are often neglected in theoretical studies, namely coverage effects and van der Waals interactions. Incorporation of these two is required to predict catalyst activities that can be compared to experimentally observed activities. Finally, this work also proves that theoretical calculations based on density functional theory are promising to search for new and more active catalysts for benzene hydrogenation, which can also be applied in other industrially important catalytic processes.

Samenvatting

Omdat katalytische reacties een sleutelrol bekleden in de chemische industrie is de ontwikkeling van katalysatoren met optimale eigenschappen van groot belang. De katalytische hydrogenering van benzeen is een belangrijke industriële reactie voor verschillende redenen: de reactie wordt gebruikt om de kwaliteit van diesel te verbeteren, om monomeren voor de productie van nylon te verkrijgen, en om milieuvriendelijker brandstoffen te produceren. Benzeenhydrogenering vindt plaats door middel van een complex reactienetwerk met meerdere reactiepaden en intermedeairen op het oppervlak. Kwantumchemische methoden, zoals dichtheidsfunctionaaltheorie, kunnen accurate en gedetailleerde data op moleculair niveau aanreiken. Deze methoden kunnen gebruikt worden om een beter begrip van het reactiemechanisme te verkrijgen en om de katalytische activiteit als functie van de reactiecondities te voorspellen. Bovendien kunnen deze methoden ook de essentiële verschillen tussen katalysatoren ophelderen, wat toelaat om betere en/of goedkopere katalysatoren met optimale eigenschappen voor benzeenhydrogenering te identificeren.

Dit werk poogt ten eerste om een goed begrip te verkrijgen van benzeenhydrogenering op Pd als functie van de fractionele bedekkingsgraad, op moleculair niveau. Theoretische studies zijn typisch beperkt tot lage, vaste bedekkingsgraden, wat toelaat de berekeningstijden te beperken en bovendien de moeilijke geometrie-optimalisaties te omzeilen die vaak gepaard

gaan met hogere bedekkingsgraden door de toegenomen afstotende laterale interacties. Op het oppervlak van een werkelijke katalysator onder industriële reactiecondities worden echter typisch hoge bedekkingsgraden waargenomen. Daarom is de beschrijving van het effect van bedekkingsgraden op adsorptie-evenwichten en reactiesnelheidscoëfficiënten mogelijk cruciaal om theoretische resultaten te bereiken die in overeenstemming zijn met experimentele waarnemingen.

Ten tweede past dit werk de kennis vergaard op Pd toe om verschillende Pd-gebaseerde bimetallische legeringen te evalueren voor hun benzeenhydrogeneringsactiviteit, met als doel het bepalen van optimale katalysatoren als functie van de reactiecondities. Bovendien worden in dit werk ook Ni-gebaseerde katalysatoren geëvalueerd, gezien het feit dat Ni naast een actieve hydrogeneringskatalysator ook vele malen goedkoper is dan Pd.

Doel Op basis van ab initio gebaseerde modellering stelt dit werk zich als doel om (i) een gedetailleerde beschrijving op moleculair niveau te verkrijgen van benzeenhydrogenering op Pd, en (ii) een model op te bouwen dat optimale bimetallische katalysatoren kan bepalen voor benzeenhydrogenering als functie van de reactiecondities.

Hoofdstuk 1 voorziet in een algemene inleiding tot de katalytische hydrogenering van benzeen waarbij de nadruk gelegd wordt op de adsorptie- en reactiestappen op metaalkatalysatoren. Dit hoofdstuk introduceert de aanpak die gevolgd kan worden om optimale katalysatoren te ontwerpen op basis van theoretische berekeningen als functie van de reactiecondities. Tot slot wordt een kort literatuuroverzicht gegeven van de mogelijke bimetallische katalysatoren voor benzeenhydrogenering.

Hoofdstuk 2 behandelt de coadsorptie van benzeen en waterstof op Pd(111) als functie van de bedekkingsgraad. Eerst wordt de adsorptie van de afzonderlijke moleculen in detail besproken, en de resultaten worden gebruikt om hun coadsorptie als functie van de waterstofbedekkingsgraad te onderzoeken. Berekende Gibbs-oppervlakenergieën worden gebruikt om thermodynamische toestandsdiagramma te construeren die de meest stabiele oppervlakbedekking als functie van de reactiecondities beschrijven. Verschillende benaderingswijzen om de Gibbs-oppervlakenergieën te berekenen worden beschouwd in dit hoofdstuk. Vergelijking van de resultaten met experimentele resultaten duidt erop dat de thermodynamische toestandsdiagramma geconstrueerd dienen te worden waarbij zowel rekening gehouden wordt met (i) vibrationele bijdragen en (ii) een correcte beschrijving van van der Waals (vdW) interacties, in tegenstelling tot de traditioneel beschouwde aannames in theoretische studies.

Hoofdstuk 3 beschrijft een uitgebreide studie over de invloed van oppervlakbedekkingen op de katalytische hydrogenering van benzeen over Pd(111). De basis hiertoe is de beschrijving van de invloed van de bedekkingsgraad op evenwichtscoëfficiënten voor adsorptie en snelheidscoëfficiënten voor (de)hydrogenering. Met toenemende oppervlakbedekking wordt een afname in evenwichtscoëfficiënten voor adsorptie en een toename in snelheidscoëfficiënten voor hydrogenering waargenomen. Voor de reacties op het oppervlak correleren de activerings- en reactie-energieën zeer goed met elkaar. De resultaten worden gebruikt om een bedekkingsgraadafhankelijk microkinetisch model te construeren dat kan opgelost worden als functie van de reactiecondities. De katalytische activiteit zoals berekend door het bedekkingsgraadafhankelijk model met correcte beschrijving van vdW interacties is vergelijkbaar met deze verkregen uit experimentele waarnemingen, in tegenstelling tot de resultaten verkregen bij lage bedekking of zonder correcte beschrijving van vdW interacties.

Hoofdstuk 4 handelt over de adsorptie van benzeen op Pd(100) en Pd(110) als functie van de bedekkingsgraad. Omdat de Pd nanodeeltjes in industriële katalysatoren uit verschillende oppervlakken bestaan is het belangrijk te weten waar benzeen adsorbeert op deze oppervlakken en wat de afhankelijkheid van de bedekkingsgraad is, om zo benzeenhydrogenering op werkelijke Pd deeltjes accuraat te kunnen modelleren.

Een grote afname in stabiliteit van geadsorbeerd benzeen bij monolaagadsorptie in vergelijking tot een matige bedekkingsgraad is waar te nemen op beide oppervlakken, maar vooral op Pd(110). De vergelijking van deze resultaten met experimentele data laat toe de preferentiële adsorptieplaatsen voor benzeen op beide oppervlakken vast te stellen, wat het aantal mogelijke adsorptieplaatsen in grote mate doet afnemen.

In **Hoofdstuk 5** worden verschillende Pd- en Ni-gebaseerde bimetallische katalysatoren voor benzeenhydrogenering onderzocht. Ten eerste wordt de meest stabiele segregatietoestand voor het onbedekte oppervlak bepaald. Voor de meest stabiele toestand wordt benzeen geadsorbeerd op de verschillende stabiele adsorptieplaatsen, waarbij tegelijk mogelijke veranderingen in de segregatietoestand geïnduceerd door benzeenadsorptie geëvalueerd worden. Omwille van de lange duur van de berekeningen van benzeenadsorptie op deze katalysatoren worden correlaties geëvalueerd die benzeenhydrogenering relateren aan de koolstofadsorptie-energie en de gemiddelde energie van de d-elektronen van de oppervlakatomen van de katalysator. De benzeenhydrogeneringsactiviteit van de geselecteerde legeringen wordt ingeschat op basis van de reactiviteit van de eerste hydrogeneringsstap. Een goede correlatie tussen de activeringsenergie van deze stap en de adsorptie-energie van benzeen is waar te nemen, waaruit af te leiden valt dat de benzeenadsorptie-energie kan gebruikt worden als katalysatordescriptor die de essentiële verschillen tussen de katalysatoren beschrijft. De resultaten, uitgedrukt relatief ten opzichte van Pd(111), worden geïmplementeerd in het geconstrueerde microkinetisch model voor benzeenhydrogenering op Pd(111). De activiteit voor een breed bereik in de katalysatordescriptor en reactiecondities wijzen erop dat, voor temperaturen tussen 400 en 500 K, activiteitsmaxima zijn waar te nemen voor katalysatoren die benzeen 10-20 kJ mol^{-1} sterker binden dan Pd(111), zoals bvb. de legeringen Ni_3Ru en Ni_3Os.

In **Hoofdstuk 6** worden tot slot de belangrijkste conclusies van dit doctoraat gegeven, samen met mogelijkheden voor toekomstig werk in dit onderzoeksveld. Dit werk bevestigt de bruikbaarheid van ab initio berekeningen voor het verkrijgen van inzicht in katalytische reacties op moleculair niveau. De resultaten benadrukken het belang van twee effecten op de snelheidscoëfficiënten die vaak verwaarloosd worden, met name het effect van bedekkingsgraad en van der Waals interacties. Correcte beschrijving van beide effecten is vereist om katalytische activiteiten te kunnen beschrijven die in overeenstemming zijn met experimenteel waargenomen activiteiten. Tot slot toont dit werk ook aan dat theoretische berekeningen met dichtheidsfunctionaaltheorie veelbelovend zijn in de zoektocht naar nieuwe en actievere katalysatoren voor benzeenhydrogenering, een aanpak die ook kan toegepast worden voor andere industrieel belangrijke katalytische processen.

Chapter 1

Introduction

The catalytic hydrogenation of benzene is an important industrial reaction that consists of several elementary steps, comprising a complex catalytic network. The reaction mechanism and surface chemistry of benzene are not completely understood. Quantum chemistry (QM) and computational catalysis methods, such as density functional theory (DFT), can provide molecular level insights and accurate thermodynamic parameters, which may allow unraveling the complex reaction mechanism. The results from DFT can be further used to predict catalytic activities at actual reaction conditions, by implementing the ab initio calculated data in a microkinetic model. Finally, the catalytic activity trends of benzene hydrogenation from one metal to the next can be determined with QM methods. This allows to rationally design new catalysts with optimal properties, which is an important goal in industry to minimize energy and raw material consumption.

Aiming to design bimetallic catalysts for benzene hydrogenation, as a first step this work obtained a detailed DFT molecular level description of the catalytic hydrogenation of benzene on the commonly used Pd catalyst. The adsorption of benzene and hydrogen are the first elementary steps for hydrogenation, and the (111) is the most abundant surface plane in Pd industrial nanoparticles. Therefore, knowledge of the most stable catalysts surface coverages of benzene and hydrogen coadsorption on Pd(111) at typical hydrogenation conditions is essential. The expected coverages can be further considered to obtain a coverage dependence of the kinetics and thermodynamics for benzene hydrogenation. This dependence can be used to predict the catalytic activity at actual reaction conditions. Next, although the (111) is the most abundant surface of Pd nanoparticles, different activities can be achieved on catalysts exhibiting other typical surface planes, such as Pd(100) and Pd(110). Investigation of the preferred adsorption sites on these surfaces as a function of coverage is required for a future modeling of benzene hydrogenation on multifaceted Pd-based catalysts.

Having established a molecular level description of benzene hydrogenation on Pd(111), the next step in this work consists of understanding the variations in catalytic activity from one metal to the next. To this end catalyst descriptors, that represent the essential differences between the catalysts, need to be identified. Bimetallic catalysts exhibit catalytic activities that exceed those achieved with the parental monometallic catalysts. Therefore, bimetallic alloys obtained as combination of the commonly used Pd(111) and Ni(111) with transition metals are screened for benzene hydrogenation.

The first section of this introductory chapter presents the catalytic hydrogenation of benzene from a general point of view, and focuses first on the adsorption of reactants and secondly on the reaction mechanism. The last section of the chapter discusses the approach to perform catalyst design for benzene hydrogenation.

1.1 Catalytic hydrogenation of benzene

Catalysis is a process in which the rate of a chemical reaction is increased by a substance called catalyst, which unlike other reagents it is not consumed after the reaction cycle. As explained in 1895 by Wilhelm Ostwald, the catalyst modifies the reaction kinetics without affecting the position of the equilibrium of the overall reaction. More than 90% of the chemical processes in industry involve catalytic reactions.[1] Most of these reactions would not be possible without catalysts, and many others would require too strong reaction conditions. Therefore, catalysis offers an alternative path for chemical reactions, more complex but energetically much more favorable.

Benzene is the simplest aromatic compound and the most difficult to hydrogenate at moderate conditions.[2] Therefore, studies usually focus on benzene as a model for aromatic hydrogenation. The catalytic hydrogenation of aromatic compounds is a key step in the petroleum refinery, where this reaction is performed for various reasons. Firstly, the lower the aromatic concentration, the higher the cetane number of diesel fuels, which gives an indication of its combustion speed and is one of the factors to determine the quality of these fuels.[3] Secondly, a lower concentration of aromatics decreases the smoke point of jet fuels, [4] and this reaction is also performed to produce kerosene, lubricants, solvents, and to improve the viscosity index of engine oil.[4] Furthermore, the petrochemical industry catalytically hydrogenates benzene to produce cyclohexane, which is used to synthesize caprolactam and adipic acid, precursors of Nylon 6 and Nylon 6-6, respectively.[4] Moreover, this reaction is also an integral part in the production of clean fuels; aromatic compounds have hazardous and carcinogenic effects, and benzene, classified as human carcinogenic type A, is one of the most tightly regulated substances in the world.[5]

The catalytic hydrogenation of benzene, illustrated in Figure 1-1, can proceed in both homogeneous and heterogeneous phase; however, the industrial reaction is usually performed heterogeneously.[6] The typical industrial conditions are 300–500 K and 25–100 bar of H_2,[1] while benzene hydrogenation in the absence of a catalyst only occurs at very high temperatures (> 900 K) required to break the H–H hydrogen bond.[7] This reaction is highly exothermic, thus equilibrium limitations may impede a complete conversion of the reactants at high temperatures.[6]

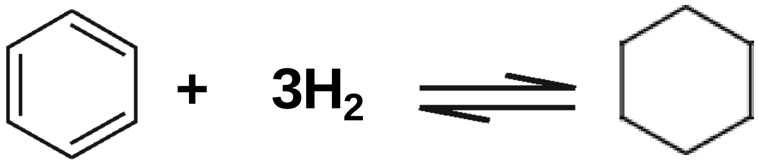

Figure 1-1: Hydrogenation of benzene to produce cyclohexane.

1.1.1 Adsorption on metal catalysts

The adsorption of hydrogen and benzene on the catalyst surface is the first elementary step for the catalytic hydrogenation toward cyclohexane. The adsorption strength of the reactants can strongly affect the reaction performance, hence the catalyst must facilitate both adsorption and surface reaction to yield optimal behavior.[8] Too weak bonding inhibits the conversion into products, and too strong bonding leads to completely covered surfaces without free sites for the other species, and hence no reaction.[8] Knowledge of the interaction of the reactants, benzene and hydrogen, with the surface can provide a better understanding of this reaction.

Benzene adsorption. The adsorption of benzene on the various Pd surfaces has been evaluated by a large variety of surface analytical techniques [9-29] and a lesser number of periodic density functional theory (DFT) studies. [30-32] The adsorption proceeds with the aromatic ring parallel to the surface, and large repulsive interactions between neighboring molecules at high coverage can force the tilting of benzene.[16, 33] Coverage can strongly affect the adsorption and hydrogenation thermodynamics. On the one hand, experimental studies have evaluated benzene adsorption at different coverages, however, the interpretation of the results is sometimes not straightforward. On the other hand, theoretical studies usually pertain to a single coverage to minimize the computational cost, thus evaluation of coverage effects by theoretical studied can provide extremely useful insights.

Benzene can be adsorbed at several adsorption sites on the most common surfaces of Pd, namely (111), (100), and (110) surfaces, as illustrated in Figure 1-2. On the most abundant Pd(111), the bridge(30) and hollow-hcp(0) have been proposed to be preferred.[9, 31] However, the change of the most stable site may occur with increasing coverage or with the presence of other coadsorbed species on the surface.[10] On Pd(100), a comparable benzene adsorption orientation as on Pd(111) has been proposed from the similar variation of photoemission spectra with emission angle observed on both surfaces.[34] On Pd(110), the detailed atomic structure of the adsorbed benzene and the corresponding site symmetry is still under debate despite the large number of studies that focused on this surface.[11, 12, 20, 24, 26, 29, 35] On the one hand, angle resolved UPS (ARUPS) [11] and HREELS measurements [12] lead to conclude that at saturation coverage benzene is tilted toward the [001] direction. On the other hand, STM studies[14, 25, 29] and quantum chemical calculations[26 35] indicate a rotation of benzene relative to the direction perpendicular to the surface, however, the molecular plane remains parallel to the surface.

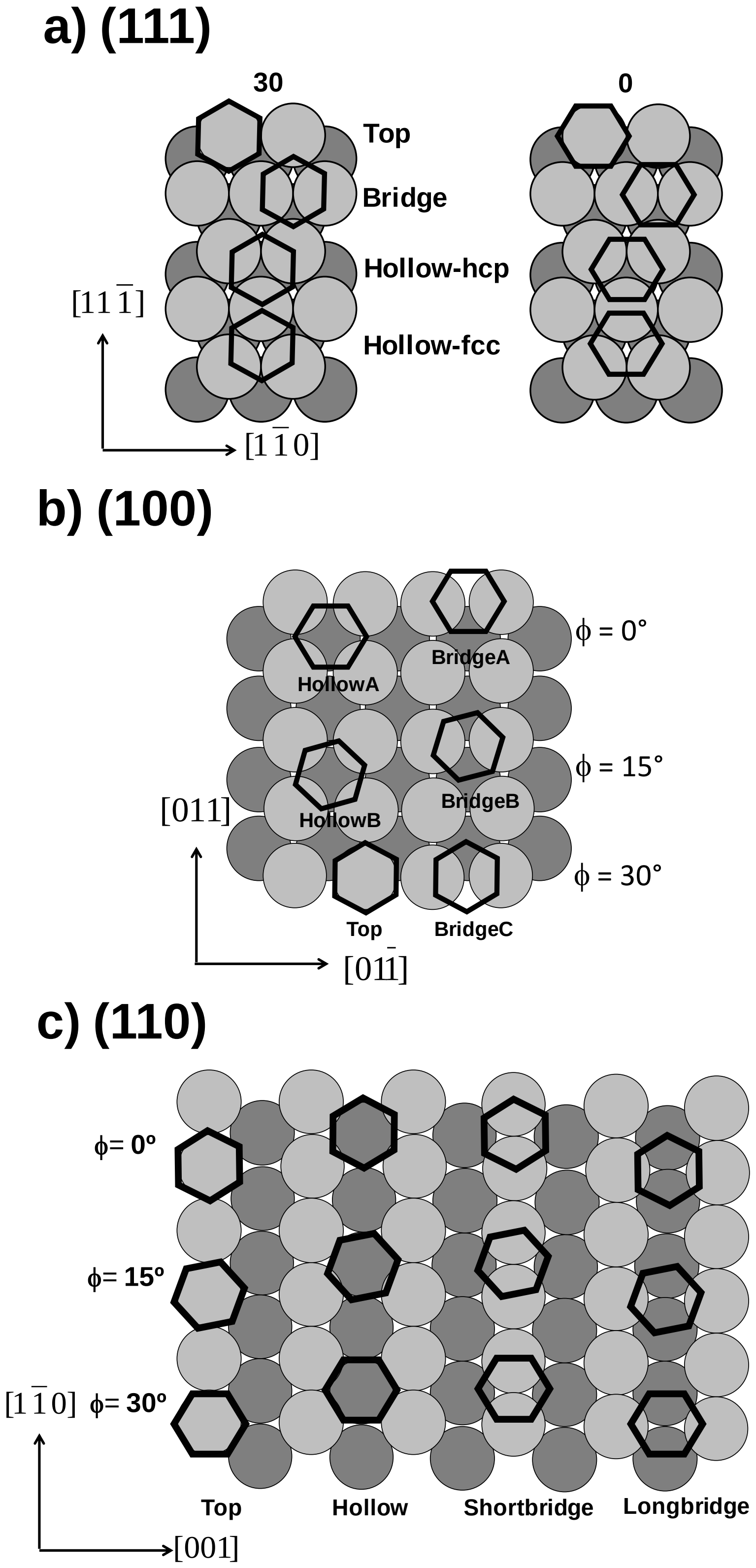

Figure 1-2: Benzene adsorption sites on (a) (111), (b) (100), and (c) (110) surfaces. Only the atoms in the two first top layers are shown, with different grey colors for easier visualization.

Hydrogen adsorption. The adsorption of hydrogen on Pd has been evaluated in detail[36-43], not only because this metal is industrially used to saturate aromatics but also due to the unique ability of this metal for hydride formation,[37] hydrogen storage,[44] fuel cells and hydrogen purification processes.[45, 46] Multiple adsorption sites have been identified for hydrogen on Pd(111), as illustrated in Figure 1-3, and the hollow *fcc* and *hcp* surface sites are usually reported as the energetically preferred adsorption sites up to saturation coverage.[38, 43, 47] The high pressures that are used in industry for hydrogenation reactions can, however, lead to hydrogen coverages above saturation, at which both surface and subsurface sites are populated.[48]

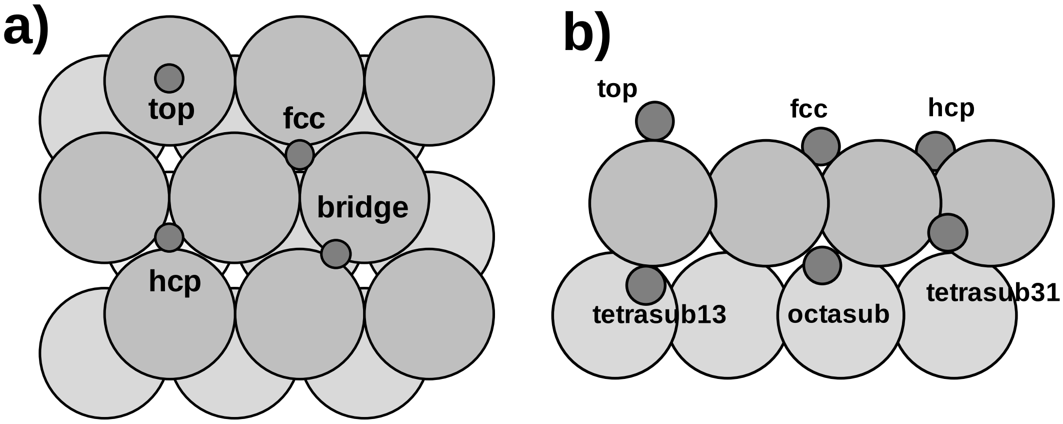

Figure 1-3: (a) Top view of the surface hydrogen adsorption sites on a (111) surface, with only the two first atomic top layers shown. (b) Side view of the (111) surface with the three subsurface sites together with surface sites.

Benzene and hydrogen coadsorption. Despite the large number of studies that have focused on the adsorption of benzene and hydrogen on metal surfaces, these studied often, if not always, consider the adsorption of single species at low temperatures and pressures. At reaction conditions, where both gas-phase species are present, the surface coverage may be different as compared to those observed for the separate species. Therefore, evaluation of the most stable coadsorption coverages that can be expected at typical hydrogenation conditions is required, since surface kinetics are strongly coverage dependent.

1.1.2 Mechanism for benzene hydrogenation

The hydrogenation of benzene to cyclohexane consists of the addition of six hydrogen atoms to saturate the carbon atoms (see Figure 1-1). This reaction is considered to proceed via the Horiuti-Polanyi mechanism,[49] i.e., the consecutive hydrogenation of the six carbon atoms. If a single adsorption site is considered for benzene on the surface, and if diffusion between different sites is neglected for the reaction intermediates, the complex reaction network from benzene to cyclohexane consists of twenty different hydrogenation reactions via 13 possible reactions paths, as illustrated in Figure 1-4. Accounting for additional adsorption sites for the intermediate species can increase the number of possible reaction paths above 180. Despite the large number of experimental and theoretical studies on the catalytic hydrogenation of benzene, there is no consensus on the exact reaction mechanism.[50] Some postulate that gas-phase hydrogen reacts with chemisorbed benzene following an Eley-Rideal mechanism. [51, 52] However, the general agreement is that the reaction proceeds with both chemisorbed hydrogen and hydrocarbon species, [50, 53-57] mechanism referred to as Langmuir-Hinshelwood-Hougen-Watson. Furthermore, competition between benzene and hydrogen for the active sites has been claimed,[58-60] and denied by others.[61-65] The first hydrogen addition has often been considered as the rate determining step on Ni, [57, 65, 66] Pd, [65] or Pt,[67, 68] although the fourth [69] and fifth reactions[70] have also been proposed on Pt, or for Ni catalysts it has been considered that the six sequential hydrogenation steps have the same rate coefficient.[16, 20] Including dehydrogenation reactions in the model could explain the formation of carbonaceous species [67] or the decrease in free sites because of their presence on the surface.[53] However, benzene dehydrogenation is neither thermodynamically nor kinetically favored compared to hydrogenation.[71] The presence of adsorbed cyclohexene on the surface has been reported during benzene hydrogenation experiments,[72-77] but the formation of gas-phase cyclohexene is thermodynamically less favorable as compared to the major product cyclohexane.[72, 73] Since cyclohexane is typically expected to desorb fast and irreversibly,[56] surface inhibition by adsorbed cyclohexane is discarded.[78] The catalytic activity reaches a maximum as a function of temperature, [57, 59, 62, 79, 80] which is explained by the balance between the decrease in surface concentration of the reactants with temperature and the increase in surface reaction rate coefficients.

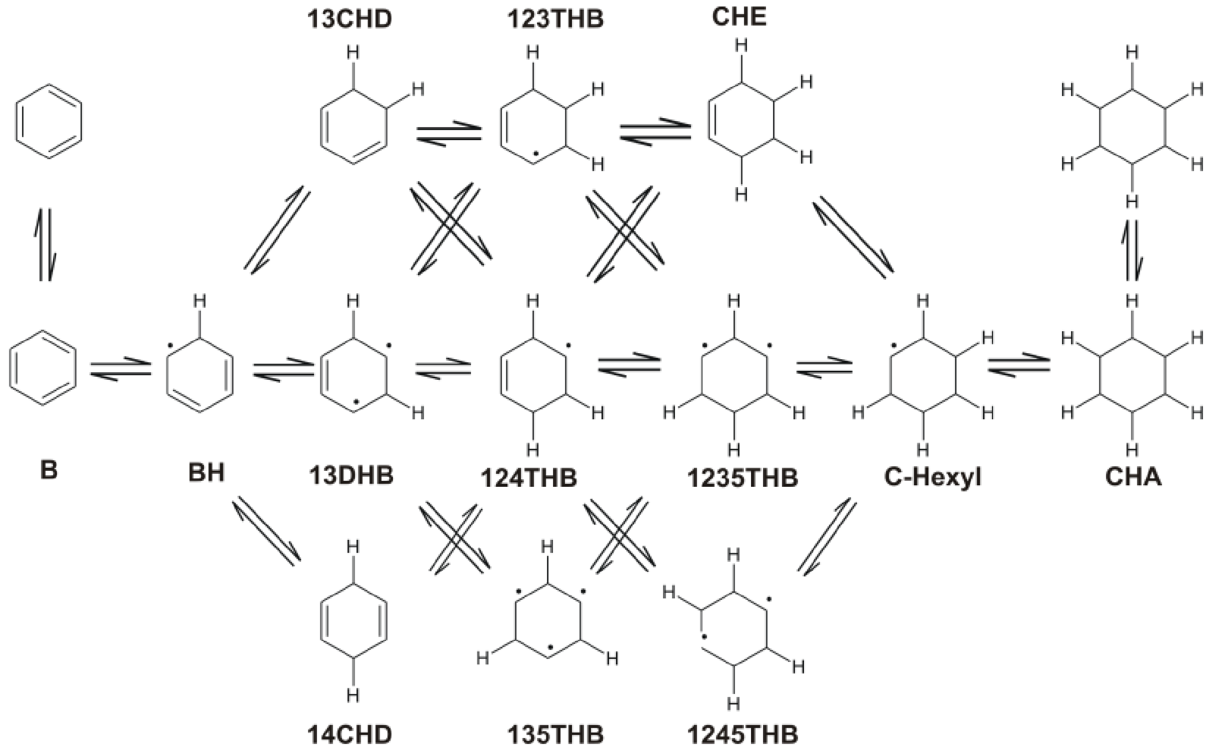

Figure 1-4: Reaction network of the catalytic hydrogenation of benzene to cyclohexane, considering a single adsorption site for the surface intermediates.

1.2 Catalyst design for benzene hydrogenation

One of the main goals in industry is to develop new catalysts with novel catalytic properties. These catalysts can allow e.g. to use milder reaction conditions to achieve the same conversion as common catalysts, therefore, reducing costs for installation and operation to a large extent. Furthermore, the development of new catalysts can allow decreasing the large amount of expensive catalysts that is required for industrial reactions, such as on hydrotreatment processes of oil fractions.

Experimental design of catalysts for industrial reactions is currently performed by trial-and-error techniques, and a more efficient, knowledge-based approach is required. DFT methods are extremely useful to screen the activity on different catalysts, searching for materials with optimal activity. Catalysts properties that show the essential differences between the catalysts need to be identified, i.e., catalysts descriptors, such as the adsorption energy[81] or the d-band center.[82]

Transition metals such as Ni and Pd are very good catalysts for hydrogenation reactions because they can achieve high activity. However, these expensive metals are easily deactivated by poisons such as sulfur containing organic compounds, hence more sulfur tolerant metal catalysts are needed. The catalytic hydrogenation over bimetallic catalyst exhibits activities, selectivities, and poisoning tolerance that exceed those obtained from the parent metal catalysts.[83] Particularly, large number of studies have evaluated Pd-Pt catalysts because they are more active than Pd and Pt separately,[4, 84, 85] similarly as Pd-Rh, Pd-Ir, Pd-Re, [86-88] Pd-Cr, and Pd-W catalysts.[89] Alloying Pd with other metals can also enhance its sulfur resistance.[3, 85, 90-93] Particularly, excellent sulfur resistances have been reported for supported Pt-Pd catalysts.[90, 94] Although this work does not evaluate selectivity (nor poisoning tolerance), selective hydrogenation toward a desired product is even of greater importance than activity for some processes, e.g. in the hydrogenation of alkyne molecules from ethylene or propylene feed to produce polymers, where Pd catalysts are used.[95] In benzene hydrogenation, cyclohexane is the main reaction product[72, 73] and is thermodynamically preferred. [96] However, the selective hydrogenation to cyclohexene can be of greater interest in the petrochemical industry to produce polymers,[97] due to some economical advantages [97] and because it is also more easily separated from benzene than cyclohexane.[98] Ru-based catalysts are the most effective material in selective hydrogenation of benzene to cyclohexene. [99-107]

The design of bimetallic catalysts with specific properties has also been applied because of the large number of possible combinations that can be obtained with the appropriate synthesis techniques.[108] Two main factors contribute to the differences from monometallic to bimetallic catalysts. First, the electronic structure of the alloy differs due to the coupling between electronic states of the different metals involved. Secondly, there are also geometrical factors governing the differences between bimetallic and monometallic catalysts, namely site blocking, ensemble effects, template effects and coordination effects.[102] For bimetallic surfaces with the same crystallographic structure, e.g. the (111) surface plane, the effect of alloying should be ascribed to variations in the electronic structure, and particularly in the d-band for transition metal alloys. The average energy of the electrons in the occupied *d* states, d-band center ($\varepsilon_{d\text{-band}}$), has been shown in previous works to be a good catalyst descriptor of bond energies for different mono and bimetallic surfaces.[82, 109-113]

In this work, design of catalysts for benzene hydrogenation is performed by screening bimetallic surfaces obtained by alloying Pd(111) and Ni(111) with other transition metals. The observed trend in reactivity needs to be quantitatively related to the appropriate catalyst descriptor (e.g. the adsorption enthalpy or d-band center). Implementation of the catalyst descriptors in a microkinetic model previously obtained on Pd(111) for benzene hydrogenation may allow assessing activities exhibited by virtual candidate catalysts with simulations for a broad range of catalyst descriptor values and operating conditions. The developed modeling tools will also allow predicting a maximum yield of the desired products as a function of both the catalyst descriptors and the operating conditions.

1.3 Objectives and outline of this work

The aim of this research is to develop the modeling tools to perform a rational design of bimetallic catalysts from density functional theory calculations (DFT) for the catalytic hydrogenation of benzene. The first step to pursued this goal is to obtain a detailed molecular understanding of the surface chemistry during benzene adsorption and hydrogenation on Pd. This metal has been chosen because it is commonly used for catalytic hydrogenation, with improved activity as compared to other transition metals. Special attention is given to the effect of coverage on the adsorption and reaction kinetics and thermodynamics, which is often neglected in theoretical studies. In a second step, Pd-based and Ni-based bimetallic catalysts are screened for benzene hydrogenation, describing the calculated trends with catalysts properties that allow predicting those alloys with optimal activity as a function of the conditions.

Chapter 2 studies the adsorption and coadsorption of hydrogen and benzene on Pd(111). This is evaluated as a function of the coverage, and the results are used to construct the thermodynamic phase diagrams that indicate which catalyst surface coverages should be expected as a function of the conditions.

Chapter 3 performs a DFT coverage dependence study of the kinetics and thermodynamics of benzene hydrogenation on Pd(111). The results are used to construct a coverage-dependent microkinetic model that predicts catalytic activity, explicitly accounting for coverage dependence on the rate coefficients calculated with DFT.

Chapter 4 focuses on benzene adsorption on Pd(100) and Pd(110) as a function of coverage. These surfaces are found on Pd nanoparticles, and knowledge of the most stable benzene adsorption sites as a function of coverage can be applied in future studies of benzene hydrogenation on multifaceted particles.

Chapter 5 aims to search for optimal catalysts for benzene hydrogenation. The metal catalysts that are considered are bimetallic surfaces prepared by modifying Pd(111) and Ni(111) with other transition metals. The most stable segregation state of the catalyst is first evaluated. For this state, benzene adsorption is evaluated in detail, searching for correlations with the computationally less expensive carbon adsorption and d-band center descriptors. As a first step for the design of bimetallic catalysts, the first hydrogenation of benzene is screened, and catalysts descriptors are implemented in the microkinetic model obtained for Pd(111) to search for alloys that yield optimal activity as a function of the conditions.

Chapter 6 summarizes the main conclusions of this PhD, and proposes important points that should be further investigated to obtain a detailed model that can describe benzene hydrogenation network on multifaceted Pd-based catalysts.

Additional information on the methodology, together with e.g. adsorption geometries, adsorption energies, vibrational frequencies, segregation energies, and activation energies for this PhD is shown in **Appendices A-D**

This PhD thesis comprises a series of journal papers published within this research and the manuscripts that are to be submitted for publication in the near future. Therefore, from Chapter 2 to Chapter 5, each is readable as a self-standing part.

1.4 References

1. J. Hagen, *Industrial catalysis: a practical approach*, Wiley-VCH, Weinheim ; New York, 1999.
2. A. Stanislaus and B. H. Cooper, *Catal Rev*, 1994, **36**, 75-123.
3. B. H. Cooper and B. B. L. Donnis, *Appl. Catal., A*, 1996, **137**, 203-223.
4. M. Sanati, B. Harrysson, M. Faghihi, B. Gevert and S. Jaras, in *Catalysis*, ed. J. J. Spivey, Royal Society of Chemistry, Cambridge, Editon edn., 2002, pp. 1-42.
5. A. C. Capleton and L. S. Levy, *Chem. Biol. Interact.*, 2005, **153**, 43-53.

6. K. Weissermel and H.-J. Arpe, *Industrial organic chemistry*, 4th edn., Wiley-VCH, Weinheim, 2003.
7. M. C. Schoenmaker-Stolk, *Kinetics and mechanism of benzene hydrogenation over supported Ru, Cu and Ru-Cu catalysts*, Delft university press, Delft, , 1986.
8. J. K. Norskov, M. Scheffler and H. Toulhoat, *Mrs Bull*, 2006, **31**, 669-674.
9. H. Ohtani, B. E. Bent, C. M. Mate, M. A. Van Hove and G. A. Somorjai, *Appl. Surf. Sci.*, 1988, **33-4**, 254-260.
10. H. Ohtani, M. A. Van Hove and G. A. Somorjai, *J. Phys. Chem.*, 1988, **92**, 3974-3982.
11. F. P. Netzer, G. Rangelov, G. Rosina, H. B. Saalfeld, M. Neumann and D. R. Lloyd, *Phys. Rev. B: Condens. Matter Mater. Phys.*, 1988, **37**, 10399-10402.
12. M. Fujisawa, T. Sekitani, Y. Morikawa and M. Nishijima, *J. Phys. Chem.*, 1991, **95**, 7415-7422.
13. A. Barbieri, M. A. Van Hove and G. A. Somorjai, *Surf. Sci.*, 1994, **306**, 261-268.
14. J. Yoshinobu, H. Tanaka, T. Kawai and M. Kawai, *Phys. Rev. B: Condens. Matter Mater. Phys.*, 1996, **53**, 7492-7495.
15. G. Hamm, T. Schmidt, J. Breitbach, D. Franke, C. Becker and K. Wandelt, *Surf. Sci.*, 2004, **562**, 170–182.
16. H. Hoffmann, F. Zaera, R. M. Ormerod, R. M. Lambert, L. P. Wang and W. T. Tysoe, *Surf. Sci.*, 1990, **232**, 259-265.
17. R. M. Lambert, A. F. Lee, K. Wilson, A. Goldoni, A. Baraldi and G. Paolucci, *J Phys Chem B*, 2000, **104**, 11729-11733.
18. G. D. Waddill and L. L. Kesmodel, *Phys. Rev. B: Condens. Matter Mater. Phys.*, 1985, **31**, 4940-4946.
19. W. T. Tysoe, R. M. Ormerod, R. M. Lambert, G. Zgrablich and A. Ramirez-Cuesta, *J. Phys. Chem.*, 1993, **97**, 3365-3370.
20. J. Zhou, S. Dag, S. D. Senanayake, B. C. Hathorn, et al., *Phys. Rev. B: Condens. Matter Mater. Phys.*, 2006, **74**, 125318.
21. L. L. Kesmodel, *Phys. Rev. Lett.*, 1984, **53**, 1001-1004.
22. V. H. Grassian and E. L. Muetterties, *J. Phys. Chem.*, 1987, **91**, 389-396.
23. J. F. M. Aarts and N. R. M. Sassen, *Surf. Sci.*, 1989, **214**, 257-275.
24. M. Nishijima, M. Fujisawa, T. Takaoka and T. Sekitani, *Surf. Sci.*, 1993, **283**, 121-125.
25. J. Yoshinobu, M. Kawai, I. Imamura, F. Marumo, et al., *Phys. Rev. Lett.*, 1997, **79**, 3942-3945.
26. G. Treboux and M. Aono, *J. Phys. Chem. B*, 1997, **101**, 4620-4622.
27. G. L. Nyberg and N. V. Richardson, *Surf. Sci.*, 1979, **85**, 335-352.
28. P. Hofmann, K. Horn and A. M. Bradshaw, *Surf. Sci.*, 1981, **105**, L260-L264.
29. J. Yoshinobu, M. Kawai, I. Imamura, F. Marumo, et al., *J. Electron. Spectrosc. Relat. Phenom.*, 1998, **88**, 997-1002.
30. M. C. T. D. M. Cruz, J. W. D. M. Carneiro, D. A. G. Aranda and M. Buhl, *J. Phys. Chem. C*, 2007, **111**, 11068-11076.

31. C. Morin, D. Simon and P. Sautet, *J. Phys. Chem. B*, 2004, **108**, 5653-5665.
32. J. Carrasco, W. Liu, A. Michaelides and A. Tkatchenko, *J. Chem. Phys.*, 2014, **140**, 084704.
33. A. F. Lee, K. Wilson, R. M. Lambert, A. Goldoni, A. Baraldi and G. Paolucci, *J. Phys. Chem. B*, 2000, **104**, 11729-11733.
34. D. R. Lloyd, C. M. Quinn and N. V. Richardson, *Solid State Commun.*, 1977, **23**, 141-145.
35. F. Favot, A. Dal Corso and A. Baldereschi, *Europhys. Lett.*, 2000, **52**, 698-704.
36. H. Conrad, G. Ertl and E. E. Latta, *Surf. Sci.*, 1974, **41**, 435-446.
37. T. E. Felter, E. C. Sowa and M. A. Vanhove, *Phys. Rev. B: Condens. Matter Mater. Phys.*, 1989, **40**, 891-899.
38. J. F. Paul and P. Sautet, *Phys. Rev. B: Condens. Matter Mater. Phys.*, 1996, **53**, 8015-8027.
39. W. Dong, V. Ledentu, P. Sautet, A. Eichler and J. Hafner, *Surf. Sci.*, 1998, **411**, 123–136.
40. U. Muschiol, P. K. Schmidt and K. Christmann, *Surf. Sci.*, 1998, **395**, 182-204.
41. O. M. Lovvik and R. A. Olsen, *Phys. Rev. B: Condens. Matter Mater. Phys.*, 1998, **58**, 10890-10898.
42. A. Winkler, *Appl. Surf. Sci.*, 2009, **256**, 1114-1119.
43. C. Chizallet, G. Bonnard, E. Krebs, L. Bisson, C. Thomazeau and P. Raybaud, *J. Phys. Chem. C*, 2011, **115**, 12135-12149.
44. B. D. Adams, C. K. Ostrom, S. A. Chen and A. C. Chen, *J. Phys. Chem. C*, 2010, **114**, 19875–19882.
45. A. Basile, *Top. Catal.*, 2008, **51**, 107-122.
46. S. H. Israni, B. K. R. Nair and M. P. Harold, *Catal. Today*, 2009, **139**, 299-311.
47. G. W. Watson, R. P. K. Wells, D. J. Willock and G. J. Hutchings, *J. Phys. Chem. B*, 2001, **105**, 4889-4894.
48. J. A. Konvalinka and J. J. F. Scholten, *J. Catal.*, 1977, **48**, 374-385.
49. P. Horiuti and M. Polanyi, *T Faraday Soc*, 1934, **30**, 1164-1172.
50. S. S. E. H. Elnashaie and S. S. El Shishini, *Modelling, simulation and optimization of industrial fixed bed catalytic reactors*, Gordon and Breach, Philadelphia, 1993.
51. J. P. G. Kehoe and J. B. Butt, *J Appl Chem Biotechn*, 1972, **22**, 23-&.
52. M. Xi and B. E. Bent, *J Vac Sci Technol B*, 1992, **10**, 2440-2446.
53. P. Chou and M. A. Vannice, *J. Catal.*, 1987, **107**, 140-153.
54. F. Mittendorfer and J. Hafner, *J. Phys. Chem. B*, 2002, **106**, 13299-13305.
55. M. V. Rahaman and M. A. Vannice, *J. Catal.*, 1991, **127**, 251-266.
56. M. Saeys, M. F. Reyniers, M. Neurock and G. B. Marin, *J. Phys. Chem. B*, 2005, **109**, 2064-2073.
57. R. Z. C. Vanmeerten and J. W. E. Coenen, *J. Catal.*, 1977, **46**, 13-24.

58. P. C. Aben, J. C. Platteeu and B. Stoutham, *Recl. Trav. Chim. Pays-Bas*, 1970, **89**, 449.
59. J. M. Orozco and G. Webb, *Appl. Catal.*, 1983, **6**, 67-84.
60. L. P. Lindfors, T. Salmi and S. Smeds, *Chem. Eng. Sci.*, 1993, **48**, 3813-3828.
61. H. A. Franco and M. J. Phillips, *J. Catal.*, 1980, **63**, 346-354.
62. M. A. Keane and P. M. Patterson, *Ind. Eng. Chem. Res.*, 1999, **38**, 1295-1305.
63. R. Z. C. Van Meerten, T. F. M. Degraaf and J. W. E. Coenen, *J. Catal.*, 1977, **46**, 1-12.
64. R. Z. C. Van Meerten, A. C. M. Verhaak and J. W. E. Coenen, *J. Catal.*, 1976, **44**, 217-225.
65. U. K. Singh and M. A. Vannice, *Aiche J*, 1999, **45**, 1059-1071.
66. C. Mirodatos, J. A. Dalmon and G. A. Martin, *J. Catal.*, 1987, **105**, 405-415.
67. S. D. Lin and M. A. Vannice, *J. Catal.*, 1993, **143**, 539-553.
68. K. M. Bratlie, C. J. Kliewer and G. A. Somorjai, *J. Phys. Chem. B*, 2006, **110**, 17925-17930.
69. J. W. Thybaut, M. Saeys and G. B. Marin, *Chemical Engineering Journal*, 2002, **90**, 117-129.
70. S. L. Lu, W. W. Lonergan, J. P. Bosco, S. R. Wang, et al., *J. Catal.*, 2008, **259**.
71. M. Saeys, M. F. Reyniers, M. Neurock and G. B. Marin, *J. Phys. Chem. B*, 2003, **107**, 3844-3855.
72. Y. Derbents, P. Tetenyi and Z. Paal, *Z Phys Chem Neue Fol*, 1972, **80**, 51-&.
73. P. Tetenyi and Z. Paal, *Z Phys Chem Neue Fol*, 1972, **80**, 63-&.
74. X. C. Su, K. Y. Kung, J. Lahtinen, Y. R. Shen and G. A. Somorjai, *J. Mol. Catal. A: Chem.*, 1999, **141**, 9-19.
75. M. Yang, K. C. Chou and G. A. Somorjai, *J. Phys. Chem. B*, 2003, **107**, 5267-5272.
76. D. P. Land, C. L. Pettiettehall, R. T. Mciver and J. C. Hemminger, *J. Am. Chem. Soc.*, 1989, **111**, 5970-5972.
77. K. M. Bratlie, L. D. Flores and G. A. Somorjai, *J. Phys. Chem. B*, 2006, **110**, 10051-10057.
78. T. Takahashi, K. Yamashita, T. Kai and I. Fujiyoshi, *Can J Chem Eng*, 1986, **64**, 1008-1013.
79. P. Chou and M. A. Vannice, *J. Catal.*, 1987, **107**, 129-139.
80. M. A. Vannice and W. C. Neikam, *J. Catal.*, 1971, **23**, 401-405.
81. S. L. Lu, C. A. Menning, Y. X. Zhu and J. G. Chen, *ChemPhysChem*, 2009, **10**, 1763-1765.
82. B. Hammer and J. K. Norskov, *Surf. Sci.*, 1995, **343**, 211-220.
83. J. G. Chen, C. A. Menning and M. B. Zellner, *Surf Sci Rep*, 2008, **63**, 201-254.
84. B. Pawelec, V. La Parola, S. Thomas and J. L. G. Fierro, *J. Mol. Catal. A: Chem.*, 2006, **253**, 30-43.

85. R. M. Navarro, B. Pawelec, J. M. Trejo, R. Mariscal and J. L. G. Fierro, *J. Catal.*, 2000, **189**.
86. Y. M. Chung and H. K. Rhee, *J. Mol. Catal. A: Chem.*, 2003, **206**, 291-298.
87. S. Albonetti, G. Baldi, A. Barzanti, E. R. Castellon, et al., *Catal. Lett.*, 2006, **108**, 197-207.
88. A. S. Rocha, E. L. Moreno, G. P. M. da Silva, J. L. Zotin and A. C. Faro, *Catal. Today*, 2008, **133**.
89. L. J. Hu, G. F. Xia, L. L. Qu, C. Li, Q. Xin and D. D. Li, *J. Mol. Catal. A: Chem.*, 2001, **171**, 169-179.
90. W. H. Qian, Y. Yoda, Y. Hirai, A. Ishihara and T. Kabe, *Appl. Catal., A*, 1999, **184**, 81-88.
91. L. J. Hu, H. Nie, L. L. Qu, G. F. Xia, Y. H. Shi and D. D. Li, *Abstr Pap Am Chem S*, 1999, **217**, U804-U804.
92. H. Yasuda, T. Kameoka, T. Sato, N. Kijima and Y. Yoshimura, *Appl. Catal., A*, 1999, **185**.
93. Y. Yoshimura, H. Yasuda, T. Sato, N. Kijima and T. Kameoka, *Appl. Catal., A*, 2001, **207**.
94. H. Yasuda and Y. Yoshimura, *Catal. Lett.*, 1997, **46**, 43-48.
95. D. Teschner, J. Borsodi, Z. Kis, L. Szentmiklosi, et al., *J. Phys. Chem. C*, 2010, **114**, 2293-2299.
96. F. Hartog and P. Zwietering, *J. Catal.*, 1963, **2**, 79-81.
97. W. F. Hoelderich and G. Dahlhoff, *Chem Innov*, 2001, **31**, 29-40.
98. G. C. Bond, *Metal-catalysed reactions of hydrocarbons*, Springer Science, New York, 2005.
99. S. C. Hu and Y. W. Chen, *Ind. Eng. Chem. Res.*, 1997, **36**, 5153-5159.
100. H. Nagahara, M. Ono, M. Konishi and Y. Fukuoka, *Appl. Surf. Sci.*, 1997, **121**, 448-451.
101. S. C. Hu and Y. W. Chen, *Ind. Eng. Chem. Res.*, 2001, **40**, 6099-6104.
102. G. Held, *J. Phys.: Condens. Matter*, 2003, **15**.
103. Y. J. Zhao, J. Zhou, J. G. Zhang and S. D. Wang, *Catal. Commun.*, 2008, **9**, 459-464.
104. P. Q. Yuan, B. Q. Wang, Y. M. Ma, H. M. He, Z. M. Cheng and W. K. Yuan, *J. Mol. Catal. A: Chem.*, 2009, **309**, 124-130.
105. Z. Y. Liu, H. J. Sun, D. B. Wang, W. Guo, et al., *Chinese J Catal*, 2010, **31**, 150-152.
106. C. Fan, Y. A. Zhu, X. G. Zhou and Z. P. Liu, *Catal. Today*, 2011, **160**, 234-241.
107. H. J. Sun, W. Guo, X. L. Zhou, Z. H. Chen, Z. Y. Liu and S. C. Liu, *Chinese J Catal*, 2011, **32**, 1-16.
108. J. H. Sinfelt, *Bimetallic catalysts : discoveries, concepts, and applications*, Wiley, New York, 1983.
109. V. Pallassana and M. Neurock, *J. Catal.*, 2000, **191**, 301-317.

110. C. Klanner, D. Farrusseng, L. Baumes, M. Lengliz, C. Mirodatos and F. Schuth, *Angew Chem Int Edit*, 2004, **43**, 5347-5349.

111. M. C. Escano, T. Q. Nguyen, H. Nakanishi and H. Kasai, *J. Phys.: Condens. Matter*, 2009, **21**.

112. N. Schweitzer, H. L. Xin, E. Nikolla, J. T. Miller and S. Linic, *Top. Catal.*, 2010, **53**, 348-356.

113. J. K. Norskov, T. Bligaard, J. Rossmeisl and C. H. Christensen, *Nat Chem*, 2009, **1**, 37-46.

Chapter 2

Thermodynamic study of benzene and hydrogen coadsorption on Pd(111)

The following pages include the paper:

G. Candela-Rodriguez, M. K. Sabbe, M.–F. Reyniers, J.–F. Joly and G. B. Marin, Thermodynamic study of benzene and hydrogen coadsorption on Pd(111).

Physical Chemistry Chemical Physics **16** (2014) 23754 – 23768

Abstract

Periodic density functional theory (DFT) has been used to study the coadsorption of hydrogen and benzene on Pd(111). The most stable coverages are predicted by constructing the thermodynamic phase diagram as a function of gas-phase temperature and pressure. The common approximation that neglects vibrational contributions to the surface Gibbs free energy, using the PW91 functional, is compared to the one that includes vibrational contributions. Higher coverages are predicted to be thermodynamically the most stable including vibrational frequencies, mainly due to the different entropy contributions. The first approach is also compared to the one using the (optPBE-vdW) vdW-DF functional without vibrational contributions, which predicts higher benzene coverages for benzene adsorption, and lower hydrogen coverages for hydrogen adsorption and coadsorption with a fixed benzene coverage. Inclusion of vibrational contributions with the optPBE-vdW functional has not been implemented due to computational constraints. However, an estimate of the expected result is proposed by adding PW91 vibrational contributions to the optPBE-vdW electronic energies, and under typical hydrogenation conditions high coverages of about $\theta_H = 0.89$ are expected. Inclusion of vibrational contributions to the surface Gibbs free energy and a proper description of van der Waals interaction are recommended to predict the thermodynamically most stable surface coverage.

2.1 Introduction

Benzene is a type A carcinogenic and stringent legislations enforce to reduce its concentration.[1] The catalytic hydrogenation of benzene is industrially performed to meet fuel specifications and to obtain intermediate compounds for the production of nylon polymers.[2] Optimal catalysts are required in industry to improve the efficiency of hydrogenation reactions, and quantum chemical modeling can be used to better understand these catalytic reactions. The adsorption of benzene and hydrogen on metal surfaces has been the subject of several studies. These studies mostly focus on the adsorption of single species at low temperatures and/or pressures. However, hydrogenation reactions are usually performed at high hydrogen pressure and moderate temperatures (350-550 K), hence high concentrations of hydrogen can be expected on the metallic surface. Since surface rate coefficients may be strongly coverage dependent, evaluation of the expected coverages at typical hydrogenation conditions is required. Therefore, this work focuses first on the adsorption of hydrogen and benzene on Pd(111), and evaluates their coadsorption as a function of hydrogen coverage.

Hydrogen adsorption has been extensively studied on Pd catalysts.[3-10] This is not only because Pd nanoparticles are used in industry to saturate aromatics, but also due to the unique ability of this metal for hydride formation,[4] which is also applied for hydrogen storage,[11] fuel cells[12] and hydrogen purification processes.[13] The adsorption of hydrogen on the most abundant (111) surface plane of Pd is not activated[10, 14] and, although multiple adsorption sites have been identified for hydrogen, the three-fold hollow surface site is usually reported as the energetically preferred one below saturation.[5, 10, 15] The high pressures used in industry can, however, lead to hydrogen coverages above saturation, *i.e.* coverages at which population of both surface and subsurface sites has been observed on Pd.[16] The latter has been reported to be even more reactive than surface hydrogen. [17-19]

Benzene adsorbs with the aromatic ring parallel to the Pd(111) surface, as confirmed by theoretical[20-24] and experimental studies.[25-31] However, large repulsive interactions between neighboring molecules at very high coverages force the tilting of the adsorbates.[29-31] The coadsorption of benzene with other species is expected to affect adsorption geometries, which can also lead to the tilting of benzene.[30] Tilting has been investigated previously for the coadsorption of CO and H_2[32], alkenes/alkynes species and H_2 [10, 33, 34], and benzene and CO [35-42]. However, to our knowledge, only a single surface science study has evaluated the coadsorption of benzene and hydrogen, and this on Ru(0001).[43] HREELS and TPD experiments at half and close to benzene saturation coverage were performed, and only small differences compared to the adsorption of the single species were observed.[43] Others have estimated thermodynamic parameters for benzene and hydrogen adsorption by fitting a kinetic model to experimental benzene hydrogenation data obtained on Pd catalysts.[44, 45] The competition of both species for the same surface sites has been proposed,[46] similarly as for toluene hydrogenation.[47] However, the non competitive adsorption has also been reported.[48-51] In addition, Mirodatos [52] showed with an isotopic transient study of benzene hydrogenation that the Ni surface is mainly covered with adsorbed hydrogen, in contrast to the usually reported assumption of high benzene coverage associated with the zero partial benzene reaction order. [53, 54] Weakly adsorbed hydrogen has also been reported as the only reactant,[45, 51] without however discarding the existence of spectator forms of adsorbed hydrogen. [53]

Density Functional Theory (DFT) can be easily implemented in a thermodynamic model to predict the preferred coverages on the catalyst as a function of the macroscopic state variables. This approach has been previously used to evaluate relevant industrial processes and catalysts, such as buta-1,3-diene and but-1-ene adsorption on Pd(111) and Pd(100) under

H_2 pressure,[10] supported Pt clusters,[55] or for the study of the supports for HDS reactions [56].Often, if not always, vibrational contributions to the surface Gibbs free energy are neglected and the inclusion of these may give a more accurate picture for large molecules such as benzene. Also, the common gradient-corrected functionals used in DFT to describe the attractive and repulsive electron interactions, *i.e.* PW91 or PBE functionals, underestimate long-range dispersive interactions such as van der Waals (vdW).[57] These dispersive interactions can affect binding or activation energies for adsorption and reaction of organic molecules on metal surfaces.[58] The first principles vdW-DF method introduced by Dion and co-workers[59] properly accounts for these important vdW interactions and calculates the energy of the exchange and correlation term as the sum of the exchange energy from the generalized gradient approximation (GGA) functional, the local correlation energy from the Local Density Approximation (LDA) functional and includes the non-local correlation energy from electron densities interacting via a model response function.[57]

In the present work periodic DFT calculations are performed to investigate the effect of coverage on adsorption geometries and energies for hydrogen and benzene on Pd(111), and also for their coadsorption, using gradient-corrected (PW91) and vdW-DF (optPBE-vdW) functionals. Surface Gibbs free energies are used to construct thermodynamic phase diagram allowing to predict the most stable catalyst coverage as a function of gas-phase conditions. The common approach that neglects vibrational contributions to the surface Gibbs free energy, and uses the PW91 to optimize the geometries, is first compared to the approach that includes vibrational contributions with the same PW91 functional, and second to the approach that uses the optPBE-vdW functional, also neglecting vibrational contributions. Since optPBE-vdW vibrational contributions have not been calculated due to computational limitations, the thermodynamic phase diagram constructed by adding PW91 vibrational contributions to the vdW-DF results is proposed to obtain an estimate of the expected result.

2.2 Methodology

2.2.1 Electronic energy calculations

Periodic DFT calculations are performed with the Vienna Ab initio Simulation Package (VASP)[60-63] to calculate geometries and electronic energies at 0 K. The calculations are performed with pseudopotentials and plane-wave basis sets by using the projector augmented wave method (PAW) [64, 65] with a 400 eV cut-off kinetic energy. The first-order Methfessel Paxton method is applied to describe the partial occupancies close to the Fermi level, applying a smearing width of 0.3 eV. Brillouin-zone integration for surface slab calculations is done on a 5×5×1 Monkhorst-Pack grid,[66] while gas-phase calculations are performed considering only the Γ point. With these settings, the magnetization obtained for the bulk system using spin-polarized calculations is below zero, and the adsorption energy of benzene is converged within 5 kJ mol^{-1}. As a result, non-magnetic systems are considered with the consequent save in computational cost. The default DFT functional applied is the non-local generalized gradient Perdew-Wang PW91 functional.[67, 68] The inclusion of van der Waals interactions (vdW) has been investigated by performing the optimization with the vdW-DF approach[59, 69], using the opt-PBE functional implemented in VASP by Klimeš et al.[57, 70]. The optPBE-vdW functional is used within the vdW-DF approach because it has shown to provide with results that are in good agreement with experimental data for benzene adsorption on Pd(111). [71, 72]

The iterative solution of the Kohn-Sham equations in the electronic minimization is performed with the quasi-Newton RMM-DIIS algorithm, and the molecular geometry is optimized using the conjugate-gradient algorithm for geometries far from the minimum. The electronic iteration is performed until the energy convergence criterion of 10^{-8} eV is satisfied. The force criterion applied for the geometry relaxation is 0.015 eV/ Å. These two criteria are required to have strictly optimized geometries that are accurate enough to perform the subsequent frequency analysis reliably.

The unit cell used to (co)adsorb benzene and hydrogen is repeated in the three directions to model an infinite surface, and periodic boundary conditions are applied. In the unit cell, a vacuum layer of 11 Å and an artificial dipole layer are introduced to avoid interactions between periodic images. Coverage effects are evaluated in two ways; by modifying the size of the unit cell with a constant number of adsorbates, or with the adsorption of an increasing number of species in the same unit cell. For benzene, the first approach is used and the different benzene coverages are investigated by adsorbing a single benzene molecule on the (4×4), (3×3), (3×2) and (2×2) unit cells; the surface area and consequent coverage at each unit cell are described in the results section. The second approach is used to investigate the adsorption of the smaller hydrogen atoms and, hence an increasing number of atoms are adsorbed on a fixed (2×2) unit cell to model the coverage effects, *i.e.* (2×2)-nH with n from 1 to 8 atoms. A similar approach has also been used to evaluate the effect of hydrogen coverage on the coadsorption with benzene. A (3×3) unit cell is used to adsorb an increasing number of hydrogen atoms (from 1 to 17) while keeping the benzene coverage fixed to a single molecule per unit cell. Furthermore, all unit cells are composed of 4 atomic layers to model the thickness of the slab. This approach has previously been shown to give an accurate description of the Pd surface.[23] The two top layers of the unit cell are allowed to fully relax during the geometry optimization, together with the adsorbed species, while the two bottom layers are fixed to the bulk structure.

Adsorption energies are reported to compare the adsorption strength of different adsorption sites and the trend with coverage. The adsorption energy is calculated as the energy released, per mole of atomic hydrogen adsorbed or per mole of benzene adsorbed on a clean surface, at the corresponding coverage, as shown below.

$$\Delta E_{ads,nH} = \frac{1}{n} \cdot (E_{el,nH/Pd(111)} - E_{el,Pd(111)} - \frac{n}{2} E_{el,\mathrm{H_{2,gas}}}) \tag{1}$$

$$\Delta E_{ads,benzene} = (E_{el,B/Pd(111)} - E_{el,Pd(111)} - E_{el,\mathrm{B_{gas}}}) \tag{2}$$

2.2.2 Thermodynamic calculations

Hydrogenation reactions typically occur at pressures above 10 bar and temperatures between 350 K and 600 K.[73] For these temperatures, DFT can provide enthalpies and entropies of elementary reactions steps, based on the electronic energies, vibrational frequencies, and default statistical thermodynamics equations. The vibrational frequencies need to be obtained from a strictly optimized geometry to avoid spurious imaginary frequencies. In our calculations, only the vibrational frequencies of the two top layers are calculated together with those of the adsorbates, since the geometry of the two bottom layers of the unit cell is not optimized. The harmonic oscillator approach (HO) is used to numerically calculate the vibrational frequencies with a step size of 0.015 Å. Accounting for the anharmonicity factor in the frequency analysis may provide frequencies that are closer to experimental observations as compared to the harmonic oscillator approximation.[74, 75] However, the same approach has been consistently applied to evaluate relative stabilities and, hence, deviations for not accounting for the anharmonicity factor are assumed to cancel out and to have a minor influence on the results. Even for strictly optimized geometries, the frequency analysis of coadsorption geometries at high hydrogen coverage can lead to spurious imaginary frequencies, or very low positive frequencies. In those cases, the spurious frequencies are replaced by a common value that is usually obtained in geometries without imaginary frequencies (25 cm^{-1}). The effect of the frequency cutoff on the thermodynamic phase diagram has been evaluated by using a higher value of 50 cm^{-1} and comparing the results to the ones obtained with the 25 cm^{-1} frequency cutoff. Despite a change in surface Gibbs free energy due to the different frequency cutoffs, the change is more or less similar for both systems and, hence, the relative stability remains the same as illustrated in Appendix A. Therefore, it is assumed that the frequency cutoff has only a minor influence on the resulting phase diagrams provided a consistent frequency cutoff is used. The cases in which this has been performed are listed in Table A1 in Appendix A.

In the adsorption process, the catalysts surface is assumed to be in thermodynamic equilibrium with the surrounding gas phase reservoir, and different adsorption sites and coverage patterns may be preferred depending on the conditions. The most stable surface coverage as a function of the gas phase conditions has been evaluated with the surface Gibbs free energy (Γ in J m^{-2}) calculated from the Gibbs free energy, which includes the contribution from the vibrational frequencies. The surface Gibbs free energy represents the reversible work required to create a surface from the bulk and the adsorbate in gas phase[76] as defined in the generalized eq. (3):

$$\Gamma(T, p_i) = \left(\frac{G_{ads}(T) - n_{Pd} G_{bulk}(T) - \sum_i n_i G_{m,gas,i}(T, p_i)}{2 \cdot A} \right) \tag{3}$$

With G_{ads}, the Gibbs free energy of the relaxed slab with the considered adsorbate coverages (*ads*), G_{bulk} the Gibbs free energy per Pd atom of the bulk unit cell, n_{Pd} is the number of Pd atoms in the unit cell used for the calculation, n_i is the number of molecules adsorbed on the slab at the corresponding evaluated coverage, $G_{m,gas,i}$ is the molar Gibbs free energy of the i gas phase species, and A is the surface area of the unit cell, which is multiplied by two because of the two surfaces in the slabs used in the periodic DFT calculations as explained in detail in the Appendix A.

Four different approaches have been used to calculate surface Gibbs free energies. The first one (*PW91-*E_{el}) assumes that the thermodynamic properties obtained from the vibrational frequencies have only a small contribution to the surface Gibbs free energy and, therefore, can be neglected. This follows most, if not all, theoretical studies in literature that construct thermodynamic phase diagrams since vibrational analysis for adsorbed species is computationally very demanding and not always straightforward. In this approach, Gibbs free energies are approximated by the electronic energy from the PW91 functional, neglecting all vibrational contributions and retaining only rotational and translational contributions for gas phase molecules; the derivation and a detailed explanation is provided in the Appendix A.

The second approach, i.e. *PW91-G*, includes vibrational contributions for every term in eq. (3) because entropy contributions to the surface Gibbs free energies may play an important role in the thermodynamic phase diagram, particularly for larger molecules such as benzene. Adsorbates are considered immobile[77] for the whole range of coverages and, therefore, Gibbs free energy contributions from translational and rotational modes are only included for gas phase species.

The third approach, i.e., *vdW-DF-*E_{el}, calculates Gibbs free energies neglecting vibrational contributions, as the first approach, but it relies on the vdW-DF method by approximating Gibbs free energies to the electronic energy obtained with the optPBE-vdW functional. The fourth and last approach (*vdW-DF-*G_{PW91}) is a rough approximation to the one that would include vibrational contributions and calculate the electronic energy both with the optPBE-vdW functional (*vdW-DF-G*). Since vibrational contributions to the optPBE-vdW geometries has not been performed due to computational limitations, this *vdW-DF-*G_{PW91} approach combines the vibrational contributions obtained with the PW91 functional with the electronic energies calculated with the optPBE-vdW functional. The equations and the explanation of each approach in detail can be found in the Appendix A.

Once surface Gibbs free energies are calculated at each pressure (from 10^{-10} bar to 100 bar) and for increasing temperatures (from 100 K to about 1000 K), the thermodynamic phase diagram is constructed to represent the most stable adsorbate-surface complex at each (T, p) condition, thus the one with the lowest surface Gibbs free energy. The lines in this diagram represent the transition between two coverages, which are obtained by calculating the intersection temperature at which the two consecutive coverages have the same surface Gibbs free energy. Since the computational tools available allow to simulate discrete coverages only, the areas between the lines are approximated to represent single coverages. However, in reality a gradual change in coverage may be expected.

For benzene and hydrogen coadsorption, the benzene coverage has been fixed in the periodic DFT calculations because varying benzene coverage requires the use of very large unit cells, and this leads to computationally unfeasible calculations. The thermodynamic phase diagrams are studied as a function of hydrogen pressure and temperature. Hence, in principle each condition (T,p_{H2}) requires a different benzene pressure in order to fix the benzene coverage at $\theta_B = 0.11$. The surface Gibbs free energy for coadsorption depends on both hydrogen and benzene gas-phase pressures. However, the transition line in the thermodynamic phase diagram between two consecutive coverages, which are obtained in the same unit cell and at the same benzene coverage, is not affected by benzene pressure, as it is shown in Figure A2 in Appendix A. Therefore, the thermodynamic diagram for coadsorption does not include benzene pressure.

The transition line from clean surface to adsorbed benzene is also included in the thermodynamic phase diagram. This line is clearly dependent on benzene pressure, and it is obtained as follows: first, for every point in the transition from benzene adsorbed to the first thermodynamic most stable coadsorbed system, the pressures of benzene required to obtain the fixed benzene coverage at a given temperature and hydrogen pressure are calculated using a simple Langmuir model for coadsorption, as shown more into detail in the Appendix A, with the adsorption equilibrium coefficients obtained from the DFT calculations with the corresponding functional. Assuming that for a given hydrogen pressure the obtained benzene pressures remains constant with increasing temperatures, the same Langmuir model is then used to find the temperatures at which the benzene coverage decreases to a coverage low enough to represent the transition from the clean surface to the benzene covered surface (see all the values in Table A2 in the Appendix A).

2.3 Results

2.3.1 Hydrogen adsorption as a function of coverage

2.3.1.a Adsorption geometries and energies

The monolayer of hydrogen on Pd(111) is reported to amount to 1.47 10^{19} hydrogen atoms per m^2 of Pd [3, 16, 78], equal to the number of Pd surface atoms per m^2. The hydrogen coverage θ_H is expressed as the number of hydrogen atoms per Pd surface atoms *i.e.* a fraction of the monolayer coverage. The adsorption of hydrogen is evaluated from $\theta_H = 0.25$ to 2 with the adsorption of 1 to 8 hydrogen atoms on a (2×2) unit cell. Hydrogen adsorbs on several adsorption sites on Pd(111) (see Figure 2-1), and adsorption of hydrogen on each of these sites only has been first evaluated up to the monolayer coverage, *i.e.* $\theta_H = 1$; the adsorption energies as a function of coverage are reported in Table A3 in Appendix A. The results obtained with the PW91 functional indicate that the hollow fcc is the most stable site, in agreement with previous studies [3-5, 10, 79-81] and closely followed by the hollow hcp site by 5 kJ mol^{-1}. The effect of coverage on the adsorption energy of the most stable hollow site is small up to $\theta_H = 1$, for which a decrease of 6 kJ mol^{-1} in adsorption energies is obtained from $\theta_H = 0.25$ to 1, *i.e.* –54 and –48 kJ mol^{-1} respectively. This indicates weak H-H lateral repulsions, which is in line with theoretical studies that have also reported a decrease in energies from about –50 kJ mol^{-1} to about –40 kJ mol^{-1} [5, 6, 8].

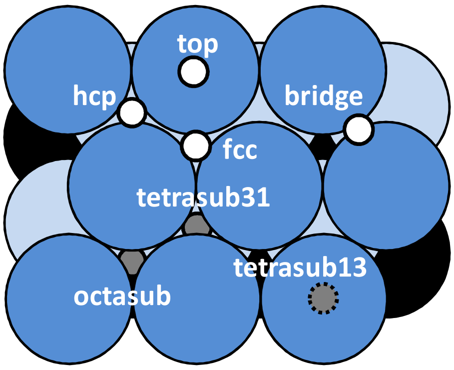

Figure 2-1: Top view of the four surface (white) and three subsurface (grey) adsorption sites investigated for hydrogen on Pd(111). The tetrasub13 site is shown with dotted borderline to indicate that it lies below a surface Pd atom.

Next, higher hydrogen coverages between $1 < \theta_H \leq 2$ are investigated by exploring combinations of different adsorption sites on the surface and/or subsurface, and the adsorption energies are reported in Table A4 in Appendix A. Four different cases have been investigated; first the successive addition of surface hydrogen to reach coverages between $0.25 \leq \theta_{H,surface} \leq 1$ on a H-covered surface with (i) surface hydrogen $\theta_{H,surface} = 1$ or (ii) subsurface hydrogen $\theta_{H,subsurface} = 1$. Secondly, the successive addition of subsurface hydrogen to reach coverages between $0.25 \leq \theta_{H,subsurface} \leq 1$ on a H-covered surface with (iii) surface hydrogen $\theta_{H,surface} = 1$ or (iv) with subsurface hydrogen $\theta_{H,subsurface} = 1$. The results indicate that at such high coverages the systems with surface-only or subsurface-only atoms are less favourable than the combination of surface with subsurface sites due to very strong repulsive interactions. The most stable combination is $0.25 \leq \theta_{H,subsurface} \leq 1$ hydrogen atoms at tetrasub13 subsurface sites on a surface covered with a monolayer of surface hydrogen atoms ($\theta_{H,surface} = 1$) at the fcc sites . These results are in excellent agreement with a similar study by Chizallet et al.,[10] and also agree with the results from Kovalinka and Scholten[16], who reported the desorption of subsurface hydrogen atoms by TPD only after pulse loading of coverages above the monolayer.

Compared to the PW91, the optPBE-vdW functional results in ~10 kJ mol^{-1} weaker adsorption at each hydrogen coverage studied (see Table A3 and A4 in Appendix A). This may be explained with a larger stabilization of the gas phase H_2 molecule with optPBE-vdW, since a smaller H-H gas-phase bond length is predicted (745 pm) as compared to one obtained with the PW91 functional (752 pm), which is closer to the experimental value of 741 pm.[82] Both shorter gas phase H–H bond length and weaker adsorption with the optPBE-vdW functional have already been reported by Puisto et al.[83] on Ru(0001).

2.3.1.b Thermodynamic phase diagram

The electronic energies calculated at 0 K are very useful to predict the preferred sites and adsorption energies as a function of coverage. However, hydrogenation reactions proceed at much higher temperatures and hydrogen pressures, which can change the adsorption preference for hydrogen. Therefore, surface Gibbs free energies are used to predict the most stable coverage on the catalyst, as a function of the hydrogen pressure and temperature, by constructing the thermodynamic phase diagrams depicted in Figure 2-2. The diagram represents the coverages with the lowest surface Gibbs free energies as a function of the conditions. These are obtained for the adsorption of hydrogen up to $\theta_H = 2$ with the combination of surface hollow fcc for $0 \leq \theta_{H,surface} \leq 1$ coverages and further addition of subsurface hydrogen between $1.25 \leq \theta_{H,subsurface} \leq 2$ at tetrasub13 subsurface sites. Previous work from Chizallet et al.[10] has already evaluated the thermodynamic phase diagram of hydrogen adsorption on Pd(111) with the commonly used approach that neglects vibrational contributions to the surface Gibbs free energy, i.e. the *PW91-E_{el}* approach. Excellent agreement is obtained for the *PW91-E_{el}* approach compared to Chizallet et al.[10] (see Figure 2-2a). In this work, we have extended the latter by evaluating three more approaches to calculate Gibbs surface free energies, as explained in the methodology section: the *PW91-G* approach calculates surface Gibbs free energy including for vibrational contributions in adsorbate, bulk and gas phase species (see Figure 2-2b). The *vdW-DF-*E_{el} neglects vibrational contributions and uses the electronic energies calculated with the optPBE-vdW functional (see Figure 2-2c). Finally, the *vdW-DF-*G_{PW91} approximation is evaluated by adding PW91 vibrational contributions to the optPBE-vdW electronic energies (see Figure 2-2d), since optPBE-vdW vibrational contributions have not been calculated due to computational limitations.

The comparison between *PW91-*E_{el} and *PW91-G*, shown in Figure 2-2a and Figure 2-2b, indicates that including vibrational contributions (*PW91-G*) does not change the general picture obtained with *PW91-*E_{el}. In line with the results from Chizallet et al.[10], both approaches predict $\theta_H = 1$ hydrogen coverage over a broad range of conditions, which include the typical hydrogenation conditions (350 K ≤ T ≤ 550 K and 1 bar ≤ p_{H2} ≤ 100 bar). However, some differences between the two are also observed in Figure 2-2. First, *PW91-G* predicts that hydrogen coverages below $\theta_H < 1$ populate the surface up to higher temperatures, for a given hydrogen pressure, as compared to *PW91-*E_{el}. Furthermore, coverages above $\theta_H \geq 1$ are less favoured in *PW91-G* over *PW91-*E_{el} at the same conditions, particularly for $\theta_H = 1.75$ as depicted in Figure 2-2.

To understand the difference between the two approaches, the surface Gibbs free energy (Γ) is investigated and illustrated in Figure 2-3 for a hydrogen pressure of $p_{H2} = 1$ bar, together with its constituent enthalpy (Γ_H) and entropy (Γ_S) terms, *i.e.* $\Gamma = \Gamma_H + \Gamma_S$ as explained in the Appendix A. The difference in the enthalpy term between the two approaches is small because both use the same PW91 functional to calculate electronic energies, and only small enthalpy contributions are calculated from the vibrational frequencies. On the other hand, the entropy term (Γ_S) is very different between the two, as shown in the right panels of Figure 2-3, hence the variation from one approach to the other is attributed to this term. For $\theta_H \geq 1$, *PW91-G* calculates a positive entropy term including vibrational contributions, meaning that the increase in entropy with temperature in the adsorbed complex does not compensate the increase in entropy of bulk and gas phase species, i.e. $-TS_{ads} > -TS_{bulk} - TS_{gas}$ as explained in the Appendix A. For $\theta_H < 1$, however, *PW91-G* calculates a negative entropy term that leads to the decrease in the surface Gibbs free energy, and hence increases the stability of the adsorbate. On the other hand, *PW91-E_{el}* predicts a positive entropy term for every coverage with temperature (see right panel in Figure 2-3a) by assuming that the vibrational contribution of adsorbate is the same as bulk and gas phase vibrational contributions. Furthermore, the change from negative values for the entropy term in *PW91-G* for coverages $\theta_H \leq 0.75$, to positive values for coverages $\theta_H > 0.75$ may also be understood from the adsorption entropy loss, which at 800 K is $\Delta S_{ads} < -60$ J mol^{-1} K^{-1} for hydrogen coverages $\theta_H \leq 0.75$, compared to the values that exceed –64 J mol^{-1} K^{-1} for coverages $\theta_H \geq 1$. The agreement between *PW91-G* and *PW91-E_{el}* at typical hydrogenation conditions for hydrogen adsorption does not necessarily need to be observed for other adsorbates or catalysts, therefore, inclusion of vibrational contributions in the Gibbs free energy is recommended.

The *PW91-E_{el}* and *vdW-DF-E_{el}*, shown respectively in Figure 2-2a and Figure 2-2c, both neglect vibrational contributions and use the results obtained with the PW91 and optPBE-vdW functionals respectively. The weaker hydrogen adsorption predicted with the optPBE-vdW functional leads to a higher enthalpy (electronic) term at every coverage as compared to the *PW91-E_{el}* approach (see Figure A3 in Appendix A). Therefore, the optPBE-vdW functional predicts that each hydrogen coverage populates the surface up to lower temperatures as compared to the PW91. This has a large effect particularly on the presence of subsurface hydrogen ($\theta_H > 1$), which was already more weakly absorbed than surface hydrogen with the PW91 functional. As a result, coverages above $\theta_H = 1$ are not expected from the thermodynamic phase diagram with the *vdW-DF-E_{el}* approach, while they are observed with the *PW91-E_{el}* between 90 K and 200 K.The vibrational frequencies in the geometries optimized with the optPBE-vdW functional have not been calculated due to computational constraints. However, a rough picture of the expected result of optPBE-vdW vibrational contributions added to the optPBE-vdW electronic energy (*vdW-DF-G*) is proposed by adding the vibrational contributions obtained with the PW91 functional to the electronic energies calculated with the optPBE-vdW functional, i.e. *vdW-DF-G_{PW91}* approach. This is illustrated in Figure 2-2d, and indicates that coverages between $0.5 \leq \theta_H \leq 1$ are expected to populate the surface at typical hydrogenation conditions, lower than the ones predicted in the previous approaches.

A previous experimental study reported hydrogen coverages of $\theta_H = 3.7\ 10^{-3}$, 0.4 and 0.9 at 350 K, 300 K and 250 K, for hydrogen pressures of 10^{-10} bar by molecular-beam investigations on Pd(111).[84] This is consistent with what it is observed in Figure 2-2, particularly in the diagram obtained with *PW91-G (*Figure 2-2b). Furthermore, temperature-programmed-desorption experiments (TPD) detected a desorption peak at ~310 K for pressures of 10^{-13} bar.[85] Although Figure 2-2 does not show pressures below 10^{-10}, the line indicating the transition from the clean surface ($\theta_H = 0$) to the H-covered surface with $\theta_H = 0.25$ is predicted at a similar temperature as the one experimentally observed. Konvalinka and Scholten[16] observed two major TPD desorption peaks at $p_{H2} = 3\ 10^{-3}$ bar when exposing the surface above monolayer coverage. The peak with maximum at T = 407 K was attributed to desorption of surface hydrogen atoms, and this may be compared to the temperatures at which the transition $\theta_H = 0.75/\ \theta_H = 1$ is predicted by *PW91-G* and *vdW-DF-E_{el}.* The second experimental peak, with maximum at 293 K,[16] was always absent for coverages $\theta_H < 1$ and it is attributed to desorption of subsurface hydrogen. Subsurface hydrogen has also been reported at temperatures of 170 K for pressures of 10^{-9} bar [85], however, for these conditions the different approaches we have considered predict coverages of $\theta_H = 1$.

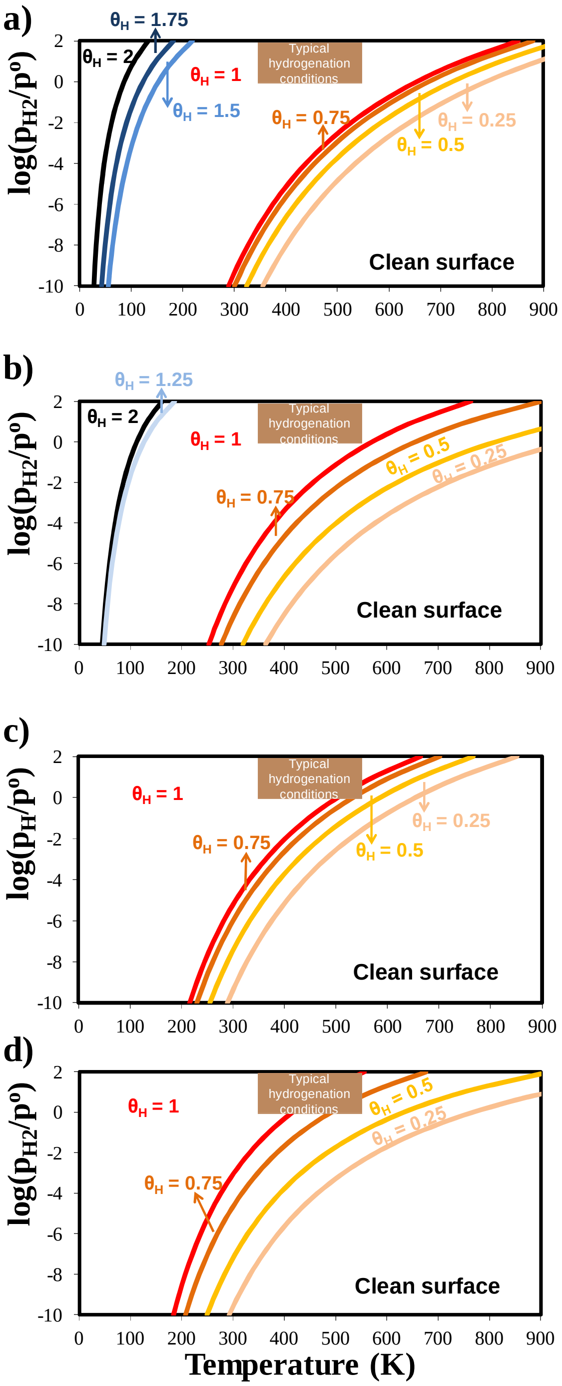

Figure 2-2: Thermodynamic phase diagram of hydrogen adsorption on Pd(111) as a function of temperature (K) and hydrogen pressure (bar) for standard pressure of p^o = 1 bar. (a) *PW91-E$_{el}$* diagram, which neglects vibrational contributions and uses the PW91 functional. (b) *PW91-G* diagram, which includes vibrational contributions and uses the PW91 functional. (c) *vdW-DF-E$_{el}$* diagram, which neglects vibrational contributions and uses the optPBE vdW-DF functional.[59, 69] (d) *vdW-DF-G$_{PW91}$* diagram, which is an approximation obtained by combining the results from (b) and (c). Hydrogen adsorbs on surface fcc sites for coverages between $0 < \theta_H \leq 1$ and on tetrasub13 subsurface hydrogen for $1 < \theta_H \leq 2$. Typical hydrogenation conditions are shown with a rectangle.

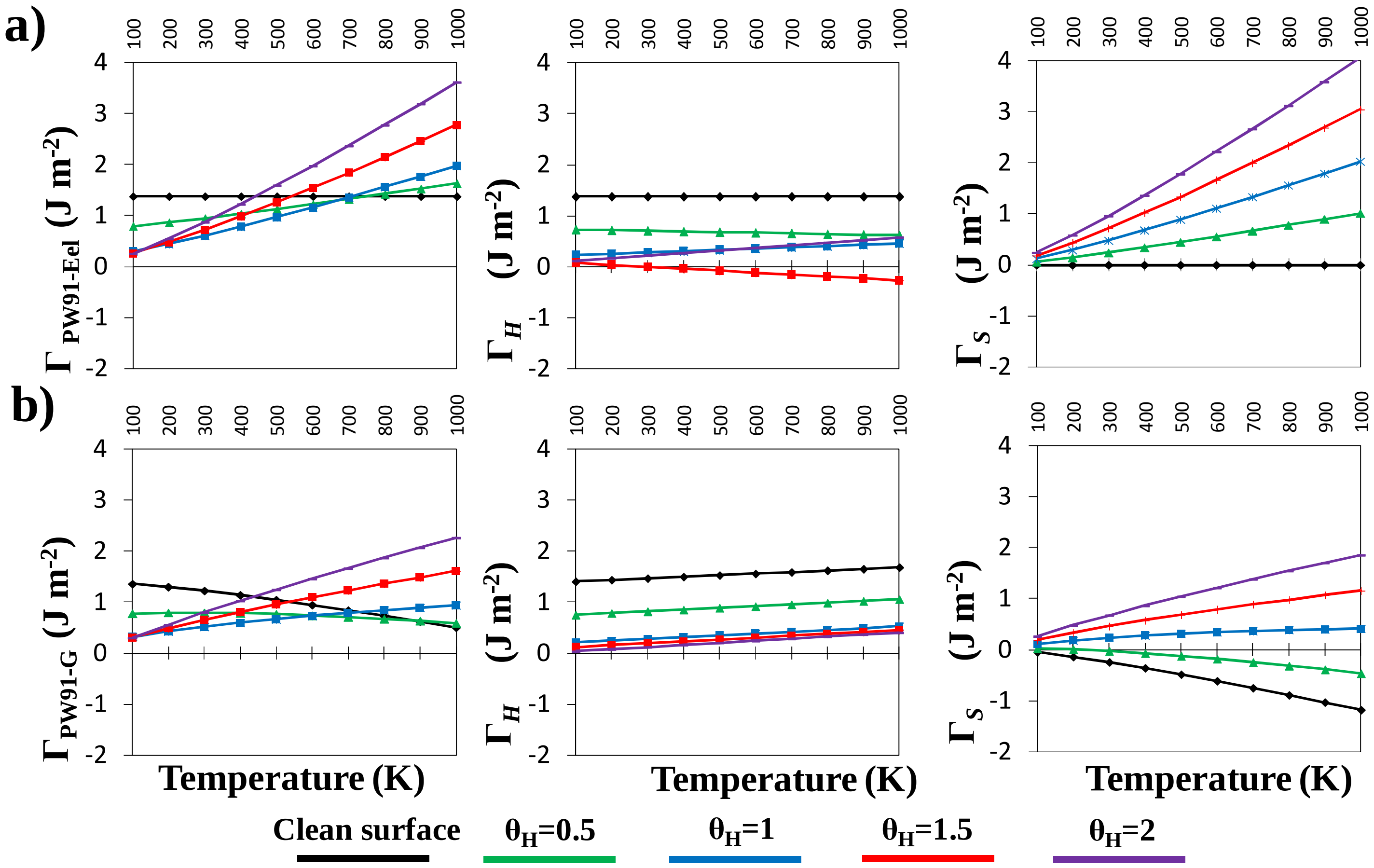

Figure 2-3: Surface Gibbs free energies (J m^{-2}) as a function of temperature (K) at p_{H2} = 1 bar for hydrogen adsorption on a clean surface (black line) and for hydrogen coverages of θ_H = 0.5 (green), θ_H = 1 (blue), θ_H = 1.5 (red) and θ_H = 2 (purple) using the (a) *PW91-E_{el}* and (b) *PW91-G* approaches. Left panels show the surface Gibbs free energy (Γ), and this term is broken into the enthalpy (Γ_H) and entropy (Γ_S) terms in middle and right panels. These are in turn calculated from the values for the adsorbed complex minus bulk and gas phase species.

2.3.2 Benzene adsorption as a function of coverage

2.3.2.a Adsorption geometries and energies

Benzene adsorbs with the aromatic ring parallel to the (111) surface up to saturation of the surface, [23, 26, 27, 30, 38, 86] *i.e.*, with a flat geometry, and increasing the concentration of benzene can force the molecule to tilt over.[29-31] As illustrated in Figure 2-4, flat adsorption of benzene has been evaluated at eight high-symmetry sites on the (4×4) and (3×3) unit cells of Pd(111) (see Figure 2-5) with the adsorption energies listed in Table 2-1, and the geometrical parameters in Table A5 and A6. The coverage of a single benzene molecule on the (4×4) and (3×3) unit cells corresponds to $\theta_B = 6.25\ 10^{-2}$ and $\theta_B = 0.11$, with coverage expressed as number of benzene molecules per Pd surface atoms. At these coverages, the bridge(30) is the most stable adsorbate followed by the hollow-hcp(0) site, in agreement with previous theoretical studies. [22, 23] From temperature programmed desorption spectra (TPD), Tysoe et al.[30] estimated a benzene adsorption energy of –130 and –95 kJ mol^{-1} at coverages corresponding to $\theta_B = 5\ 10^{-2}$ and $9\ 10^{-2}$ resp. These values may be related to the ones we have obtained at $\theta_B = 6.25\ 10^{-2}$ and 0.11 coverages respectively for the bridge(30) and hollow-hcp(0) sites (see Table 2-1).

Higher benzene coverages have been evaluated with the adsorption of a single molecule in the (3×2) and (2×2) unit cells of Pd(111), see Figure 2-5, which correspond to benzene coverages of $\theta_B = 0.17$ and 0.25. At $\theta_B = 0.17$, both hollow-hcp(0) and bridge(30) adsorbates yield a similar adsorption energy of –26 kJ mol^{-1} (see Table 2-1). At $\theta_B = 0.25$, however, both flat adsorbates are unstable, thus we propose the saturation coverage at $\theta_B \sim 0.17$, *i.e.* $2.4\ 10^{18}$ molecule per m^2 and similar to the $2.3\ 10^{18}$ molecule per m^2 experimentally reported on Pt(111) at 300 K.[87] The difference in adsorption energy between the bridge(30) and hollow-hcp(0) decreases from the lowest (θ_B = 6.25 10^{-2}) to the saturation coverage (θ_B = 0.17). This agrees with the azimuthal re-orientation of benzene from a bridge(30) site to a hollow(0) site at saturation coverage on Ni(111)[88], and also with the hollow adsorbate proposed to coadsorb with CO on a Pd(111)-(3×3)-C_6H_6+2CO overlayer structure.[38] At the highest coverage of benzene evaluated of θ_B = 0.25, at which the flat geometry is found to be unstable, the adsorption of benzene with a tilted "hollow" geometry yields an exothermic adsorption energy of –12.2 kJ mol^{-1}. The benzene molecular plane forms an angle of 54° relative to the surface Pd atoms, larger than the value of ~30° reported by Hoffmann et al.[29] Tilted benzene on Pd(111) has been observed at coverages of about θ_B = 0.22,[30] and desorption from these sites has been reported at temperatures from 150 K [31] to 280 K.[30, 89]

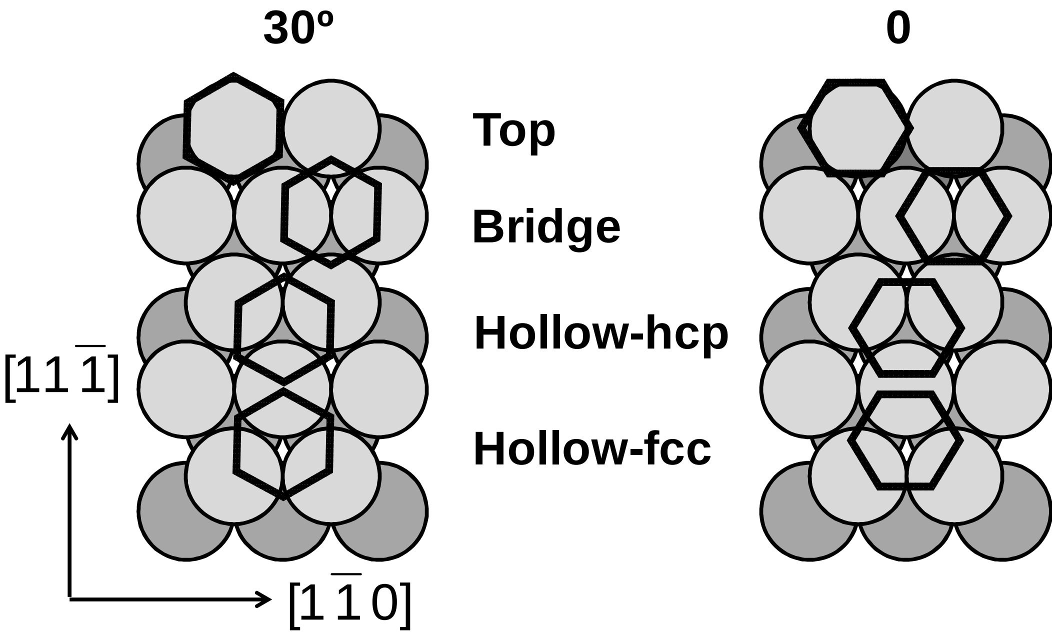

Figure 2-4: Evaluated flat adsorption sites of benzene on Pd(111).

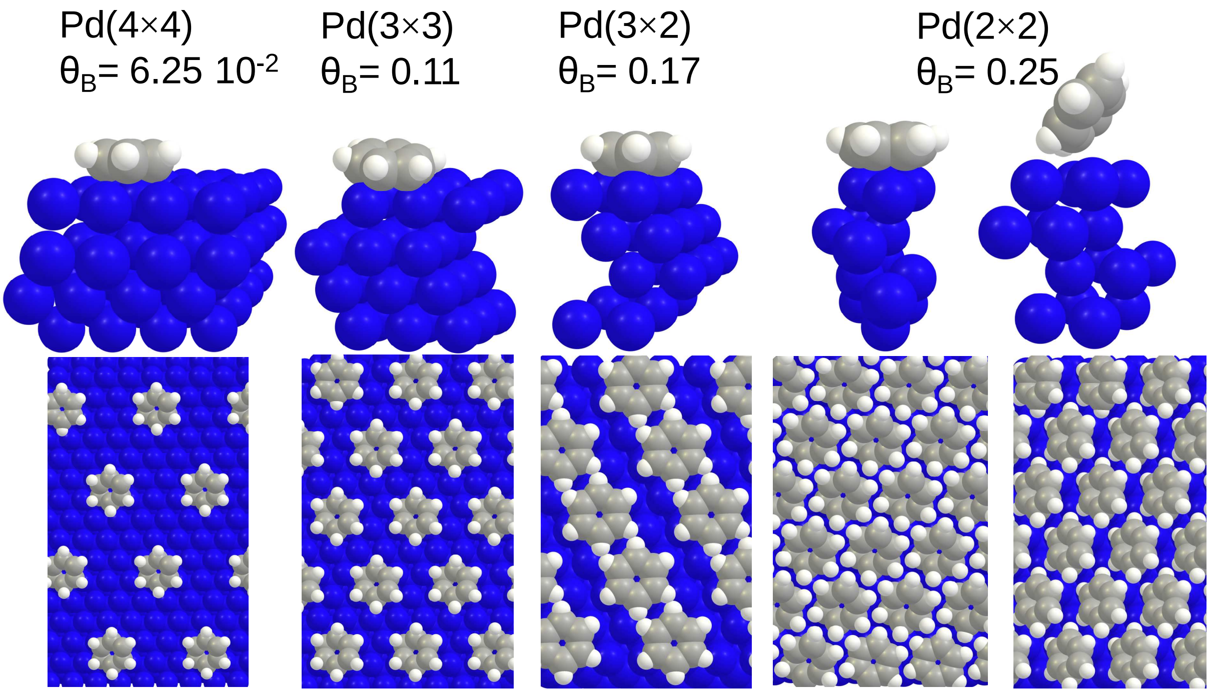

Figure 2-5: Front view of the unit cells used to evaluate the adsorption of benzene at increasing coverages (top) and surface overlayers (bottom). For θ_B = 0.25 both flat and tilted geometries are shown.

An increase in adsorption energy of about ~50 kJ mol^{-1} is obtained for all adsorbates below a coverage of $\theta_B \leq 0.11$ using the optPBE-vdW functional, as shown in Table 2-1 with values between brackets. At $\theta_B = 0.25$, the increase in adsorption energy with the vdW-DF cannot compensate the large repulsive interaction between flat neighboring molecules, and similarly to the PW91 functional the adsorption of flat adsorbates is endothermic. Therefore, the same $\theta_B = 0.17$ saturation coverage is proposed as with the PW91 functional. At $\theta_B = 0.17$, a ~10 kJ mol^{-1} stronger adsorption energy is calculated for the bridge(30) compared to the hollow-hcp(0) site, while they are equally stable with the PW91 functional. At $\theta_B > 0.25$ the largest increase in adsorption energies by some ~64 kJ mol^{-1} is calculated for the tilted adsorbate. Despite large differences in adsorption energies between both functionals, the use of the vdW-DF functional has only a small effect on adsorption geometries, as previously reported,[71, 90] and the largest change amounts to ~0.03 Å for the C–Pd bond length.

Table 2-1: Adsorption energies (kJ mol^{-1}) of benzene on Pd(111) at different sites and coverages. The surface area and coverage, in molecules per m^2 and per Pd surface atom, are shown for each of the coverages. The adsorption energies calculated with the vdW-DF functional [57, 91] are shown between brackets. Estimated values by Tysoe et al. [30] at coverages of $\theta_B = 5\ 10^{-2}$ and $9\ 10^{-2}$ from TPD experiments on Pd(111) are also shown.

	Unit cells			
	(4×4)	**(3×3)**	**(3×2)**	**(2×2)**
Surface area (m^2)	$1.09\ 10^{-18}$	$6.10\ 10^{-19}$	$4.07\ 10^{-19}$	$2.71\ 10^{-19}$
Coverage in molecules/m^2	$9.22\ 10^{17}$	$1.64\ 10^{18}$	$2.46\ 10^{18}$	$3.69\ 10^{18}$
Coverage in molecules/$n_{Pdsurface}$	$6.25\ 10^{-2}$	0.11	0.17	0.25
Adsorption site	ΔE_{ads} (kJ/mol)			
bridge(0)	–92.1 (–141.8)	–80.7 (–134.4)	-	-
bridge(30)	–124.4 (–172.4)	–115.2 (–164.6)	–26.6 (–90.9)	(not converged)
hollow-hcp(0)	–110.8 (–160.8)	–99.8 (–151.3)	–26.0 (–81.0)	96.1 (28.7)
hollow-fcc(0)	–106.7 (–155.3)	–93.7 (–147.9)	-	-
hollow-hcp(30)	–98.6 (–149.0)	–88.4 (–142.1)	-	-
hollow-fcc(30)	–91.0 (–140.7)	–83.8 (–136.9)	-	-
top(0)	–48.0 (–79.4)	–45.2 (–92.1)	-	-
top(30)	–16.7 (–82.1)	–20.2 (–86.9)	-	-
tilted adsorbate	-	-	305.9	-12.2 (–76.2)
exp. (TPD experiments) [30]	-130.0 [a]	-95.0 [b]	-	-

[a] Adsorption energy at $\theta = 5\ 10^{-2}$, in molecules/$n_{Pdsurface}$

[b] Adsorption energy at $\theta = 9\ 10^{-2}$, in molecules/$n_{Pdsurface}$

2.3.2.b Thermodynamic phase diagram

The most stable adsorption coverage of benzene on Pd(111) is evaluated as a function of temperature and pressure. Only the results obtained for the hollow-hcp(0) adsorbate are shown in this section because this is more stable when coadsorbed with hydrogen compared to the bridge adsorbate, as will be discussed in the next section. In addition, selection of hollow-hcp(0) adsorption sites is made on account of its higher hydrogenation reactivity on Pd(111), as already observed on Pt(111)[92] and confirmed by preliminary calculations on Pd(111). In any case, small relative changes are observed compared to the results obtained for the bridge(30) site, and a similar picture and conclusions are obtained with both adsorbates, as shown in Figure A4 in Appendix A. In line with the results shown for the adsorption of hydrogen on Pd(111), four approaches have been used to construct the thermodynamic phase diagram. From top to bottom, Figure 2-6 shows the diagrams for *PW91-*E_{el}, *PW91-G*, *vdW-DF-*E_{el}, and finally *vdW-DF-*G_{PW91}.

The thermodynamic diagrams obtained with the *PW91-*E_{el} and *PW91-G* approaches yield a similar picture but have several important differences (see Figure 2-6*a* and Figure 2-6*b*). Using both approaches, the $\theta_B = 0.11$ coverage encompasses a broad range of conditions, and the benzene coverages of $\theta_B = 0.17$ and 0.25 are not expected at any condition. For temperatures and benzene pressures at which hydrogenation reactions are performed ($p_B > 1$ bar and $350 \leq T \leq 550$ K), *PW91-G* predicts coverages of $\theta_B = 0.11$ on the Pd(111) surface. However, at the same conditions *PW91-*E_{el} also predicts that the $\theta_B = 6.25\ 10^{-2}$ coverage and the clean surface are expected depending on the conditions. To understand these differences, the surface Gibbs free energy has been evaluated at $p_B = 1$ bar, and it is broken down into its constituent enthalpy and entropy terms, as shown in Figure 2-7. Similarly as for hydrogen adsorption, the enthalpy term Γ_H has only a small contribution to the surface Gibbs free energy, as compared to the large differences observed in the entropy term Γ_S. The neglect of vibrational contributions with *PW91-*E_{el} results in positive entropy terms, which decreases the stability of the adsorbate because it increases surface Gibbs free energies. Furthermore, with *PW91-G* the difference in entropy term between the clean surface and θ_B = 6.25 10^{-2}, and between the latter and θ_B = 0.11 is smaller than the difference with *PW91-*E_{el}. Therefore, the decrease in surface Gibbs free energies contribution from a negative entropy term with *PW91-G* for θ_B = 6.25 10^{-2} compared to the clean surface, and for θ_B = 0.11 compared to θ_B = 6.25 10^{-2} is larger including vibrational contributions. This leads to the θ_B = 0.11 and 6.25 10^{-2} benzene coverage to populate the surface up to higher temperatures, for a given pressure, as compared to *PW91-*E_{el}.

Large differences are observed between the *PW91-*E_{el} and *vdW-DF-*E_{el} diagrams, Figure 2-6a and Figure 2-6c, which have been constructed by neglecting vibrational contributions and using the PW91 and vdW-DF functionals respectively. In *vdW-DF-*E_{el}, a larger stabilization of every coverage relative to the stability of the clean surface is observed. This is explained with the ~50 kJ mol^{-1} stronger vdW-DF adsorption energies that are calculated compared to the PW91 values, and is also understood from the comparison of the electronic energy contribution shown in Figure A5 in Appendix A. Remarkably, the coverage of θ_B = 0.25 (tilted geometry) populates the surface above ~ 90 K at p_B=10^{-10} bar and below ~ 200 K at p_B=100 bar. This range agrees with the temperatures between 150 and 280 K at which desorption of tilted adsorbates has been experimentally reported [30, 31, 89]. Similarly to the approach that includes vibrational contributions (*PW91-G*), *vdW-DF-*E_{el} predicts that coverages of benzene of θ_B = 0.11 are the most stable in the whole range of typical hydrogenation conditions.

More accurate results can be obtained if vibrational contributions are calculated for the vdW-DF geometries. However, as already mentioned, this has not been performed due to

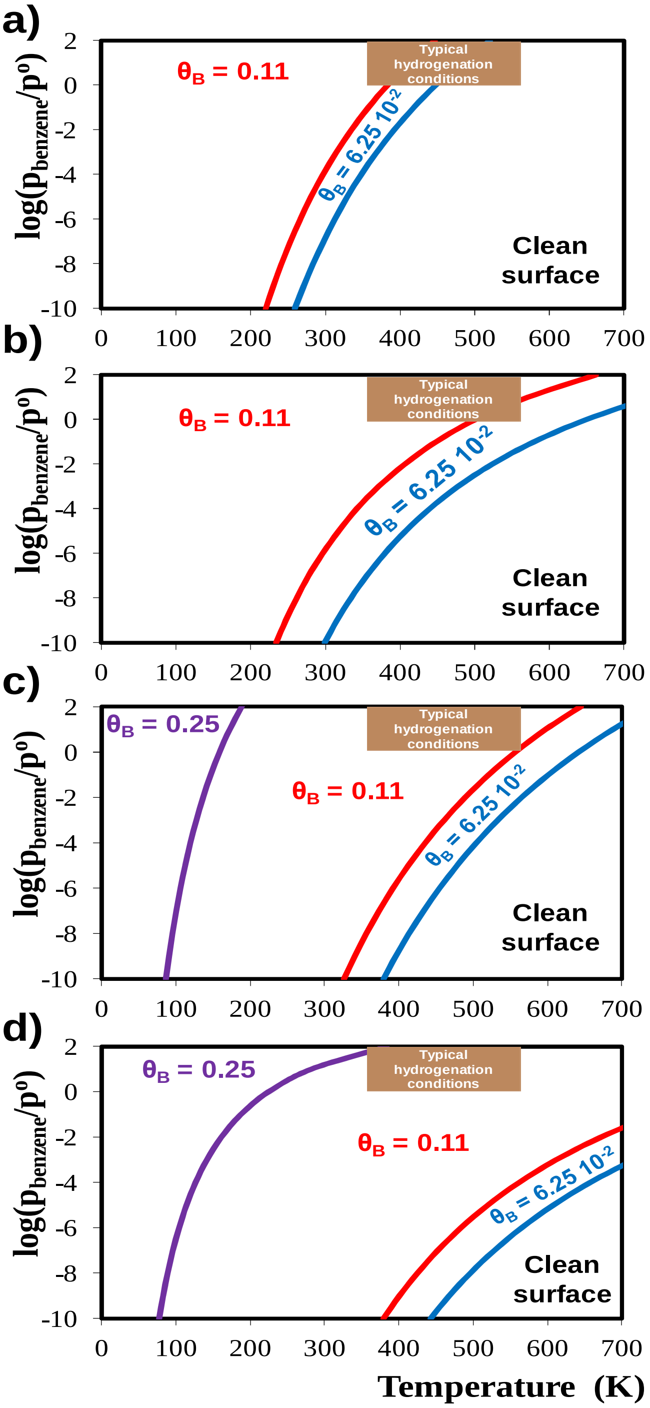

Figure 2-6: Thermodynamic phase diagram of benzene adsorption on Pd(111) as a function of temperature (K) and benzene pressure (bar) for standard pressure of p^o = 1 bar with the (a) *PW91-E_{el}* approach, which neglects vibrational contributions and uses the PW91 functional, the (b) *PW91-G* approach, which includes vibrational contributions with the PW91 functional, the (c) *vdW-DF-E_{el}* approach, which neglects vibrational contributions and uses the optPBE vdW-DF functional [59, 69], and the (d) *vdW-DF-G_{PW91}*, which is obtained combining the results from *PW91-G* and *vdW-DF-E_{el}*. Typical hydrogenation conditions are shown with a rectangle.

computational constraints. The addition of the PW91 vibrational contributions to the vdW-DF results (*vdW-DF-G$_{PW91}$*) may, however, provide with a rough picture of the expected results (see Figure 2-6d). Good agreement is observed for the reported TPD desorption temperatures of 380 K and 520 K at low pressures ($p_B \sim 10^{-10}$ bar) for the flat-lying benzene [30]. Although the $\theta_B = 0.25$ coverage spans over a broader range of conditions than in previous approaches, the $\theta_B = 0.11$ coverage is still preferred at hydrogenation conditions. This coverage is considered in the next section to evaluate the coadsorption of a fixed benzene coverage with increasing hydrogen.

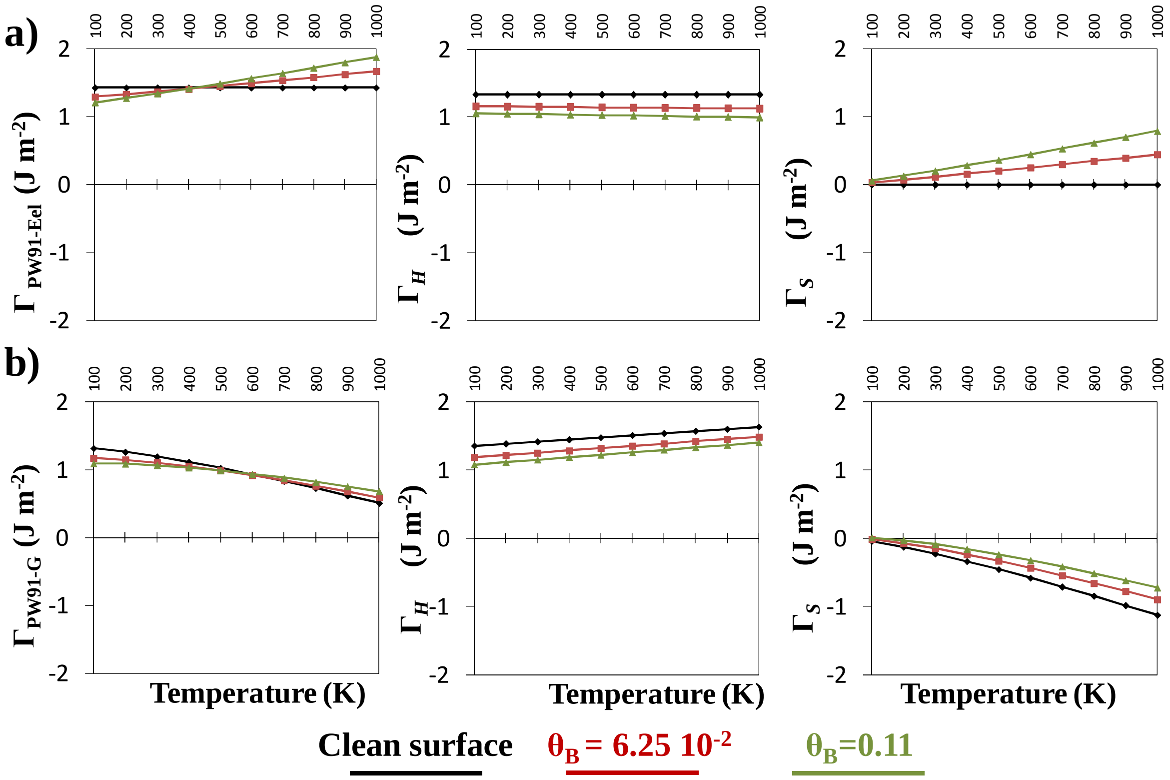

Figure 2-7: Surface Gibbs free energies (J m^{-2}) as a function of temperature (K) at p_B = 1 bar for the adsorption of benzene on the clean surface (black line) and benzene coverages of $\theta_B = 6.25\ 10^{-2}$ (red) and $\theta_B = 0.11$ (green) using the (a) *PW91-E$_{el}$* and (b) *PW91-G* approaches. Left panels show the surface Gibbs free energy Γ, and this term is broken into the enthalpy (Γ_H) and entropy (Γ_S) terms. These are in turn calculated as the values for the adsorbed complex, minus the ones for bulk and gas phase species. The enthalpy and entropy terms in *PW91-G* include vibrational contributions, and rotational and translational modes only for gas phase species. The terms in *PW91-E$_{el}$* includes only the rotational and translations contributions in gas phase.

2.3.3 Benzene and hydrogen coadsorption as a function of hydrogen coverage

Hydrogenation reactions are usually performed at high hydrogen pressure (p_{H2} > 1 bar), and the adsorption patterns may differ from the commonly studied adsorption at low coverages. Therefore, periodic DFT calculations have been used to evaluate the coadsorption of benzene with increasing hydrogen coverages. The optimization of the coadsorption geometries is computationally much more demanding than that for single species at low coverage. Benzene-hydrogen and hydrogen-hydrogen interactions at increasing coverage can also induce geometry convergence problems. In addition, hydrogen atoms can be adsorbed on multiple sites, and we have shown that the (3×3) unit cell can accommodate up to 18 hydrogen atoms from the results obtained for the single adsorption of hydrogen species. This leads to a very large number of possible combinations, which is computationally challenging particularly for the highest hydrogen coverages. Although several attempts were made to consider all possible combination of sites at each coverage, some other combination of sites leading to more stable energies cannot be discarded.

2.3.3.a Adsorption geometries and energies

To study the coadsorption of benzene and hydrogen, the coverage of benzene has been fixed to a single molecule in a (3×3) unit cell at the hollow-hcp(0) site, which corresponds to a benzene coverage of $\theta_B = 0.11$. Coverages of hydrogen between $0.11 \leq \theta_H \leq 1.89$ coadsorbed with benzene are studied by sequentially adding from 1 to 17 hydrogen atoms in a (3×3) unit cell. For coadsorption of benzene with hydrogen coverages above $\theta_H = 0.33$, benzene is less stable at bridge(30) sites than at hollow-hcp(0) sites, see Table A7 in Appendix A. This is explained from the larger repulsive interactions for the four-fold bridge(30) site than for the three-fold hollow-hcp(0) site. Therefore, only the results for the hollow-hcp(0) are shown.

The coadsorption of benzene with hydrogen coverages up to saturation has been evaluated by studying combinations of benzene with the most stable hydrogen sites; for hydrogen adsorbed on the surface, atoms on fcc and hcp sites have been evaluated, while for benzene coadsorption with subsurface hydrogen, combinations of the three most stable, octasubsurface, tetrasub13, and tetrasub31, sites have been studied. The values and geometries that are shown correspond to the most stable ones, and a more detailed explanation is given in the Appendix B. As for the adsorption of hydrogen only on Pd(111), the results for the coadsorption indicate that hydrogen atoms occupy surface hollow sites up to $\theta_H = 0.89$, as illustrated in Figure 2-8. Up to this coverage, the absorption of hydrogen in subsurface sites compared to surface sites leads to ~30 kJ mol^{-1} less stable systems per hydrogen atom in the (3×3) unit cell. The most stable hydrogen sites at $\theta_H = 0.11$, 0.22, 0.33, 0.44 and 0.55–0.89 coverages are respectively: 100% fcc, 50% fcc + 50% hcp, 66% fcc + 33% hcp, 75% fcc + 25% hcp and 100% fcc sites (see Figure 2-8). For hydrogen coverages above $\theta_H = 0.89$, additional hydrogen atoms preferentially absorb at subsurface sites rather than at surface sites, as illustrated in Figure 2-8. For the coadsorption of benzene with hydrogen in the range of coverages between $0.89 < \theta_H \leq 1.33$, every combination of benzene with $\theta_H = 0.89$ surface fcc hydrogen and with $0.11 \leq \theta_{H,subsurface} \leq 0.44$ subsurface hydrogen, on octasubsurface, tetrasub13, and/or tetrasub31 sites has been evaluated. For coverages above $\theta_H > 1.33$, only the combinations that were considered to be preferred have been evaluated, following the results obtained for hydrogen adsorption, and for coadsorption of benzene and hydrogen at lower coverages. Other combinations were evaluated for some, but not all, coverages. A more detailed explanation can be found in Appendix B. The competition of benzene and hydrogen for the same surface sites explains why in the case of coadsorption subsurface sites start being occupied above $\theta_H > 0.89$, rather than from the saturation coverage of $\theta_H = 1$ calculated for the adsorption of hydrogen only on Pd(111). At coverage $\theta_H = 1$, the most stable combination is $\theta_{H,surface} = 0.89$ fcc hydrogen with $\theta_{H,subsurface} = 0.11$ of octasubsurface (8fcc + 1octasub on the (3×3) unit cell, as shown in Figure 2-8), and at $\theta_H = 1.11$ a combination of $\theta_{H,surface} = 0.89$ fcc hydrogen with octasubsurface ($\theta_H = 0.11$) and tetrasubsurfac13 hydrogen ($\theta_H = 0.11$) is the most favourable case. Finally, for $1.22 \leq \theta_H \leq 1.89$ hydrogen coverages the most stable combination is the $\theta_{H,surface} = 0.89$ surface fcc with $0.33 \leq \theta_H \leq 1$ tetrasub13 subsurface sites, as shown in the bottom row panels in Figure 2-8.

The adsorption energy of hydrogen on a $\theta_B = 0.11$ benzene-covered slab decreases with hydrogen coverage, as illustrated in the top panel of Figure 2-9. The adsorption with the optPBE-vdW functional (grey line in Figure 2-9) is about 10 kJ mol^{-1} weaker at each coverage than that obtained with the PW91 functional (full black). This agrees with the results previously shown for hydrogen adsorption, and was explained with a larger stabilization of the gas phase hydrogen molecule with optPBE-vdW, which lowers the adsorption energy. Furthermore, the stronger adsorption calculated for hydrogen on a clean surface (black dotted line) than on a benzene-covered surface (full black), both with the PW91 functional, is explained with a rather constant ~10 kJ mol^{-1} interaction energy. Mirodatos et al.[52] already observed small difference in adsorption enthalpy for hydrogen adsorption on a clean or benzene-covered Ni surface. Furthermore, the hydrogen adsorption enthalpy of –35 kJ mol_H^{-1} on Pd/SiO_2 estimated by Aben et al.[46], by fitting a kinetic model to experimental benzene hydrogenation data, can be compared to the values we have obtained for coverages above $\theta_H \geq 1$ (PW91) or between $0.44 \leq \theta_H \leq 0.89$ (optPBE-vdW) on a benzene covered surface. In a similar way, Chou and Vannice[45] obtained low adsorption enthalpies of about –6 kJ mol_H^{-1} at 413 K, $p_B = 6.67\ 10^{-2}$ bar and $p_{H2} = 0.9$ bar, which were attributed to weakly bound hydrogen atoms and can be related to our values at high coverage.

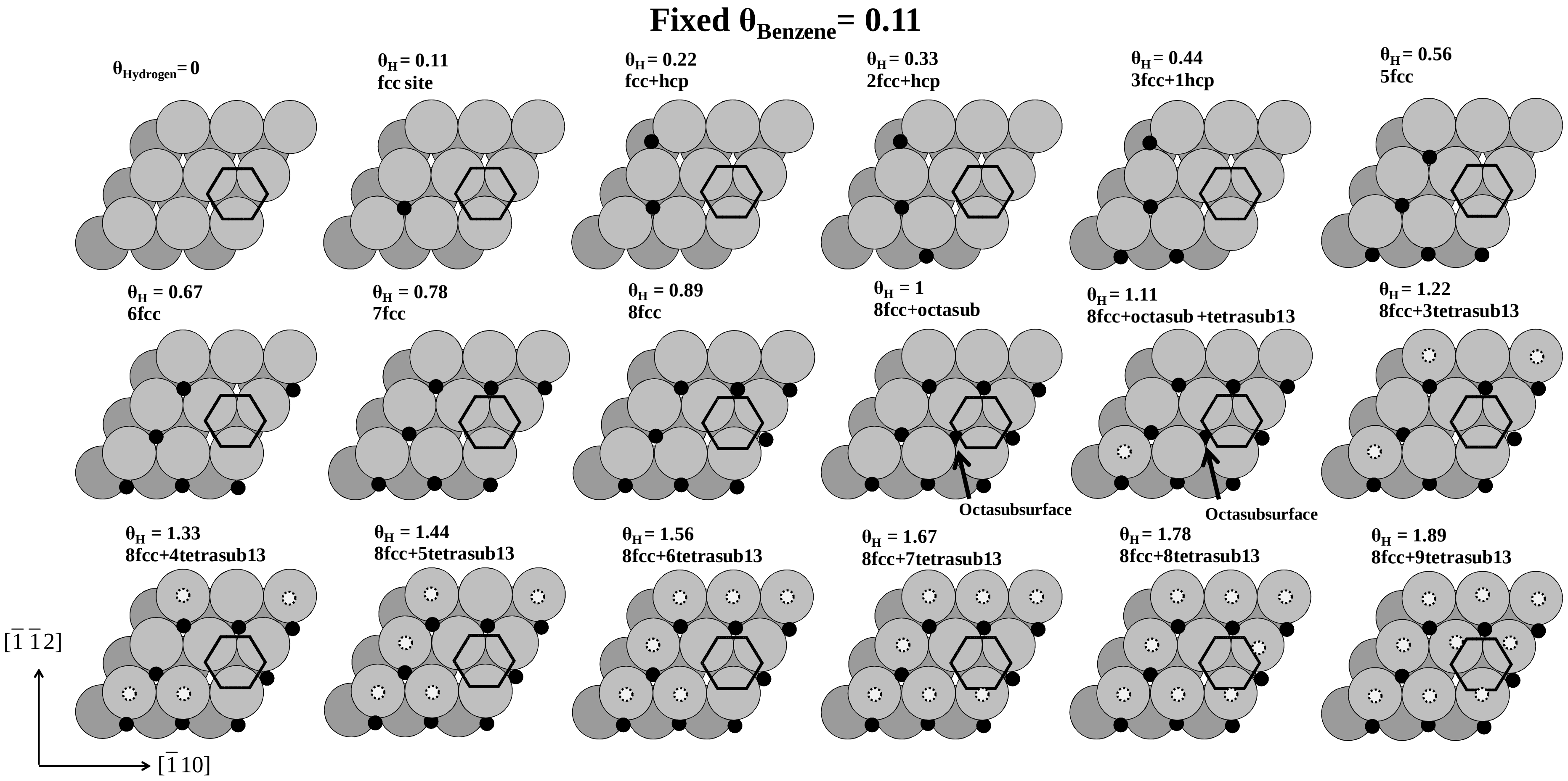

Figure 2-8: Top view of the unit cell with a fixed θ_B = 0.11 benzene coverage at hollow-hcp(0) sites, coadsorbed with the most stable hydrogen obtained at increasing coverage, from θ_H = 0.11 to 1.89, from left to right and top to bottom. White circles with dotted lines represent tetrasub13 hydrogen atoms, which are situated below surface Pd atoms.

For the adsorption of benzene on a hydrogen-covered Pd(111), a decrease in benzene adsorption energy is also obtained with increasing hydrogen coverage (see bottom panel of Figure 2-9). The decrease is more pronounced than for the adsorption of hydrogen on a benzene-covered surface, indicating a larger destabilization effect on the aromatic molecule. The decrease in benzene adsorption energy is similar with both PW91 and vdW-DF functionals (black and grey lines respectively in Figure 2-9), but a ~50 kJ mol^{-1} stronger adsorption energy is calculated using the vdW-DF method, similar to the results for benzene adsorption on a clean surface. The geometry of benzene is also affected by the increase in H-coverage, as shown in Figure 2-10 for six examples between $0.11 \leq \theta_H \leq 1.89$. These geometries do not substantially change using the vdW-DF method compared to the PW91 functional, and the largest change is computed for the C-Pd bonds that increase with less than 0.03 Å with the optPBE-vdW. Similar geometries for benzene at different transition metals have already been reported using the two functionals[71, 90] and hence, the values discussed below correspond only to the PW91 functional.

Benzene remains adsorbed parallel to the surface of Pd(111) below benzene coverages of $\theta_H \leq 0.67$ (see Figure 2-10). A strong decrease in adsorption energy is observed for benzene adsorption on a $\theta_H = 0.55$ H-covered surface, compared to the values at $\theta_H = 0.44$. This is explained with the increase in repulsive interactions between both species, which lead to the breaking of Pd-C bonds at one side of the aromatic ring and tilts the molecule by ~7^o relative to the surface (see Figure 2-10). The distance between the benzene molecule and the Pd surface increases from ~220 pm at the lowest coverage to 226 pm at $\theta_H = 0.56$, which is in line to the 225 ± 5 pm distance measured by Ohtani et al.[38] by LEED on Pd(111)-(3×3)-C_6H_6+2CO. The further addition of hydrogen for $\theta_H > 0.78$ leads to the breaking of the remaining bonds, lifting the whole molecule to a physisorbed geometry that remains up to the highest $\theta_H = 1.89$ hydrogen coverage studied. The physisorbed geometry was also evaluated for $0.56 \leq \theta_H < 0.78$, however, at these coverages the chemisorbed adsorbate is more stable by 20 to 50 kJ mol^{-1}. For hydrogen coverage $\theta_H > 1$ small changes are observed in the benzene-surface distance, and values of about ~380 pm are obtained (see Figure 2-10). In the physisorbed benzene molecule the C–C bond distances, C–C–H and C–C–C bond angles remain constant up to the highest coverage, and these are also similar to the gas-phase values of 140 pm, 120° and 120° resp. (all bond length and angles are listed in Table A8 in Appendix A). From hydrogen coverages of $\theta_H = 0.67$ up to 1.89 a rather constant benzene adsorption energy is obtained, and these energies indicate a ~ 50 kJ mol^{-1} lower adsorption energy than those calculated for benzene adsorption on a $\theta_H = 0.44$ H-covered surface. The reason for the constant values is the large distance between physisorbed benzene and the surface, which leads to a constant repulsive interaction between benzene and particularly the subsurface atoms, in line with previous studies on Pd(100)[10] and Ni(111).[93] Chou and Vannice [45] reported benzene adsorption enthalpies of –58 - –70 kJ mol^{-1} by fitting a kinetic model to hydrogenation experiments. These correspond to the values on a H-covered surface with $0.33 < \theta_H < 0.56$ (PW91), or with higher hydrogen coverages above $\theta_H = 0.67$ for the optPBE-vdW.

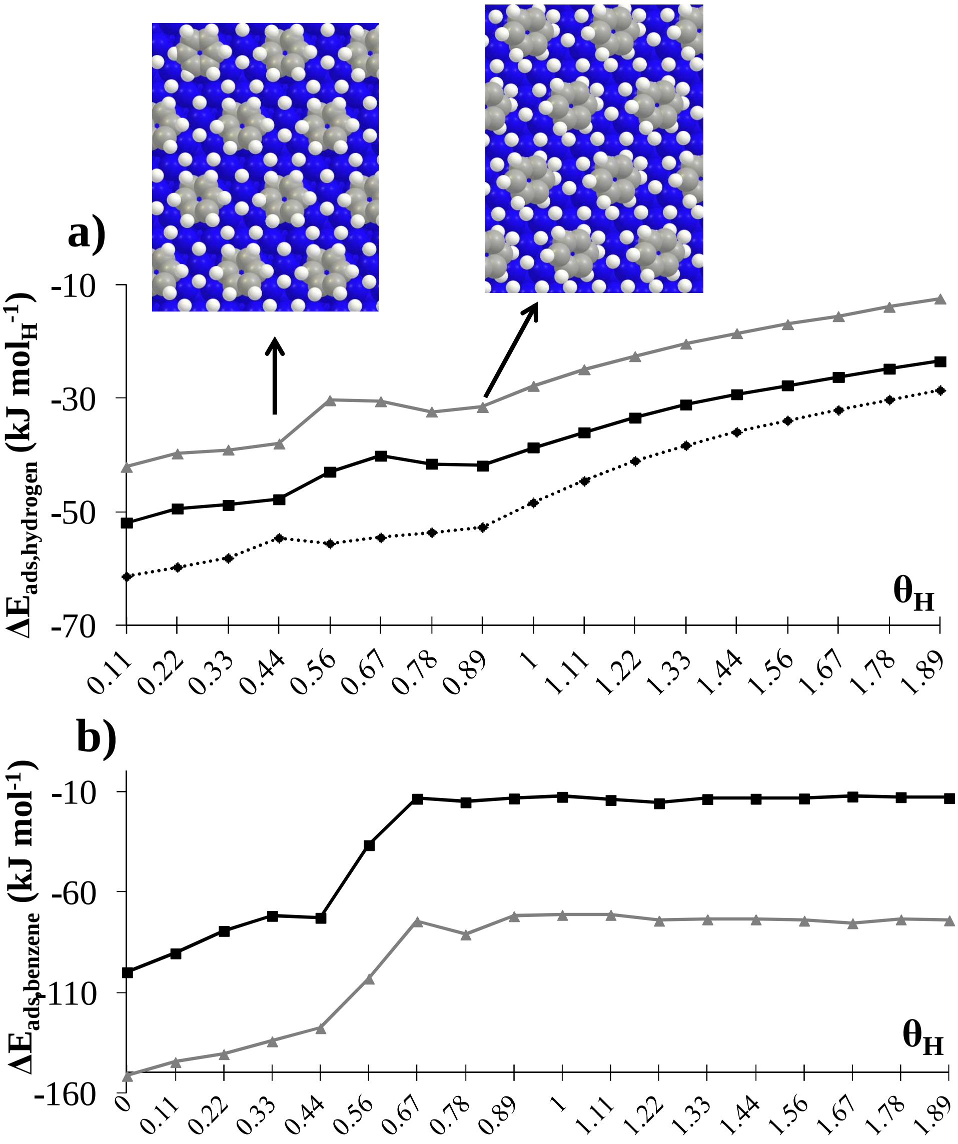

Figure 2-9: (a) Adsorption energy of hydrogen (kJ mol_H^{-1}) on a $\theta_B = 0.11$ benzene-covered surface obtained with the PW91 (full black line), with the vdW-DF optPBE functionals (grey line), and for adsorption on a clean surface with the PW91 functional (dotted black line). (b) Adsorption energy of benzene on a H-covered surface with the PW91 (black line) and vdW-DF functional (grey line).

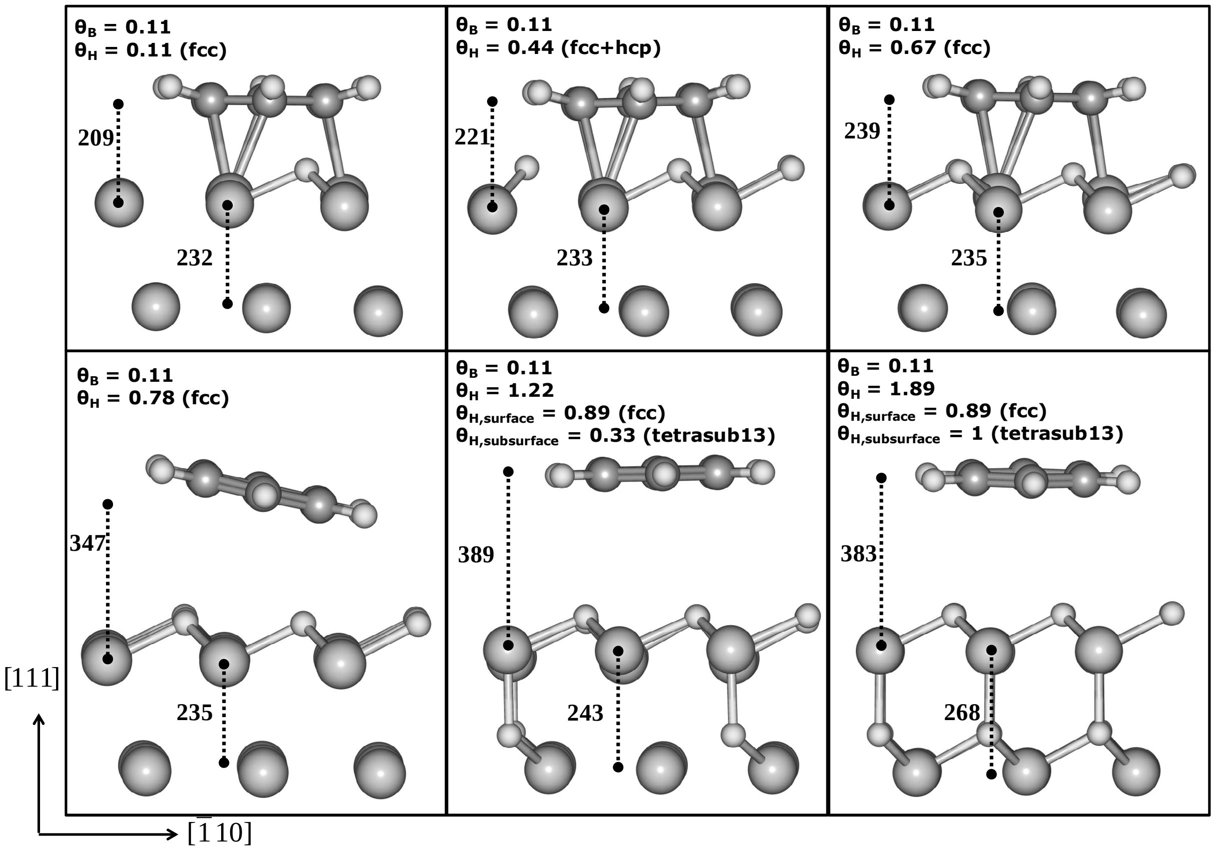

Figure 2-10: Side view of the adsorption geometry of $\theta_B = 0.11$ benzene coadsorbed with increasing coverages of hydrogen. The distances between the benzene centre of mass and the top Pd surface layer, and between the top surface and the subsurface layer are indicated in picometer. Due to the projection, no all hydrogen atoms are shown.

2.3.3.b Thermodynamic phase diagram

The thermodynamic most stable coverage of the catalytic surface has been evaluated as a function of pressure and temperature based on surface Gibbs free energies. These have been calculated for the coadsorption geometries illustrated in Figure 2-8 using the same four approaches as for the adsorption of benzene and hydrogen.

For coadsorption, benzene is considered to adsorb only on hollow-hcp(0) sites and at a fixed coverage of $\theta_B = 0.11$. As explained in the methodology section and illustrated in Figure A2 in Appendix A, the evaluation of the most stable hydrogen coverages coadsorbed with a fixed benzene coverage is not dependent on benzene pressures. The transition line between clean surface and adsorbed benzene, however, does depend on benzene pressure. Calculation of this line, which is discussed in detail in Appendix A, involves obtaining the benzene pressures that are required to have a fixed benzene coverage at a certain hydrogen pressure, by using a Langmuir model for coadsorption. The line is shown in each panel of Figure 2-11 with a blue dotted line. It is observed that the transition from clean to benzene covered surface occurs at higher temperatures using the equilibrium coefficients from PW91 (Figure 2-11a and Figure 2-11b) than from the vdW-DF method (Figure 2-11b and Figure 2-11d). The reason is that using the optPBE-vdW functional the adsorption of benzene is enhanced while the adsorption of hydrogen is hindered as compared to the PW91 results. Therefore, the benzene pressures required to fix the benzene coverage at θ_B = 0.11 from the Langmuir model are lower in *vdW-DF-*E_{el}.

The comparison between *PW91-*E_{el} and *PW91-G* (see Figure 2-11a and Figure 2-11b) follows the results obtained for the adsorption of hydrogen and benzene. The inclusion of Gibbs free energy vibrational contributions in *PW91-G* predicts a lower entropy term compared to PW91-Eel. A lower entropy term leads to a lower surface Gibbs free energy, and it is more pronounced for benzene coadsorbed with hydrogen coverages of θ_H = 0.22, 0.89 and 1. Therefore, these coverages are observed to populate the surface up to higher temperatures in *PW91-G* as compared to *PW91-*E_{el}. The comparison between the *PW91-*E_{el} and *vdW-DF-*E_{el} approaches (see Figure 2-11a and Figure 2-11c), which neglect Gibbs free energy vibrational contributions and use the results obtained with the PW91 and optPBE-vdW functionals resp., shows that coadsorption of benzene with hydrogen coverages of θ_H = 0.11, 0.22 and 0.44 is expected on the surface for a wider range of conditions with the *vdW-DF-*E_{el} than with the *PW91-*E_{el} approach. Furthermore, hydrogen coverages above $\theta_H > 0.89$ are not expected at any condition, similar to the results obtained for adsorption of hydrogen on a clean Pd(111) surface.

At typical industrial and lab-scale hydrogenation conditions, *i.e.* $350 \leq T \leq 550$ K and $1 \leq p_{H2} \leq 100$ bar indicated in each diagram with a rectangle, the *PW91-E$_{el}$* approach shown in Figure 2-11a indicates that surface-only $\theta_H = 0.89$ coverage is expected to populate the surface when coadsorbed with benzene, and if vibrational contributions to the surface Gibbs free energy are neglected. However, if these contributions are included (*PW91*-G), we predict that $\theta_H = 1$ populates the surface coadsorbed with benzene at typical hydrogenation conditions (see Figure 2-11b). The approach that uses the vdW-DF method and neglects vibrational contributions predicts at these conditions that hydrogen coverages between $0.44 \leq \theta_H \leq 0.89$ More accurate results could be obtained if the optPBE-vdW functional is used to optimize the geometries, and also to perform a vibrational analysis to obtain the vibrational contributions to the surface Gibbs free energy. This has not been performed due to computational constraints. However, a rough picture of the expected result is proposed by adding the PW91vibrational contributions to the vdW-DF electronic energies (*vdW-DF-G$_{PW91}$* shown in Figure 2-11d). This approximation results in hydrogen coverages of $\theta_H = 0.89$ at typical hydrogenation conditions. Due to the large difference in entropy contributions and adsorption energy between the *PW91-E$_{el}$* and resp. the *PW91-G* and *vdW-DF-E$_{el}$*, the inclusion of vibrational contributions and a proper description of van der Waals interactions are strongly recommended to predict the thermodynamically most stable catalyst surface state.

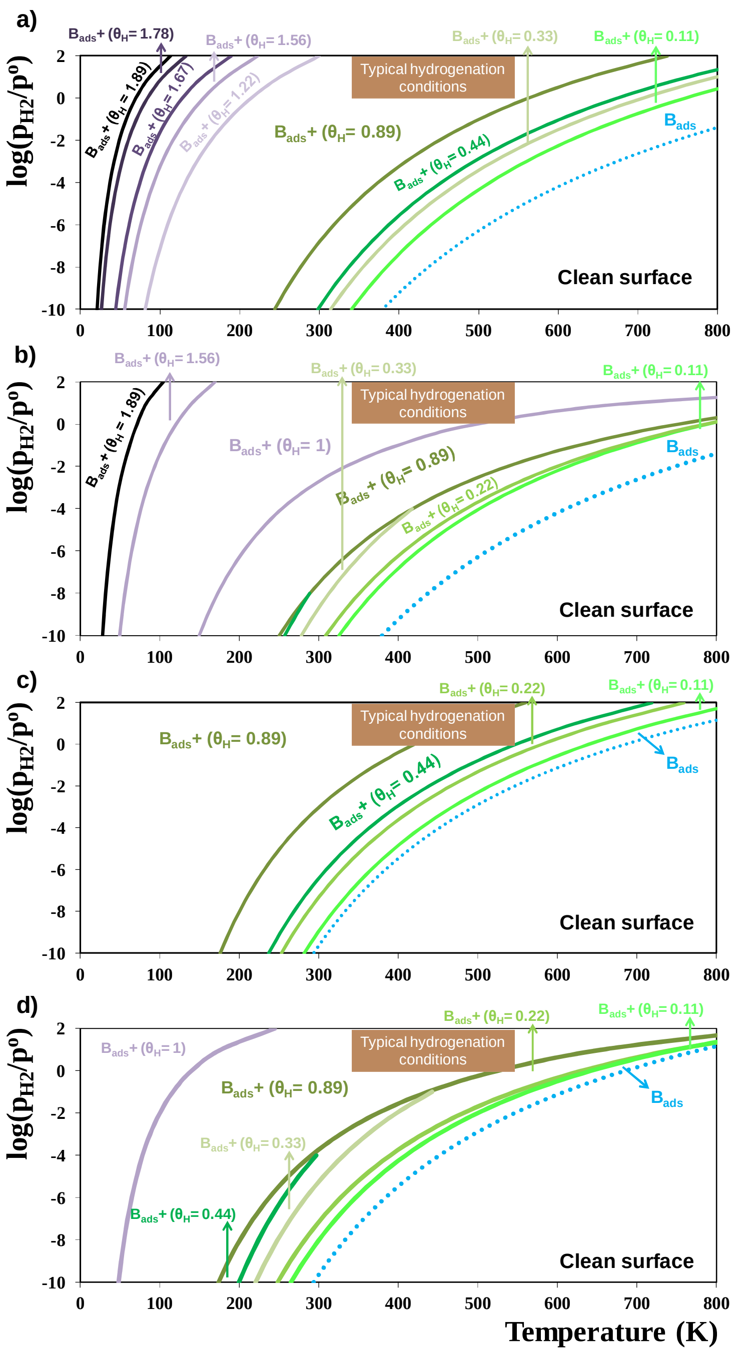

Figure 2-11: Thermodynamic phase diagram of benzene and hydrogen coadsorption on Pd(111) as a function of temperature and hydrogen pressure for a standard pressure of p^o=1 bar. The diagrams are constructed for a fixed benzene coverage of θ_B = 0.11 and hydrogen coverages up to θ_H = 1.89 with the (a) *PW91-E_{el}* approach, which neglects vibrational contributions and uses the PW91 functional, (b) *PW91-G* approach, which calculates surface Gibbs free energies including vibrational contributions with the PW91 functional, the (c) *vdW-DF-E_{el}* approach, which neglects vibrational contributions and uses the optPBE-vdW functional [59, 69], and the (d) *vdW-DF-G_{PW91}* approach, which is obtained by adding the PW91 vibrational contributions to the optPBE-vdW electronic energies. Typical hydrogenation conditions are shown with a rectangle.

2.4 Conclusions

Periodic density functional theory (DFT) calculations have been used to investigate the adsorption and coadsorption of benzene and hydrogen on Pd(111) with both gradient-corrected (PW91) and vdW-DF (optPBE-vdW) functionals. The results have been embedded in a thermodynamic model to calculate surface Gibbs free energies and construct the thermodynamic phase diagram. This diagram allows to predict the most stable coverages on the catalyst surface, as a function of the gas-phase temperature and pressure. In literature, the vibrational contribution to the surface Gibbs free energy is often neglected. We have shown, however, that large different coverages can be observed as compared to the approach that includes these vibrational contributions, caused by the different entropy contributions in each approach. Furthermore, a thermodynamic phase diagram has also been constructed using the optPBE-vdW results, although neglecting vibrational contributions. In this approach, the diagram obtained for the adsorption of benzene predicts higher benzene coverages than to the equivalent one from PW91, connected to the stronger benzene adsorption energies calculated by the optPBE-vdW functional. On the other hand, lower hydrogen coverages are predicted for hydrogen adsorption and coadsorption with a fixed benzene coverage. This is also explained with the weaker hydrogen adsorption obtained with the optPBE-vdW method compared to the PW91 functional. A more accurate diagram can be obtained if optPBE-vdW vibrational contributions are used to construct the thermodynamic phase diagram, but has not been performed due to computational limitations. However, a rough picture of the expected results is proposed by combining the PW91 vibrational contributions with the electronic energies calculated with the optPBE-vdW functional. This approximation infers that hydrogen coverages of about $\theta_H = 0.89$ can be coadsorbed with benzene at typical hydrogenation conditions. Inclusion of vibrational contributions to the surface Gibbs free energy and the use of the vdW-DF method is recommended to construct thermodynamic phase diagrams to predict the most stable catalyst coverage as a function of the conditions.

2.5 References

1. A. C. Capleton and L. S. Levy, *Chem. Biol. Interact.*, 2005, **153**, 43-53.
2. M. Sanati, B. Harrysson, M. Faghihi, B. Gevert and S. Jaras, in *Catalysis*, ed. J. J. Spivey, Royal Society of Chemistry, Cambridge, Editon edn., 2002, pp. 1-42.
3. H. Conrad, G. Ertl and E. E. Latta, *Surf. Sci.*, 1974, **41**, 435-446.
4. T. E. Felter, E. C. Sowa and M. A. Vanhove, *Phys. Rev. B: Condens. Matter Mater. Phys.*, 1989, **40**, 891-899.
5. J. F. Paul and P. Sautet, *Phys. Rev. B: Condens. Matter Mater. Phys.*, 1996, **53**, 8015-8027.
6. W. Dong, V. Ledentu, P. Sautet, A. Eichler and J. Hafner, *Surf. Sci.*, 1998, **411**, 123–136.
7. U. Muschiol, P. K. Schmidt and K. Christmann, *Surf. Sci.*, 1998, **395**, 182-204.
8. O. M. Lovvik and R. A. Olsen, *Phys. Rev. B: Condens. Matter Mater. Phys.*, 1998, **58**, 10890-10898.
9. A. Winkler, *Appl. Surf. Sci.*, 2009, **256**, 1114-1119.
10. C. Chizallet, G. Bonnard, E. Krebs, L. Bisson, C. Thomazeau and P. Raybaud, *J. Phys. Chem. C*, 2011, **115**, 12135-12149.
11. B. D. Adams, C. K. Ostrom, S. A. Chen and A. C. Chen, *J. Phys. Chem. C*, 2010, **114**, 19875–19882.
12. A. Basile, *Top. Catal.*, 2008, **51**, 107-122.
13. S. H. Israni, B. K. R. Nair and M. P. Harold, *Catal. Today*, 2009, **139**, 299-311.
14. A. E. Baber, H. L. Tierney, T. J. Lawton and E. C. H. Sykes, *Chemcatchem*, 2011, **3**, 607-614.
15. G. W. Watson, R. P. K. Wells, D. J. Willock and G. J. Hutchings, *J. Phys. Chem. B*, 2001, **105**, 4889-4894.
16. J. A. Konvalinka and J. J. F. Scholten, *J. Catal.*, 1977, **48**, 374-385.
17. A. Michaelides, P. Hu and A. Alavi, *J. Chem. Phys.*, 1999, **111**, 1343-1345.
18. S. T. Ceyer, *Acc. Chem. Res.*, 2001, **34**, 737-744.
19. D. Stacchiola and W. T. Tysoe, *Surf. Sci.*, 2003, **540**, L600-L604.
20. J. R. Lomas and G. Pacchioni, *Surf. Sci.*, 1996, **365**, 297-309.
21. M. Saeys, M. F. Reyniers, G. B. Marin and M. Neurock, *J. Phys. Chem. B*, 2002, **106**, 7489-7498.
22. F. Mittendorfer, C. Thomazeau, P. Raybaud and H. Toulhoat, *J. Phys. Chem. B*, 2003, **107**, 12287-12295.
23. C. Morin, D. Simon and P. Sautet, *J. Phys. Chem. B*, 2004, **108**, 5653-5665.
24. S. J. Jenkins, *Proc. R. Soc. Lond. A. Math. Phys. Sci.*, 2009, **465**, 2949-2976.
25. V. H. Grassian and E. L. Muetterties, *J. Phys. Chem.*, 1987, **91**, 389-396.
26. G. D. Waddill and L. L. Kesmodel, *Phys. Rev. B: Condens. Matter Mater. Phys.*, 1985, **32**, 2107-2114.
27. G. D. Waddill and L. L. Kesmodel, *Phys. Rev. B: Condens. Matter Mater. Phys.*, 1985, **31**, 4940-4946.

28. H. Ohtani, B. E. Bent, C. M. Mate, M. A. Van Hove and G. A. Somorjai, *Appl. Surf. Sci.*, 1988, **33-4**, 254-260.
29. H. Hoffmann, F. Zaera, R. M. Ormerod, R. M. Lambert, L. P. Wang and W. T. Tysoe, *Surf. Sci.*, 1990, **232**, 259-265.
30. W. T. Tysoe, R. M. Ormerod, R. M. Lambert, G. Zgrablich and A. Ramirez-Cuesta, *J. Phys. Chem.*, 1993, **97**, 3365-3370.
31. A. F. Lee, K. Wilson, R. M. Lambert, A. Goldoni, A. Baraldi and G. Paolucci, *J. Phys. Chem. B*, 2000, **104**, 11729-11733.
32. M. P. Kiskinova and G. M. Bliznakov, *Surf. Sci.*, 1982, **123**, 61-76.
33. W. Widdra, C. Huang, S. I. Yi and W. H. Weinberg, *J. Chem. Phys.*, 1996, **105**, 5605-5617.
34. S. G. Podkolzin, R. M. Watwe, Q. L. Yan, J. J. de Pablo and J. A. Dumesic, *J. Phys. Chem. B*, 2001, **105**, 8550-8562.
35. C. M. Mate and G. A. Somorjai, *Surf. Sci.*, 1985, **160**, 542-560.
36. E. Bertel, G. Rosina and F. P. Netzer, *Surf. Sci.*, 1986, **172**, L515-L522.
37. M. A. Van Hove, R. F. Lin and G. A. Somorjai, *J. Am. Chem. Soc.*, 1986, **108**, 2532-2537.
38. H. Ohtani, M. A. Van Hove and G. A. Somorjai, *J. Phys. Chem.*, 1988, **92**, 3974-3982.
39. W. Huber, H. P. Steinruck, T. Pache and D. Menzel, *Surf. Sci.*, 1989, **217**, 103-126.
40. A. Wander, G. Held, R. Q. Hwang, G. S. Blackman, et al., *Surf. Sci.*, 1991, **249**, 21-34.
41. A. Barbieri, M. A. Van Hove and G. A. Somorjai, *Surf. Sci.*, 1994, **306**, 261-268.
42. P. V. Jasen, G. Brizuela, Z. Padin, E. A. Gonzalez and A. Juan, *Appl. Surf. Sci.*, 2004, **236**, 394-405.
43. P. Jakob and D. Menzel, *Langmuir*, 1991, **7**, 134-139.
44. M. A. Vannice and W. C. Neikam, *J. Catal.*, 1971, **23**, 401-405.
45. P. Chou and M. A. Vannice, *J. Catal.*, 1987, **107**, 140-153.
46. P. C. Aben, J. C. Platteeu and B. Stoutham, *Recl. Trav. Chim. Pays-Bas*, 1970, **89**, 449-459.
47. L. P. Lindfors, T. Salmi and S. Smeds, *Chem. Eng. Sci.*, 1993, **48**, 3813-3828.
48. F. Jiracek, J. Pasek and J. Horak, *Collect. Czech Chem. C*, 1968, **33**, 3266-3270.
49. R. Z. C. Van Meerten, A. C. M. Verhaak and J. W. E. Coenen, *J. Catal.*, 1976, **44**, 217-225.
50. R. Z. C. Van Meerten, T. F. M. Degraaf and J. W. E. Coenen, *J. Catal.*, 1977, **46**, 1-12.
51. M. A. Keane and P. M. Patterson, *Ind. Eng. Chem. Res.*, 1999, **38**, 1295-1305.
52. C. Mirodatos, *J. Phys. Chem.*, 1986, **90**, 481-487.
53. P. Chou and M. A. Vannice, *J. Catal.*, 1987, **107**, 129-139.
54. S. D. Lin and M. A. Vannice, *J. Catal.*, 1993, **143**, 539-553.
55. C. Mager-Maury, G. Bonnard, C. Chizallet, P. Sautet and P. Raybaud, *Chemcatchem*, 2011, **3**, 200-207.
56. P. Raybaud, D. Costa, M. C. Valero, C. Arrouvel, et al., *J. Phys.: Condens. Matter*, 2008, **20**, 1-11.
57. J. Klimeš, D. R. Bowler and A. Michaelides, *J. Phys.: Condens. Matter*, 2010, **22**, 022201.
58. M. Mura, A. Gulans, T. Thonhauser and L. Kantorovich, *Phys. Chem. Chem. Phys.*, 2010, **12**, 4759-4767.
59. M. Dion, H. Rydberg, E. Schroder, D. C. Langreth and B. I. Lundqvist, *Phys. Rev. Lett.*, 2004, **92**, 246401.
60. G. Kresse, *J. Non-Cryst. Solids*, 1995, **193**, 222-229.
61. G. Kresse and J. Furthmuller, *Comput. Mater. Sci.*, 1996, **6**, 15-50.

62. G. Kresse and J. Furthmuller, *Phys. Rev. B: Condens. Matter Mater. Phys.*, 1996, **54**, 11169-11186.
63. G. Kresse and J. Hafner, *Phys. Rev. B: Condens. Matter Mater. Phys.*, 1994, **49**, 14251-14269.
64. P. E. Blochl, *Phys. Rev. B: Condens. Matter Mater. Phys.*, 1994, **50**, 17953-17979.
65. G. Kresse and D. Joubert, *Phys. Rev. B: Condens. Matter Mater. Phys.*, 1999, **59**, 1758-1775.
66. H. J. Monkhorst and J. D. Pack, *Phys. Rev. B: Condens. Matter Mater. Phys.*, 1976, **13**, 5188-5192.
67. J. P. Perdew, J. A. Chevary, S. H. Vosko, K. A. Jackson, et al., *Phys. Rev. B: Condens. Matter Mater. Phys.*, 1992, **46**, 6671-6687.
68. J. P. Perdew, J. A. Chevary, S. H. Vosko, K. A. Jackson, et al., *Phys. Rev. B: Condens. Matter Mater. Phys.*, 1993, **48**, 4978-4978.
69. H. Rydberg, B. I. Lundqvist, D. C. Langreth and M. Dion, *Phys. Rev. B: Condens. Matter Mater. Phys.*, 2000, **62**, 6997-7006.
70. J. Klimeš, D. R. Bowler and A. Michaelides, *Phys. Rev. B: Condens. Matter Mater. Phys.*, 2011, **83**, 195131.
71. H. Yildirim, T. Greber and A. Kara, *J. Phys. Chem. C*, 2013, **117**, 20572-20583.
72. J. Carrasco, W. Liu, A. Michaelides and A. Tkatchenko, *J. Chem. Phys.*, 2014, **140**, 084704.
73. M. C. Schoenmakerstolk, J. W. Verwijs, J. A. Don and J. J. F. Scholten, *Appl. Catal.*, 1987, **29**, 73-90.
74. C. Cappelli, F. Lipparini, J. Bloino and V. Barone, *J. Chem. Phys.*, 2011, **135**, 104505.
75. C. Humbert, O. Pluchery, E. Lacaze, A. Tadjeddinea and B. Busson, *Phys. Chem. Chem. Phys.*, 2012, **14**, 280-289.
76. R. Dingreville, J. M. Qu and M. Cherkaoui, *J. Mech. Phys. Solids*, 2005, **53**, 1827-1854.
77. B. A. De Moor, M. F. Reyniers and G. B. Marin, *Phys. Chem. Chem. Phys.*, 2009, **11**, 2939-2958.
78. P. C. Aben, *J. Catal.*, 1968, **10**, 224-229.
79. J. F. Paul and P. Sautet, *Surf. Sci.*, 1996, **356**, L403 L409.
80. I. Efremenko, *J. Mol. Catal. A: Chem.*, 2001, **173**, 19-59.
81. V. Ledentu, W. Dong and P. Sautet, *J. Am. Chem. Soc.*, 2000, **122**, 1796-1801.
82. P. W. Atkins and J. De Paula, *Atkins' Physical chemistry*, 8th edn., Oxford University Press, Oxford ; New York, 2006.
83. M. Puisto, H. Nenonen, A. Puisto and M. Alatalo, *Eur. Phys. J. B*, 2013, **86**, 1-9.
84. T. Engel and H. Kuipers, *Surf. Sci.*, 1979, **90**, 162-180.
85. G. E. Gdowski, T. E. Felter and R. H. Stulen, *Surf. Sci.*, 1987, **181**, L147-L155.
86. P. Hofmann, K. Horn and A. M. Bradshaw, *Surf. Sci.*, 1981, **105**, L260-L264.
87. H. Ihm, H. M. Ajo, J. M. Gottfried, P. Bera and C. T. Campbell, *J. Phys. Chem. B*, 2004, **108**, 14627-14633.
88. O. Schaff, V. Fernandez, P. Hofmann, K. M. Schindler, et al., *Surf. Sci.*, 1996, **348**, 89-99.
89. W. T. Tysoe, G. L. Nyberg and R. M. Lambert, *Surf. Sci.*, 1983, **135**, 128-146.
90. K. Toyoda, Y. Nakano, I. Hamada, K. Lee, S. Yanagisawa and Y. Morikawa, *Surf. Sci.*, 2009, **603**, 2912-2922.
91. J. Klimes, D. R. Bowler and A. Michaelides, *J Phys-Condens Mat*, 2010, **22**, 1-12.
92. M. Saeys, M. F. Reyniers, M. Neurock and G. B. Marin, *J. Phys. Chem. B*, 2005, **109**, 2064-2073.
93. K. L. Haug, T. Burgi, M. Gostein, T. R. Trautman and S. T. Ceyer, *J. Phys. Chem. B*, 2001, **105**, 11480-11492.

Chapter 3

Ab initio coverage-dependent microkinetic modelling of benzene hydrogenation on Pd(111)

Abstract

The effect of hydrogen coverage on the Pd(111) catalyzed hydrogenation of benzene has been investigated with optPBE-vdW density functional theory calculations. At both low and high coverage, a dominant path is identified consisting of the consecutive hydrogenation of carbon atoms located in ortho position relative to the previously hydrogenated carbon atom. Adsorption equilibrium coefficients decrease with the presence of hydrogen on the surface, and surface reaction rate coefficient increase due to the larger destabilization of reactants as compared to transition states. The ab initio kinetics are used to construct a coverage-dependent microkinetic model that explicitly accounts for coverage-dependence on rate coefficients. The simulated catalytic activities are comparable to experimental observations, exceeding those obtained using the low-coverage microkinetic model by several orders of magnitude. The reactions with the largest influence on the global rate obtained with the coverage-dependent microkinetic model change with the reaction conditions, and differ from those calculated using low coverage kinetics, or those proposed from the rate coefficients. Accurate DFT modeling of catalytic hydrogenation reactions requires both coverage dependence on the kinetics and thermodynamics and the use of a DFT functional that better describes van der Waals interactions than generalized gradient approximation (GGA) functionals.

3.1 Introduction

The hydrogenation of benzene is industrially performed in the refining industry to improve the quality of diesel fuels, and in the petrochemical industry to obtain intermediates in the production of Nylon 6 and Nylon 6-6 polymers.[1] Benzene hydrogenation is also a key reaction in the production of clean fuels that meet the stringent legislations on the concentration of the carcinogenic benzene in fuels.[2] Despite the large number of experimental and theoretical studies on benzene hydrogenation, there is no consensus on the mechanism of this complex reaction network.[3] The mechanism can be investigated using microkinetic modelling. This approach analyzes catalytic reactions in terms of elementary surface steps,[4] and allows describing and understanding complex reactions incorporating the surface chemistry into a kinetic model. The surface chemistry of complex catalytic reactions can be evaluated by electronic-structure theoretical methods, such as density functional theory (DFT), providing reliable results at the molecular scale for adsorption and surface reactions.

Benzene hydrogenation has been experimentally studied on catalysts such as Ni,[5-14] Pd, [13, 15-17] and Pt,[13, 17-26] due to their outstanding ability to saturate hydrocarbon molecules. A large variety of kinetic models has been proposed based on the experimental data. Some postulated that gas-phase hydrogen reacts with chemisorbed benzene following an Eley-Rideal mechanism.[27, 28] The general agreement is however that the reaction proceeds via a Langmuir-Hinshelwood-Hougen-Watson mechanism involving reaction between chemisorbed hydrogen and chemisorbed hydrocarbon species.[3] Furthermore, competition between benzene and hydrogen for the active sites has been claimed,[13, 14, 17] and denied by others.[5, 6, 11, 12, 29] The first hydrogen addition has often been considered as the rate determining step on Ni,[8, 10, 29] Pd, [29] and Pt.[19, 23] The fourth[30] and fifth reactions[31] have also been proposed on Pt as rate determining step, and for Ni it has also been considered that the six sequential hydrogenation steps have the same rate coefficient. [5, 10] Accounting for dehydrogenation of benzene could explain the formation of carbonaceous species[19] and the decrease in active sites,[16] but benzene dehydrogenation is neither thermodynamically nor kinetically favored compared to hydrogenation.[32] The presence of adsorbed cyclohexene has been reported during benzene hydrogenation experiments,[20, 21, 33-35] although the formation of gas-phase cyclohexene is thermodynamically less favorable as compared to the major product cyclohexane [33, 36]. Inhibition by adsorbed cyclohexane has been discarded, [37] because its surface concentration is assumed to be negligible since cyclohexane is typically expected to desorb fast and irreversibly.[38] The catalytic activity reaches a maximum as a function of temperature at about ~500 K for Pd catalysts.[15, 17] This maximum is explained by the balance between the decrease in surface concentration of the reactants with temperature and the increase in surface reaction rate coefficients. Furthermore, the partial reaction order with respect to hydrogen is usually in the range from 0.5 to 3,[15] while it is close to zero for benzene.[13, 15] This could indicate a higher surface concentration of benzene as compared to hydrogen.

Few theoretical studies have investigated benzene hydrogenation,[38-40] and these usually consider low to moderate coverages of reactants and use common gradient-corrected functionals (GGA) in DFT, such as PW91 or PBE. Mittendorfer and Hafner[39] proposed that the mechanism for benzene hydrogenation on Ni(111) proceeds with both molecules adsorbed prior to reaction, *i.e.*, a Langmuir-Hinshelwood type of mechanism, which resulted in a much lower activation barrier than the Eley-Rideal mechanism. On Pd(111), Morin et al.[40] assumed that the reaction path follows a Horiuti-Polanyi mechanism,[41] with the stepwise hydrogenation of the consecutive carbon atoms in ortho position relative to the previously hydrogenated carbon atom (ortho path), and the first hydrogen addition as limiting step assuming a linear relationship between activation and reaction barriers. The same step was proposed on Ni(111) from activation barriers, in line with what was previously proposed in literature because the aromaticity of benzene is not broken upon adsorption.[8, 10, 29] On Pt(111), the reaction path involving the hydrogenation of carbon atoms in the meta position (for the first three hydrogenation steps) was found to be preferred on Pt_{22} clusters, with the fifth reaction having the largest activation energy.[38] However, the ortho path was later identified based on regression to experimental data [42], which agree with the observations of cyclohexene for benzene hydrogenation [26] and cyclohexane dehydrogenation [43] on Pt catalysts, although cyclohexane could also be formed via other reaction paths.

One of the main goals in the catalytic research is to incorporate most, if not all, molecular insights into a model that can fully describe a catalytic reaction at the reactor scale. Hydrogenation reactions are industrially performed at high hydrogen pressures, which lead to catalyst surfaces that often differ from those (low to medium coverage) considered in DFT studies. DFT methods are commonly used to calculate preferred adsorption sites, together with adsorption and activation energies at a given surface coverage. However, they are often not able to predict experimental data because adsorbate–adsorbate interactions at reaction conditions can affect chemical kinetics to a large extent.[43-46] Semiempirical approaches have been applied combining theoretical and experimental results into a microkinetic model to describe coverage dependence.[47-49] E.g., the approach based on the combination of the unity bond index quadratic exponential potential (UBI-QEP),[50] transition-state theory, surface science experiments and optimization of the rate coefficient by validation against experimental data.[45, 51] Following a DFT based approach, the surface coverages expected on the catalyst surface at the reaction conditions can be first predicted with the calculation of surface Gibbs free energies.[52-54] In a second step, the reaction kinetics and thermodynamics can be calculated considering the expected surface coverage under reaction conditions. This is typically done based on the assumption that adsorbates are uniformly distributed on the catalysts surface, i.e., on the mean field approximation.[55] Ideally, the full range of possible coverages should be evaluated and included, but this is computationally not feasible. A range of coverages can however be evaluated to construct a coverage-dependent microkinetic model, calculating activation entropies and energies as a function of the surface concentration modeled with DFT. This explicit coverage-dependent model can be solved to predict production rates and surface concentrations at reaction conditions. However, to the best of our knowledge, this has not been done based on ab initio results only.

This work aims at constructing a coverage-dependent microkinetic model for benzene hydrogenation on Pd(111) based on periodic DFT calculations, in which explicit coverage effects and van der Waals interactions are included on both adsorption and surface rate coefficients. First, the full reaction network is evaluated at low coverage with both gradient-corrected PW91 and optPBE-vdW functionals, and a dominant path is identified. Secondly, this dominant path is further evaluated with the optPBE-vdW functional at increasing hydrogen coverages on the surface. The results are used to construct a coverage-dependent microkinetic model that is solved to predict catalytic activities, and the results are compared to experimental results reported in the literature.

3.2 Methodology

3.2.1 Electronic energy calculations

The Vienna Ab initio Simulation Package (VASP) [56-59] is used to perform periodic density functional theory (DFT) calculations, using the projector augmented wave method (PAW) [60, 61]to describe the interactions between electrons and nuclei. The PAW method uses pseudopotentials and plane-wave basis sets, and a 400 eV cutoff energy is considered in the calculations. The first-order Methfessel Paxton method [62] is used to describe partial electronic occupancies close to the Fermi level with a smearing width of 0.3 eV, and Brillouin-zone integration is performed with a 5×5×1 Monkhorst-Pack grid.[63] The generalized gradient Perdew-Wang PW91 exchange-correlation functional is used to describe the attraction and repulsion between electrons.[64, 65] Using these settings, a magnetization of the bulk below 10^{-4} is calculated. The adsorption energy of benzene calculated with non-spin polarization is within 6 kJ mol^{-1} from the one considering spin-polarized calculations, therefore, non-magnetic systems are considered.

The catalyst slab is modeled with a (3×3) unit cell and four atomic layers, which has been proven to be accurate enough for describing surface reactions.[40] The two top Pd layers and the adsorbates on the surface are fully relaxed during the geometry optimization, and the two bottom Pd layers are fixed to the bulk structure (calculated lattice parameter a = 395.7 pm). The unit cell is repeated in the three directions to model an infinite surface, and periodic boundary conditions are applied. A 11 Å vacuum gap and a dipole layer are included in the direction perpendicular to the slab to avoid interactions between periodic images.

Very strict converge criteria are required to perform a subsequent frequency analysis, amounting to 10^{-8} eV on the energy for the electronic minimization and of 0.015 eV/Å for the maximum force for the geometry convergence. The *quasi-Newton RMM-DIIS algorithm* is applied for the geometry optimization.

The commonly used GGA functionals in DFT do not properly describe the nonlocal nature of the electron correlation, and in particular van der Waals interactions (vdW).[66] This can hamper the calculation of adsorption or activation energies.[67] This can be addressed using the nonlocal van der Waals density functional (vdW-DF), developed by Rydberg and Dion[68, 69] and implemented in VASP by Klimeš et al. [66, 70] The optPBE-vdW functional is used in this work because it has shown to provide adsorption energies and geometries for benzene adsorption on Pd(111) in line with experimental observations.[71]

In a previous work, [54] we have shown that at typical hydrogenation conditions the surface of Pd(111) is populated with higher hydrogen coverages compared to those that are often used in DFT studies. Therefore, this work investigates the effect of increasing hydrogen coverage on the thermodynamics and kinetics of benzene hydrogenation. This coverage dependence is performed calculating adsorption and surface rate coefficients at four different hydrogen coverages, which are defined as $\theta_{H,initial}$. These coverages are coadsorbed with the corresponding hydrocarbon molecules that are obtained along the reaction path. The hydrocarbon coverage is fixed to a single molecule per (3×3) unit cell ($\theta_{BHi} = 0.11$), with coverage defined as number of adsorbed molecules, or atoms in the case of hydrogen, per surface Pd atom. Different hydrocarbon coverages could also be evaluated to have a full picture of coverage effects. However, this would be computationally too expensive and it has not been evaluated.

The four hydrogen coverage evaluated are: $\theta_{H,initial} = 0$, 0.11, 0.44 and 0.67. In the first one ($\theta_{H,initial} = 0$), it is considered that $\theta_{BHi} = 0.11$ and $\theta_H = 0.11$ are adsorbed in different unit cells. The other three $\theta_{H,initial} = 0.11$, 0.44 and 0.66 consider, respectively, 1, 4, and 6 hydrogen atoms in the (3×3) unit cell, coadsorbed with the $\theta_{BHi} = 0.11$ hydrocarbon molecule. Hydrogen atoms are assumed to be adsorbed always on the same sites, regardless of the presence of hydrocarbon species. These sites correspond to the most stable combination calculated in a previous study for each hydrogen coverage coadsorbed with benzene.[54] Hence, it is assumed that these positions will remain the same if the hydrogen atoms are coadsorbed with hydrocarbons other than benzene.

Once the geometries of reactants and products are known, the minimum energy path between the two is calculated with the Nudged Elastic Band method.[72] Along the reaction path, a series of images are created and connected with springs. These images are optimized by force minimization, relaxing the images down the minimum energy path.[72] The geometry of the saddle point is further used as the initial guess for the Dimer method, [73] an effective method to find the energy and configuration of the transition state. The optimization of transition states for surface reactions at high hydrogen coverage is a computationally very demanding calculation, due to the increased number of atoms and the repulsive interaction that often lead to convergence problems. Therefore, the geometry of the transition state that is optimized at the lowest hydrogen coverage is further used as initial geometry in the calculation at increasing hydrogen coverages, properly adapting the amount of hydrogen atoms on the surface to obtain the corresponding coverage. This approach is considered to be accurate enough because it provides the same electronic energy and geometry as the computationally more intensive approach that performs the NEB calculation followed by the DIMER method.

3.2.2 Construction of the microkinetic model

Vibrational frequencies are required to calculate thermodynamic properties as a function of temperature using statistical thermodynamics. The frequency calculation is performed from a strictly optimized geometry to avoid imaginary frequencies. VASP numerically evaluates the Hessian matrix calculating the second derivative of the energy with respect to the nuclear motion with the harmonic oscillator approach (HO), for which a step size of 0.015 Å is used. The vibrational frequencies are calculated for those atoms that are relaxed in the geometry optimization, i.e., the two top Pd layers of the slab and the adsorbates.

Once vibrational frequencies are calculated, vibrational partition functions, zero-point energies, thermal corrections to the enthalpy and entropy can be obtained from statistical thermodynamic equations, as shown in detail in Appendix B (for more information the reader is referred to Cramer,[74] McQuarrie,[75] and Jensen[76]). From these values, kinetic and thermodynamic parameters can be calculated as a function of temperature, as also shown in Appendix B.

Periodic DFT calculations (NEB) for hydrogen diffusion between high-stability adsorption sites at high coverage show that hydrogen is most likely not mobile at 450 K, with electronic barriers above 15 kJ mol^{-1} at half the saturation coverage, and presumably this is also the case in the presence of adsorbed hydrocarbon molecules. Therefore, all results shown in this work consistently consider immobile surface species and, hence, only vibrational contributions are considered for surface species without translational or rotational contributions. For gas-phase species, on the other hand, rotation and translation are considered together with vibrational contributions to calculate the thermodynamic parameters.

A microkinetic model is constructed consisting of the adsorption and surface elementary reactions, using the DFT kinetics and thermodynamics. Adsorption rate coefficients are described as a product of the incident Hertz-Knudsen molecular flux, F, and the sticking probability s. Adsorption is considered as a non-activated process for all species, thus the sticking probability is approximated to equal that on a clean surface (s_0), as shown in eq. (1), and this is assumed to be 1 for all adsorbates. Desorption rate coefficients are obtained using the thermodynamic equilibrium coefficient from DFT adsorption enthalpies and entropies, as shown in eq. (2).

$$k_{ads} = \frac{s_0 \cdot F}{p} = \frac{s_0}{n_t \sqrt{2\pi \cdot m \cdot k_B \cdot T}} \tag{1}$$

$$k_{des} = \frac{k_{ads}}{K_{eq}} \tag{2}$$

In eq. (1), F the incident flux of gas-phase molecules on a surface, p the pressure in bar, n_t the number of active sites per m^2 (1.64 10^{18} m^{-2}), m the molecular mass (kg), k_B the Boltzmann constant and T the temperature (K).

Surface rate coefficients (k in s^{-1}) are described with an Arrhenius expression, see eq. (3), using the activation energies (E_a) and pre-exponential factors (A) calculated as explained in Appendix B.

$$k = A\exp\left(\frac{-E_a}{RT}\right) \tag{3}$$

Thermodynamic consistency is required when constructing microkinetic models,[55] not only for the surface reactions but also between surface and gas-phase thermodynamics. The first is accomplished if every surface reaction satisfies eq. (4) and eq. (5). [55]

$$E_{a,rev} = E_{a,for} - \Delta_r H^o \tag{4}$$

$$A_{for} = A_{rev}\exp\left(\frac{\Delta_r S^o}{R}\right) \tag{5}$$

Where $E_{a,for}$ and $E_{a,rev}$ are the forward and reverse activation enthalpies, respectively; A_{for} and A_{rev} are the forward and reverse pre-exponential factors, respectively, and $\Delta_r S^o$ is the reaction entropy. The procedure to calculate these parameters is explained in detail in Appendix B.

The second thermodynamic constraint is that the sum of reaction enthalpies in each path from reactants to products must equal the gas-phase global reaction enthalpy ($\Delta_r H^o_{gas}$),[55] see eq. (6), which can be known from gas-phase thermodynamics. Similarly, the pre-exponential factors for each path are related to the gas-phase reaction entropy,[55] which can be obtained from the gas-phase global reaction entropy ($\Delta_r S^0_{gas}$), the temperature and the universal gas constant, see eq. (7).

$$\sum_i \left(E_{a,for} - E_{a,rev}\right)_i = \Delta_r H^o_{gas} \tag{6}$$

$$\prod_i \left(\frac{A_{for,i}}{A_{rev,i}}\right) = \exp\frac{\left(\Delta_r S^o_{gas}\right)}{R} \tag{7}$$

The hydrogen coverage coadsorbed with the reactants ($\theta_{H,initial}$) is assumed to remain unaltered throughout every path. For hydrogenation steps, however, the coverage of hydrogen coadsorbed with the product ($\theta_{H,final}$) is lower than $\theta_{H,initial}$, see first reaction in eq. (8) and Figure 3-1. Therefore, the hydrogen coverage in the product is restored to $\theta_{H,initial}$ with adsorption of hydrogen on the surface covered with the product of each reaction. This yields the initial coverage $\theta_{H,initial}$ for the next hydrogenation reaction (see eq. (9) and Figure 3-1). The hydrogen adsorption parameters are calculated from eq. (9) to maintain thermodynamic consistency between surface and gas-phase species. Furthermore, a single hydrogen adsorption value can be introduced in the mean-field microkinetic model that is solved at each hydrogen coverage. Therefore, an average value of the six individual hydrogen adsorptions shown in eq. (9) is considered for a reaction path consisting of six consecutive hydrogenation steps. The adsorption of hydrogen to replenish the hydrogen coverage does not necessary yield the most stable configuration, and hydrogen atoms would diffuse to the lowest energy configuration. However, this work assumes that the additional hydrogen is adsorbed on the adsorption site that leads to the most stable configuration and, hence, that the diffusion enthalpy is zero.

$$BH_i^* + H_{\theta,initial}^* \rightleftharpoons TS_i + H_{\theta,\,final}^* \rightleftharpoons BH_{i+1}^* + H_{\theta,\,final}^* \tag{8}$$

$$BH_{i+1}^* + H_{\theta,\,final}^* + \frac{1}{2}H_{2,gas} \rightleftharpoons BH_{i+1}^* + H_{\theta,initial}^* \tag{9}$$

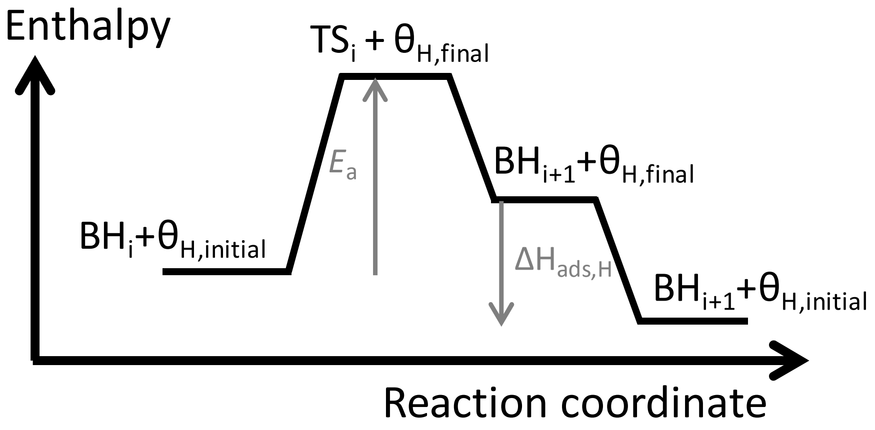

Figure 3-1: Procedure used to obtain the same hydrogen coverage for every hydrogenation step in a reaction path with periodic DFT calculations. The coverage of hydrogen coadsorbed with the reactants ($\theta_{H,initial}$) is higher than with products ($\theta_{H,final}$) because one hydrogen has been added to the hydrocarbon. Hydrogen is adsorbed on a surface covered by $\theta_{H,final}$ and the product hydrocarbon to obtain the same $\theta_{H,initial}$ coverage as initially, after which the next reaction can proceed analogously.

The gas-phase equilibrium coefficient calculated with VASP does not match the experimentally determined equilibrium coefficient from the National Institute of Standards and Technology database (NIST).[77] This is attributed to the overestimation of the reaction enthalpy in DFT, e.g. from benzene to cyclohexane by 22 and 41 kJ mol^{-1} with the PW91 and optPBE-vdW functionals, since the difference in reaction entropies is negligible. The difference in overestimation (of 20 kJ mol^{-1}) between the two functionals is explained from the hydrogen adsorption enthalpy calculated with both functionals. This is evidenced from the difference in $H_{2,gas}$ atomization energy of 18.2 kJ mol^{-1} obtained from the optPBE-vdW functional to the CBS-QB3 method, [78] as compared to the difference of ~1 kJ mol^{-1} between the CBS-QB3 and PW91. The CBS-QB3 is used to compare the values because of its good agreement with experiments.[78, 79] In order to correct for this, optPBE-vdW hydrogen adsorption enthalpies are increased by 18.2 kJ mol_{H2}^{-1}, and every hydrogen adsorption enthalpy shown in this work includes this correction. Further changes to match the NIST has phase experimental equilibrium have been done adapting adsorption enthalpies and entropies for the three product species only, i.e., cyclohexadiene, cyclohexene and cyclohexane. The original and modified values can be found in Table B6 and B11, respectively, in Appendix B.

A coverage-dependent microkinetic model has been constructed using the DFT kinetic and thermodynamic parameters at the four different hydrogen coverages $\theta_{H,initial}$. This has been done by regression of the kinetic parameters to a third-order polynomial as a function of the total coverage θ_{total}, see eq (10). The total coverage is defined as the coverage of hydrogen plus the coverage of the hydrocarbon on the surface, which can be assumed to be equal to 1 minus the free sites ($\theta_{total} = 1- \theta_*$).

$$L = a\theta_{total}^3 + b\theta_{total}^2 + c\theta_{total} + d \tag{10}$$

L being a parameter in the Arrhenius ($E_{a,f}$, $E_{a,r}$, $\Delta^{\ddagger}S_f$, $\Delta_{\ddagger}S_r$) or adsorption equilibrium coefficient expressions (ΔH_{ads}, ΔS_{ads}). All coefficients are shown in Appendix B in Tables B13 to B15.

3.2.3 Microkinetic modelling

Catalytic activities are simulated solving the microkinetic model as a function of reaction conditions in a reactor model. These simulations are performed with an in-house developed python code. The adsorption rate r_j of species i is calculated as shown in eq. (11).

$$r_j = \left(k_{i,ads} \cdot \theta_* \cdot p_i\right) - \left(k_{i,des} \cdot \theta_i\right) \tag{11}$$

The rate r_j of every surface reaction, eq. (12), is solved with the eq. (13).

$$BH_i^* + H^* \rightleftharpoons BH_{i+1}^* + * \tag{12}$$

$$r_j = k_{j,for} \cdot \theta_{BHi} \cdot \theta_H - k_{j,rev} \cdot \theta_{BHi+1} \cdot \theta_* \tag{13}$$

The code solves the surface coverage of the different species with the pseudo stationary state approximation (PSSA) applying eq. (14), with R_i the net production frequency of component i (molecules site^{-1} s^{-1}).

$$R_i = \sum_j \nu_{ji} r_j = 0 \qquad (14)$$

It is assumed that the sum of all fractional surface coverage amounts to one, as shown in eq. (15)

$$1 = \theta_* + \theta_H + \theta_B + \sum_{i=1} \theta_{BHi} \qquad (15)$$

These results are embedded in a reactor model that algebraically solves the outlet flows of component *i* in the mass balance for a differentially operated reactor [80], see eq. (16) below.

$$\frac{dF_i}{dW} = C_t R_i = C_t \sum_j \nu_{ji} r_j \qquad (16)$$

F_i, being the molar flow of component *i* (mol s^{-1}), *W* the catalyst mass (1.28 10^{-3} kg) and C_t the concentration of active sites (9.6 10^{-2} $mol_{activesite}/kg_{cat}$ from CO chemisorption on Pd powder [15]). The turnover frequency of benzene hydrogenation (TOF) is calculated as the molecules of benzene consumed per active site per second (s^{-1}). Thermodynamic consistency with the experimental gas-phase equilibrium coefficient is checked in every simulation.

The typical lab-scale hydrogenation conditions correspond to $350 < T < 550$, 0.1 bar $< p_{H2} <$ 10 bar, 0.001 bar $< p_B <$ 1 bar. The effect of temperature on catalytic activities has been evaluated by performing simulations in a range of typical hydrogenation conditions, *i.e.*, 350 to 650 K, in steps of 50 K, and fixing hydrogen and benzene pressure to, respectively, 0.9 and 6.7 10^{-2} bar to compare to the results reported by Chou and Vannice.[15] A zero inlet flow of product species is considered. Furthermore, the partial reaction order of hydrogen is evaluated by fixing benzene pressure to 6.7 10^{-2} bar and varying hydrogen pressures between 4.0 10^{-2} to 0.9 bar. The partial reaction order of benzene is evaluated fixing hydrogen pressure to 0.9 bar and varying benzene pressures from 4.0 10^{-2} to 9 10^{-2} bar. The partial reaction order is calculated from the exponential coefficient (*n*) obtained fitting a power regression of the global reaction rate as a function of the corresponding partial pressure, i.e., $TOF = a \cdot p^n$.

The influence of the different elementary reactions steps on the global rate is performed with the rate of production (ROP) and sensitivity analyses (SA). The first calculates the ROP coefficient X_{ROP} as the ratio between the rate of each elementary step r_j and the turnover frequency, eq. (17). Those reactions with a much smaller rate than the TOF can be neglected in the reaction network, i.e., $\mathrm{X}_{\mathrm{ROP,i}} \sim 0$. A dominant path would then be composed of the reaction steps with rates similar to the TOF, *i.e.,* $X_{ROP} \sim 1$.

$$\mathrm{X}_{ROP,i} = \frac{r_j}{TOF} \tag{17}$$

The sensitivity analysis quantifies the importance of elementary reaction steps on the catalytic activity. It introduces a change in the pre-exponential factor for forward and reverse reactions, while keeping the temperature and the rate coefficients of the other reaction steps constant, see eq. (22) below. The sensitivity coefficient $X_{SA,j}$ is then calculated regarding the increase or decrease in the turnover frequency with the modified pre-exponential factor as compared to that using the original pre-exponential factor.

$$\mathrm{X}_{SA,j} = \frac{\dfrac{TOF' - TOF}{TOF}}{\dfrac{A_j' - A_j}{A_j}} \tag{18}$$

With *TOF* as the turnover frequency calculated with the original parameters, TOF’ the turnover frequency calculated with the modified pre-exponential factor for forward and reverse reaction of step *j*, A_j the original pre-exponential factor, and A_j’ the modified pre-exponential factor, taken as 1.01 times A_i .

3.3 Results

Periodic DFT calculations have been performed to study the catalytic hydrogenation of benzene to cyclohexane on Pd(111). The first part discusses the results obtained for the reaction network considering low hydrogen coverage in the DFT calculations. In the she second part the optPBE-vdW functional is used to perform a coverage study of adsorption and hydrogenation reactions. The calculated kinetics and thermodynamics are further used to construct a coverage-dependent microkinetic model that predicts catalytic activities at actual reaction conditions.

3.3.1 Kinetic analysis at low coverage

Benzene and hydrogen can be adsorbed on several adsorption sites on the Pd(111) surface, and for each combination of sites a reaction network for benzene hydrogenation can be considered. Assuming that the product of every reaction step is adsorbed on the same site as the reactant, and that there is no diffusion between different sites, every network consists of twenty different hydrogenation steps from benzene to cyclohexane, via 13 possible reactions paths (see Figure 3-2). The evaluation with theoretical calculations of all possible networks that originate from considering the different adsorption sites is computationally too expensive. Therefore, only the two reaction networks that originate from the adsorption of benzene on the two preferred adsorption sites have been evaluated, as will be discussed below. In this section, the thermodynamic and kinetic parameters are calculated assuming that the reacting hydrocarbon and hydrogen are adsorbed in different unit cells, therefore, these parameters do not include repulsive interactions between hydrocarbon–hydrogen species. In this section, gas-phase cyclohexane is the only reaction product, and the results shown have been obtained using the gradient-corrected PW91 functional.

The adsorption of a single hydrogen atom in the (3×3) unit cell corresponds to $\theta_H = 0.11$, low compared to the saturation coverage of 1.47 10^{19} atoms/m^2.[81] At $\theta_H = 0.11$, the adsorption enthalpy of –125 kJ mol_{H2}^{-1} is calculated at 450 K for the most stable hollow fcc site, shown in the right panel of Figure 3-3. This value is stronger than the adsorption energy reported in previous theoretical studies at lower coverages,[52, 82] and also stronger by 40 kJ mol^{-1} as compared to the experimental value.[83]

For benzene, the two most stable adsorption sites are the 4-fold bridge(30) and 3-fold hollow-hcp(0), see Figure 3-3a and b, in agreement with previous studies on Pd(111) [84] and other (111) transition metals. [85-87] The adsorption enthalpy of, respectively, –109 and –96 kJ mol^{-1} is calculated at 450 K in a (3×3) unit cell, *i.e.,* benzene coverage of $\theta_B = 0.11$. The value of $\theta_B = 0.11$ represents a moderate benzene coverage regarding the saturation coverage reported on Pd(111) [88] of $\theta_B = 0.17$, or 2.46 10^{18} molecules/m^2. The calculated adsorption of both bridge and hollow adsorbates is weaker than the experimentally reported adsorption, of –140 - –196 kJ mol^{-1},[89] which may indicate that the gradient-corrected PW91 functional is not able to properly describe adsorption of benzene. We have also shown in a previous study that hollow adsorbate becomes more stable than the bridge adsorbate when coadsorbed with hydrogen.[54] The latter results together with the small difference in stability between the two bridge and hollow adsorbates justify the study of both reaction networks originating from the hydrogenation of benzene adsorbed on the separate bridge and hollow sites. The two networks are defined as the bridge and hollow networks.

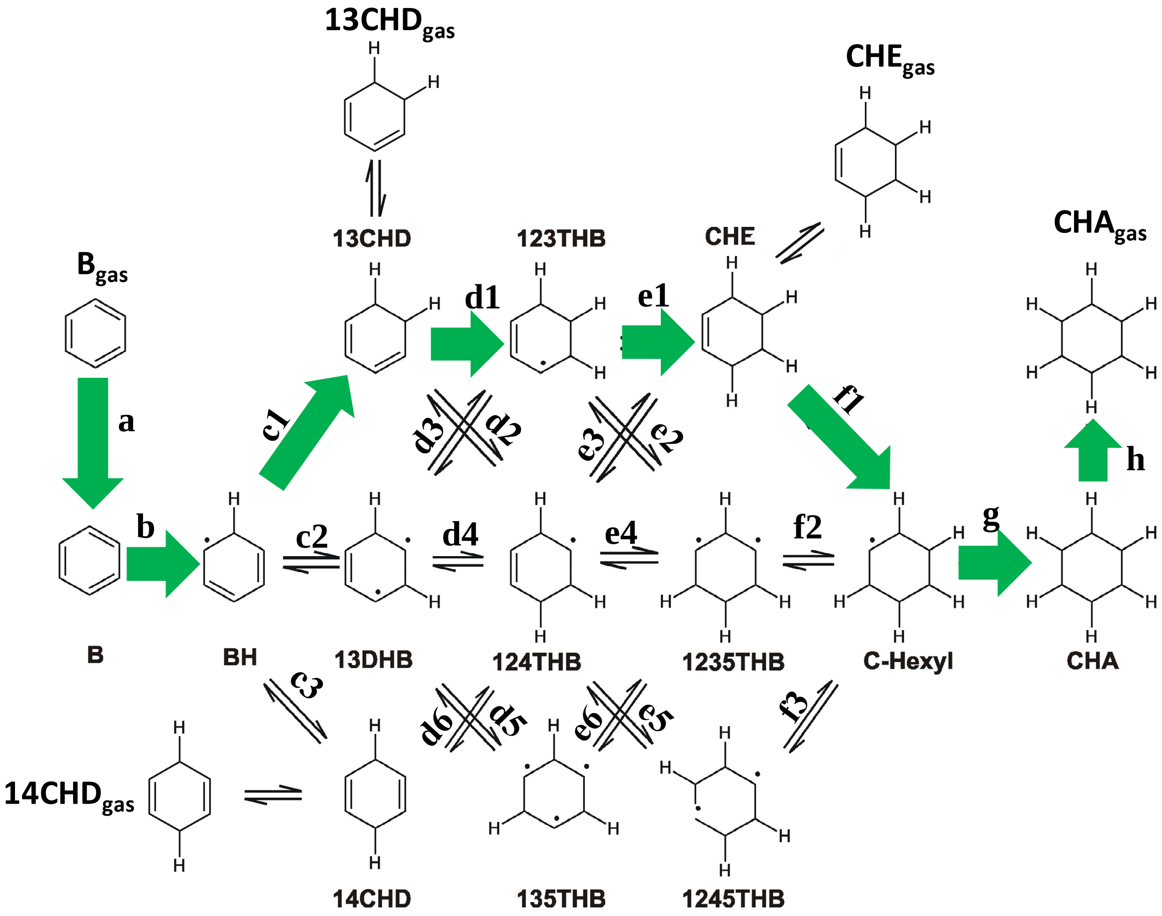

Figure 3-2: Full reaction network of the catalytic hydrogenation of benzene to cyclohexane, with labeling of the hydrogen steps and indication of the identified dominant path with green arrows. The following nomenclature is used for the surface species: *B* refers to benzene, *BH* to monohydrobenzene, *13CHD* to 1,3-cyclohexadiene, *13DHB* to 1,3-dihydrobenzene, *14CHD* to 1,4-cyclohexadiene, *123THB* to 1,2,3-trihydrobenzene, *124THB* to 1,2,4-trihydrobenzene, *135THB* to 1,3,5-trihydrobenzene, *CHE* to cyclohexene, *1235THB* to 1,2,3,5-tetrahydrobenzene, *1245THB* to 1,2,4,5-tetrahydrobenzene, *C-hexyl* to cyclohexyl, and finally *CHA* to cyclohexane.

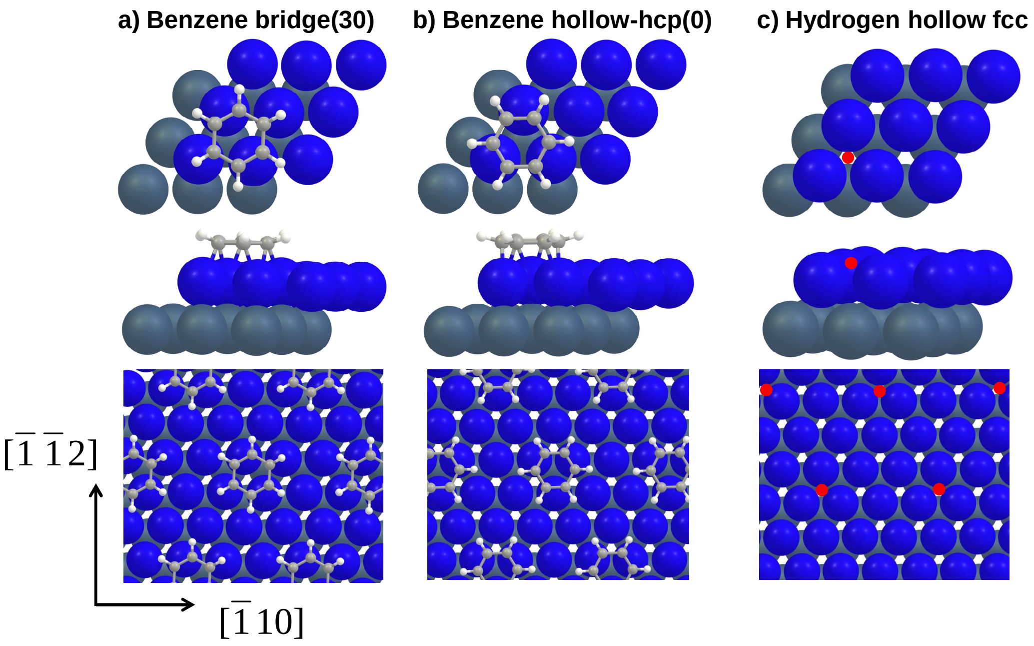

Figure 3-3: Preferred adsorption sites for benzene, (a) bridge(30) and (b) hollow-hcp(0), and for hydrogen on the (c) hollow fcc surface site (shown in red for easier identification).

The kinetic and thermodynamic parameters of every elementary reaction step in both bridge and hollow networks have been calculated with periodic DFT calculations (see all calculated parameters in Tables B1 and B2 in Appendix B). The kinetic and thermodynamic parameters are used to construct a microkinetic model for each of the two networks, which are solved at actual reaction conditions at the reactor scale (see equations and the approach used in the methodology section). The turnover frequency (TOF) is defined as molecules of benzene consumed per active site per second (s^{-1}). The simulated TOF in the hollow network is larger than the one obtained using the bridge network (up to 30 times larger at 400 K and 1.5 larger at 550 K), see Figure 3-4a. The TOF for both networks follow the same trend with temperature, and a maximum is observed at 550 K, while experimentally this is usually reported at 500 K. [15, 17] This maximum is explained with the decrease in surface concentration of the reactants with temperature, particularly benzene as shown in Figure 3-4b, which cannot compensate for the increase in surface hydrogenation rate. Because of the higher reactivity of benzene hollow, only this network is further discussed below.

The turnover frequency calculated at 413 K ($W/F_{B,in}$ = 62.5 kg_{cat} s mol^{-1}; $F_{B,in}$ = 2.1 10^{-5} mol s^{-1}; $F_{H2,in}$ = 2.8 10^{-4} mol s^{-1}, $p_{B,in}$ = 6.7 10^{-2} bar; $p_{H2,in}$ = 0.9 bar) of TOF = 1.4 10^{-6} s^{-1} is more than three orders of magnitude lower than the experimental value of 6 10^{-3} s^{-1} by Chou and Vannice on Pd power at the same conditions.[15] The partial reaction order for benzene and hydrogen calculated at 450 K are ~ 0.2 and ~ 4.2, as illustrated in Figure B2 in Appendix B. The value for benzene agrees with the experimentally observed zero order [15, 90, 91], however, the order on hydrogen is larger than experimental observations (ranging between 0.5 - 3.5). [15]

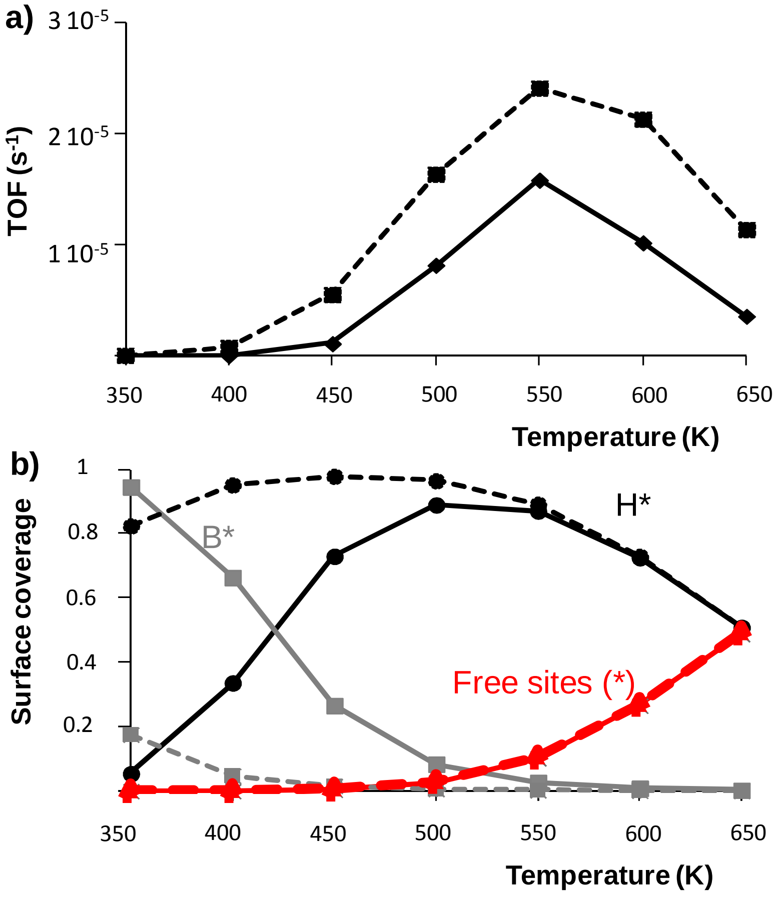

Figure 3-4: (a) Simulated turnover frequency (TOF) (s^{-1}) as a function of the temperature (K) for the bridge and hollow networks (full and dotted lines, respectively). (b) Surface coverage of benzene, hydrogen, and free sites (grey, black, and red, respectively) as a function of temperature, obtained for the simulation of the bridge and hollow networks. As a coincidence, both full and dotted red lines (free sites) almost overlap (($W/F_{B,in}$ = 62.5 kg_{cat} s mol^{-1}; $F_{B,in}$ = 2.1 10^{-5} mol s^{-1}; $F_{H2,in}$ = 2.8 10^{-4} mol s^{-1}, $p_{B,in}$ = 6.7 10^{-2} bar; $p_{H2,in}$ = 0.9 bar).

Simplification of the reaction network to a single dominant path can allow to evaluate other important effects on the catalytic performance that would be computationally too expensive in the full network, such as increasing coverage or a proper description of van der Waals interactions. Based on the DFT rate coefficients, a dominant path is identified in the full hollow reaction network (and also in the bridge network), consisting of the six consecutive surface reactions with the largest rate coefficients. This path follows a consecutive hydrogen addition to carbon atoms located in ortho position relative to the previously hydrogenated carbon (ortho path). This paths runs from benzene (B) to monohydrobenzene (BH), proceeding over 1,3-cyclohexadiene (13CHD), 1,2,3-trihydrobenzene (123THB), cyclohexene (CHE) and cyclohexyl (c-hexyl) to cyclohexane (CHA), as depicted with green arrows for the *b*, *c1*, *d1*, *e1*, *f1* and *g* reactions in Figure 3-2. The same dominant path is also identified with the rate of production analysis (ROP). As explained in the methodology section, this analysis calculates the reaction rate of each elementary step and compares it to the global rate (TOF). For temperatures in the range of 350 K < T < 650 K, the rate of production coefficient X_{ROP} =1 for the first, fourth, fifth and sixth reaction steps (*b*, *e1*, *f1* and *g* reactions, see Table B3 in Appendix B). For the second and third hydrogenation steps, $X_{ROP} \geq 0.8$ for the *c1* and *d1* reactions, while $X_{ROP} \geq 0.2$ for, respectively, the *c2* (BH* + H* ↔ 13DHB*) and *d3* reactions (13DHB + H* ↔ 123THB*). This ortho dominant path has also been suggested on Pd(111) by Morin et al.[40] from a thermodynamic basis, and by Tetenyi and Paal [33] from the hydrogenation of ^{14}C-labelled benzene and cyclohexadiene. Considering the dominant path, the underestimation of the TOF is below 10 % for the whole range of temperatures (see Figure B1 in Appendix B), therefore, the results discussed below correspond to the dominant path calculated for the hollow network only.

Based on the rate coefficients calculated for the reaction in the dominant path, the first hydrogenation step (see reaction *b* in Figure 3-2 or $B^{*}+H^{*} \rightarrow BH^{*} + {}^{*}$) is proposed to have the largest influence on the global rate. This has also been suggested by Morin et al. [40] on Pd(111) assuming that the activation energies of the hydrogenation steps scale with their calculated reaction barriers. The first hydrogenation step has also been proposed as rate determining from theoretical considerations, because the aromaticity of benzene is not broken on Pd(111) and it should therefore break during the first H addition step. [8, 10, 29] However, the sensitivity analysis performed in this work indicates that other reactions have greater influence on the rate at actual reaction conditions. Below 450 K, the third hydrogen addition (*d*1 reaction) in the dominant path has a sensitivity coefficient of $X_{SA,d1} = 0.8$, as shown in see Table B4 in Appendix B. Above 450 K, the sensitivity coefficient for the fifth reaction (reaction *f1* in Figure 3-2) raises to a value of $X_{SA,f1} = 0.8$ at 550 K.

Finally, the hollow dominant path has been evaluated at the same coverage but using the optPBE-vdW functional. This is done because of the underestimation of benzene adsorption enthalpies with the PW91 functional as compared to experimental values. The same dominant path as the one calculated with the PW91 functional is obtained with the optPBE-vdW functional. In this path, the reactions have an activation energy that is at least 15 kJ mol^{-1} lower than the values calculated for the alternative reactions (see Table B5 in Appendix B). A benzene adsorption enthalpy $\Delta H_{ads} = -163$ kJ mol^{-1} is calculated at 450 K and $\theta_B = 0.11$ with the optPBE-vdW functional. This represents an increase of 67 kJ mol^{-1} as compared to the PW91 functional, and agrees with previous theoretical values by Yildirim et al. [71] using the same functional (–168 kJ mol^{-1}), but for a lower coverage, and also with the experimental range of adsorption enthalpies (–140 - –196 kJ mol^{-1}). [89] For hydrogen adsorption, however, the adsorption enthalpy calculated with the optPBE-vdW functional is 23 kJ mol^{-1} weaker than with the PW91 functional. Although the value is closer to the experimentally reported $\Delta H_{ads} = -86$ kJ mol^{-1}[183], the weaker adsorption is attributed to an incorrect description of the gas phase H_2 molecule with the optPBE-vdW; the atomization energy of H_2 with the PW91 and optPBE-vdW functional is, respectively, –1.4 and 18.2 kJ mol^{-1} larger than the value with the CBS-QB3 energy. In the next section, the hollow dominant path is further evaluated with the optPBE-vdW considering surfaces with an increasing hydrogen coverage.

3.3.2 Kinetic analysis as a function of coverage

This section first discusses the kinetic and thermodynamic parameters for adsorption and reaction in the dominant path at increasing hydrogen coverages with the optPBE-vdW DFT functional. Secondly, a coverage-dependent microkinetic model is constructed, and finally, this model is solved at actual reaction conditions to predict catalyst activities.

3.3.2.a Thermodynamics and kinetics from DFT calculations

The presence of a possible dominant path at increasing hydrogen coverage has been first investigated with the optPBE-vdW functional. The activation barriers of the different reactions are calculated at a higher coverage of θ_H = 0.44 on the surface. The activation energies of the reactions in the ortho dominant path are lower, by about 25 kJ mol^{-1}, than the ones for the reactions that are not in this dominant path (see Table B5 in Appendix B). Therefore, this section considers the simplified ortho dominant path to study coverage effects. The simplification of the full reaction network by a dominant path allows performing a coverage study, which otherwise would be computationally too expensive for the full network. Additionally, the adsorption and desorption of the stable intermediates, namely 1,3-cyclohexadiene and cyclohexene, are also investigated.

The adsorption and surface reactions occurring in the dominant path are studied with DFT considering four different surfaces, each with a different hydrogen coverage $\theta_{H,initial}$, as illustrated for hydrogen in red in Figure 3-5 coadsorbed with benzene as an example. The first $\theta_{H,initial}$ (see Figure 3-5a) has been discussed in the previous section. The values at $\theta_{H,initial}$ = 0 are calculated relative to θ_{BHi} = 0.11 hydrocarbon coverage and $\theta_{H,initial}$ = 0.11 fcc hydrogen adsorbed in different unit cells. The effect of increasing coverage is studied by considering three more $\theta_{H,initial}$ hydrogen coverages; for these cases the θ_{BHi} = 0.11 hydrocarbon coverage is coadsorbed in the same unit cell with $\theta_{H,initial}$ = 0.11, 0.44 and 0.67 hydrogen coverage (modeled with 1, 4, and 6 hydrogen atoms in the (3×3) unit cell, as observed in top and middle panels of Figure 3-5b,c,d, respectively). The most stable sites for hydrogen coverages of $\theta_{H,initial}$ = 0.11, 0.44 and 0.67 have been calculated in a previous study[54] and are, respectively, i) fcc hollow site, ii) three fcc and a single hcp atoms in the (3×3) unit cell, and iii) all hydrogen atoms adsorbed on fcc sites (see Figure 3-5,b,c,d). Hydrogen is assumed to occupy the same sites regardless of the presence of other molecules than benzene on the surface.

The adsorption of benzene and products in the dominant path, namely 1,3-cyclohexadiene, cyclohexene and cyclohexane, is evaluated on a clean and H-covered surface with $\theta_{H,initial}$ = 0.11, 0.44 and 0.67 (see geometries of 1,3-cyclohexadiene, cyclohexene and cyclohexane species on a clean surface in Figure B3 in Appendix B). For all the species except cyclohexane, a decrease in adsorption enthalpy is calculated with increasing H-coverage on the surface (see Figure 3-6 and all values reported in Table B6 in Appendix B). The cyclohexane adsorption enthalpy, however, remains similar regardless of H-coverage, due to the low repulsive interactions between the physisorbed cyclohexane and the surface hydrogen atoms. The adsorption enthalpy of benzene on a θ_H = 0.67 H-covered surface (–77.5 kJ mol^{-1}) is in line with the range estimated by Chou and Vannice on Pd [15] fitting a kinetic model to benzene hydrogenation experiments (–58 to –70 kJ mol^{-1}), and it is close to the estimate, also fitting a kinetic model, of –82 kJ mol^{-1} by Singh and Vannice on Pd/Al_2O_3.[29]

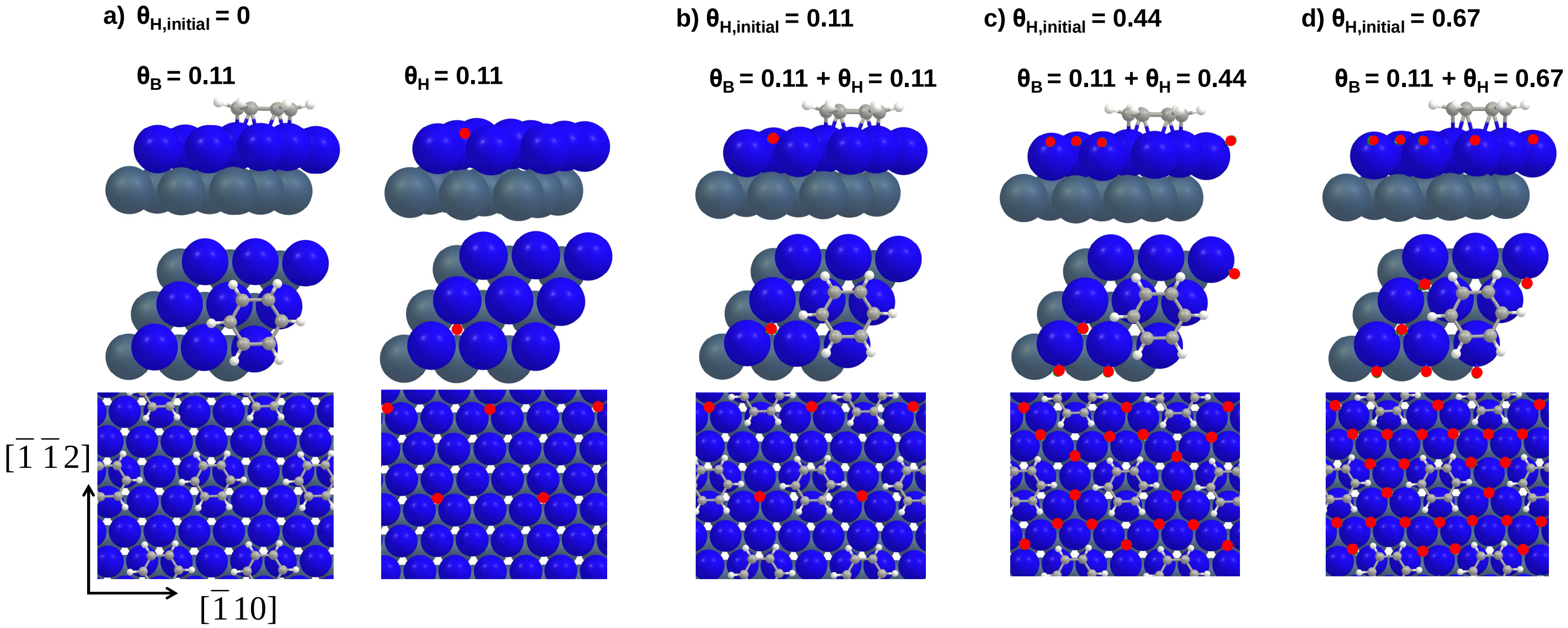

Figure 3-5: Benzene adsorbed at hollow-hcp(0) sites together with hydrogen coverage of (a) $\theta_H = 0.11$ (in different unit cells), and (b) $\theta_H = 0.11$, (c) $\theta_H = 0.44$ and (d) $\theta_H = 0.67$ in the same unit cell. Top and middle panel show side and top views of the (3×3) unit cell used, bottom panels illustrate a top view of the surface overlayer at each coverage. Pd atoms in the second layer are colored in grey and adsorbed hydrogen atoms in red for easier identification.

To the best of our knowledge, no adsorption enthalpies have been reported on Pd(111) for cyclohexane and cyclohexene. The calculated adsorption enthalpy of cyclohexane (–78 to –84 kJ mol^{-1}) is more exothermic than the experimental values from TPD experiments on Pt(111), –59 kJ mol^{-1} [92], and on Ni(111), –55 kJ mol^{-1}. [93]. For cyclohexene, the range (–66 to –109 kJ mol^{-1}) agrees with the coverage-dependent heats of adsorption on Pt(111) obtained from calorimetric measurements at ~100 K. [94]

For hydrogen, the values for the adsorption of an increasing coverage on a clean surface are shown in Figure 3-6. The values at $\theta_H = 0$ and $\theta_H = 0.11$ correspond to the same adsorption of $\theta_H = 0.11$ on a clean surface. Hydrogen adsorption enthalpy weakens with increasing coverage by less than 15 kJ mol^{-1}, in line with the small decrease of some 10 kJ mol^{-1} reported in previous studied. [82, 95, 96] Furthermore, the adsorption entropy of all species shows also a very small dependence on the H-coverage at the surface.

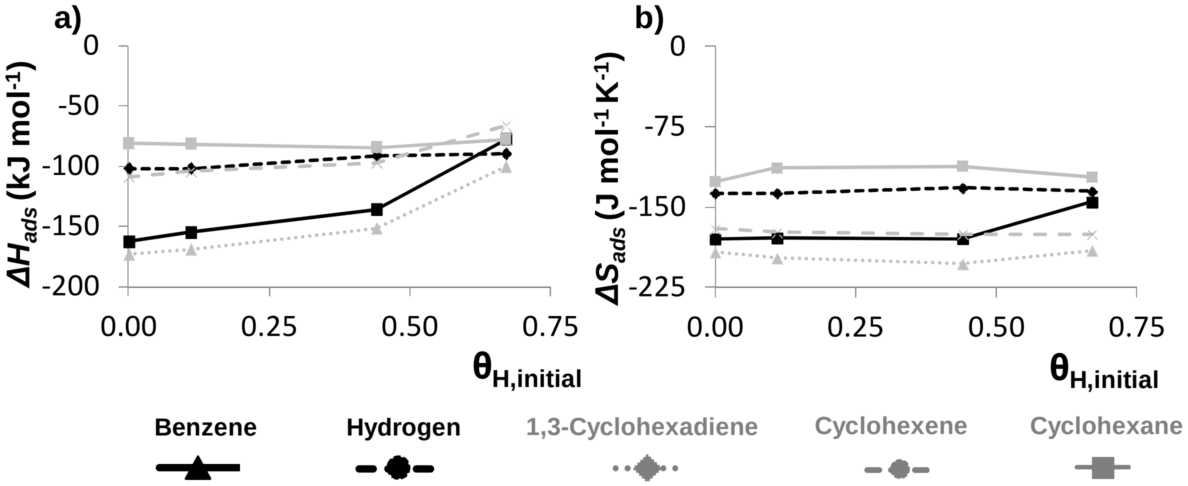

Figure 3-6: Adsorption (a) enthalpy (kJ mol^{-1}) and (b) entropy (J mol^{-1} K^{-1}) of benzene, 1,3-cyclohexadiene, cyclohexene and cyclohexane as a function of the hydrogen coverage on the surface. These values are directly calculated from DFT calculations, and no adaptation has been done to have thermodynamic consistency with gas-phase experimental equilibrium coefficient. For hydrogen, the values correspond to the adsorption of θ_H on a clean surface, and $\theta_H = 0$ and $\theta_H = 0.11$ both refer to the same adsorption of $\theta_H = 0.11$ on a clean slab.

For surface reactions, the influence of H-coverage on the kinetic and thermodynamic parameters of the six hydrogenation steps in the dominant path has also been studied at the four hydrogen coverages $\theta_{H,initial}$ = 0, 0.11, 0.44 and 0.67. The calculated values are shown in Appendix B from Table B7 to B10. For each hydrogenation step, the reaction enthalpy and activation energy decrease with increasing H-coverage (see left panel in Figure 3-7). This is explained with a larger destabilization of reactants as compared with transition states and products, because of the higher hydrogen coverage coadsorbed with reactants ($\theta_{H,initial}$). For each of the six hydrogenation steps, an excellent correlation is obtained between activation and reaction energy as a function of hydrogen coverage. This correlation allows predicting the computationally demanding activation energy at higher coverages from the more easily calculated reaction energy. Furthermore, an increase in equilibrium coefficients with hydrogen coverage is calculated for every hydrogenation step (see right panel in Figure 3-7). Equilibrium coefficients increase by several orders of magnitude from the values considering $\theta_{H,initial}$ = 0 to those obtained at the highest hydrogen coverage studied $\theta_{H,initial}$ = 0.67.

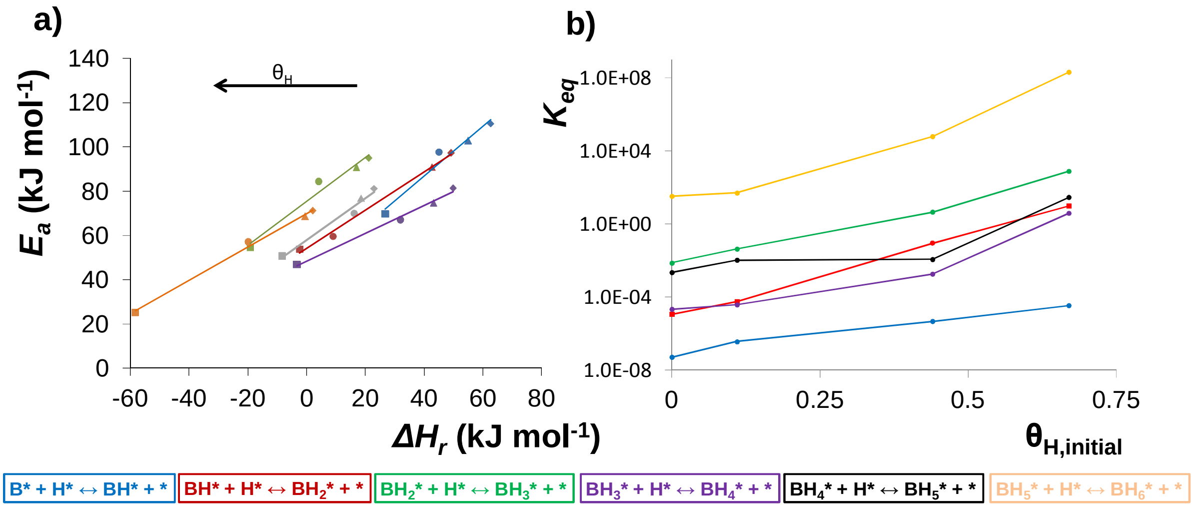

Figure 3-7: (a) Forward activation energy as a function of the reaction enthalpy (for the reaction: $BH_i + \theta_{H,initial} \leftrightarrow BH_{i+1} + \theta_{H,final}$) for the six reaction steps in the dominant path at the four different $\theta_{H,initial}$ hydrogen coverages considered to be coadsorbed with benzene: $\theta_{H,initial}$ = 0 (rhombus), 0.11 (triangles), 0.44 (circles) and 0.67 (squares). (b) Equilibrium coefficients for the six elementary surface reactions as a function of the same hydrogen coverages.

3.3.2.b Construction of the microkinetic model

A coverage-dependent microkinetic model is constructed using the results obtained from the DFT calculations, which explicitly accounts for coverage-dependence on rate coefficients. However, as mentioned in the methodology section, some of the DFT parameters that are shown in the section above have been adjusted to fulfill both: i) thermodynamic consistency with gas-phase experimental equilibrium coefficient, and ii) the use of a single hydrogen adsorption enthalpy and entropy in the microkinetic model, as it is explained below.

First, the DFT gas-phase equilibrium coefficient calculated does not match the experimentally determined equilibrium coefficient, attributed to the overestimation of the reaction enthalpy. Therefore, the adsorption enthalpy of product species, namely 1,3-cyclohexadiene, cyclohexene, and cyclohexane, has been adapted. These adaptations were also introduced in the low coverage microkinetic model. Adsorption enthalpies are adjusted by adding –16, –16 and –14 kJ mol^{-1} to the values shown in the previous section for cyclohexadiene, cyclohexene and cyclohexane, respectively. Adsorption entropies are adjusted by adding –7, –7 and 0 J mol^{-1} K^{-1}. The values are listed in Table B11 in Appendix B, and depicted in Figure 3-8.

Secondly, the proper hydrogen adsorption enthalpy and entropy is required to have a thermodynamically consistent microkinetic model. In the DFT calculations, the hydrogen coverage coadsorbed with the (partially hydrogenated) product of every hydrogenation step (defined as $\theta_{H,final}$) is lower than the hydrogen coverage coadsorbed with the reactants (defined as $\theta_{H,initial}$). In order to construct a microkinetic model that consists of the consecutive hydrogenation steps in the dominant path, hydrogen is adsorbed on the surface covered by the product species of each hydrogenation step to replenish the surface and have the same $\theta_{H,initial}$ in every consecutive reaction, i.e., $\theta_{H,final} + \theta_{BHi} + ½H_2 \leftrightarrow \theta_{H,initial} + \theta_{BHi}$. This is illustrated in Figure 3-9, which represents the enthalpy diagram of the dominant path at each of the four $\theta_{H,initial}$ studied. For $\theta_{H,initial}$ =0.11, 0.44 and 0.67, the six hydrogen adsorptions are observed

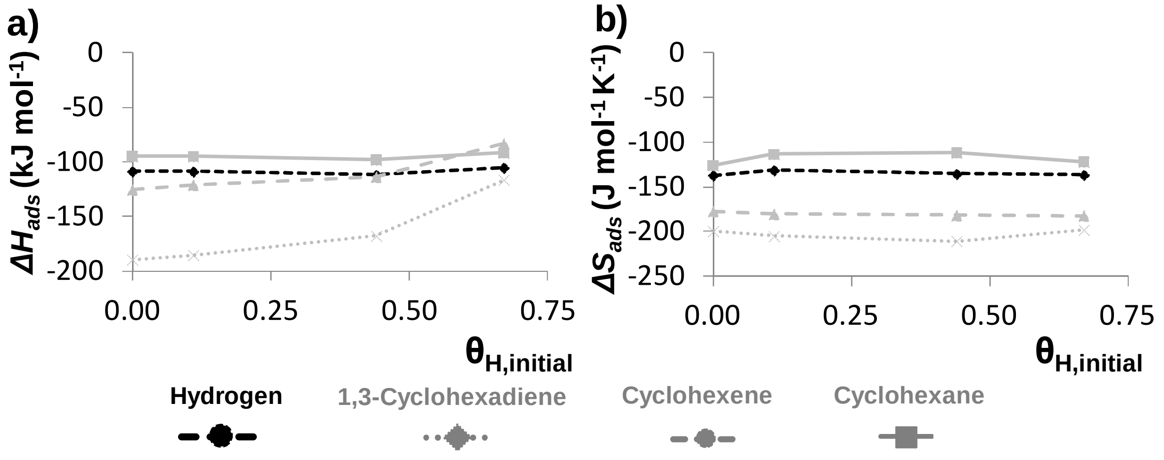

Figure 3-8: Adsorption (a) enthalpy (kJ mol^{-1}) and (b) entropy (J mol^{-1} K^{-1}) for hydrogen 1,3-cyclohexadiene, cyclohexene and cyclohexane used in the microkinetic model. For the hydrocarbon species, the values refer to the adsorption on a clean slab ($\theta_H = 0$), and on a H-covered surface with $\theta_H = 0.11$, 0.44 and 0.67. These values are obtained by adjusting those based on DFT to match the experimentally determined equilibrium coefficient. For hydrogen, the values represent the average of the six hydrogen adsorption on a surface covered with the product of the six sequential hydrogenation steps and $\theta_{H,final}$.

after each hydrogenation. However, a single adsorption enthalpy and entropy needs to be introduced in the mean-field microkinetic model, corresponding to a unique hydrogen adsorbed species. Therefore, these six values are averaged to have a single hydrogen value in the microkinetic model that leads to thermodynamic consistence (see values in Figure 3-8 and Table B12 in Appendix B). In the $\theta_{H,initial} = 0$ case, hydrogen and hydrocarbons are considered to be adsorbed in different unit cells. Therefore, regardless of the hydrogenation step, the adsorption of hydrogen corresponds to $\theta_H = 0.11$ adsorption on a clean surface.

Hydrogen adsorption enthalpy weakens with increasing coverage on the surface more pronouncedly than for the adsorption on a clean surface. Figure 3-8 and Figure 3-9 show the decrease in adsorption enthalpy from the adsorption of $\theta_H = 0.11$ on a clean surface ($\theta_{H,initial} = 0$) of –125 kJ mol_{H2}^{-1}, to the average value calculated for adsorption of $\theta_H = 0.11$ on a surface covered with $\theta_{H,final} = 0.56$ and a hydrocarbon molecule (–58 kJ mol_{H2}^{-1}). This range of adsorption enthalpies agrees with the value of –70 kJ mol_{H2}^{-1} estimated by Aben et al.[97] on Pd/SiO_2 fitting a kinetic model to experimental benzene hydrogenation data.

Furthermore, for each $\theta_{H,initial}$ = 0.11, 0.44 and 0.67 case, hydrogen adsorption enthalpy is stronger with increasing the degree of hydrogenation of the hydrocarbon present on the surface (see Table B12 in Appendix B). This is understood from the decrease in repulsive interactions between adsorbed hydrogen and hydrocarbons; from benzene to the partially hydrogenated intermediates, which are bound to 1 or 2 Pd atoms, and finally to the fully hydrogenated physisorbed cyclohexane, leading to a difference in hydrogen adsorption enthalpy of up to ~30 kJ mol^{-1}. Surface hydrogenation steps are not adapted, and the microkinetic model incorporates the values that are shown in the previous section.

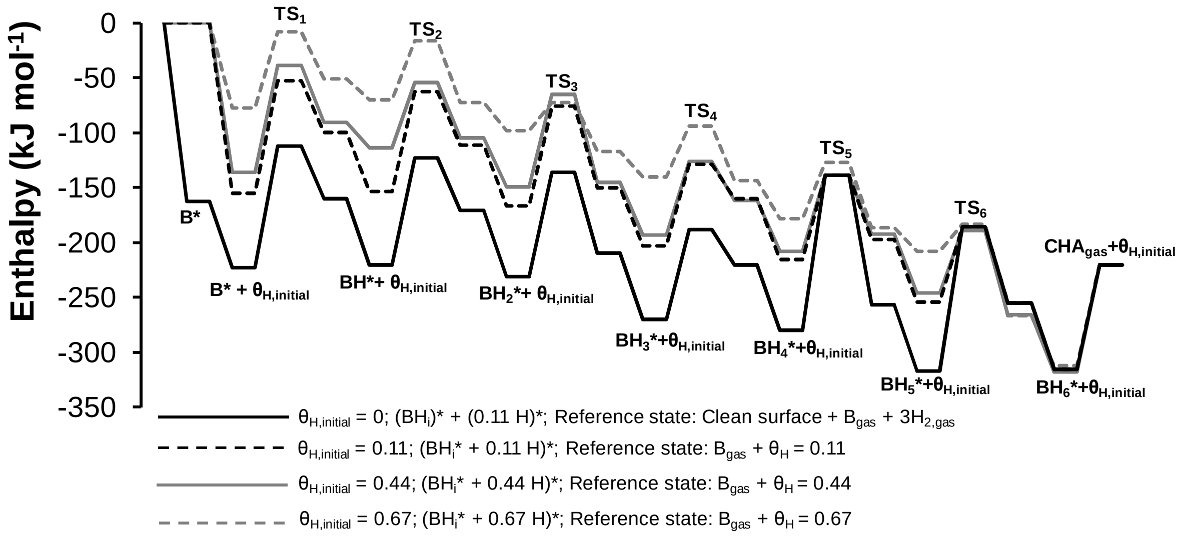

Figure 3-9: Enthalpy diagram of the hollow dominant path of benzene hydrogenation, calculated at 450 K with the optPBE-vdW functional considering four different covered surfaces. The black line represents the case where the reactants (hydrocarbon and hydrogen) are adsorbed in different unit cells (expressed by BH_i^* + $0.11H^*$ in the inset). The other lines correspond to the coadsorption of the hydrocarbon with θ_H = 0.11 (black dotted), 0.44 (grey full) and 0.67 (grey dotted) hydrogen coverage in the same unit cell.

A coverage dependence is calculated from every kinetic and thermodynamic parameter obtained at the different coverages. The dependence is described by regression of the kinetic parameters to a third-order polynomial as a function of the total coverage θ_{total}. The total coverage represents the occupied sites on the surface (θ_{total} =1 – θ_*); i) θ_{total} = 0.11 when considering θ_{BHi} = 0.11 and θ_H = 0.11 adsorbed in different unit cells ($\theta_{H,initial}$ = 0), ii) θ_{total} =

0.22, when considering θ_{BHi} = 0.11 and θ_H = 0.11 adsorbed in the same unit cell ($\theta_{H,initial}$ = 0.11), iii) θ_{total} = 0.55 when θ_{BHi} = 0.11 and $\theta_{H,initial}$ = 0.44, and finally iv) θ_{total} = 0.78 when θ_{BHi} = 0.11 and $\theta_{H,initial}$ = 0.67. All coefficients obtained from the regression are shown in Table B13, B14, and B15 in Appendix B.

3.3.2.c Validation of the microkinetic modeling

The coverage-dependent microkinetic model constructed in the previous section is solved to predict catalyst activities at actual reaction conditions, and the results are compared to previous experimental observations from literature.[15, 17, 90, 91, 98, 99] Contrary to the low-coverage microkinetic model presented in section 3.1, the coverage-dependent microkinetic model constructed from the values in section 3.2.2 is solved explicitly introducing in the simulations the coverage dependent rate coefficients.

The results indicate that the TOF from the hollow coverage-dependent model (defined as *model A*) is orders of magnitude larger than that from the low-coverage model in the previous section. The turnover frequency at 413 K ($W/F_{B,in}$ = 62.5 kg_{cat} s mol^{-1}; $F_{B,in}$ = 2.1 10^{-5} mol s^{-1}; $F_{H2,in}$ = 2.8 10^{-4} mol s^{-1}, $p_{B,in}$ = 6.7 10^{-2} bar; $p_{H2,in}$ = 0.9 bar) is TOF = 3.5 10^{-3} s^{-1}, which is in line with experimental observations at the same conditions, *i.e.*, 6 10^{-3} s^{-1} using Pd power catalyst[15] (see Table 3-1 and shown in Figure 3-10a at 413 K with a grey triangle), and smaller than over supported Pd [13, 15, 90, 91, 98, 99] (see the range of values in Table 3-1 and also shown in Figure 3-10a at 413 K with grey circles). The cyclohexane surface coverage resulting from the simulations is ~0.8 below 550 K (see Figure 3-10b), which leads to low benzene and hydrogen surface coverages. The cyclohexane coverage is much larger than expected, since the desorption of this species is usually considered as fast and irreversible, thus its concentration is often neglected.[15]

A second model (*model B*) is constructed to avoid the high spurious cyclohexane coverage resulting from *model A*. Since adsorbed cyclohexane is experimentally not expected, *model B* considers that the hydrogenation of adsorbed cyclohexyl directly produces gas-phase cyclohexane, instead of adsorbed cyclohexane that would desorb as in *model A.* The reverse reaction, therefore, corresponds to the dissociative adsorption of cyclohexane, yielding adsorbed cyclohexyl and atomic hydrogen. The latter has been previously reported for other molecules on metallic surfaces, such as ethane on Pt,[100] and propane on Ni.[101] *Model B* predicts higher TOF as compared to *model A* and experimental observations (see Figure 3-10a and Table 3-1). Furthermore, surface coverages of benzene and hydrogen (see Figure 3-10b) are in better agreement with experimental results [15, 16] than those in *model A*; in *model B* benzene is the most abundant surface species and a rather low hydrogen and, of course, no adsorbed cyclohexane is predicted. As the temperature increases, the TOF in both models reaches a maximum at about 550 K (see Figure 3-10b), which is the same predicted at low-coverage kinetics, and higher than the experimentally observed temperature at ~ 500 K. [15, 17] The partial reaction orders calculated in *model A* for benzene and hydrogen are both similar to experimental values at 413 K, as listed in Table 3-1. Good agreement is also obtained for benzene in *model B,* however, this model overestimates the partial reaction order of hydrogen (m = 3.3 at 413 K) as compared to experimental observations (~1). This is explained with the smaller hydrogen coverage than benzene coverage in *model B*, as compared to *model A* (see Figure 3-10b). In both models, the production of intermediate species (1,3-cyclohexadiene and cyclohexene) is negligible as compared to cyclohexane, which is the main reaction product in line with previous studies. [33, 36]

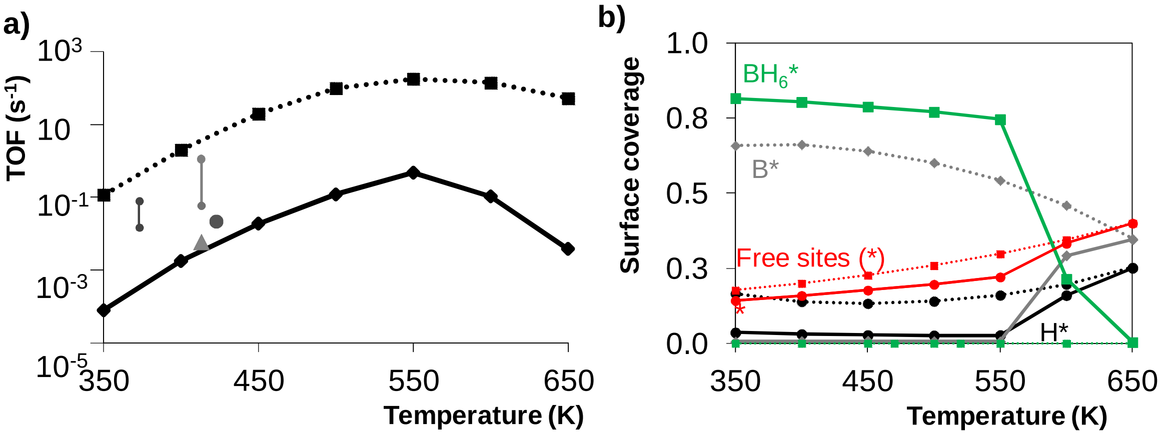

Figure 3-10: (a) Turnover frequency (TOF) (s^{-1}) as a function of the temperature simulated for the coverage-dependent kinetic *model A* (full) and *B* (dotted line). Experimental TOF are shown in grey for supported Pd catalysts (circle markers)[15, 91, 99] and for unsupported Pd power (triangle)[15]. (b) Calculated surface coverage of benzene (grey), hydrogen (black), cyclohexane (green), and free sites (red) ($W/F_{B,in}$ = 62.5 kg_{cat} s mol^{-1}; $F_{B,in}$ = 2.1 10^{-5} mol s^{-1}; $F_{H2,in}$ = 2.8 10^{-4} mol s^{-1}, $p_{B,in}$ = 6.7 10^{-2} bar; $p_{H2,in}$ = 0.9 bar).

Next, the reactions with the largest influence on the global rate have been evaluated using the sensitivity analysis. The results indicate that in both models the second hydrogenation step, from monohydrobenzene (BH) to 1,3-cyclohexadiene (13CHD), has the largest influence on the global rate below 500 K, temperature at which the sensitivity coefficient is $X_{SA,c1}$ ~ 0.7. This reaction is followed by the third hydrogenation reaction ($X_{SA,d1}$ = 0.3), which becomes the one with the largest coefficient above 500 K, *i.e.*, $X_{SA,c1}$ = 0.7 at 550 K. These results indicate that there is not a single reaction with the largest influence on the global rate, that these reactions change with the conditions, and that they are different from those predicted with the low-coverage model or based on rate coefficients instead of rates. Therefore, accounting for reaction rates at actual conditions and use of coverage-dependent kinetics is crucial for determining the reactions with the largest influence on the rate.

Summarizing, this work has shown that accounting for coverage effects on DFT kinetics and thermodynamics and the use of a DFT functional that better describes van der Waals interactions than a generalized gradient approximation (GGA) functional is required to predict catalytic performances that are comparable to experimental observations. This has been performed with the construction of an explicit coverage-dependent microkinetic model based on optPBE-vdW DFT calculations as a function of the surface coverages. This model is solved at the reactor scale as a function of the conditions. Regardless of the coverage, the reactions with the largest sensitivity coefficient differ from those proposed from rate coefficients. Additionally, the reactions with the largest influence on turnover frequencies in the coverage-dependent model are different from those identified in the low-coverage model.

Table 3-1: Turnover frequencies (TOF in s^{-1}), temperature T_{max} at which the maximum in TOF is located (K), and partial reaction orders for benzene and hydrogen, (n and m), obtained from the two coverage-dependent models (*model A* and *model B*), and compared to previous experimental data. The results in *model A* and *B* are obtained using the following conditions: W/F_B^0 = 62.5 kg_{cat} s mol^{-1}; F_B^0 = 7.4 10^{-2} mol h^{-1}; F_{H2}^0 = 1.0 mol h^{-1}, p_B^0 = 6.7 10^{-2} bar; p_{H2}^0 = 0.9 bar)

	Catalyst	TOF s^{-1}	T_{max} K	TOF = $k\, p_B^n\, p_{H2}^m$ (T=413 K) n	m
Model A	Pd(111)	3.5 10^{-3}	550	0.04	0.7
Model B [a]	Pd(111)	3.8	550	–0.06	3.3
Chou and Vannice [15 b]	Pd powder	6 10^{-3}	495	0.2	1
	Supported Pd[c]	6 10^{-2} – 1.1	495	–0.5 - 0.15	~1
Orozco and Webb [17 d]	Pd/SiO_2 ; Pd/Al_2O_3	2 10^{-1} ; 7 10^{-2}	460-480	---	---
Vannice and Neikan [91 e]	Pd/Al_2O_3	2 10^{-2}	---	0	
Figueras et al. [90 f]	Supported Pd [c]	6 10^{-2} – 2.5 10^{-1}	---	0	---
Fuentes et al. [98 d]	Pd/SiO_2 ; Pd/Al_2O_3	2.6 10^{-2} ; 7 10^{-2}	---	---	---
Moss et al. [99 g]	Pd/SiO_2	1.5 10^{-2} – 8 10^{-2}	---	--	---

[a] *Model B* considers the reaction: c-hexyl* + H* ↔ CHA_{gas} + 2* , instead of the two reactions of *model A*: c-hexyl* + H* ↔ CHA* + * and CHA*↔ CHA_{gas} + *

[b] Experimental TOF obtained from measured activities at 413 K, p_{H2}= 0.9 bar, p_B= 6.6 10^{-2} bar, based on chemisorption of CO.

[c] Pd supported on several supports, such as Zeolites, TiO_2, SiO_2-Al_2O_3, Al_2O_3, and SiO_2

[d] Pressure conditions not available

[e] T=423 K, p_{H2}= 1 bar, p_B= 2 10^{-4} bar

[f] T= 350 - 450 K, p_{H2}= 0.9 bar, p_B= 7 10^{-2} bar

[g] T=373 K, p_{H2}= 1 bar, p_B= 2 10^{-2} bar

3.4 Conclusions

Periodic optPBE-vdW density functional theory has been used to evaluate the catalytic hydrogenation of benzene over Pd(111). The aim of this work is to develop a coverage-dependent microkinetic model from density functional theory (DFT) calculations that can be solved at actual reaction conditions, explicitly accounting for the coverage dependence on rate coefficients.

The 26 reactions paths in the two reaction networks that correspond to the two most stable benzene adsorption sites, bridge(30) and hollow(0), are simplified to a single hollow(0) dominant path, which corresponds to the most reactive hollow(0) site, as compared to the bridge(30). The dominant path, which remains dominant regardless of surface coverage, follows the consecutive hydrogenation of carbon atoms located in ortho position relative to the previously hydrogenated carbon atom.

Adsorption equilibrium coefficients decrease due to the decrease in adsorption enthalpy with increasing surface coverage. The rate coefficients for surface hydrogenation increase as a function of coverage due to the lower destabilization of transition states as compared to reactants with increasing surface coverage. For the latter reactions, activation energies and reaction enthalpies show an excellent correlation in the range of coverages studied. This correlation can be used to predict computationally more demanding activation energies at higher coverages using more straightforward reaction energies only. These coverage-dependent rate coefficients are used to construct a microkinetic model, which predicts turnover frequencies in the same order of magnitude as experimental observations. This is in contrast to the results obtained using low-coverage kinetics or using coverage-dependent PW91 kinetics. Furthermore, the reaction on which the overall rate is most sensitive does not only change with the conditions but it is also different from those obtained with the low-coverage model. Therefore, accounting for coverage dependences on the DFT kinetics and thermodynamics and the use of a non-local DFT functional that better describes van der Waals interactions than a generalized gradient approximation (GGA) functional required to predict catalytic performances that can be compared to experimental data.

3.5 References

1. M. Sanati, B. Harrysson, M. Faghihi, B. Gevert and S. Jaras, in *Catalysis*, ed. J. J. Spivey, Royal Society of Chemistry, Cambridge, Editon edn., 2002, pp. 1-42.
2. A. C. Capleton and L. S. Levy, *Chem. Biol. Interact.*, 2005, **153**, 43-53.
3. S. S. E. H. Elnashaie and S. S. El Shishini, *Modelling, simulation and optimization of industrial fixed bed catalytic reactors*, Gordon and Breach, Philadelphia, 1993.
4. J. A. Dumesic, *The Microkinetics of heterogeneous catalysis*, American Chemical Society, Washington, D.C., 1993.
5. H. A. Franco and M. J. Phillips, *J. Catal.*, 1980, **63**, 346-354.
6. M. A. Keane and P. M. Patterson, *Ind. Eng. Chem. Res.*, 1999, **38**, 1295-1305.
7. G. A. Martin and J. A. Dalmon, *J. Catal.*, 1982, **75**, 233-242.
8. C. Mirodatos, J. A. Dalmon and G. A. Martin, *J. Catal.*, 1987, **105**, 405-415.
9. R. Z. C. Vanmeerten and J. W. E. Coenen, *J. Catal.*, 1975, **37**, 37-43.
10. R. Z. C. Vanmeerten and J. W. E. Coenen, *J. Catal.*, 1977, **46**, 13-24.
11. R. Z. C. Van Meerten, T. F. M. Degraaf and J. W. E. Coenen, *J. Catal.*, 1977, **46**, 1-12.
12. R. Z. C. Van Meerten, A. C. M. Verhaak and J. W. E. Coenen, *J. Catal.*, 1976, **44**, 217-225.
13. P. C. Aben, J. C. Platteeu and B. Stoutham, *Recl. Trav. Chim. Pays-Bas*, 1970, **89**, 449.
14. L. P. Lindfors, T. Salmi and S. Smeds, *Chem. Eng. Sci.*, 1993, **48**, 3813-3828.
15. P. Chou and M. A. Vannice, *J. Catal.*, 1987, **107**, 129-139.
16. P. Chou and M. A. Vannice, *J. Catal.*, 1987, **107**, 140-153.
17. J. M. Orozco and G. Webb, *Appl. Catal.*, 1983, **6**, 67-84.
18. A. Palazov, T. Bonev and D. Shopov, *React Kinet Catal L*, 1978, **9**, 383-387.
19. S. D. Lin and M. A. Vannice, *J. Catal.*, 1993, **143**, 539-553.
20. M. Yang, K. C. Chou and G. A. Somorjai, *J. Phys. Chem. B*, 2003, **107**, 5267-5272.
21. K. M. Bratlie, L. D. Flores and G. A. Somorjai, *J. Phys. Chem. B*, 2006, **110**, 10051-10057.
22. K. M. Bratlie, L. D. Flores and G. A. Somorjai, *Abstr Pap Am Chem S*, 2006, **231**.
23. K. M. Bratlie, C. J. Kliewer and G. A. Somorjai, *J. Phys. Chem. B*, 2006, **110**, 17925-17930.
24. K. M. Bratlie, H. Lee, K. Komvopoulos, P. D. Yang and G. A. Somorjai, *Nano Lett*, 2007, **7**, 3097-3101.
25. K. M. Bratlie, Y. M. Li, R. Larsson and G. A. Somorjai, *Catal. Lett.*, 2008, **121**, 173-178.

26. K. M. Bratlie, M. O. Montano, L. D. Flores, M. Paajanen and G. A. Somorjai, *J. Am. Chem. Soc.*, 2006, **128**, 12810-12816.
27. J. P. G. Kehoe and J. B. Butt, *J Appl Chem Biotechn*, 1972, **22**, 23-&.
28. M. Xi and B. E. Bent, *J Vac Sci Technol B*, 1992, **10**, 2440-2446.
29. U. K. Singh and M. A. Vannice, *Aiche J*, 1999, **45**, 1059-1071.
30. J. W. Thybaut, M. Saeys and G. B. Marin, *Chemical Engineering Journal*, 2002, **90**, 117-129.
31. S. L. Lu, W. W. Lonergan, J. P. Bosco, S. R. Wang, et al., *J. Catal.*, 2008, **259**.
32. M. Saeys, M. F. Reyniers, M. Neurock and G. B. Marin, *J. Phys. Chem. B*, 2003, **107**, 3844-3855.
33. P. Tetenyi and Z. Paal, *Z Phys Chem Neue Fol*, 1972, **80**, 63-&.
34. X. C. Su, K. Y. Kung, J. Lahtinen, Y. R. Shen and G. A. Somorjai, *J. Mol. Catal. A: Chem.*, 1999, **141**, 9-19.
35. D. P. Land, C. L. Pettiettehall, R. T. Mciver and J. C. Hemminger, *J. Am. Chem. Soc.*, 1989, **111**, 5970-5972.
36. Y. Derbents, P. Tetenyi and Z. Paal, *Z Phys Chem Neue Fol*, 1972, **80**, 51-&.
37. T. Takahashi, K. Yamashita, T. Kai and I. Fujiyoshi, *Can J Chem Eng*, 1986, **64**, 1008-1013.
38. M. Saeys, M. F. Reyniers, M. Neurock and G. B. Marin, *J. Phys. Chem. B*, 2005, **109**, 2064-2073.
39. F. Mittendorfer and J. Hafner, *J. Phys. Chem. B*, 2002, **106**, 13299-13305.
40. C. Morin, D. Simon and P. Sautet, *Surf. Sci.*, 2006, **600**, 1339.
41. P. Horiuti and M. Polanyi, *T Faraday Soc*, 1934, **30**, 1164-1172.
42. T. Bera, J. W. Thybaut and G. B. Marin, *Ind. Eng. Chem. Res.*, 2011, **50**, 12933-12945.
43. O. Lytken, W. Lew and C. T. Campbell, *Chem Soc Rev*, 2008, **37**, 2172-2179.
44. H. Ihm, H. M. Ajo, J. M. Gottfried, P. Bera and C. T. Campbell, *J. Phys. Chem. B*, 2004, **108**, 14627-14633.
45. P. Aghalayam, Y. K. Park and D. G. Vlachos, *Aiche J*, 2000, **46**, 2017-2029.
46. A. C. Lausche, A. J. Medford, T. S. Khan, Y. Xu, et al., *J. Catal.*, 2013, **307**, 275-282.
47. A. B. Mhadeshwar and D. G. Vlachos, *J. Catal.*, 2005, **234**, 48-63.
48. M. Maestri and K. Reuter, *Angew. Chem.-Int. Edit.*, 2011, **50**, 1194-1197.
49. S. Singh, S. Li, R. Carrasquillo-Flores, A. C. Alba-Rubio, J. A. Dumesic and M. Mavrikakis, *Aiche J*, 2014, **60**, 1303-1319.
50. E. Shustorovich and H. Sellers, *Surf Sci Rep*, 1998, **31**, 5-119.
51. Y. K. Park, P. Aghalayam and D. G. Vlachos, *J. Phys. Chem. A*, 1999, **103**, 8101-8107.
52. C. Chizallet, G. Bonnard, E. Krebs, L. Bisson, C. Thomazeau and P. Raybaud, *J. Phys. Chem. C*, 2011, **115**, 12135-12149.
53. M. K. Sabbe, M. F. Reyniers and K. Reuter, *Catal Sci Technol*, 2012, **2**, 2010-2024.
54. G. Canduela-Rodriguez, M. K. Sabbe, M. F. Reyniers, J. F. Joly and G. B. Marin, *Phys. Chem. Chem. Phys.*, 2014, **16**, 23754.
55. J. A. Dumesic, D. F. Rudd, L. M. Aparicio, J. E. Rekoske and A. A. Treviño, *The Microkinetics of heterogeneous catalysis*, American Chemical Society, Washington, D.C., 1993.
56. G. Kresse, *J. Non-Cryst. Solids*, 1995, **193**, 222-229.
57. G. Kresse and J. Furthmuller, *Comput. Mater. Sci.*, 1996, **6**, 15-50.
58. G. Kresse and J. Furthmuller, *Phys. Rev. B: Condens. Matter Mater. Phys.*, 1996, **54**, 11169-11186.
59. G. Kresse and J. Hafner, *Phys. Rev. B: Condens. Matter Mater. Phys.*, 1994, **49**, 14251-14269.
60. P. E. Blochl, *Phys. Rev. B: Condens. Matter Mater. Phys.*, 1994, **50**, 17953-17979.

61. G. Kresse and D. Joubert, *Phys. Rev. B: Condens. Matter Mater. Phys.*, 1999, **59**, 1758-1775.
62. M. Methfessel and A. T. Paxton, *Phys. Rev. B: Condens. Matter Mater. Phys.*, 1989, **40**, 3616-3621.
63. H. J. Monkhorst and J. D. Pack, *Phys. Rev. B: Condens. Matter Mater. Phys.*, 1976, **13**, 5188-5192.
64. J. P. Perdew, K. Burke and M. Ernzerhof, *Phys. Rev. Lett.*, 1996, **77**, 3865-3868.
65. J. P. Perdew, J. A. Chevary, S. H. Vosko, K. A. Jackson, et al., *Phys. Rev. B: Condens. Matter Mater. Phys.*, 1992, **46**, 6671-6687.
66. J. Klimeš, D. R. Bowler and A. Michaelides, *J. Phys.: Condens. Matter*, 2010, **22**, 022201.
67. M. Mura, A. Gulans, T. Thonhauser and L. Kantorovich, *Phys. Chem. Chem. Phys.*, 2010, **12**, 4759-4767.
68. H. Rydberg, B. I. Lundqvist, D. C. Langreth and M. Dion, *Phys. Rev. B: Condens. Matter Mater. Phys.*, 2000, **62**, 6997-7006.
69. M. Dion, H. Rydberg, E. Schroder, D. C. Langreth and B. I. Lundqvist, *Phys. Rev. Lett.*, 2004, **92**, 246401.
70. J. Klimeš, D. R. Bowler and A. Michaelides, *Phys. Rev. B: Condens. Matter Mater. Phys.*, 2011, **83**, 195131.
71. H. Yildirim, T. Greber and A. Kara, *J. Phys. Chem. C*, 2013, **117**, 20572-20583.
72. G. Mills, H. Jonsson and G. K. Schenter, *Surf. Sci.*, 1995, **324**, 305-337.
73. G. Henkelman and H. Jonsson, *J. Chem. Phys.*, 1999, **111**, 7010-7022.
74. C. J. Cramer, *Essentials of computational chemistry: theories and models*, 2nd edn., Wiley, Chichester, West Sussex, England ; Hoboken, NJ, 2004.
75. D. A. McQuarrie, *Statistical mechanics*, University Science Books, Sausalito, Calif., 2000.
76. F. Jensen, *Introduction to computational chemistry*, 2nd edn., John Wiley & Sons, Chichester, England ; Hoboken, NJ, 2007.
77. *National Institute of Standards and Technology Chemistry webbook, Standard Reference Database 69, June 2005 Release*, http://webbook.nist.gov.
78. J. A. Montgomery, M. J. Frisch, J. W. Ochterski and G. A. Petersson, *J. Chem. Phys.*, 1999, **110**, 2822-2827.
79. M. K. Sabbe, M. Saeys, M. F. Reyniers, G. B. Marin, V. Van Speybroeck and M. Waroquier, *J. Phys. Chem. A*, 2005, **109**, 7466-7480.
80. G. B. Marin and G. S. Yablonsky, *Kinetics of chemical reactions : decoding complexity*, Wiley-VCH, Weinheim, 2011.
81. J. A. Konvalinka and J. J. F. Scholten, *J. Catal.*, 1977, **48**, 374-385.
82. J. F. Paul and P. Sautet, *Phys. Rev. B: Condens. Matter Mater. Phys.*, 1996, **53**, 8015-8027.
83. H. Conrad, G. Ertl and E. E. Latta, *Surf. Sci.*, 1974, **41**, 435-446.
84. C. Morin, D. Simon and P. Sautet, *J. Phys. Chem. B*, 2004, **108**, 5653-5665.
85. M. Saeys, M. F. Reyniers, G. B. Marin and M. Neurock, *J. Phys. Chem. B*, 2002, **106**, 7489-7498.
86. F. Mittendorfer, C. Thomazeau, P. Raybaud and H. Toulhoat, *J. Phys. Chem. B*, 2003, **107**, 12287-12295.
87. M. K. Sabbe, L. Lain, M. F. Reyniers and G. B. Marin, *Phys. Chem. Chem. Phys.*, 2013, **15**, 12197-12214.
88. W. T. Tysoe, R. M. Ormerod, R. M. Lambert, G. Zgrablich and A. Ramirez-Cuesta, *J. Phys. Chem.*, 1993, **97**, 3365-3370.

89. A. F. Lee, K. Wilson, R. M. Lambert, A. Goldoni, A. Baraldi and G. Paolucci, *J. Phys. Chem. B*, 2000, **104**, 11729-11733.
90. F. Figueras, R. Gomez and M. Primet, *Adv Chem Ser*, 1973, 480-489.
91. M. A. Vannice and W. C. Neikam, *J. Catal.*, 1971, **23**, 401-405.
92. C. Xu, Y. L. Tsai and B. E. Koel, *J. Phys. Chem.*, 1994, **98**, 585-593.
93. P. Zebisch, W. Huber and H. P. Steinruck, *Surf. Sci.*, 1991, **244**, 185-196.
94. O. Lytken, W. Lew, J. J. W. Harris, E. K. Vestergaard, J. M. Gottfried and C. T. Campbell, *J. Am. Chem. Soc.*, 2008, **130**, 10247-10257.
95. W. Dong, V. Ledentu, P. Sautet, A. Eichler and J. Hafner, *Surf. Sci.*, 1998, **411**, 123–136.
96. O. M. Lovvik and R. A. Olsen, *Phys. Rev. B: Condens. Matter Mater. Phys.*, 1998, **58**, 10890-10898.
97. P. C. Aben, J. C. Platteeu and B. Stoutham, *Recl. Trav. Chim. Pays-Bas*, 1970, **89**, 449-459.
98. S. Fuentes and F. Figueras, *J Chem Soc Farad T 1*, 1978, **74**, 174-181.
99. R. L. Moss, D. Pope, B. J. Davis and D. H. Edwards, *J. Catal.*, 1979, **58**, 206-219.
100. V. Galvita, G. Siddiqi, P. P. Sun and A. T. Bell, *J. Catal.*, 2010, **271**, 209-219.
101. A. V. Hamza and R. J. Madix, *Surf. Sci.*, 1987, **179**, 25-46.

Chapter 4

Periodic DFT study of benzene adsorption on Pd(100) and Pd(110) as a function of coverage

The following pages include the paper:

G. Canduela-Rodriguez, M. K. Sabbe, M.–F. Reyniers, J.–F. Joly and G. B. Marin, Periodic DFT study of benzene adsorption on Pd(100) and Pd(110) as a function of coverage

The Journal of Physical Chemistry C **118** (37) (2014) 21483 – 21499

Abstract

Benzene adsorption on Pd(100) and Pd(110) has been investigated using Periodic Density Functional Theory (DFT) calculations. Four-fold hollow geometries are preferentially adopted on both surfaces, and due to stronger repulsive interactions on Pd(100) a larger decrease in adsorption energy is calculated from medium to saturation coverage (~120 kJ mol^{-1}) compared to Pd(110) (~15 kJ mol^{-1}). On Pd(100), a slight energetic preference is calculated at saturation coverage for an adsorbate with two C–C bonds parallel to the $[01\bar{1}]$ direction. However, an adsorption geometry with alternately two types of benzene adsorbates, rotated azimuthally by 30° relative to one another, cannot be discarded since both geometries are compatible with UPS and HREELS observations. On Pd(110), there is a slight energetic preference for the hollow(0) site relative to the hollow(15) and hollow(30) at saturation coverage, and their calculated electronic features match UPS experiments. For the hollow(30), calculated vibrational features are not compatible with HREELS experiments, indicating that benzene does not populate hollow(30) sites at saturation coverage. Calculated STM images confirm that the experimentally observed two-lobed protrusion separated by a single depression oriented with its direction some 50° from $[1\bar{1}0]$ can only correspond to the hollow(15) adsorbate. Inclusion of van der Waals interactions (vdW-DFT) increases adsorption energies by some 50 kJ mol^{-1}, but the relative ordering of the various adsorption sites remains unaltered as compared to PW91.

4.1 Introduction

The adsorption of benzene on noble metal surfaces is a key step in various industrially important processes, such as hydrotreatment of petroleum feedstock, production of caprolactam and adipic acid, and for environmental protective technologies.[1] Pd nano-sized particles are widely employed as catalysts in industrial heterogeneous reactions, due to their improved catalytic properties compared to their bulk counterparts,[2] e.g. larger surface-to-volume ratio.[3] These catalysts can have different particle shapes, e.g. icosahedral, tetrahedral, octahedral, cuboctahedral, and decahedral,[4] which usually exhibit the (111), (100) and (110) surfaces, together with edges and steps. The particle shape can be controlled by careful selection of the preparation techniques[3] and, usually, the (111) surface is the most abundant surface. [5] However, this does not imply that the other surfaces do not influence the adsorption mechanism and reaction kinetics; different catalytic performances have been observed with different shaped and sized catalysts, suggesting an influence of the other surfaces, step and/or kink sites.[6, 7] Structure sensitivity has been previously reported for the hydrogenation of benzene [8, 9] and other unsaturated hydrocarbons. [10, 11]

Insights in the interaction of benzene with the different Pd surfaces can help to understand and improve the behavior of Pd nano-sized catalysts. Benzene adsorption on various Pd surfaces has been studied extensively using a variety of surface analytical techniques, including low-energy electron diffraction (LEED),[12-18] near-edge X-ray absorption fine structure spectroscopy (NEXAFS),[19, 20] thermal desorption spectroscopy (TPD),[15, 18, 21-23] electron energy loss spectroscopy (EELS)[12, 15, 18, 21, 24-27], scanning tunneling microscopy (STM)[17, 23, 28, 29] and ultraviolet photoemission spectroscopy (UPS). [18, 19, 28, 30-32] In addition, benzene adsorption on various transition metals has been studied using theoretical techniques such as periodic density functional theory (DFT). [23, 33-37]

The adsorption of benzene on Pd(100) has not been extensively studied. UPS studies[30, 31, 38] have proposed a flat geometry based on the downward shift of the benzene π-orbitals, which indicates that bonding with the surface mainly occurs via the π-states.[30] Lloyd et al.[38] pointed out that the photoemission spectra of Ni(111), Pd(111) and Pd(100) are very similar and suggested the same adsorbate orientation for the different surfaces in view of the similar variation of the intensities with the emission angle. In addition, they suggested a reduced metal/adsorbate interaction through the π-electrons for Pd compared to Ni. Furthermore, Nyberg et al.[30] proposed an adsorbate with C_{2v} symmetry or possibly lower, and Hoffmann et al.[31] observed an ordered overlayer of benzene with (2×2) structure that desorbed at 500 K leaving behind a carbon residue.

Although benzene adsorption on Pd(110) has been studied extensively, the detailed atomic structure of the adsorbed benzene and the corresponding site symmetry are still under debate. LEED[15, 27] and STM measurements[17, 28, 32] have established that on Pd(110) benzene prefers the four-fold hollow sites and forms a c(4×2) overlayer at saturation coverage. Analysis of angle resolved UPS (ARUPS) experiments lead Netzer et al.[14] to conclude that at saturation coverage the adsorbed complex should have a lower than C_{2v} symmetry. These authors proposed that the benzene molecules are azimuthally oriented with two of the C-C bonds parallel to the $[1\bar{1}0]$ direction ($\phi = 0°$) and tilted towards the [001] direction with a tilt angle θ of 10-20º. It was hypothesized that the driving force for the tilted configuration of benzene is the decrease of lateral repulsions between neighboring benzene molecules in the densely packed c(4×2) overlayer on Pd(110). Fujisawa et al.[15] also proposed a tilt of the molecular plane based on the coverage dependence of the intensity ratio of the two out-of-plane losses observed at 705 and 745 cm^{-1} in HREELS measurements. However, STM studies and quantum chemical calculations reported by Yoshinobu et al.[17, 28, 32] and Treboux and Aono[29] indicate that the low site symmetry might rather be due to an asymmetric azimuthal rotation of benzene relative to the substrate lattice, while the molecular plane remains parallel to the surface. As pointed out by Yoshinobu et al.,[28] the observed nodal depression with its direction 50°-60° from $[1\bar{1}0]$ in the STM images suggests an azimutal rotation of 10° - 20° from the [001] direction and a C_2 site symmetry. For the Ni(100) case, Huber et al.[39] also reported a preference for flat adsorption of benzene based on analyses of ARUPS measurements. At half the saturation coverage on Ni(100), these authors observed C_{2v} symmetry and concluded that benzene prefers the four-fold hollow site with its molecular plane parallel to the surface and two of the C-C bonds parallel to the [001] direction ($\phi = 30°$, $\theta = 0°$). At saturation coverage, they observed that the molecule remained flat but a new conformation with C1 symmetry was adopted due to strong lateral interactions that lead to an azimuthal rotation of the molecule away from the high symmetry adsorption site. More recently, Favot et al.[34] performed periodic DFT calculations in the local density approximation (LDA) using ultrasoft Vanderbilt pseudopotentials for the Pd(110)-c(4×2)-benzene system and predicted a C2 low-symmetry configuration with an azimuthal angle ϕ of ~ 11°. A distortion of the carbon ring from the planar geometry was observed and the C−H bonds were tilted some 20-25° out of the molecular plane away from the metal surface. STM images calculated for the C_2 configuration were found to be compatible with the experimental data.

To minimize the computational cost, theoretical studies on benzene adsorption usually pertain to a single coverage. However, the benzene surface coverage can have a large effect on the adsorption energy and on the reaction rates, even more than the variation from one metal to the next [40]. Therefore, the interaction between benzene and the surface needs to be assessed also at high coverage. In this work, periodic DFT calculations are used to study the adsorption of benzene on the (100) and (110) surfaces of Pd at medium coverage for various adsorption sites, and at saturation coverage for the most stable ones. Calculated adsorption energies and geometries, vibrational frequencies, electronic properties and STM images are used to compare different adsorption sites and to evaluate the coverage effects on the adsorption.

4.2 Methodology

Periodic (DFT) calculations have been performed with the Vienna Ab initio Simulation Package (VASP)[41-44] to obtain adsorption geometries, energies and vibrational frequencies. The interaction between electrons and nuclei is modeled using the projector augmented wave method (PAW),[45, 46] and the wave function is expanded in terms of plane-wave basis sets with a cutoff of 400 eV. The exchange and correlation effects are described with the nonlocal generalized gradient Perdew-Wang PW91 functional.[47, 48] The partial occupancies close to the Fermi level are evaluated with the first-order Methfessel Paxton method, for which a smearing width of 0.3 eV is applied. A 5×5×1 Monkhorst-Pack[49] grid is used for Brillouin-zone integration, and non spin-polarized calculations are performed. The electronic energy convergence criterion of 10^{-8} eV is considered, and the geometry optimization is performed until the maximum forces on the atoms are at least lower than 0.015 eV/Å using a quasi-Newton RMM-DIIS algorithm. These strict criteria are required to avoid spurious imaginary frequencies in the vibrational analysis.

The generalized gradient approximation (GGA) functionals commonly used in DFT, such as PW91 and PBE, do not properly describe the nonlocal nature of the electron correlation, *i.e.* Van der Waals interactions (vdW).[50] This shortcoming can hamper the calculation of binding energies, energy barriers for diffusion, activation barriers for reaction, as well as interaction energies between molecules and surfaces,[51] particularly in cases where van der Waals interactions have a significant contribution to the total energy.[52] In the case of aromatic adsorption, noble metals such as Ag, Au and Cu have been the subject of numerous studies[51, 53-58] since no covalent bonds are formed between the surface and the aromatic molecule, and hence physisorption controls the adsorption mechanism. These interactions may be less pronounced on metals such as Pd or Pt, however, accounting for dispersion interactions is necessary to assure accurate results closer to experimental values. Recent developments in numerical algorithms [59] have made affordable the implementation of the nonlocal van der Waals density functional (vdW-DF) developed by Rydberg and Dion,[60, 61] in VASP by Klimeš et al.[50, 62]. This is a completely DFT first-principles approach without any fitting parameters. This approach replaces the contribution of the correlation energy contained in the GGA functional by the one from the local density approximation (LDA) to avoid possible double-counting, and adds the non-local correlation. The optPBE-vdW functional[50] is used in the vdW-DF approach because it provides results that are in good agreement with experimental adsorption energies of benzene on transition metal surfaces. [63, 64]

To represent medium and saturation coverages, the $(2\sqrt{2}\times2\sqrt{2})R45^{o}$ and (2×2) unit cells are used for Pd(100) (see Figure C1 in Appendix C), while the (4×2) and (2×2) unit cells are considered for Pd(110) (see Figure C2). Four and five layers of Pd atoms are used respectively to model the (100) and (110) slabs. During geometry optimization, for both surfaces, the bulk structure is imposed on the two bottom layers of the slabs while benzene and the top layers are relaxed. The geometry of the fcc bulk unit cell is optimized as a function of the volume with the same computational settings as the super cell but with a finer 15×15×15 Monckhorst-Pack grid and an energy cutoff of 520 eV. In the unit cell of both surfaces, a vacuum layer of 11 Å is used in the direction perpendicular to the slab, and an artificial dipole layer is included to correct for possible dipole interactions between periodic slabs. Convergence tests indicate that this approach yields adsorption energies within 1 kJ mol^{-1} of those calculated with a vacuum layer of 70 Å in the absence of dipole corrections.

To compare the stability between the different possible adsorbates, the adsorption energy (ΔE_{ads}) is calculated as the difference in electronic energy between the adsorbate-surface complex, the gas phase molecules and the clean slab, as shown in eq. (1).

$$\Delta E_{\mathrm{ads,benzene}} = E_{\mathrm{adsorbate}} - E_{\mathrm{gas}} - E_{\mathrm{slab}} \tag{1}$$

With $E_{adsorbate}$, E_{gas}, and E_{slab} as the electronic energies of the adsorbate-surface complex with a particular coverage, the gas phase benzene molecule, and the clean unit cell respectively. To understand trends in adsorption energies it can be helpful to decompose the adsorption energy in three parts:

$$\Delta E_{ads} = E^{\mathrm{dist}}_{\mathrm{molecule}} + E^{\mathrm{dist}}_{\mathrm{surface}} + E_{\mathrm{interact}} \tag{2}$$

$E^{\mathrm{dist}}_{\mathrm{molecule}}$ represents the distortion energy of the molecule, and is calculated as the difference between the energy of the molecule in the gas-phase and the energy of the isolated gas phase benzene in the distorted adsorption geometry. $E^{\mathrm{dist}}_{\mathrm{surface}}$ is the distortion energy of the surface, calculated as the difference between the energy of the clean unit cell and the energy of the clean unit cell in the distorted geometry of the adsorbed complex. E_{interact} is the interaction energy between the molecule and the surface, calculated as the difference between the adsorption energy and the sum of the distortion energies of the molecule and the surface.

The harmonic frequencies are obtained from a partial Hessian vibration analysis (PHVA) of the optimized geometry by using a step size of 0.015 Å. The frequencies are calculated for the adsorbate and the Pd atoms in the layers that are relaxed during the geometry optimization. For comparison with experimental HREELS spectra, the infrared intensities and vibrational frequencies are calculated with ASE[65] using the methodology described by Porezag and Pederson[66]. The intensities of the simulated spectra are computed by using the finite difference approximation of the dipole moment gradient perpendicular to the surface, and the finite difference approximation of the dynamical matrix is used for the frequencies. For comparison with experimental spectra, a line broadening of 60 cm^{-1} and 36 cm^{-1} for the (100) is applied for the (100) and (110) respectively according with the spectra reported by Waddill and Kesmodel[21] and Fujisawa et al.[15].

The projected density of states (PDOS) of the adsorbates on the benzene gas phase molecular orbitals has been obtained using the grid-based projector-augmented wave method (GPAW) program[67, 68] within the ASE environment.[65] The uniform real-space grid representation of the electronic wavefunctions within GPAW[67] facilitates expressing the wavefunctions in terms of a localized atomic-orbital basis set.[68] The single-point GPAW calculations are performed on the geometries relaxed in VASP using the same setting, but without dipole correction field, and the gas phase orbitals are obtained on the molecule constrained to its geometry in the adsorbed state (in the same unit cell).[69]

The simulated scanning tunneling microscopy (STM) images are obtained from the partial (band decomposed) charge density generated by VASP, using the Tersoff-Hamann method[70] implemented in the p4vasp visualization program.

4.3 Benzene adsorption on Pd(100) at medium and saturation coverage

In this section, benzene adsorption on Pd(100) is evaluated at medium coverage and the most stable sites are further investigated at saturation coverage. Adsorption energies and geometries, vibrational frequencies, electronic properties and STM images are used to compare different adsorption sites and to evaluate the coverage effects on the adsorption.

4.3.1 Adsorption energies

Six high-symmetry sites are evaluated for benzene on Pd(100) at medium coverage (see Figure 4-1) using a (2√2×2√2)R45° overlayer (see left panels in Figure 4-2). The surface area of the unit cell used amounts to 6.2 10^{-19} m^2, therefore, the calculations correspond to a coverage of 1.6 10^{18} molecules per m^{-2}, *i.e.* half of the experimentally observed (2×2) saturation overlayer structure at 300 K.[31] The calculated adsorption energies are given in Table 4-1, and indicate that on Pd(100) the four-fold hollowB site is the most stable site with an adsorption energy of −159 kJ mol^{-1}, closely followed by the hollowA site with a 3 kJ mol^{-1} lower adsorption energy. At the hollowB site, two C-C bonds of benzene are parallel to the [001] direction, and benzene is azimuthally rotated away by 15° from the high symmetry hollowA site. The three bridge sites (A, B and C) and the top site are discarded as possible adsorption sites since they are more than 70 kJ mol^{-1} less stable than the hollow sites. Larger adsorption energies have been calculated for hollowB benzene on Pd(100) with periodic DFT calculations by Li et al.[37] (−208 kJ mol^{-1}) and Orita et al.[71] (−196 kJ mol^{-1}) but for much lower coverage (1/4 and 1/3 of the experimental saturation coverage, resp.). The same relative ordering in stability of the three types of sites was found in a DFT study of the Ni(100) case by Mittendorfer and Hafner.[72] At half saturation coverage on Ni(100), the four-fold hollow sites are strongly preferred over the bridge and top sites. However, in contrast to our calculations on Pd(100), there is a slight preference for the hollowA site (ΔE_{ads} = −206 kJ mol^{-1}) over the hollowB site (ΔE_{ads} = −203 kJ mol^{-1}) on Ni(100). Our calculations also confirm the weaker adsorption on Pd compared to Ni as suggested by the UPS analysis of Lloyd et al. [46]. Inclusion of van der Waals long-range interactions does not change the ordering in adsorption strength, see values between brackets in Table 4-1, and an increase of ~ 50 kJ mol^{-1} in adsorption energies is obtained compared to the PW91 values.

Geometrical characteristics of benzene adsorbed at the hollowA and hollowB sites at medium coverage are summarized in Table 4-2, and illustrated respectively in Figure C3 and C4 of the Appendix C. Only the PW91 values are shown and discussed since the inclusion of van der Waals forces (opt-PBE)[50, 62] has only a very limited influence on the geometry of the adsorption complexes; changes remain below 0.02 Å as compared to the values obtained with the PW91 functional, in line with the observations made by Toyoda et al. [55] in their theoretical study of benzene adsorption on noble metals.

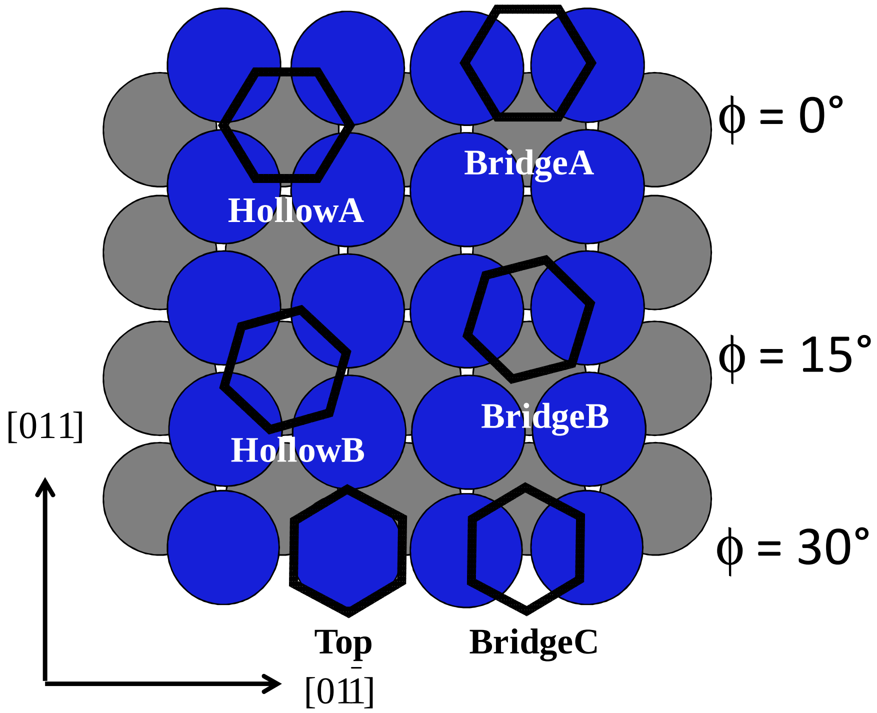

Figure 4-1. The six adsorption geometries evaluated for benzene on Pd(100). Pd atoms in the top layer are colored blue for ease of interpretation.

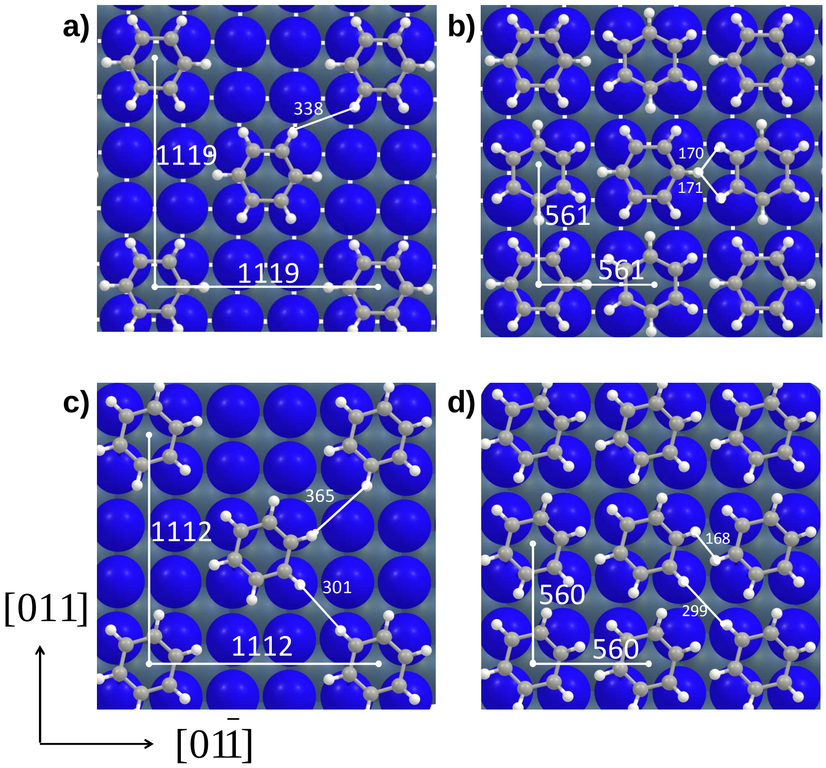

Figure 4-2. Surface overlayer of benzene adsorption at medium coverage on (a) hollowA and (c) hollowB sites, and at saturation coverage on (b) hollowA and (d) hollowB sites. Distances between the centers of neighboring benzene molecules in the $[011]$and $[01\bar{1}]$ directions, and the closest H-H distances are shown in picometer.

Table 4-1. Adsorption energies of benzene at the six adsorption sites evaluated on Pd(100) at medium coverage (1.8 10^{18} molecules per m^{-2}) with the azimuthal angle (ϕ) shown in °. The adsorption energies calculated using the opt-PBE vdW-DF functional are shown between brackets.

Adsorption site (ϕ)	**ΔE_{ads} (kJ mol^{-1})**
HollowB (15°)	–159.1 (–204.3)
HollowA (0°)	–156.4 (–201.7)
BridgeA (0°)	–90.9 (–139.0)
BridgeB (15°)	–86.8 (–135.8)
BridgeC (30°)	–83.3 (–137.1)
Top (30°)	–14.7 (–71.1)

At both hollow sites, the carbon ring expands as the C-C distances increase from 140 pm in gas phase benzene up to 145 pm but remains planar with two of the C-C bonds parallel to the high symmetry direction of the crystal, i.e. the [001] direction for hollowB and the $[01\bar{1}]$ direction for hollowA, at a distance of 215-230 pm from the first Pd layer (see Table 4-2). Like in the case of the Ni(100) surface,72 maximization of the overlap between the Pd d-states and the benzene Cpz orbitals causes a tilting of the hydrogen bonds. At the hollowB site, the tilt angle is less pronounced for the hydrogen atoms connected to the four carbon atoms that are involved in a π-type interaction with the surface and have Pd-C distances of ~230 pm (tilt angle of 18°). For the other two hydrogen atoms connected to the two carbon atoms that are involved in a σ-type interaction with the surface ($d\sigma_{Pd\text{-}C}$ = 215 pm), the tilt angle amounts to 23°. At the hollowA site, the C–H tilt angle for the hydrogen atoms connected to the two C–atoms that bridge the Pd-rows is less pronounced (14°) than for those connected to the four σ-bonded C-atoms (24°).

Benzene adsorption at the two most stables hollowA and hollowB sites has also been investigated at the experimentally reported saturation coverage at 300 K,[31] see Figure 4-2. This is performed for a (2×2) overlayer, and the calculations thus correspond to a coverage of $3.2\ 10^{18}$ benzene molecules per m^{-2}. At saturation coverage, only the hollowB site was found to remain stable for the (2×2) overlayer, yielding an adsorption energy of –39 kJ mol^{-1}, see Table 4-2. The hollowA adsorbate, however, was found to rotate in the optimization to adopt the hollowB geometry due to repulsive interactions between neighboring molecules. The decrease in adsorption strength of 120 kJ mol^{-1} of the hollowB site as compared to the medium coverage case (see Table 4-2) is mainly due to the more pronounced distortion of benzene, see the geometries in Figure C3 and C4 in Appendix C, and to the occurrence of strong adsorbate-adsorbate repulsive interactions between neighboring benzene molecules. The distortion of benzene modifies mainly the C–C bond lengths and the C–C–C angles.

Although the C–H bond lengths remain unaltered, the hydrogen atoms are also lifted somewhat further out of the plane of the carbon ring (22° and 24° compared to 18º and 23º at medium coverage). The closest distance between the hydrogen atoms of neighboring benzene molecules amounts to 168 pm (see right bottom panel in Figure 4-2) and, hence, important repulsive interactions can be expected. An adsorbate-adsorbate repulsion energy of about 80 kJ mol^{-1} is estimated by calculating the difference in energy between distorted gas phase benzene in the hollowB geometry in the (2×2) unit cell and in a very large unit cell (15×15×15 Å^3), in which the lateral interactions are excluded. The inclusion of van der Waals interactions increases the stability of the hollowB site by 47 kJ mol^{-1} (see in Table 4-2 the values between brackets). The calculated adsorption energy of –86 kJ mol^{-1} is some 30-35 kJ mol^{-1} less than the value reported by Hofmann et al. [31] These authors reported a desorption peak at 500 K for the (2×2) surface overlayer on Pd(100) and estimated an adsorption energy of −120 kJ mol^{-1} assuming first-order desorption kinetics and non-dissociative adsorption. This peak could also correspond to the decomposition of the molecule since a carbon residue was observed after desorption. However, Gentle and Muetterties[73] reported that benzene is stable at 500 K with maximal thermal desorption and dehydrogenation near 550 K.[24]

Although the hollowB geometry agrees with the observed (2×2) overlayer[31] and the reported C_{2v} or lower symmetry at saturation coverage,[30, 31] alternative geometries that are also consistent with the experimental data can be considered. Therefore, we have evaluated two alternative structures in which adsorbate-adsorbate interactions are somewhat alleviated. The first alternative has been suggested by Nyberg et al.[30]; it contains two benzene molecules per (2√2×2√2)R45º unit cell with both benzene molecules oriented parallel to high symmetry directions, i.e. hollowA’, but azimuthally rotated relative to one another ($\phi 1 = 0°$; $\phi 2 = 30°$; see the top right panel of Figure 4-2). This is found to be 5 kJ mol-1 less stable than the

Table 4-2. Adsorption energies and geometrical characteristics for the adsorption of benzene on Pd(100) for the (2√2×2√2)R45º (medium coverage) and (2×2) overlayers (saturation coverage). The opt-PBE vdW-DF adsorption energies with are shown between brackets.

		Medium coverage		**Saturation coverage**		
		hollowA	**hollowB**	**hollowA’**	**hollowB**	**hollowB’ (θ = 17°)**
ϕ_1, ϕ_2 (°)		0, -	15, -	0, 30	15, -	15, -
ΔE_{ads}	kJ mol^{-1}	–156.4 (–201.8)	–159.1 (–204.3)	–34.1 (–83.7)	–38.6 (–86.0)	–20.2 (–75.6)
E^{int}	kJ mol^{-1}	–250.3	–249.6	–216.3	–220.3	–101.3
E^{dis} (slab)	kJ mol^{-1}	14.3	15.3	14.7	8.4	5.9
E^{dis} (benzene)	kJ mol^{-1}	79.6	75.2	167.5	173.3	75.2
$d_{C\text{-}C}$	pm	143/145	140/145	141/145	140/144	138-143
$d\pi_{C\text{-}Pd}$	pm		227/231		226/228	223-225
$d\sigma_{C\text{-}Pd}$	pm	217/220	215	215/219	214	227-228
$d_{C\text{-}H}$	pm	109	108/109	107/109	109	108-109
$d_{Benzene\text{-}1stPdlayer}$	pm	213	212	207	206	205
$d_{1st\text{–}2nd\text{-}Pdlayers}$	pm	199	201	226	203	202
CCC	º	119/121	119/121	118/124	116/122	117-122
CCH	º	14/24	18/23	22-25	22-24	11-21

hollowB site at saturation coverage (see Table 4-2). Another possibility to alleviate adsorbate-adsorbate interactions is that benzene at the hollowB site would adopt a tilted conformation. A tilted conformation with the molecular plane inclined at 30° from the metal surface has been observed for Pd(111).[19] A conformation with the benzene molecular plane tilted by 17° was identified as a minimum on the potential energy surface (i.e. hollowB' in Table 4-2), however, this tilted conformation is 18 kJ mol-1 less stable than benzene in a flat geometry at the hollowB site.

4.3.2 Vibrational properties

The effect of coverage on the calculated vibrational spectra has been evaluated for benzene adsorbed at the four-fold hollowA and hollowB sites on Pd(100). Details on the vibrational frequencies of the two hollow sites at medium and saturation coverage can be found in Table C2 of the Appendix C.

Four types of vibrational modes are observed at medium and saturation coverage, as illustrated in Figure 4-3, namely the γ_{CH} out-of-plane bending, ν_{CC} stretching motions (ring deformation), δ_{CH} in-plane bending, and ν_{CH} stretching motions. Clearly, the vibrational frequencies for the hollowA/A' and hollowB sites are very similar (see Figure 4-3). At saturation coverage, two peaks are calculated for the ν_{CH} stretching mode, *i.e.* 3002 and 3220 cm^{-1} for hollowB and 3079 and 3371 cm^{-1} for hollowA', while at medium coverage only one is found (3096 cm^{-1}). Visualization of the vibrational modes at saturation coverage shows the breakup of this ν_{CH} stretching mode in two separate peaks, each in a different range of frequencies, corresponding with two different types of C-H bonds. For the hollowB site, the stretching mode of the two C-H bonds with the carbons involved in the σ-type bond with Pd is found at 3002 cm^{-1} while the loss at 3220 cm^{-1} corresponds to the deformation of the other four C-H bonds with the carbons involved in the π-type bond with the surface. Both ν_{CH}

stretching modes are more or less equal in intensity. For the hollowA’ site the ν_{CH} stretching mode that corresponds with the deformation of the four C-H bonds, involving the carbons that are σ-bound to the Pd atoms, is found at 3079 cm^{-1}. This mode is more intense than the 3371 cm^{-1} ν_{CH} stretching peak of the C-H bonds involving the carbon atoms that bridge the Pd rows. Experimentally, a single loss at 3010 cm^{-1} is observed at 300 K for this ν_{CH} stretching mode in the HREELS spectrum [21]. For the hollowB site but not for the hollowA’ site, a similar breakup at saturation coverage was also observed for a ring deformation mode with two computed peaks at 1320 and 1520 cm^{-1} that stem from a single mode at 1454 cm^{-1} at medium coverage, as shown in the inset of the right panel in Figure 4-3. Here too, the calculated frequency of 1442 cm^{-1} for the hollowA’ site is in better agreement with the experimentally observed loss at 1425 cm^{-1}. However, the experimental spectrum in off-specular mode reported by the same authors shows an additional peak at 1320 cm^{-1}, which may be related to the one we have computed at 1320 cm^{-1} for the hollowB site at saturation coverage. This mode has a small contribution in the direction perpendicular to the surface, which can explain why this peak is obtained in the IR spectrum applying the dipole selection rule.

For the δ_{CH} in-plane bending mode the calculated values of 1176 cm^{-1} for hollowA’ and of 1157 cm^{-1} hollowB at saturation coverage are in good agreement with the experimentally observed loss at 1115 cm^{-1} at the same coverage. The same frequency of 927 cm^{-1} is computed for the out-of-plane C-H bending mode for both sites in fair agreement with the experimental loss at 817 cm^{-1}. Also for the high-intensity out-of-plane C-H bending mode experimentally observed at 720 cm^{-1} very similar values are calculated for the hollowA’ and hollowB sites (715 and 721 cm^{-1} respectively).

It can be concluded that the calculated spectrum for the hollowA’ site better matches the experimental HREELS data than the one for the hollowB site, in contrast to what could be expected based on the slight energetic preference at saturation coverage for the latter site (see Table 4-2).

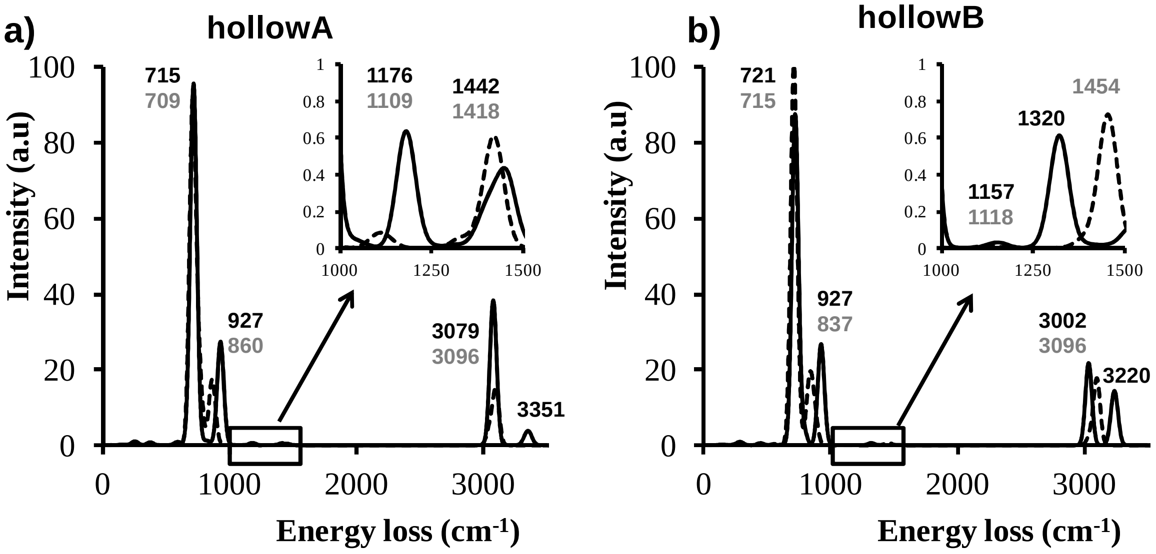

Figure 4-3. Calculated infrared spectra for benzene adsorbed at the (a) hollowA/A' and (b) hollowB sites on Pd(100) at medium (dotted lines and grey numbers) and saturation coverage (full lines and black numbers).

4.3.3 Electronic properties

The electronic density of states (DOS) of benzene adsorbed at the hollowA/A' and hollowB sites on the Pd(100) surface at medium and at saturation coverage is illustrated in Figure 4-4. Since the electronic structure obtained including van der Waals interactions is very similar to the one from the PW91 calculations (see the comparison in Figure C5 in the Appendix C), only the results using the PW91 functional are discussed. The calculated electronic structures are in good agreement with photoemission spectroscopy experiments[30, 31].

The Pd(100) 3d-band of the clean active site extends up to bonding energies of −5.2 eV and overlaps with the gas phase benzene π ($1a_{2u}$, $1e_{1g}$ and e_{2u}) and $3e_{2g}$ (σ) states (see top panel of Figure 4-4); the gas phase $1a_{2u}$ (π) state also overlaps with the bottom of the s-band. For convenience the gas phase benzene molecular orbitals are shown in Figure C6 of the

Appendix C. At medium coverage, the work function decreases by −1.3 eV for both adsorbates, while larger decreases of −1.4 eV and −1.75 eV are computed at saturation coverage for the hollowA' and hollowB, respectively (see Table 4-3) indicating a net electron transfer from benzene to the Pd(100) surface.

Comparison of the right panels in Figure 4-4b and Figure 4-4c reveals that at medium coverage the contribution of the benzene states to the DOS of the adsorbed complex is very similar for both adsorbates. Analysis of the PDOS projected on the distorted gas phase benzene molecular orbitals (see Figure 4-5) confirms the flat configuration of benzene at both sites [30, 31, 38], since bonding with the Pd-surface mainly occurs via interaction with the benzene π-states ($1a_{2u}$, $1e_{1g}$ and e_{2u}). At medium coverage, the benzene π-states are resonantly broadened and shifted by interaction with the metal bands, while the σ-states are only weakly perturbed (see Table 4-4). Coupling of the benzene $1e_{1g}$ (π, HOMO) orbitals with the Pd t_{2g} states leads to a strong depletion of Pd d_{xz}+d_{yz} states from binding energies of −10 eV up to −7.5 eV (see top panel in Figure C7 in the Appendix C) and the appearance of new Pd d_{xz}+d_{yz} states with binding energies ranging from −5 eV up to and extending above the Fermi level. As illustrated in the bottom panel of Figure C7, interaction of the benzene $1a_{2u}$ orbital with the Pd d_{z2} states leads to a depletion of Pd d_{z2} states in the range of −10 eV up to −7 eV and the appearance of new Pd d_{z2} states at binding energies from −5 eV onwards and extending above the Fermi level.

The PDOS shown in Figure 4-5 indicates that both the $1e_{1g}$ and e_{2u} derived states are strongly broadened. In line with an STM study by Yoshinobu et al.[32] for the Pd(110) case and a DFT study of Mittendorfer and Hafner for Ni(100), [72] the HOMO (e_{1g}) derived states are split up with the bonding states peaking around −4.8 eV below the Fermi level, while the antibonding states extend up to the Fermi level. Hence, a downward shift of the $1e_{1g}$ states of some 1.8 - 2 eV relative to the less perturbed $2a_{1g}$ can be suggested. In agreement with UPS [14, 31, 39, 74, 75] and inverse photoemission spectroscopy (IPES)[76, 77] measurements for benzene adsorbed on transition metals, the LUMO derived e_{2u} states peak at some 2-3 eV above the Fermi level. Our calculations also confirm the findings of Nyberg et al.[30] and Hofmann et al.[31] who reported that in the UPS spectra π-states resulting from the interaction with the $1a_{2u}$ benzene orbital appear at the leading edge of the $3e_{1u}$ σ-states located at bonding energies around 7 eV below the Fermi level. Analysis of the PDOS (see Figure 4-5) further reveals that, at medium coverage, the benzene σ-states are slightly broadened and that the degeneracy of the $1b_{2u}$ and $2b_{1u}$ states is lifted as is the degeneracy of the two $3e_{2g}$ states albeit at saturation coverage only. Also, the canting of the p_z-states to maximize the p_z-t_{2g} overlap and the concomitant tilting of C-H bonds, as mentioned before, is reflected in the small contribution of the p_z orbitals to the $3a_{1g}$ derived states as can be seen in Figure C8 in Appendix C.

At saturation coverage, the shortest distance between the benzene molecules in the (2×2) overlayer is strongly reduced as compared to medium coverage and amounts to some 170 pm (see Figure 4-2). Therefore, adsorbate-adsorbate interactions become important at saturation coverage (see section 3.1). The presence of strong lateral interactions at saturation coverage is particularly evident in the shape of the bands originating from the σ-levels as illustrated in Figure 4-5. The PDOS thus confirms the important effect of repulsive interactions on the stability of benzene adsorbed on the Pd (100) surface with increasing coverage. In agreement with UPS experiments [31], the increased dispersion of the σ-states induced by adsorbate-adsorbate interactions is most strongly pronounced on the more extended $3a_{1g}$ and the $3e_{1u}$ states that have a large contribution from H(s) electrons (see Figure 4-5 and Figure C8 in Appendix C). Similar observations were made by Mittendorfer and Hafner [72] in their periodic DFT study of benzene adsorbed at the hollowA site of Ni(100). For the bands derived from the $1a_{2u}$, $1e_{1g}$ and e_{2u} benzene π-levels, the increased coverage induces only a small upward shift in agreement with the weaker bonding at higher coverage. From our calculations, a down shift of, respectively, 1.8 eV and 1.1 eV of the 1e$_{1g}$ and la$_{2u}$ levels relative to the vacuum level can be suggested, which agrees fairly well with the observation of Hofmann et al.[31] that the ionization energy of the π-orbitals, 1e$_{1g}$ and la$_{2u}$, is increased by about 1.1 eV relative to the σ-orbitals.

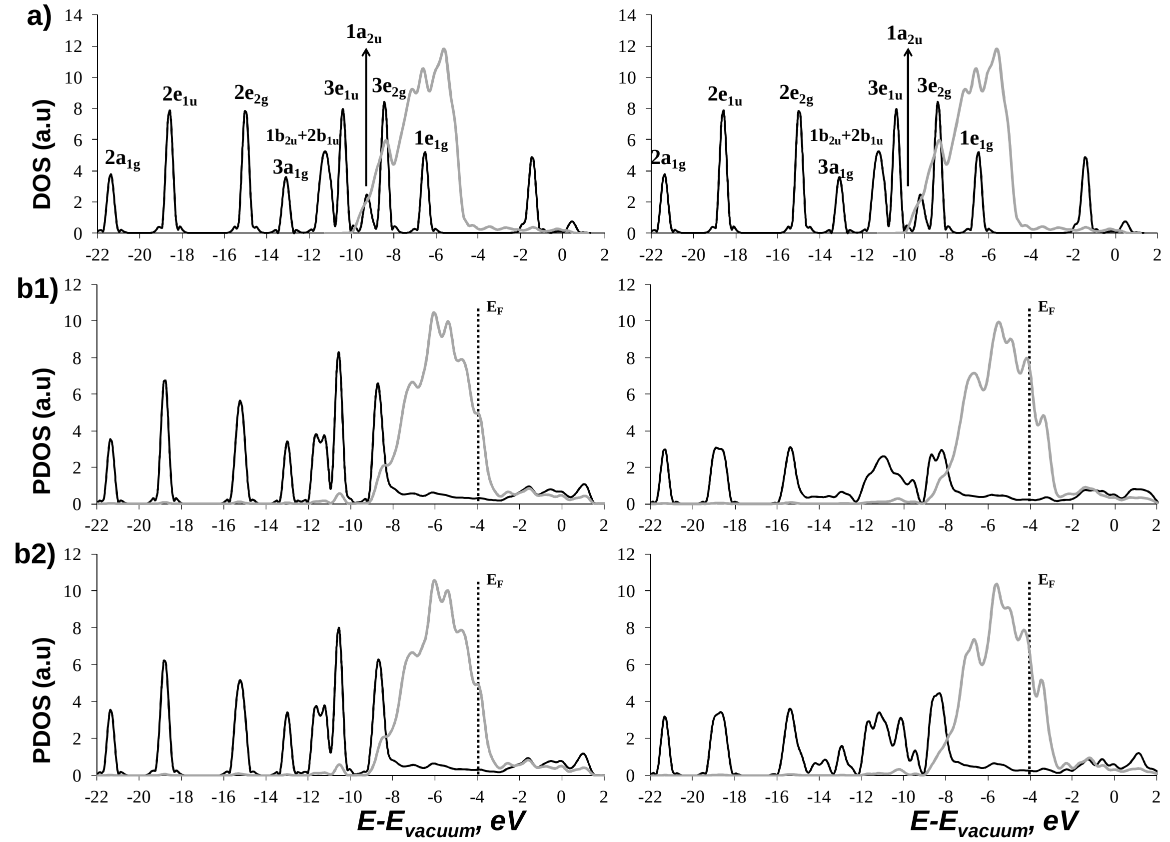

Figure 4-4. a) Density of states (DOS) of benzene in gas phase (black), together with the DOS projected on the d states of the clean active site on Pd(100) (grey). b1) DOS projected on all atoms of benzene adsorbed for the hollowA and hollowA’ geometries (black) on Pd(100), left and right panels respectively, and DOS projected on the d states of the covered active site (grey). b2) DOS projected on all atoms of benzene adsorbed for hollowB geometries (black) on Pd(100), and DOS projected on the d states of the covered active site (grey) and. Left plots represent medium coverage for the (2√2×2√2)R45° overlayer, and right panels represent the saturation coverage for the (2×2) overlayer. All energies are relative to the vacuum level. The Fermi level is indicated with dotted lines.

Table 4-3. Characteristics of the (2√2×2√2)R45° and (2×2) overlayers on Pd(100) for adsorption of benzene at the hollowA and hollowB sites.

		ΔE_{ads} (kJ mol^{-1})	Φ (eV)	$(\varepsilon_d\text{-}E_{vac})^a$ (eV)	$(\varepsilon_d\text{-}E_f)$ (eV)	d-band width^b (eV)
	Bare Pd(100)	----	–5.15	–6.89	–1.74	3.39
hollowA	(2√2×2√2)R45°	–156.4	–3.86	–5.88	–2.02	3.31
hollowA’	(2√2×2√2)R45° [c]	–34.1	–3.74	–5.67	–2.30	3.44
hollowB	(2√2×2√2)R45°	–159.1	–3.87	–5.87	–2.00	3.31
	(2×2)	–38.2	–3.40	–5.73	–2.33	3.37

[a] d-band center of the occupied states of the first (top) layer of Pd(100)

[b] d-band width at half height for all states of the active site

[c] Two benzene molecules with ϕ_1=0° and ϕ_2 =30° adsorbed on the (2√2×2√2)R45° unit cell

Table 4-4. Calculated energies of molecular eigenstates of benzene in gas phase, adsorbed at the hollowA and hollowB sites on Pd(100) at medium and saturation coverage. Energies are related to the vacuum level. All orbitals are named in line with Mittendorfer and Hafner.[72]

		Medium coverage		Saturation coverage	
Orbital	**Benzene gas**	**hollowA**	**hollowB**	**hollowA’**	**hollowB**
$1e_{1g}$ (π)	– 6.0	–8.8	–8.9	–8.8	–8.7
$3e_{2g}$	– 8.0	–9.0	–9.0	– 9.0	– 8.9
$1a_{2u}$ (π)	– 8.8	–10.7	–11.0	– 10.7	– 10.4
$3e_{1u}$	– 10.0	–11.5	–10.9	– 10.6	– 10.8
$1b_{2u}$	– 10.6	–11.7	–11.5	– 11.2	– 11.6
$2b_{1u}$	– 11.0	–12.4	–12.0	– 11.7	– 12.2
$3a_{1g}$	– 12.6	–13.8	–13.3	– 13.0	– 13.4
$2e_{2g}$	– 14.6	–16.1	–16.3	– 15.6	– 15.8
$3e_{1u}$	– 18.3	–19.2	–19.4	– 19.2	– 19.2
$2a_{1g}$	– 21.1	–22.4	–22.2	– 21.9	– 22.0

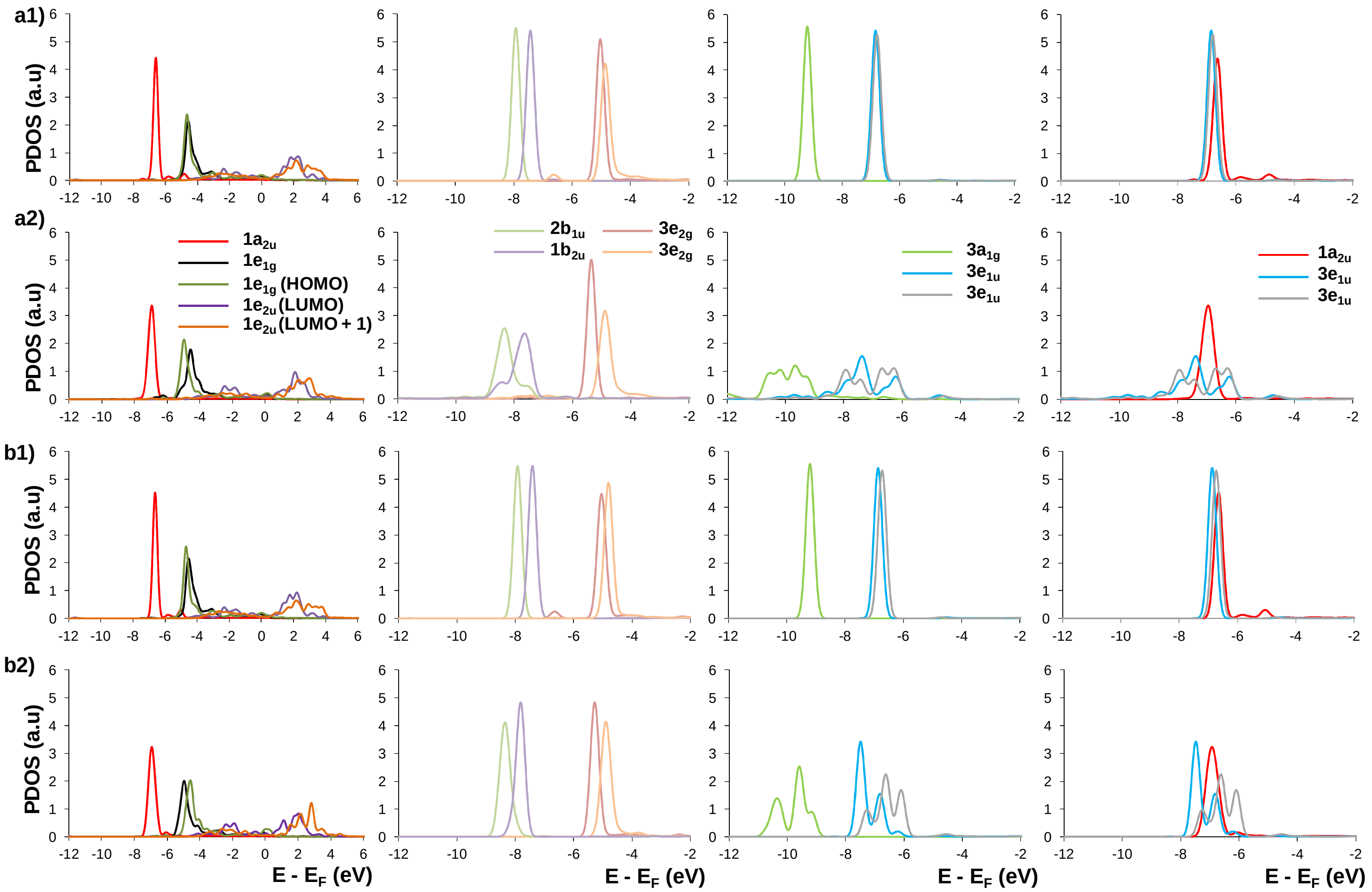

Figure 4-5. Projected DOS on selected molecular orbitals of gas-phase benzene for the hollowA adsorbate on Pd(100) at (a1) medium and (a2) saturation coverage, and for the hollowB adsorbate at (b1) medium and (b2) saturation coverage.

STM images of adsorbed molecules on solid surfaces can give valuable information on the adsorption sites and the orientation of the adsorbate with respect to the substrate lattice.[29] However, the observed internal structure of the STM images is not directly related to the atomic positions but depends on the electronic structure of the adsorbate and the surface. It is known that the local density of states (LDOS) near the Fermi level has a significant contribution to STM images.[28] Our calculated constant current STM images on a plane at ~1 Å above the carbon atoms for different tip bias potentials (ε in eV) and adsorbate orientations (A' and B) at saturation coverage are shown in Figure 4-6.

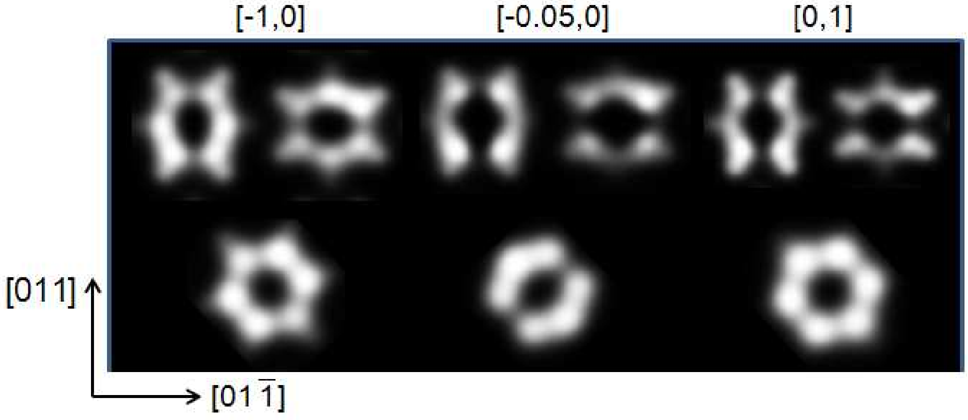

Figure 4-6. Constant current images on a horizontal plane at ~1 Å above the carbon atoms of benzene adsorbed on Pd(100) at saturation coverage for the hollowA' (top) and the hollowB (bottom) configurations at different bias potentials ε (left: ε = +1 eV; middle: ε = +0.05 eV; right: ε = –1 eV).

For both hollowA' and hollowB, the STM images at saturation coverage clearly show two protrusions separated by a node-like depression at ε = +0.05 eV while a round-like shape is calculated at higher bias voltages (ε = ±1.00 eV) for the hollowB. For the hollowA', the depression coincides with the high symmetry $[011]$ and $[01\bar{1}]$ directions while for the hollowB it forms an angle of ~45° with the $[011]$ direction. As pointed out by Sautet and Bocquet,[78] the calculated STM image can be understood from the PDOS for the molecular orbitals as well as their symmetry and spatial character in the lateral direction. For the electronic states that derive from a molecular orbital to contribute to the STM image, the

PDOS on that molecular orbital must have a substantial contribution at the Fermi level and it also must have a relatively slow decay into the vacuum region where the tip apex is located.[68] The final STM image results from the electronic interferences between the individual molecular orbital contributions and the direct tip-surface through space contribution. These effects depend on the orientation of the benzene molecule and may lead to the preponderance of one of the orbitals of *E* symmetry in the STM image.[29] As discussed above, in the hollowA', the degeneracy of the $1e_{1g}$ (HOMO) orbitals is lifted and only one of the $1e_{1g}$ orbitals contributes to the STM image. This orbital presents a nodal plane along the $[011]$ direction for one of the benzene molecules while for the other benzene molecule it is oriented along the $[01\bar{1}]$ direction. For the hollowB too, the main contribution to the DOS near the Fermi level stems from only one of the $1e_{1g}$ orbitals and the STM image reflects the symmetry of the $1e_{1g}$ orbital with the nodal plane at an angle of ~45° from the $[01\bar{1}]$ direction. Also, for the hollowB, the contribution of one of the LUMO derived e_{2u} states to the DOS becomes more important in the energy range [E_F ± 1 eV, E_F] resulting in the round-like shape of the STM image at higher bias voltages ($\varepsilon = \pm 1.00$ eV). To best of our knowledge, no experimental STM images of benzene adsorbed at Pd(110) are available in literature. However, our calculated STM images indicate that the STM pattern can be used to differentiate between the two possible configurations, hollowA' and hollowB, of the experimentally observed (2×2) benzene overlayer on Pd(100).

In summary, our DFT calculations indicate that on Pd(100) benzene prefers the four-fold hollow sites and adopts a flat geometry in which the molecular plane is oriented parallel to the surface and the C-H bonds are tilted some 18°-25° out of the plane of the carbon ring; the degree of tilting of the C-H bonds increases with coverage. At half saturation coverage benzene may populate hollowA and hollowB adsorption sites. In the (2×2) overlayer experimentally observed at saturation coverage, a slight energetic preference of 3 kJ mol^{-1} is calculated for the hollowB benzene in which two of the CC bonds are oriented parallel to the [001] direction. However, given the accuracy of the periodic DFT calculations an adsorption geometry with two benzene molecules per unit cell that are oriented parallel to high symmetry directions but azimuthally rotated by 30° relative to one another, *i.e.* hollowA', cannot be discarded. Also, the calculated vibrational and electronic features for both configurations are compatible with UPS and HREELS experiments. The decrease in stability of some 120 kJ mol^{-1} at saturation coverage as compared to medium coverage can be mainly explained by strong repulsive interactions between neighboring benzene molecules. The presence of adsorbate-adsorbate interactions can easily be observed in photoemission spectroscopy from the dispersion of the σ-states originating from the $3a_{1g}$ and the $3e_{1u}$ benzene orbitals that have an important contribution of H(s) orbitals and might also be recognizable in HREELS from the computed breakup of the ν_{CH} stretching mode that can be expected to appear at saturation coverage. The calculated STM images indicate that STM can be used to differentiate between these two possible configurations of the (2×2) overlayer at saturation coverage.

The inclusion of non-local van der Waals interactions does not change the general picture; although the absolute adsorption strengths increase by some 50 kJ mol^{-1}, the relative stability ordering of the various adsorption sites remains unaltered. Also, only minor changes in the calculated geometries and electronic structures are observed using vdW-DFT (optPBE-vdW) as compare to PW91.

4.4 Benzene adsorption on Pd(110) at medium and saturation coverage

In this section, benzene adsorption on Pd(110) is evaluated at medium coverage for various adsorption sites, and at saturation coverage for the most stable ones. Adsorption energies and geometries, vibrational frequencies, electronic properties and STM images are used to compare different adsorption sites and to evaluate the coverage effects on the adsorption.

4.4.1 Adsorption energies

The adsorption of a single benzene molecule on the (4×2) unit cell, with a surface area of 8.8 10^{-19} m^2, results in a surface concentration of 1.1 10^{18} molecules m^{-2}. This coverage corresponds to half of the c(4×2) overlayer observed by Yoshinobu et al.[17] at saturation coverage at 300 K. Four types of adsorption sites have been evaluated for benzene on Pd(110), namely top, hollow, shortbridge and longbridge, following the nomenclature of Treboux and Aono[29] (see Figure 4-7). In the shortbridge site benzene is bound with two Pd atoms along the $[1\bar{1}0]$ direction, while in the longbridge site the molecule is bounded with two Pd atoms along the [001] direction. Each of the four types of sites is studied for three different azimuthal orientations with respect to the surface and the azimuthal rotation (ϕ) in Figure 4-7 is expressed by using the smallest angle between a benzene C-C bond and the $[1\bar{1}0]$ direction in the starting geometries used for optimization.

In agreement with STM observations, [17] we obtained that at medium coverage the most stable adsorption sites are the three four-fold hollow(0), hollow(15) and hollow(30) conformations, with similar adsorption energies of about -137 kJ mol^{-1} (see Table 4-5). Although the (110) surface is the most open one, the adsorption energies are lower than on the (100) surface due to the mismatch between the C-C bond lengths and the distances between the Pd atoms. For the (4 × 3) benzene ordering, Favot et al.[34] concluded that, due to stronger metal-adsorbate interactions, the hollow(30) is favored by 10 kJmol^{-1} and 45 kJmol^{-1} over the hollow(15) and hollow(0) configuration, respectively. In contrast, our calculated adsorption energies indicate that in the absence of lateral interactions, metal-adsorbate interactions are rather similar for all three adsorbates. Also, the shorter closest distance between the hydrogen atoms of two neighboring benzenes for the hollow(30) site (308 pm) as compared to the hollow(0) site (371 pm) does not introduce repulsive adsorbate-adsorbate interactions in the hollow(30).

The hollow sites are followed in adsorption strength by the shortbridge sites with about 30 kJ mol^{-1} weaker adsorption energies, see Table 4-5. This stability ordering agrees with STM results at low benzene coverage reported by Treboux and Aono.[29] These authors used elastic scattering quantum chemistry (ESQC) calculations to resolve the adsorption site and the molecular orientation with respect to the surface plane from the STM images. They concluded that the observed two-lobed STM pattern separated by a depression can only correspond to the azimuthally rotated geometry for the hollow or shortbridge sites. Our calculations indicate that the difference in stability between the hollow and shortbridge sites is large enough to discard the bridge sites and to consider the three hollow sites as the preferred adsorption sites for benzene on Pd(110) at medium coverage.

The adsorption of benzene on the three hollow sites has also been evaluated at saturation coverage, *i.e.* for the c(4×2) benzene overlayer as shown in the bottom panels of Figure 4-8. Despite small geometric and energetic changes (see Table 4-6 and Figure C9 in Appendix C), the three hollow sites remain the most stable at saturation coverage; the shortbridge(0) and longbridge(0) sites are respectively ~25 and ~55 kJ mol^{-1} less stable than the most stable hollow(0) site (see Table 4-6). A slight energetic preference of some 5-10 kJ mol^{-1} for the hollow(0) site relative to the (15) and (30) hollow adsorbates can however be noted. In contrast, Favot et al. [34] computed that the hollow(15) site is 3 kJmol^{-1}, respectively 22 kJ mol^{-1}, more stable than the hollow(30) and the hollow(0) site. According to these authors, the preference for the hollow(15) site is suggested to be a compromise between adsorbate-surface and adsorbate-adsorbate interactions; the former promote large azimuthal angles of the adsorbate relative to the $[1\bar{1}0]$ direction, while the latter tend to favor smaller angles.

At saturation coverage, the computed closest distance between the centers of two neighboring benzene molecules is 685 pm in good agreement with the value of 670 pm reported by Favot et al. [34]. With increasing coverage, the distance between hydrogen atoms of neighboring benzene molecules in the [001] directions remains largely unchanged. In the other directions, the averaged shortest distance between hydrogen atoms of neighboring benzene molecules decreases from 266 pm for the hollow(0) site to 206 pm for the hollow(30) over 247 pm for the hollow(15) site. Estimation of the adsorbate-adsorbate repulsion energy from the energy difference between the distorted gas phase benzene in a (2×2) unit cell and in a very large unit cell (15×15×15 Å^3), revealed the absence of lateral interactions in the hollow(0) and hollow(15) adsorbates while for the hollow(30) a value of 4 kJ mol^{-1} was found. Hence, the small decrease in adsorption energies from medium to saturation coverage, e.g. from −138 to −123 kJ mol^{-1} for the hollow(0), can be explained by the quite large distance between neighboring benzene molecules which, as illustrated in Figure 4-8, is much larger than the distance at saturation coverage on the Pd(100) surface.

Fujisawa et al.[15] reported that tilted geometries are favored over flat benzene at saturation coverage. These authors used the peaks at ~350 and ~440 K in the TPD spectrum to estimate adsorption heats of −87 and −112 kJ mol^{-1} for the flat and tilted benzene respectively. [27] In contrast, our calculations indicate that tilted adsorbates are up to ~70 kJ mol^{-1} lower in stability compared to flat adsorbates, as shown in Table 4-5 for the adsorbates with tilt angle θ different from zero.

Like in the Pd(100) case, inclusion of van der Waals interactions enhance adsorption energies by about 45-50 kJ mol^{-1}, but the same trend in relative stabilities is found and only very small differences in geometries are observed. Therefore, geometries, vibrational frequencies and electronic structure are discussed only for the results obtained using the PW91 functional.

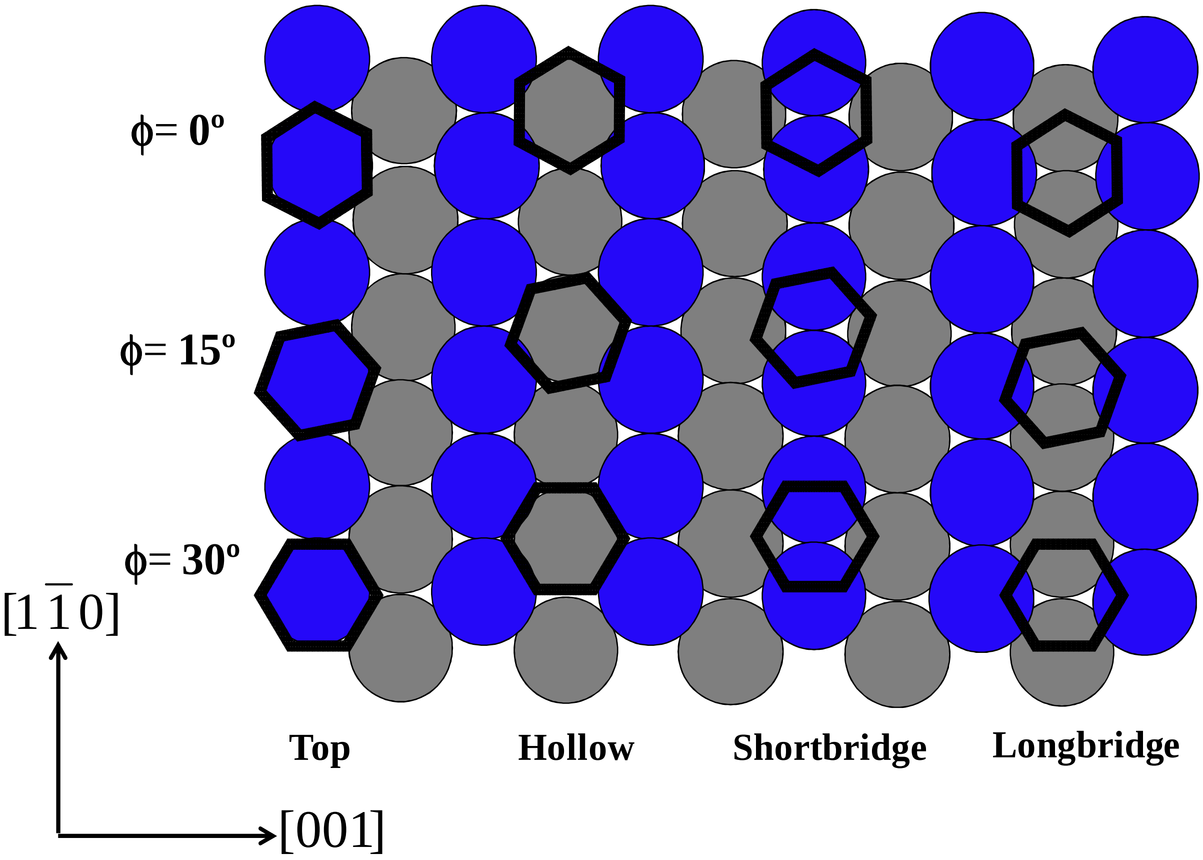

Figure 4-7. The twelve adsorption sites investigated for benzene on Pd(110). Only Pd atoms in the top layer are colored blue for easier interpretation. The azimuthal angle ϕ is shown in the left side of the figure.

Table 4-5. Adsorption energies of different sites for benzene on Pd(110) in kJ mol^{-1} at medium coverage and saturation coverage, *i.e.* p(4×2) and c(2×2) overlayers. Hollow tilted adsorbates ($\theta > 0$) are also shown at saturation coverage. The calculated azimuthal and tilting angle (ϕ, θ) is shown in º relative to the surface. The values obtained with the vdW-DF method are included between brackets.

Site (ϕ)	Tilting angle θ (º)	ΔE_{ads} (kJ mol^{-1})	
		Medium coverage p(4×2)	**Saturation coverage c(4×2)**
Hollow(0)	7	−137.6 (−181.5)	−122.8 (−175.0)
	17	---	−53.8 (−108.7)
Hollow(15)	0	−136.5 (−180.0)	−118.1 (−169.9)
	17	---	moved to hollow(15,0)
Hollow(30)	0	−136.0 (−179.0)	−115.1 (−163.7)
	26	---	−51.8 (−103.6)
Shortbridge(0)	0	−108.0 (−161.5)	−96.8 (−158.3)
Shortbridge(15)	0	−102.8 (−158.4)	---
Shortbridge(30)	0	−104.4 (−160.2)	---
Longbridge(0)	0	−81.1 (−133.7)	−65.7 (−127.1)
Longbridge(15)	0	−86.6 (−138.6)	---
Longbridge(30)	0	−84.8 (−136.1)	---
Top(0)	0	−46.6 (−104.3)	---
Top(15)	0	−59.2 (−115.5)	---
Top(30)	0	−80.2 (−135.4)	---

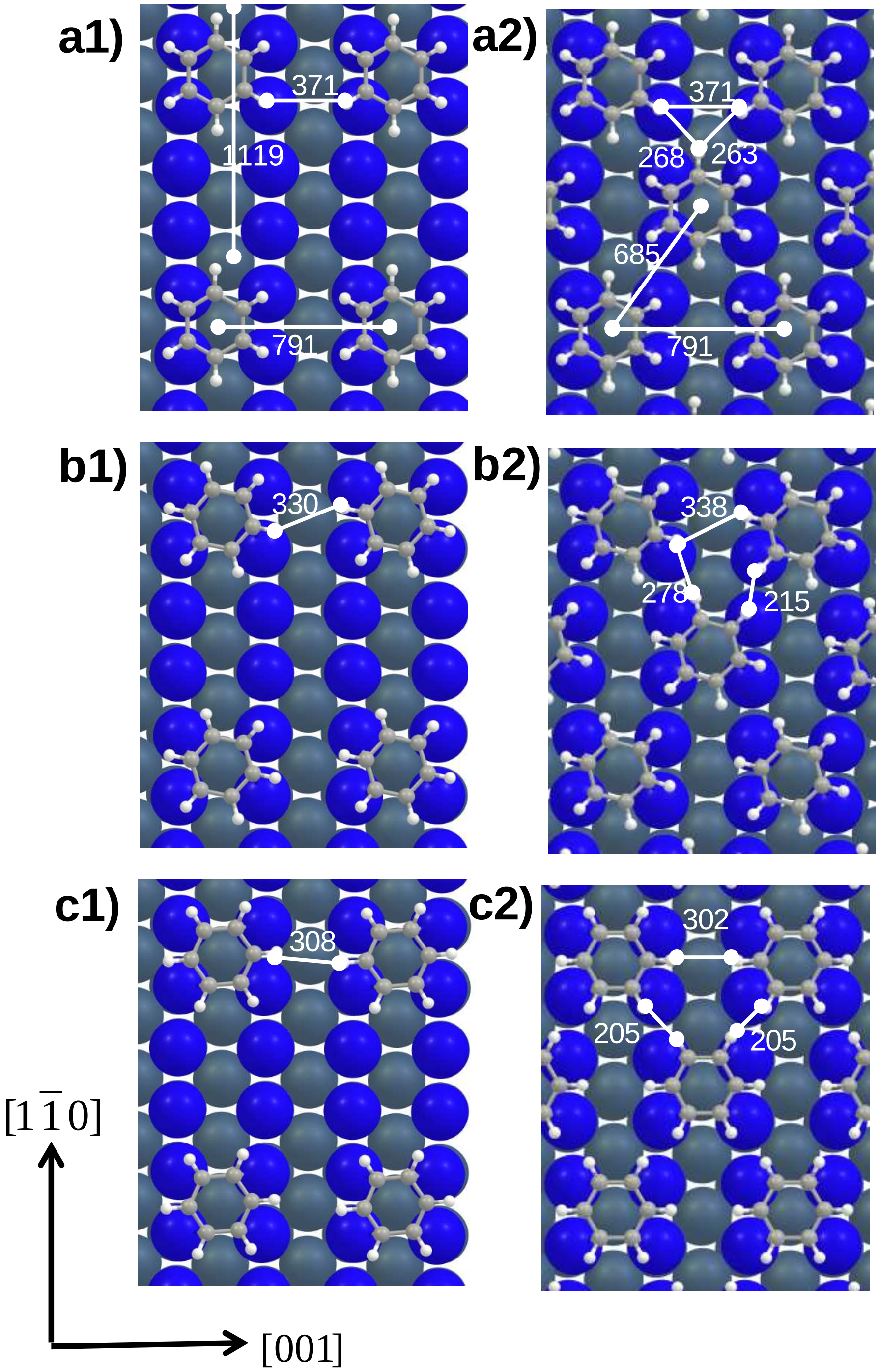

Figure 4-8. Surface overlayer of benzene adsorption at medium coverage on (a1) hollow0, (b1) hollow(15) and (c1) hollow(30) sites, and at saturation coverage on (a2) hollow(0), (b2) hollow(15) and (c2) hollow(30) sites. Distances between centers of the closest benzene neighbors in the $[1\bar{1}0]$ and [001] directions are indicated in pm for the hollow(0), and the same distances are obtained for the other two adsorbates. Closest H-H distances between neighbor benzene molecules are also shown in pm. Only Pd atoms in the top layer are colored blue for easier identification.

The most relevant adsorption features of the three most stable hollow sites are listed in Table 4-6 for medium and saturation coverage, and shown in Figure C9 of the Appendix C. At medium coverage, the hollow(0) adsorbate moves closer to one of the Pd rows in the $[1\bar{1}0]$ direction, as already reported by Mittendorfer and Hafner for benzene on Ni(110) at saturation coverage.[72] Due to this translation, the benzene molecule slightly tilts by 7º with respect to the Pd surface, so that two stronger Pd-C bonds of 219 pm can be formed. Although the molecule is canted relative to the Pd surface, the carbon ring remains flat with the C-H bonds tilted some 17-30° out of the plane of the ring. Despite the deviation from the high-symmetry site, the benzene and slab distortion energies at this site are the smallest of the three hollow sites (see Table 4-6). At medium coverage, the hollow(15) and hollow(30) rotate from their 15º and 30º angles used initially used in the optimization to angles of 18º and 35º in the optimized structures. Despite the small changes in azimuthal orientation, these sites are referred to by the initial angle of 15º and 30º to facilitate the discussion. For the three hollow adsorbates, similar benzene and slab distortion energies (see Table 4-6) are calculated, leading to similar metal-adsorbate interaction energies as discussed above. Increasing the coverage of benzene to saturation does not dramatically change the geometries; the hollow(0) site geometry remains similar to the one at medium coverage. However, even though the medium coverage geometries have been used as starting point for the optimization, the hollow(15) and hollow(30) geometries azimuthally rotate back with respect to medium coverage, adopting resp. the 16º and 30 º azimuthal orientations. The decrease in stability of the three adsorbates at saturation coverage is explained by weaker interaction energies with the surface, since the distortion energy is very similar compared to medium coverage (see Table 4-6).

Table 4-6. Adsorption, interaction and distortion energies (kJ mol^{-1}), together with bond lengths and bond angles (pm and º) for the three hollow sites at medium and saturation coverage on Pd(110), *i.e.* p(4×2) and c(4×2) overlayers. Adsorption energies including van der Waals interactions are shown between brackets.

		Hollow(0)		**Hollow(15)**		**Hollow(30)**	
		p(4×2)	**c(4×2)**	**p(4×2)**	**c(4×2)**	**p(4×2)**	**c(4×2)**
ϕ, θ	º	0, 7	0, 7	18, 0	16, 0	35, 0	30, 0
ΔE_{ads}	kJ mol^{-1}	–137.6 (–181.5)	–122.8 (–175.0)	–136.5 (–180.0)	–118.1 (–170.0)	–136.0 (–179.0)	–115.1 (–163.7)
E^{int}	kJ mol^{-1}	–264.6	–223.2	–268.3	–220.3	–267.7	–226.6
E^{dis} (slab)	kJ mol^{-1}	40.8	13.4	43.8	16.0	40.8	14.6
E^{dis} (benzene)	kJ mol^{-1}	86.2	86.9	88.5	86.3	90.9	96.9
$d_{C\text{-}C}$	pm	142-145	143/145	142/145	142/145	142-145	143-145
$d_{C\text{-}Pd}$	pm	219-223	219-224	218-227	218-227	219-226	221-224
$d_{C\text{-}H}$	pm	109-110	109-110	109-110	109-110	109-110	109-110
$d_{Benzene\text{-}1stPd}$	pm	200	196	201	197	200	193
$d_{1st–2nd\text{-}Pdlayer}$	pm	130	135	131	135	130	135
C-C-C	º	119-121	119-121	119-121	119-121	119-121	119-120
C-C-H	º	7-28	7-28	15-22	13-25	20-22	22-25

4.4.2 Vibrational spectra

The infrared intensities and vibrational frequencies have been calculated at medium and saturation coverage for the three most stable hollow(0), hollow(15) and hollow(30) sites. The infrared spectra at saturation coverage of the three adsorbates are compared in Figure 4-9 (black, light grey and dark grey lines respectively). The vibrational spectra are shown up to 1500 cm^{-1} because at higher frequencies only the highest ν_{CH} stretching mode is obtained. For the three adsorbates this mode is located at about ~3100 cm^{-1} in good agreement with the experimental loss at 3050 cm^{-1}. [15] Details on the vibrational frequencies of the three hollow sites at medium and saturation coverage can be found in Table C3 of the Appendix C.

Fukisawa et al. reported two coverage dependent peaks for the high-intensity out-of-plane γ_{CH} bending mode located at 705 and 745 cm^{-1}. These authors observed that the 745 cm^{-1} loss increased in intensity with coverage, while the opposite was observed for the loss at 705 cm^{-1}. Hence, these authors related the two peaks to the existence of flat and tilted adsorbed states respectively [15]. In view of our observation that at saturation coverage the tilted adsorbates are up to ~70 kJ mol^{-1} less stable than the flat adsorbates (see section 4.1) both these experimental losses are more likely attributed to flat hollow states. For the high-intensity out-of-plane γ_{CH} bending mode, two vibrational peaks are obtained for the hollow(0) (618 and 734 cm^{-1}) and (15) adsorbates (673 and 806 cm^{-1}), while only one is calculated for the hollow(30) (684 cm^{-1}). Increasing the coverage reduces the intensity of these peaks, as illustrated in the bottom panel of Figure 4-9. Considering that our approach may overestimate the frequency because the inharmonicity factor is not included, we suggest that the calculated hollow(0) 734 cm^{-1} peak is related with the experimental 705 cm^{-1} loss and the calculated hollow(15) 806 cm^{-1} peak with the experimental loss at 745 cm^{-1}. Furthermore, the vibrational peaks for the νCC stretching mode are observed at 1321 and 1295 cm-1 for the hollow(0) and hollow(15) sites, which is in line with the experimentally reported loss at 1330 cm-1, while no peak is observed for the hollow(30) site.

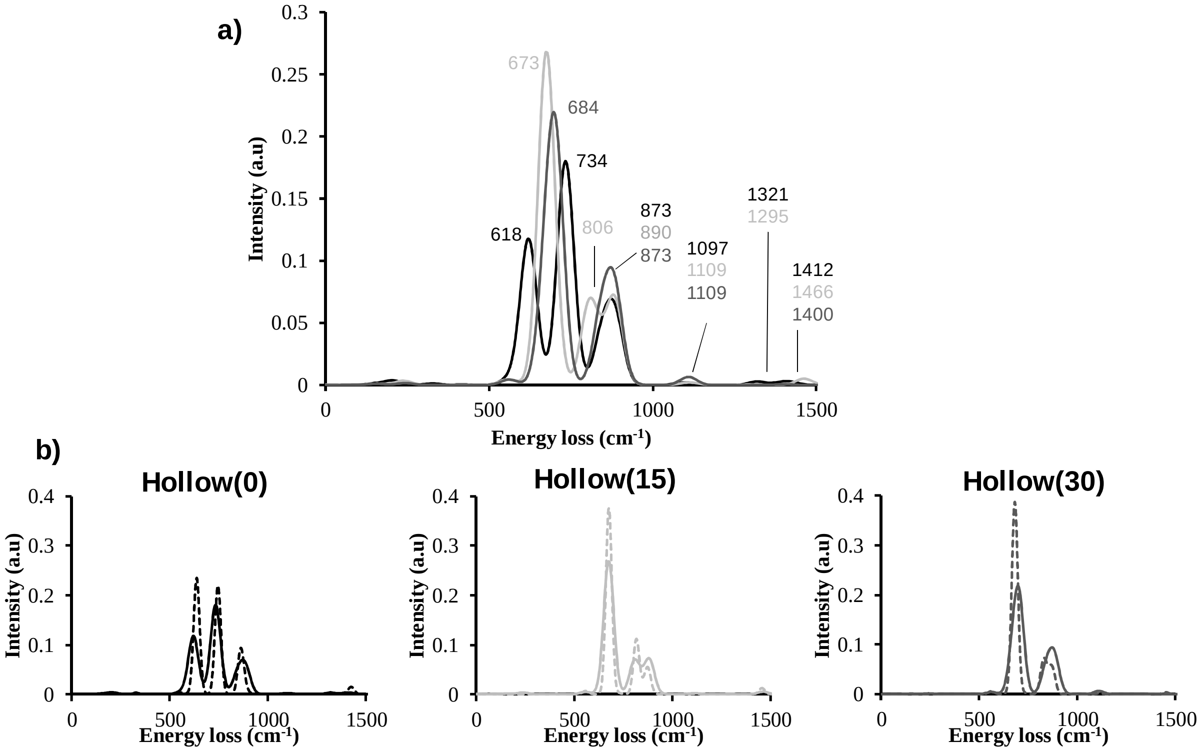

Figure 4-9. Calculated infrared spectra for benzene adsorbed at the hollow(0), hollow(15) and hollow(30) sites on Pd(110) (black, light grey and dark grey respectively) at (a) saturation coverage, and comparison of (b) medium and saturation coverage respectively with full and dotted lines for each of the three (0), (15) and (30) adsorbates from left to right.

4.4.3 Electronic properties

The electronic density of states (DOS) for the three most stable hollow sites on the Pd(110) surface at medium and at saturation coverage is illustrated in Figure 4-10. Like for the Pd(100) surface, the electronic structure obtained with the vdW-DF method is very similar to the one from the PW91 calculations. Hence, only the results obtained with the PW91 functional are discussed. The calculated electronic structures are in good agreement with photoemission spectroscopy experiments.[14]

At medium coverage, the computed work function decreases by 0.8 eV for all three adsorbates, and by some 0.6 eV less than for the Pd(100) case, in agreement with the less stronger bonding on Pd(110). At saturation coverage a larger decrease in the work function of 1.2 eV is computed for the hollow(0) and hollow(15) sites while for the hollow(30) no further decrease is observed (see Table 4-7). The experimental value of 1.1 eV for the c(4×2) overlayer[14] is in good agreement with the values computed for the hollow(0) and hollow(15) sites. A periodic DFT study in the local density approximation using ultrasoft Vanderbilt pseudopotentials of the Pd(110)-c(4 × 2)-benzene system, reported a decrease in work function of 1.2 eV ± 0.3 eV.[34]

From Figure 4-10b, it is clear that for all three adsorbates the contribution of the benzene states to the DOS of the adsorbed complex is very similar. Therefore, the calculated energies of the benzene molecular eigenstates (see Table 4-8) and the PDOS projected on the distorted gas phase benzene molecular orbitals (see Figure 4-11) are reported for the hollow(0) site only. As for the Pd(100) case, the bonding with the Pd-surface mainly occurs via interaction with the benzene π-states, ($1a_{2u}$, $1e_{1g}$ and e_{2u}). Analysis of the PDOS (Figure 4-11) reveals that both the $1e_{1g}$ and e_{2u} derived states are strongly broadened. The HOMO (e_{1g}) states peak around 4.5 eV below the Fermi level and extend up to the Fermi level. A downward shift of the $1e_{1g}$ states of some 1.8 eV relative to the unperturbed $2a_{1g}$ is computed in fair agreement with the value of 1 eV reported by Netzer et al. [14] The LUMO (e_{2u}) derived states peak at some 2-3 eV above the Fermi level. In agreement with the experimental observations, the π-states resulting from the interaction with the $1a_{2u}$ benzene orbital appear at the leading edge of the $3e_{1u}$ σ-states located at bonding energies around 7 eV below the Fermi level. Similar to the Pd(100) case, the degeneracy of the $1b_{2u}$ and $2b_{1u}$ states is lifted.

As discussed above (see section 4.1), the decrease of 70 pm in the averaged closest distances between hydrogen atoms of neighboring benzene molecules from medium coverage (306 –

370 pm) to saturation coverage (237 – 300 pm) does not result in significant adsorbate-adsorbate interaction (see section 4.1). As illustrated in Figure 4-10, Figure 4-11 and Figure C10 in Appendix C, at saturation coverage the dispersion of the bands originating from the σ-levels is not significantly different than at medium coverage confirming the limited importance of repulsive interactions on the stability of benzene adsorbed on the Pd(110) surface with increasing coverage. The computed dispersion of the $3a_{1g}$ band of 0.6 eV is in fair agreement with the experimental value of 0.4 eV [14].

Table 4-7. Adsorption features for the adsorption of benzene at the three hollow sites on Pd(110) at medium and saturation coverage.

	Pd clean active site	**hollow(0)**		**hollow(15)**		**hollow(30)**	
		p(4×2)	**c(4×2)**	**p(4×2)**	**c(4×2)**	**p(4×2)**	**c(4×2)**
ΔE_{ads} (kJ mol^{-1})	---	–137.6	–122.8	–136.5	–118.1	–135.9	–115.1
Φ (eV)	–4.84	–4.06	–3.68	–4.06	–3.67	–4.04	–4.06
$(\varepsilon_d\text{-}E_{vac})^a$ (eV)	–6.58	–6.00	–5.87	–5.97	–5.80	–5.95	–6.00
$(\varepsilon_d\text{-}E_f)$ (eV)	–1.74	–1.94	–2.19	–1.91	–2.13	–1.91	–1.94
d-band width [b]	3.28	3.51	3.48	3.41	3.37	3.35	3.46

[a] d-band center of the occupied states of the first (top) layer of Pd(100)

[b] d-band width at half height for all states of the active site

Table 4-8. Calculated energies of molecular eigenstates of benzene in gas phase, adsorbed at the hollow(0) site on Pd(110) at medium and saturation coverage, *i.e.* p(4×2) and c(4×2) surface overlayers. Energies are related to the vacuum level. All orbitals are named in line with Mittendorfer and Hafner. [72]

		Hollow(0)	
Orbital	**Benzene gas**	**p(4×2)**	**c(4×2)**
$1e_{1g}$ (π)	– 6.0	-8.6	-8.3
$3e_{2g}$	– 8.0	-8.9	-8.7
$1a_{2u}$ (π)	– 8.8	-10.5	-10.3
$3e_{1u}$	– 10.0	-10.7	-10.6
$1b_{2u}$	– 10.6	-11.4	-11.3
$2b_{1u}$	– 11.0	-12.0	-11.9
$3a_{1g}$	– 12.6	-13.2	-13.1
$2e_{2g}$	– 14.6	-15.6	-15.4
$2e_{1u}$	– 18.3	-19.1	-18.9
$2a_{1g}$	– 21.1	-21.6	-21.4

For benzene on Pd(110), Treboux and Aono[29] demonstrated that each possible high-symmetry adsorption site as well as the molecular orientation with respect to the surface plane can be resolved using STM imaging. In Yoshinobu's STM images28 at saturation coverage, each adsorbed benzene exhibits approximately a round shape at high bias voltages (±1.00 V), while at low bias voltages (±0.05 V) two elongated protrusions separated by a single depression with its direction some 50°-60° from $[1\bar{1}0]$ appear. Figure 4-12 presents our calculated STM images in a plane parallel to the surface for selected potentials (ε) and for selected benzene orientations (ϕ). The middle panels for the hollow(15) clearly show two protrusions and a node-like depression at ε = +0.05 eV, while a round-like shape is calculated at higher bias voltages (ε = ±1.00 eV).

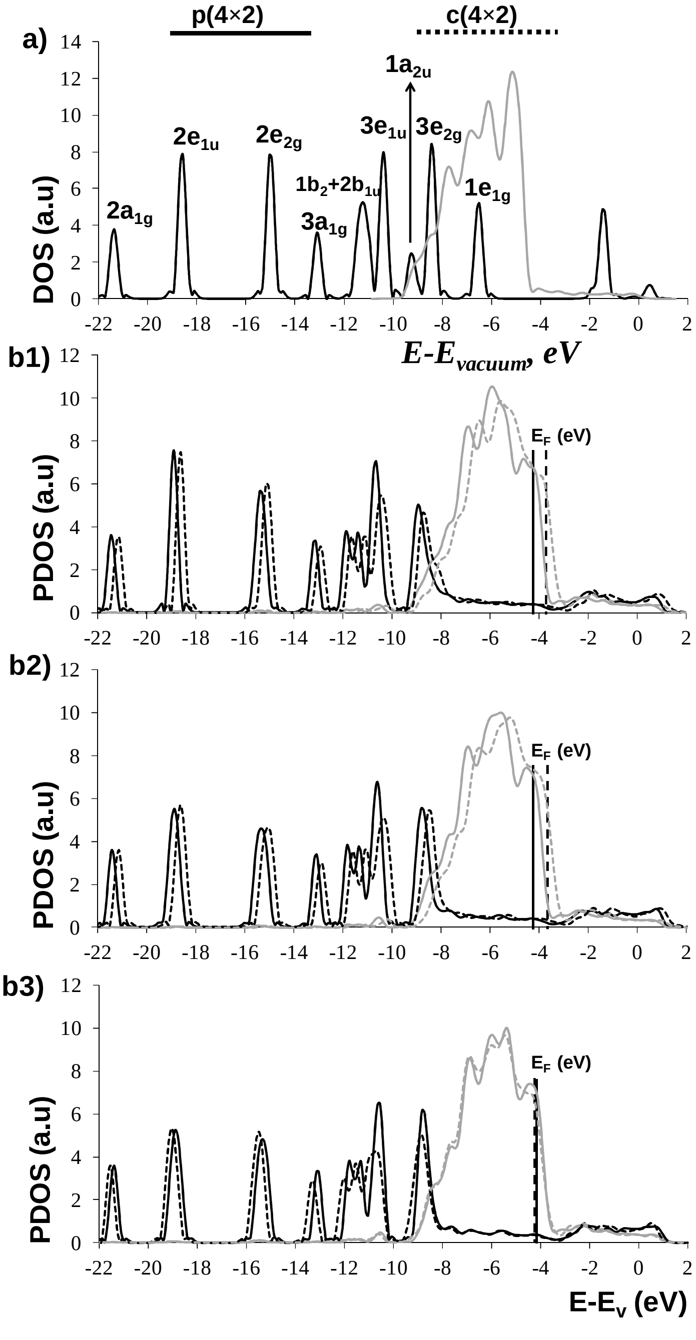

Figure 4-10. a) DOS of gas phase benzene (black) and DOS projected on the d states of the clean Pd(110) active site (grey). DOS projected on benzene (b1) hollow(0), (b2) hollow(15) and (c) hollow(30) adsorbates (black) and DOS projected on the d states of the covered active site (grey) at medium and saturation coverage, *i.e.* p(4×2) and c(4×2) surface overlayers with full and dotted lines respectively. All energies are relative to the vacuum level. All orbitals are named in line with Mittendorfer and Hafner. [72]

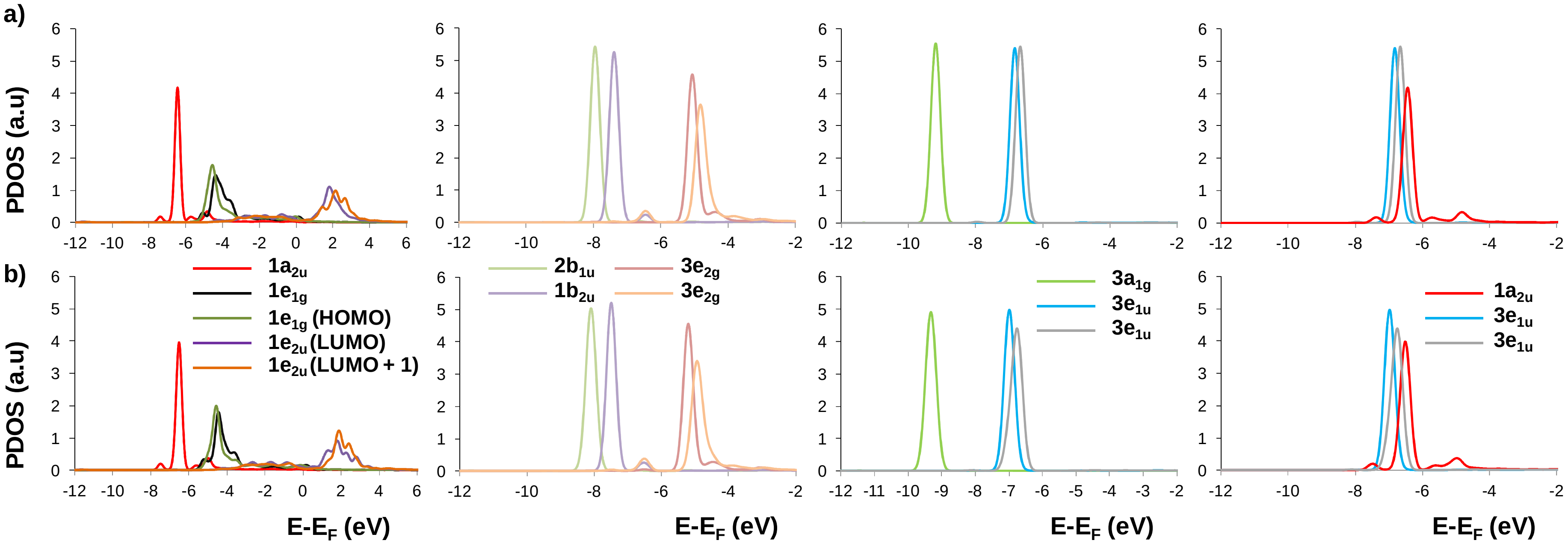

Figure 4-11. Projected DOS on selected molecular orbitals of gas-phase benzene for the hollow(0) adsorbate at (a) medium and (b) saturation coverage on Pd(110). All orbitals are named in line with Mittendorfer and Hafner.[72]

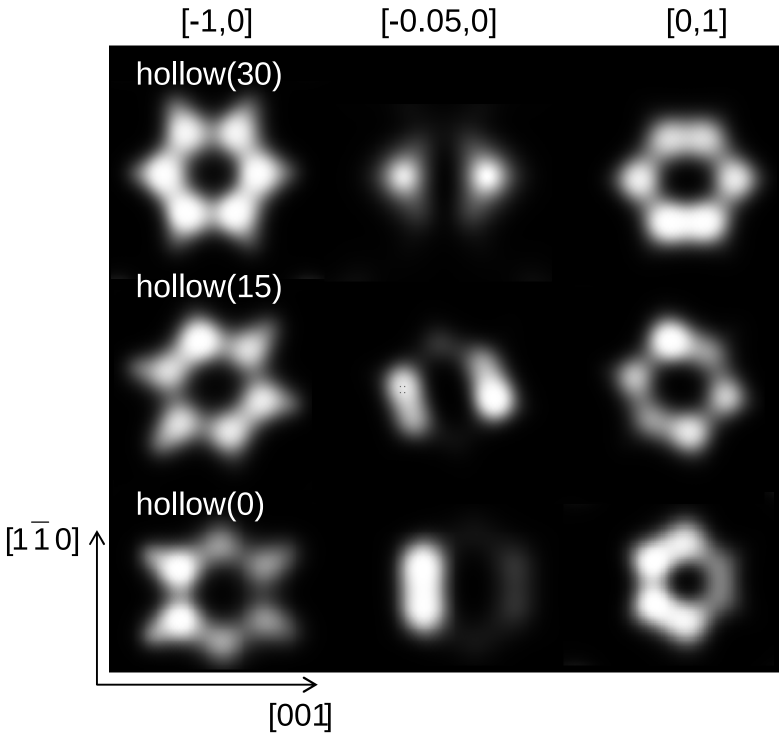

Figure 4-12. Constant current images on a horizontal plane at ~1 Å above the carbon atoms of benzene adsorbed on Pd(110) at saturation coverage for the hollow (30) (top), hollow(15) (middle) and hollow(0) (bottom) adsorbates at different potentials ε (in eV).

As discussed by Favot et al. [34], the features of the STM images can be rationalized based on the electronic structure. Near the Fermi level, the main contribution to the DOS stems from the $1e_{1g}$ derived states and the STM image reflects the symmetry of the $1e_{1g}$ orbital with the nodal plane at an angle of ~50° from the $[1\bar{1}0]$ direction. As the absolute value of the bias potential increases, the contribution of one of the LUMO derived e_{2u} states to the DOS becomes more important in the energy range $[E_F \pm 1$ eV, $E_F]$ resulting in the round-like shape of the STM image at higher bias voltages ($\varepsilon = \pm1.00$ eV).

In summary, our periodic DFT results show that at medium coverage on Pd(110) benzene equally prefers the three hollow sites. In the c(4 × 2) overlayer experimentally observed at saturation coverage we find a slight energetic preference of some 5-10 kJ mol^{-1} for the hollow(0) site relative to the hollow(15) and hollow(30) sites indicating a limited contribution of repulsive adsorbate-adsorbate interactions to the stability of benzene adsorbed on the Pd (110) surface. At the hollow(0) site two of the C-C bonds are parallel to the $[1\bar{1}0]$ direction and, although the molecule is tilted by 7° with respect to the Pd surface, the carbon ring remains flat with the C-H bonds tilted 17°-30° out of the plane of the ring. For the three hollow sites, the calculated electronic features are compatible with UPS experiments. The calculated vibrational features for the hollow(0) and hollow(15) are compatible with HREELS experiments, while this is not the case for the hollow(30). Hence, we suggest that on Pd(110) benzene does not populate hollow(30) sites at saturation coverage. Our calculated STM images confirm that STM can be used to resolve the molecular orientation with respect to the surface plane and that the experimentally observed two-lobed protrusion separated by a single depression oriented with its direction some 50° from $[1\bar{1}0]$ can only correspond to the hollow(15) adsorbate.

4.5 Conclusions

Periodic DFT calculations of benzene adsorbed on the Pd(100) and Pd(110) surfaces at half and saturation coverage have been used to evaluate the effect of coverage on the most stable adsorption sites. On both Pd(100) and Pd(110), four-fold hollow geometries are adopted by benzene, and the aromatic ring remains flat but the H atoms are tilted away from the surface. A much larger decrease in adsorption energies from medium to saturation coverage is calculated on Pd(100) compared to Pd(100). This is explained with shorter distances between neighbor molecules in Pd(100), which leads to stronger repulsive interactions. On Pd(100), a slight energetic preference is calculated at saturation coverage for the adsorbate with two C-C bonds parallel to the $[01\bar{1}]$ direction. However, an adsorption geometry with alternately two types of benzene adsorbates, rotated azimuthally by 30° relative to one another ($\phi_1 = 0°$; $\phi_2 = 30°$), cannot be discarded from the comparison of calculated vibrational and electronic features with UPS and HREELS experiments. On Pd(110), there is a slight energetic preference for the hollow(0) site compared to the hollow(15) and hollow(30). The hollow(0) adsorbate has two of the C–C bonds parallel to the $[1\bar{1}0]$ direction and, although the molecule is tilted by 7º with respect to the Pd (110) surface, the carbon ring remains flat with the C-H bonds tilted 17°-30° out of the plane of the ring. For the three hollow sites, the calculated electronic features are compatible with UPS experiments. For the hollow(30), calculated vibrational features are not compatible with HREELS experiments and we suggest that on Pd(110) benzene does not populate hollow(30) sites at saturation coverage. Calculated infrared spectra on both hollow(0) and hollow(15) sites are compatible with HREELS experimental observations, however, comparison between calculated and experimental STM images can only correspond to the hollow(15) adsorbate. Although, inclusion of non-local van der Waals interactions (optPBE-vdW functional) increase the absolute adsorption strengths the relative ordering of the various adsorption sites remains unaltered as compared to PW91.

4.6 References

1. A. C. Capleton and L. S. Levy, *Chem. Biol. Interact.*, 2005, **153**, 43-53.
2. J. D. Aiken and R. G. Finke, *J. Mol. Catal. A: Chem.*, 1999, **145**, 1-44.
3. S. S. Cheong, J. D. Watt and R. D. Tilley, *Nanoscale*, 2010, **2**, 2045-2053.
4. H. Choo, B. L. He, K. Y. Liew, H. F. Liu and J. L. Li, *J. Mol. Catal. A: Chem.*, 2006, **244**, 217-228.
5. X. Y. Ma, Y. Y. Chai, D. G. Evans, D. Q. Li and J. T. Feng, *J. Phys. Chem. C*, 2011, **115**, 8693-8701.
6. M. Boudart, *Adv. Catal.*, 1969, **20**, 153-166.
7. J. M. Nadgeri, M. M. Telkar and C. V. Rode, *Catal. Commun.*, 2008, **9**, 441-446.
8. P. W. Selwood, S. Adler and T. R. Phillips, *J. Am. Chem. Soc.*, 1955, **77**, 1462-1468.

9. G. A. Martin and J. A. Dalmon, *J. Catal.*, 1982, **75**, 233-242.
10. M. Englisch, A. Jentys and J. A. Lercher, *J. Catal.*, 1997, **166**, 25-35.
11. L. Ortiz-Soto, J. Monnier and M. Amiridis, *Catal. Lett.*, 2006, **107**, 13-17.
12. H. Ohtani, B. E. Bent, C. M. Mate, M. A. Van Hove and G. A. Somorjai, *Appl. Surf. Sci.*, 1988, **33-4**, 254-260.
13. H. Ohtani, M. A. Van Hove and G. A. Somorjai, *J. Phys. Chem.*, 1988, **92**, 3974-3982.
14. F. P. Netzer, G. Rangelov, G. Rosina, H. B. Saalfeld, M. Neumann and D. R. Lloyd, *Phys. Rev. B: Condens. Matter Mater. Phys.*, 1988, **37**, 10399-10402.
15. M. Fujisawa, T. Sekitani, Y. Morikawa and M. Nishijima, *J. Phys. Chem.*, 1991, **95**, 7415-7422.
16. A. Barbieri, M. A. Van Hove and G. A. Somorjai, *Surf. Sci.*, 1994, **306**, 261-268.
17. J. Yoshinobu, H. Tanaka, T. Kawai and M. Kawai, *Phys. Rev. B: Condens. Matter Mater. Phys.*, 1996, **53**, 7492-7495.
18. G. Hamm, T. Schmidt, J. Breitbach, D. Franke, C. Becker and K. Wandelt, *Surf. Sci.*, 2004, **562**, 170–182.
19. H. Hoffmann, F. Zaera, R. M. Ormerod, R. M. Lambert, L. P. Wang and W. T. Tysoe, *Surf. Sci.*, 1990, **232**, 259-265.
20. R. M. Lambert, A. F. Lee, K. Wilson, A. Goldoni, A. Baraldi and G. Paolucci, *J Phys Chem B*, 2000, **104**, 11729-11733.
21. G. D. Waddill and L. L. Kesmodel, *Phys. Rev. B: Condens. Matter Mater. Phys.*, 1985, **31**, 4940-4946.
22. W. T. Tysoe, R. M. Ormerod, R. M. Lambert, G. Zgrablich and A. Ramirez-Cuesta, *J. Phys. Chem.*, 1993, **97**, 3365-3370.
23. J. Zhou, S. Dag, S. D. Senanayake, B. C. Hathorn, et al., *Phys. Rev. B: Condens. Matter Mater. Phys.*, 2006, **74**, 125318.
24. L. L. Kesmodel, *Phys. Rev. Lett.*, 1984, **53**, 1001-1004.
25. V. H. Grassian and E. L. Muetterties, *J. Phys. Chem.*, 1987, **91**, 389-396.
26. J. F. M. Aarts and N. R. M. Sassen, *Surf. Sci.*, 1989, **214**, 257-275.
27. M. Nishijima, M. Fujisawa, T. Takaoka and T. Sekitani, *Surf. Sci.*, 1993, **283**, 121-125.
28. J. Yoshinobu, M. Kawai, I. Imamura, F. Marumo, et al., *Phys. Rev. Lett.*, 1997, **79**, 3942-3945.
29. G. Treboux and M. Aono, *J. Phys. Chem. B*, 1997, **101**, 4620-4622.
30. G. L. Nyberg and N. V. Richardson, *Surf. Sci.*, 1979, **85**, 335-352.
31. P. Hofmann, K. Horn and A. M. Bradshaw, *Surf. Sci.*, 1981, **105**, L260-L264.
32. J. Yoshinobu, M. Kawai, I. Imamura, F. Marumo, et al., *J. Electron. Spectrosc. Relat. Phenom.*, 1998, **88**, 997-1002.
33. J. R. Lomas and G. Pacchioni, *Surf. Sci.*, 1996, **365**, 297-309.
34. F. Favot, A. Dal Corso and A. Baldereschi, *Europhys. Lett.*, 2000, **52**, 698-704.

35. M. C. T. D. M. Cruz, J. W. D. M. Carneiro, D. A. G. Aranda and M. Buhl, *J. Phys. Chem. C*, 2007, **111**, 11068-11076.

36. S. J. Jenkins, *Proc. R. Soc. Lond. A. Math. Phys. Sci.*, 2009, **465**, 2949-2976.

37. X. A. Li, M. S. M. Wong and K. H. Lim, *Theor. Chem. Acc.*, 2010, **127**, 401-409.

38. D. R. Lloyd, C. M. Quinn and N. V. Richardson, *Solid State Commun.*, 1977, **23**, 141-145.

39. W. Huber, M. Weinelt, P. Zebisch and H. P. Steinruck, *Surf. Sci.*, 1991, **253**, 72-98.

40. B. Hammer and J. K. Norskov, *Adv. Catal.*, 2000, **45**, 71-129.

41. G. Kresse and J. Hafner, *Phys. Rev. B: Condens. Matter Mater. Phys.*, 1994, **49**, 14251-14269.

42. G. Kresse, *J. Non-Cryst. Solids*, 1995, **193**, 222-229.

43. G. Kresse and J. Furthmuller, *Comput. Mater. Sci.*, 1996, **6**, 15-50.

44. G. Kresse and J. Furthmuller, *Phys. Rev. B: Condens. Matter Mater. Phys.*, 1996, **54**, 11169-11186.

45. P. E. Blochl, *Phys. Rev. B: Condens. Matter Mater. Phys.*, 1994, **50**, 17953-17979.

46. G. Kresse and D. Joubert, *Phys. Rev. B: Condens. Matter Mater. Phys.*, 1999, **59**, 1758-1775.

47. J. P. Perdew, J. A. Chevary, S. H. Vosko, K. A. Jackson, et al., *Phys. Rev. B: Condens. Matter Mater. Phys.*, 1992, **46**, 6671-6687.

48. J. P. Perdew, J. A. Chevary, S. H. Vosko, K. A. Jackson, et al., *Phys. Rev. B: Condens. Matter Mater. Phys.*, 1993, **48**, 4978-4978.

49. H. J. Monkhorst and J. D. Pack, *Phys. Rev. B: Condens. Matter Mater. Phys.*, 1976, **13**, 5188-5192.

50. J. Klimeš, D. R. Bowler and A. Michaelides, *J. Phys.: Condens. Matter*, 2010, **22**, 022201.

51. M. Mura, A. Gulans, T. Thonhauser and L. Kantorovich, *Phys. Chem. Chem. Phys.*, 2010, **12**, 4759-4767.

52. P. Lazic, N. Atodiresei, M. Alaei, V. Caciuc, S. Blugel and R. Brako, *Comput. Phys. Commun.*, 2010, **181**, 371-379.

53. P. Sony, P. Puschnig, D. Nabok and C. Ambrosch-Draxl, *Phys. Rev. Lett.*, 2007, **99**, 176401.

54. E. R. McNellis, J. Meyer and K. Reuter, *Phys. Rev. B: Condens. Matter Mater. Phys.*, 2009, **80**, 205414.

55. K. Toyoda, Y. Nakano, I. Hamada, K. Lee, S. Yanagisawa and Y. Morikawa, *Surf. Sci.*, 2009, **603**, 2912-2922.

56. J. Wellendorff, A. Kelkkanen, J. J. Mortensen, B. I. Lundqvist and T. Bligaard, *Top. Catal.*, 2010, **53**, 378-383.

57. G. Mercurio, E. R. McNellis, I. Martin, S. Hagen, et al., *Phys. Rev. Lett.*, 2010, **104**, 036102.

58. K. Tonigold and A. Gross, *J. Chem. Phys.*, 2010, **132**, 224701.

59. G. Roman-Perez and J. M. Soler, *Phys. Rev. Lett.*, 2009, **103**, 096102.
60. H. Rydberg, B. I. Lundqvist, D. C. Langreth and M. Dion, *Phys. Rev. B: Condens. Matter Mater. Phys.*, 2000, **62**, 6997-7006.
61. M. Dion, H. Rydberg, E. Schroder, D. C. Langreth and B. I. Lundqvist, *Phys. Rev. Lett.*, 2004, **92**, 246401.
62. J. Klimeš, D. R. Bowler and A. Michaelides, *Phys. Rev. B: Condens. Matter Mater. Phys.*, 2011, **83**, 195131.
63. H. Yildirim, T. Greber and A. Kara, *J. Phys. Chem. C*, 2013, **117**, 20572-20583.
64. J. Carrasco, W. Liu, A. Michaelides and A. Tkatchenko, *J. Chem. Phys.*, 2014, **140**, 084704.
65. S. R. Bahn and K. W. Jacobsen, *Comput. Sci. Eng.*, 2002, **4**, 56-66.
66. D. Porezag and M. R. Pederson, *Phys. Rev. B: Condens. Matter Mater. Phys.*, 1996, **54**, 7830-7836.
67. J. J. Mortensen, L. B. Hansen and K. W. Jacobsen, *Phys. Rev. B: Condens. Matter Mater. Phys.*, 2005, **71**, 035109.
68. J. Enkovaara, C. Rostgaard, J. J. Mortensen, J. Chen, et al., *J. Phys.: Condens. Matter*, 2010, **22**, 253202.
69. N. Lorente, M. F. G. Hedouin, R. E. Palmer and M. Persson, *Phys. Rev. B: Condens. Matter Mater. Phys.*, 2003, **68**, 155401.
70. J. Tersoff and D. R. Hamann, *Phys. Rev. B: Condens. Matter Mater. Phys.*, 1985, **31**, 805-813.
71. H. Orita and N. Itoh, *Appl. Catal., A*, 2004, **258**, 17-23.
72. F. Mittendorfer and J. Hafner, *Surf. Sci.*, 2001, **472**, 133-153.
73. T. M. Gentle and E. L. Muetterties, *J. Phys. Chem.*, 1983, **87**, 2469-2472.
74. J. E. Demuth and D. E. Eastman, *Phys. Rev. Lett.*, 1974, **32**, 1123-1127.
75. M. Neuber, F. Schneider, C. Zubragel and M. Neumann, *J. Phys. Chem.*, 1995, **99**, 9160-9168.
76. K. H. Frank, P. Yannoulis, R. Dudde and E. E. Koch, *J. Chem. Phys.*, 1988, **89**, 7569-7576.
77. F. P. Netzer and K. H. Frank, *Phys. Rev. B: Condens. Matter Mater. Phys.*, 1989, **40**, 5223-5226.
78. P. Sautet and M. L. Bocquet, *Phys. Rev. B: Condens. Matter Mater. Phys.*, 1996, **53**, 4910-4925.

Chapter 5

First principles based design of bimetallic catalysts for benzene hydrogenation

Abstract

Periodic density functional theory (DFT) has been used to study benzene adsorption and hydrogenation on Pd_3M and Ni_3M bimetallic catalysts, aiming to develop predictive models to rationally design optimal catalysts as a function of the conditions. The most stable segregation state of the bimetallic alloys has been evaluated for the clean surface and also in the presence of benzene adsorbed. For the whole range of catalysts studied, benzene adsorption energy of the most stable site correlates well to the adsorption energy of atomic carbon. The adsorption energy of benzene can also be related to the center of the occupied d-band of all surface atoms: benzene adsorption gets stronger for increasing energy of the d-band center (closer to the Fermi level). Furthermore, reactivity trends for benzene hydrogenation are proposed from the calculated activation barrier for the first hydrogenation step. This barrier correlate quantitatively to the adsorption energy of benzene. The obtained correlations are implemented in a kinetic model to predict performances as a function of the catalyst and the conditions. A maximum in benzene hydrogenation activity is predicted at typical lab scale hydrogenation conditions ($400 \text{ K} < T < 500 \text{ K}$, $p_B = 6.7 \times 10^{-2}$ bar, $p_{H2} = 0.9$ bar) for alloys that adsorb benzene more strongly than on Pd(111), by up to –20 kJ mol^{-1}, e.g. Ni_3Ru and Ni_3Os.

5.1 Introduction

The chemical industry always strives to improve catalysts and develop new ones with novel catalytic properties. Improved catalysts can e.g. require milder reaction conditions to achieve the same conversion as common catalysts,[1] which can reduce costs for installation and operation to a large extent. Using more active catalysts can also allow to decrease the large amount of expensive metals that is required in large industrial reactors, such as for hydrotreating oil fractions for which Pd and the cheaper Ni metals are commonly used. The combination of different metals into bimetallic catalysts can lead to more active yet less expensive catalysts. These can have specific properties that can be tuned by several synthesis techniques.[2, 3] For many reactions, bimetallic catalysts exceed the performance that is achieved with the parent monometallic catalysts,[4, 5] such as oxygen reduction[4] or catalytic hydrogenation.[6] The catalytic hydrogenation of benzene is an important reaction in the refining and petrochemical industry,[7] as well as for the design of environmentally protective technologies, because of the carcinogenic nature of benzene [8]. Transition metals of group 10, such as Pd and Ni, are commonly used in industry to saturate aromatic molecules [7]. Therefore, this work aims to rationally search for Pd_3M and Ni_3M bimetallic alloys for benzene hydrogenation, by implementing in a kinetic model catalysts descriptors that are obtained with periodic density functional theory (DFT).

Benzene hydrogenation has been studied on a large number of bimetallic catalysts based on metals that are highly active for hydrogenation, such as Ni, [9-11] Pd [6, 12-19] and Pt.[11, 20, 21] Most of these studies show that the bimetallic alloys yield higher activities than the monometallic catalysts,[11, 13, 19, 22, 23] e.g. Pt-Pd,[6, 12-14] Pt-Co,[11] Pd-Cr ,[24] and Pd-W.[24] Two main factors contribute to the difference in activity from monometallic to bimetallic catalysts, and also from one alloy to the next, namely, electronic and geometric effects.[25] The electronic effect is explained from the change in electronic structure of the alloy due to the coupling between electronic states of the different metals involved. In the second, the geometric effect, alloying induces a change in the lattice parameter of the bimetallic catalyst as compared to the monometallic ones leading to, for example, changes in the metal-metal bond lengths.[6] Also, ensemble effects are typically contained within the geometric effect: the adsorbate can require an ensemble of a certain metal of minimal size in order to adsorb on the alloy.

Despite the high activity of Ni and Pd catalysts, these are easily poisoned by small amounts of sulfur compounds leading to their deactivation. Pd is already considered more sulfur tolerant than other transition metals,[7, 15, 24, 26-29] and alloying Pd with other metals can even further enhance its sulfur resistance. [7, 14, 16, 17, 30, 31] Particularly, excellent sulfur resistance has been reported for supported Pt-Pd catalysts, [7, 14, 16, 17, 31] which is attributed to the alloying effects, the metal particle size or acidic supports.[14] The optimal molar Pd:Pt composition ratio of 4:1 was observed to yield the best performance for the hydrogenation of tetralin in the presence of benzothiophene [32], and of 10:3 for the hydrogenation of phenanthrene.[30]

The evaluation of bimetallic catalysts should account for the phenomenon in which metallic atoms in alloys often spontaneously segregate from each other. Surface segregation behavior may be explained from a compromise between atomic radii, surface energy, electronegativity, and cohesive energy. [33] The segregated surfaces differ from the bulk composition, and this can enhance or hinder chemical reactions. [34] The most stable segregation state is a function of the conditions: the segregation preference for the clean surface can also reverse upon adsorption of some molecules, as it has been reported for oxygen adsorption on Pt-based bimetallic surfaces [35-37] and Cl on Pt- and Pd-based catalysts.[38] Surface segregation can be easily predicted with theoretical methods such as DFT, [34, 36, 38, 39] which can also allow to understand the mechanism and segregation trends that are often not completely understood from experiments.[36]

The experimental design of catalysts for industrial reactions is typically performed using time consuming and cost-intensive trial-and-error techniques, although knowledge-based experimental approaches have also been performed combining high throughput experiments with microkinetic modeling.[40] Theoretical methods, such as DFT, are extremely useful to understand the chemistry of catalytic reactions and, hence, to perform a rational design of optimal catalysts by screening the behavior of different materials.[41-46] Extensive interest has been focused on bimetallic catalysts because of the large number of possible combinations, which can be tuned to obtain catalysts with specific properties. [5] For bimetallic surfaces with the same crystallographic structure, e.g. the (111) surface plane, the effect of alloying should be attributed to variations in the electronic structure, and particularly in the d-band for transition metal alloys. The average energy of the electrons in the occupied d states, described by the occupied d-band center (ε_d), has shown in previous works to be a good descriptor of bond energies on different mono and bimetallic surfaces.[41, 46-50] A higher energy of the ε_d (closer to the Fermi level) is usually related to stronger metal-adsorbate bonds, because the higher ε_d the lower the occupation of antibonding states that are formed upon adsorption.[25]

Adsorption plays an important role in most catalytic reactions, for which optimal catalysts must facilitate both adsorption and reaction steps. Following the Sabatier principle, too strong adsorption can yield a completely blocked surface, without free sites for reaction. Too weak binding, however, leads to desorption of surface species before the reaction takes place. Therefore, a maximum in reactivity can be expected for catalysts that bind neither too strong nor too weak. To evaluate the performance of catalysts for benzene hydrogenation, the adsorption of the reactant benzene can be used to predict reactivity trends, similar to work performed on ammonia synthesis.[51]

In this work, catalysts for benzene hydrogenation are evaluated by screening bimetallic surfaces based on Pd(111) and Ni(111) combined with most 3d, 4d and 5d transition metals. The observed trends in adsorption strength and reactivity are quantitatively related to appropriate catalyst descriptors, e.g., carbon and benzene adsorption energy or the occupied d-band center. Implementation of the catalyst descriptors in a microkinetic model previously obtained for benzene hydrogenation on Pd(111) may allow assessing performances exhibited by virtual candidate catalysts by simulations for a broad range of catalyst descriptor values and operating conditions. The developed modeling tools also allow to predict maximum in hydrogenation activity as a function of both the catalyst descriptor and the reaction conditions.

5.2 Methodology

5.2.1 Electronic structure calculations

Electronic energies are calculated with the Vienna Ab Initio Simulation package (VASP),[52-55] which applies the projector augmented wave method (PAW).[56, 57] PAW uses pseudopotentials and plane-wave basis sets, with a cutoff energy of 400 eV. The generalized gradient Perdew-Wang PW91 functional is used to describe the exchange-correlation functional.[58, 59] The first-order Methfessel-Paxton method is employed to describe the partial electronic occupancies close to the Fermi level, with a smearing width of 0.3 and 0.1 eV for Pd_3M and Ni_3M alloys, respectively, which yield good convergence for the benzene adsorption energy on Pd(111) and Ni(111). A 5×5×1 Monkhorst-Pack [60] grid is used for the Brillouin-zone integration. Spin-polarized calculations are performed for those alloys with non-zero magnetization in the bulk, namely the Pd_3M with M=V, Cr, Mn, Fe, Co, Ni, Mo, Tc, and Re, in line with a previous study,[61] and the Ni_3M with M= Co, Ru, Rh, Pd, Re, and Pt.

The convergence criteria to obtain accurate geometries and electronic energies amounts to 10^{-8} eV on the energy for the electronic minimization, and 0.05 eV/Å for the maximum force for the geometry convergence, for which the *quasi-Newton RMM-DIIS algorithm* is applied. The activation barrier for the hydrogenation of benzene to monohydrobenzene is calculated as follows: first, the transition state is obtained coarsely by calculating the minimum energy path in the potential energy surface between reactants and products with the Nudged Elastic Band method.[62] This method creates a series of images along the reaction path, and these images are optimized by force minimization. In a second step, the image that corresponds to the saddle point in the minimum energy path is further optimized with the Dimer method.[63]

The d-band center of the occupied states of the surface layer atoms ε_d has been calculated to describe trends from one alloy to the next. This parameter is calculated by projecting the plane waves calculated by VASP onto spherical harmonic orbitals centered on the surface atoms, for both α and β spin electrons, using the Wigner-Seitz radii from PAW potentials. The ε_d is defined relative to the Fermi level (E_f), the highest occupied state, as shown in eq. (1)

$$\varepsilon_d = \frac{\int_{-\infty}^{Ef} E\rho_d(E)dE}{\int_{-\infty}^{Ef} \rho_d(E)dE} \tag{1}$$

With ρ_d being the density of states projected onto the d-orbitals of the surface atoms. To take into account only the occupied states of the system, the *d*-band is integrated up to the Fermi level.

5.2.2 Modeling the catalytic surface

The bimetallic catalysts have been evaluated using the X_3M bulk composition with fcc crystal structure (Cu_3Au-type), as it has been previously used for Pt- and Pd-based alloys.[4, 36, 38, 39, 64-68] The calculated bulk lattice parameters are within 1 % of those reported by Pasti et al. [38] and Lamas et al.[69] for the Pd_3M catalysts with M = Pt, Co, Ni, Rh and Fe. The (2×2) unit cell is used to evaluate the different segregation states for clean surfaces, and also the adsorption of atomic carbon. The adsorption of benzene in this unit cell, however, leads to coverages above saturation coverage on Pd(111), for which adsorption is no longer thermodynamically favorable.[70] Therefore, a (4×4) unit cell is used for benzene adsorption, which still possesses the X_3Y composition, and which models benzene at low to medium benzene coverage (37 % of the saturation coverage). The (111) surface is considered for the whole range of alloys because it is the most stable and, hence, typically the most abundant on metal nanoparticles. [71] The slab thickness is evaluated using a four-layer unit cell. The two top layers are relaxed during the geometry optimization, together with the adsorbates. The two bottom layers are not optimized and remain in the bulk structure. The unit cell is repeated in the three directions to model infinite surfaces, and periodic boundary conditions are used. In the direction perpendicular to the surface, a vacuum layer of 11 Å and an artificial dipole layer have been used to avoid interactions between periodic images.

Segregation consists of the motion of a solute atom from the bulk to the surface of the host metal, and antisegregation is defined as the motion of the solute atom from the surface to the bulk.[45] The most stable segregation structure of the surface of every alloy is evaluated exchanging the position of host and solute atoms, starting from the optimized (non-segregated) ideal bulk structures, to obtain the corresponding segregation state. The state with the lowest energy is considered to be preferred for the clean slab. The segregation energy

$\Delta E_{el,seg}$ is defined as the difference between the energy of the (2×2) unit cell with the segregated structure ($E_{el,segregated}$) and that with the non-segregated X_3M bulk state composition ($E_{el,X3M}$), with X being Pd or Ni and M the transition metals, see eq. (2). Similarly, the antisegregation energy $\Delta E_{el,antiseg}$ is the difference between the energy of the (2×2) unit cell with antisegregated structure ($E_{el,antisegregated}$) and that with the non-segregated Pd_3M bulk state composition ($E_{el,Pd3M}$), see eq. (3).

$$\Delta E_{seg} = E_{el,segregated} - E_{el,X_3M} \tag{2}$$

$$\Delta E_{antiseg} = E_{el,antisegregated} - E_{el,X_3M} \tag{3}$$

Negative values of $\Delta E_{el,seg}$ and $\Delta E_{el,antiseg}$ correspond to those alloys for which the segregated or antisegregated states, respectively, are thermodynamically favored over the ideal bulk X_3M non-segregated composition. Positive values are related, therefore, to those alloys that are more stable with the ideal non-segregated X_3M structure.

5.2.3 Implementing catalysts descriptors in a microkinetic model

Evaluation of the full reaction network for benzene hydrogenation on all studied alloys is computationally too expensive. Therefore, this work has focused on the first hydrogenation step, as a first step, to predict changes in reactivity from one catalysts to the next. The reactivity trend can be related to a catalysts descriptor which captures the difference in activity between catalysts. Performances exhibited by virtual candidate catalysts can be predicted implementing this catalyst descriptor in a microkinetic model.

In a previous study, a detailed coverage-dependent microkinetic model has been constructed for benzene hydrogenation on Pd(111) based on DFT calculations using the optPBE-vdW functional. In that study, a dominant path was identified at low and high surface coverage, consisting of the hydrogenation of carbon atoms in the ortho position relative to the previously hydrogenated carbon atom. Evaluation of the kinetic model for a range of conditions indicated that the overall rate was most sensitive to the second hydrogenation step and, hence, the second step was proposed to be the rate determining step on Pd(111).

This work has adapted this microkinetic model determined on Pd(111) to implement a catalyst descriptor (*D*) to predict changes in reactivity relative to Pd(111). The change in the catalysts descriptor from catalyst to catalyst is expressed relative to the value calculated on Pd(111), i.e., $\Delta\Delta D = (\Delta D_{\mathrm{X3M}} - \Delta D_{\mathrm{Pd(111)}})$, and similarly for the hydrogen adsorption enthalpy and activation energy.

For application in this paper, the kinetic model constructed for Pd(111) is simplified assuming the second hydrogenation step to be the rate determining step (RDS). The kinetic and thermodynamic parameters are expressed relative to the values obtained on Pd(111) with the optPBE-vdW functional, e.g. for benzene adsorption energy $\Delta E_{ads,B,X3M} = \Delta E_{ads.B,\mathrm{Pd(111),optPBE}} + \Delta\Delta E_{\mathrm{ads.}B}$. In order to do so, following assumptions are made: i) the relative change in adsorption energy from catalyst to catalyst is the same for the PW91 and the optPBE-vdW functional, ii) the relative change in activation energy from catalyst to catalyst is the same for the PW91 and the optPBE-vdW functional, and iii) the relative change in activation barrier from catalyst to catalyst is the same for the first and second hydrogenation. The latter assumption needs be made since the dependence of the activation energy on the catalyst is derived for the first hydrogenation step, and this model considers the second hydrogenation step as rate-determining.

From these assumptions, the turnover frequency for benzene hydrogenation (TOF in s^{-1}) is, assuming the rate determining step model with the 2^{nd} hydrogenation step as rate determining:

$$TOF = \frac{k_{2,\,forward} K_1 K_B p_B K_{H2} p_{H2}}{\left(1 + K_B p_B + \sqrt{K_{H2} p_{H2}}\right)^2} \left(1 - \frac{p_{CHA}}{K_{gas} p_B p_{H2}^3}\right) \quad (4)$$

In this equation, p_{CHA}, p_B and p_{H2} are the pressures of cyclohexane, benzene and hydrogen in bar, $k_{2,forward}$ is the forward rate coefficient for the second reaction, K_1 is the equilibrium coefficient of the first hydrogenation step, and K_B and K_{H2} are the equilibrium coefficient for benzene and hydrogen adsorption. The latter are calculated assuming the same adsorption entropy as on Pd(111), see all values in Table D7 in Appendix D. Changes in the adsorption enthalpy relative to Pd(111) are determined as:

$$K_B = \exp\left(\frac{\Delta S_{ads,B,Pd(111)}}{R}\right) \cdot \exp\left(\frac{-(\Delta H_{ads,B,Pd(111)} + \Delta\Delta E_{ads,B}}{RT}\right) \tag{5}$$

$$K_{H2} = \exp\left(\frac{\Delta S_{ads,H2,Pd(111)}}{R}\right) \cdot \exp\left(\frac{-(\Delta H_{ads,H2,Pd(111)} + \gamma \cdot \Delta\Delta E_{ads,B}}{RT}\right) \tag{6}$$

The adsorption parameters on Pd(111) are obtained by solving the coverage-dependent microkinetic model in a differentially operated reactor at T = 450 K, W/F_B^0 = 62.5 kg_{cat} s mol^{-1}, F_B^0=2.1 × 10^{-5} mol s^{-1}, F_{H2}^0 = 2.8 × 10^{-4} mol s^{-1}, p_B^0 = 6.7 × 10^{-2} bar, p_{H2}^0 = 0.9 bar, which results in a coverage of occupied sites of $\theta_{\text{occ}} = 1 - \theta_{\text{free}} = 0.82$.

Imposing a change on the benzene and hydrogen adsorption energy without changing any other parameter will change the gas phase reaction enthalpy; therefore it is clear that, if the benzene adsorption becomes more exothermic, either the hydrogenation steps or the desorption of cyclohexane should become more endothermic. In order to account for this, the equilibrium coefficients of six surface reactions needs to be adapted regarding the change in hydrogen and benzene adsorption energy, as illustrated in Figure D6 in Appendix D. For the rate determining step model used in this work, the equilibrium coefficient for the first hydrogenation is calculated as shown in eq. (7):

$$K_1 = K_{1,Pd(111)} \exp\left(\frac{-\left(-\Delta\Delta E_{ads,B} \middle/ 6 \right)}{RT} \right) \cdot \exp\left(\frac{-\left(-\Delta\Delta E_{ads,H2} \middle/ 2 \right)}{RT} \right) \tag{7}$$

Finally, the forward rate coefficient for the second hydrogenation step $k_{2,forward}$ is calculated as follows:

$$r_{2,\, forward} = A_{2,\, forward,Pd(111)} \exp\left(\frac{-\left(E_{a,Pd(111)} + m \cdot \Delta\Delta E_{ads,B} \right)}{RT} \right) \tag{8}$$

5.3 Results

Periodic DFT calculations are used to evaluate benzene hydrogenation on several bimetallic catalysts. First, the most stable segregation states of Pd_3M and Ni_3M bulk alloys are evaluated with and without benzene adsorbed. Secondly, the reactivity of selected alloys for the first hydrogenation step is related to appropriate catalyst descriptors. Finally, an optimal catalyst is identified introducing the catalyst descriptors into a microkinetic model that allows to predict performances for a broad range of values and reaction conditions.

5.3.1 Surface segregation

A large number of Pd_3M bimetallic alloys have been investigated, with M going from Ti to Ni in the 3d series, from Zr to Rh in the 4d series, and from Hf to Pt in the 5d series (see Figure 5-1-b1). First, the preferred segregation state of the clean surface is determined. Four different surface states have been evaluated (see Figure 5-1): i) non-segregated catalysts (blue in Figure 5-1a), which uniformly maintain the X_3Y bulk structure at every layer of the slab, ii) antisegregated catalysts (green), with surface enrichment in the host, e.g. leading in Pd_3M

alloys to a Pd/PdM/Pd_3M/Pd_3M four-layered slab structure, iii) segregated catalysts where solute atoms in the second layer diffuse to the surface, while third and fourth layer remain unaltered (red), i.e., partially segregated state, leading to the PdM/Pd/Ni_3M/Ni_3M slab or Pd_3M catalysts, and iv) segregated catalysts where solute atoms of each slab diffuse to the surface (orange in Figure 5-1a), i.e., fully segregated state, leading to the four-layered slab with M/Pd/Pd/Pd structure, as shown in Figure 5-1a. The most stable state of each Pd_3M and Ni_3M alloy is shown in Figure 5-1-b1, each with the corresponding color of the segregation state shown in Figure 5-1-a. The segregation energies are reported in Table D1 in Appendix D.

For Pd_3M alloys, the surfaces with M = Ti, Cr, Mn, Zr, Hf, and Pt do not segregate, possessing the Pd_3M bulk structure at every layer (see Figure 5-1-b1). The most positive segregation energy, i.e., for which the non-segregated structure is most stable compared to the (anti)segregated states, corresponds to Pd_3Hf, which is usually explained in terms of Hf having the largest atomic radius. The results for Ti, Cr, and Mn agree with results reported on Pt_3M alloys. [36] The Pd_3Pt surface shows an almost zero segregation and antisegregation energy, which is explained by the similar electronic structure of Pd and Pt metals. This leads to a small tendency of Pt atoms to segregate to the surface. Pd_3Pt is, therefore, represented with the non-segregated ideal bulk structure, in agreement with previous theoretical results, [36, 38, 39, 72] and experimental observations of Pd-enriched surfaces for Pt-Pd alloys.[73-75] For the other thirteen Pd_3M alloys, the antisegregated structure is most stable, in which Pd migrates to the surface (see Figure 5-1). The predominant antisegregation of Pd alloys can be explained as a compromise between a larger metallic radius [76] and a lower surface energy [77] of Pd as compared to the other metal atoms, as has been proposed for the behavior on Pt_3M surfaces.[36] Apart from the preference to have atoms with a lower surface energy at the surface, atoms with the larger metallic radius tend to segregate to the surface in order to reduce the strain they impose on the lattice if present in the subsurface layers [36]. The difference in surface energy [77] can explain the most negative antisegregation energy calculated for the Pd_3Re alloy (-240 kJ mol^{-1}). These results are in line with previous theoretical studies on several alloys [36, 38, 39, 72], and with experimental observations, such as those for Pt_3Ni [4]. In the latter study, they observed that the first layer is composed only of Pt, the second with 48% Pt, and the third layer being again with a majority of Pt atoms (87%), or the experimental study with X-ray diffraction spectra on Pd_3Fe, [78] and XPD experiments on Pd_3V [66]. Finally, none of the clean surfaces show neither partial or full segregation of the solute atoms to the surface, which is for Pt_3M alloys also only reported by Sabbe et al.[39] for Pt_3Ag and Pt_3Au alloys, which are not included in this study.

For Ni_3M, nine bimetallic alloys have also been evaluated with M = Cr, Co, Ru, Rh, Pd, Re, Os, Ir, and Pt. Due to the smaller radius [76] and higher surface energy [77] of Ni compared to Pd, which disfavor its presence at the surface, different segregation trends have been obtained for these alloys as compared to Pd_3M surfaces. First, none of the studied Ni-based alloys prefers the non-segregated state. Secondly, partially segregated surfaces are observed for M = Rh, Pd, Ir and Pt, as shown in Figure 5-1-b2 with red color. The alloys with partial segregation of M atoms to the surface lead to a slab with $NiM/Ni/Ni_3M/Ni_3M$ for the four layers, different to the fully segregated M/Ni/Ni/Ni structure (see Figure 5-1) that is least stable than the partially segregated state.

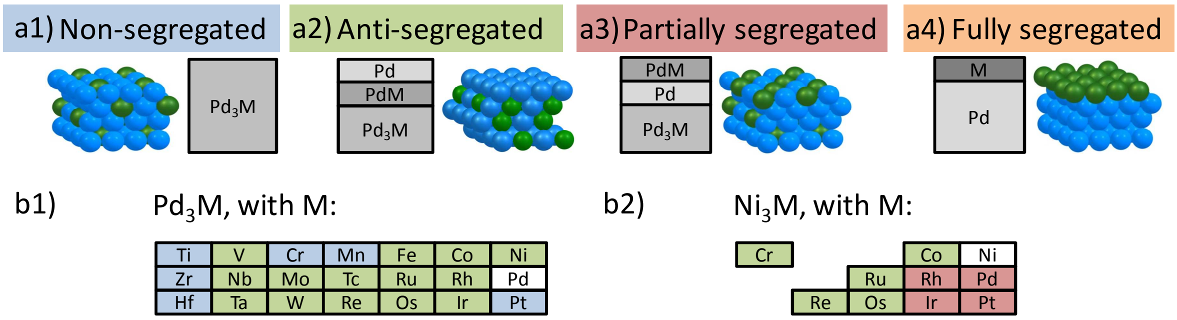

Figure 5-1: (a) The four evaluated segregation states, and the solute transitions metals (M) evaluated for (b1) Pd_3M and (b2) Ni_3M alloys, with the most stable segregation state indicated with the corresponding color from panel (a). Pd and Ni are shown in white in b1 and b2, respectively, for identification of their position in the periodic table.

5.3.2 Benzene adsorption on Pd_3M bulk alloys

The adsorption of benzene has been performed in a 4×4 unit cell. This adsorption corresponds to 9.2×10^{17} molecules m^{-2}, which is low regarding the saturation coverage of 2.5×10^{18} on Pd(111) (37 % of the saturation coverage). Screening benzene adsorption on several bimetallic catalysts is expected to provide useful insights that can be used to construct predictive models for catalyst design. Benzene can adsorb with multiple adsorption geometries on the various bimetallic surfaces. Therefore, only those with the same orientation as the most stable geometries on Pd(111), [70, 79, 80] namely bridge^{30} (bri) and hollow^{0} (hcp^{0} and fcc^{0}) sites, have been evaluated on the bimetallic surfaces. The nomenclature of every adsorption site in this work follows the one proposed previously by Sabbe et al. [39].

Non-segregated alloys. Seven adsorption geometries have been identified on non-segregated surfaces (see Figure 5-2). For hollow sites, the adsorption sites are named as the 3 metal atoms in the first layer bound to benzene, and for bridge sites the two metal atoms bound each to two carbon atoms, followed by the site geometry i.e., hcp^{0}, fcc^{0} or bri^{30}. For two bridge sites also the second-layer metal atom below the adsorbate is added in the nomenclature because the two first characteristics are the same, i.e., the Pd_2-bri^{30}-Pd and the Pd_2-bri^{30}-M.

The seven sites in Figure 5-2 have been evaluated on the Pd_3Pt and Pd_3Cr. The most stable sites on these two alloys, i.e., Pd_2-bri^{30}-Pd for Pd_3Pt and the PdM-bri^{30} for Pd_3Cr (see Table 5-1), have been further evaluated on the other non-segregated surfaces. Generally, the results show that bridge are more stable than hollow sites on both Pd_3Pt and Pd_3Cr catalysts, in line with Pd(111).[70] Similarly to Pd_3Cr, the PdM-bri^{30}-Pd site is the most stable site for the other non-segregated surfaces (see Table 5-1). Benzene bri$^{30°}$ binds by four di-σ-type and two π-type interactions to the surface, and the former is stronger than the latter [81]. The interaction of benzene with M atoms is weaker than with Pd atoms, expected from the adsorption energies in Table 5-1 as compared with the value on Pd(111) of –125 kJ mol^{-1}. Therefore, the PdM-bri^{30} site, which involves more di-σ-type interactions with Pd atoms, are more stable on all allows, except Pd3Pt, than the other adsorption sites, which have less di-σ-type interactions involving Pd atoms. For Pd_3Pt, a slightly weaker adsorption energy is obtained compared with Pd(111), which is expected from the similar electronic structures of Pt and Pd but still stronger Pd-C than Pt-C bonds.[79]

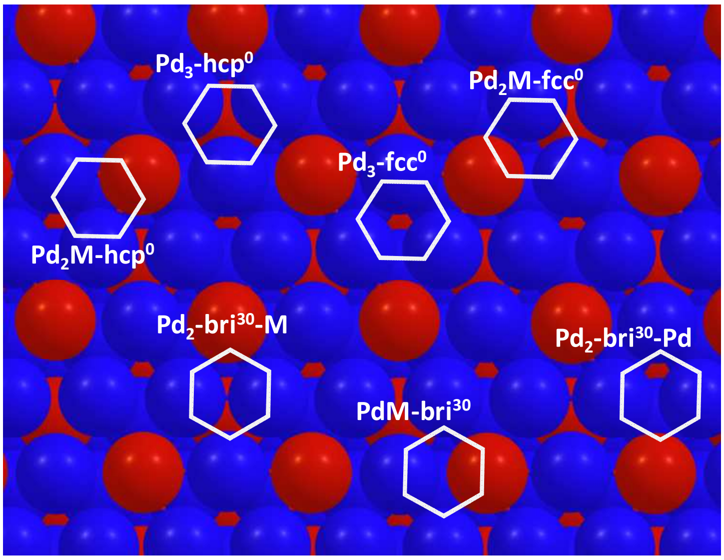

Figure 5-2: Adsorption sites of benzene on the surface evaluated for the non-segregated bulk Pd_3M alloys. Pd and M atoms are indicated in blue and red, respectively.

Table 5-1:Adsorption energies (kJ mol^{-1}) for the different adsorption sites of benzene on Pd_3Pt and Pd_3Cr non-segregated catalysts, and the values for the two most stable sites on other non-segregated alloys.

Sites	E_{ads} (kJ mol^{-1})					
	Pd_3Pt	Pd_3Cr	Pd_3Ti	Pd_3Mn	Pd_3Zr	Pd_3Hf
Pd_3-hcp^0	–79.5	–68.1	-	-	-	-
Pd_2M-hcp^0	–108.9	–67.5	-	-	-	-
Pd_3-fcc^0	–82.6	–65.5	-	-	-	-
Pd_2M-fcc^0	–102.8	–63.7	-	-	-	-
Pd_2-bri^{30}-Pd	–115.7	–62.8	–21.6	–57.1	–37.6	–9.2
Pd_2-bri^{30}-M	–104.2	–71.9	-	-	-	-
PdM-bri^{30}	–106.1	–84.7	–59.9	–72.3	–39.5	–39.9

Antisegregated alloys. The situation is more complex for antisegregated alloys due to the different composition and symmetry of the four atomic layers of the slab. Thirteen different adsorption sites are identified on the surface with brige^{30} and hollow^0 adsorption geometries, as illustrated in Figure 5-3. The hollow sites are identified by the site geometry (hcp^0 or fcc^0), followed for (i) hcp sites by the metal atom in the second layer and underlying structure of the third layer, and for (ii) fcc sites by the underlying structure of the second layer, and the metal atom found in the third layer below the adsorbate. Since bridge sites are combination of one hcp and another fcc sites, the seven bridge^{30} sites (see bri^{30} sites in Figure 5-3) are identified as site geometry *bri*^{30}, followed by the underlying structure of the third layer below the hcp site, and the underlying structure of the second layer below the fcc site, separated by a slash. Due to the large number of adsorption sites, the whole range has only been evaluated on Pd_3Rh (see Table 5-2), chosen because this alloys shows non-magnetic behavior and is computationally less demanding than magnetic alloys. The most stable site is further studied on the other antisegregated catalysts (see Table 5-3). The most stable site on Pd_3Rh does not have to correspond to the most stable on the other anti-segregated alloys, however, these results are expected to be accurate enough to express the changes in adsorption energy from one alloy to the next. On Pd_3Rh, the most stable site is the bri-M-Pd_2M^{30}/fcc-Pd_2M-M with an adsorption energy of –95.8 kJ mol^{-1} (see Table 5-2). This is closely followed with ~5 kJ mol^{-1}

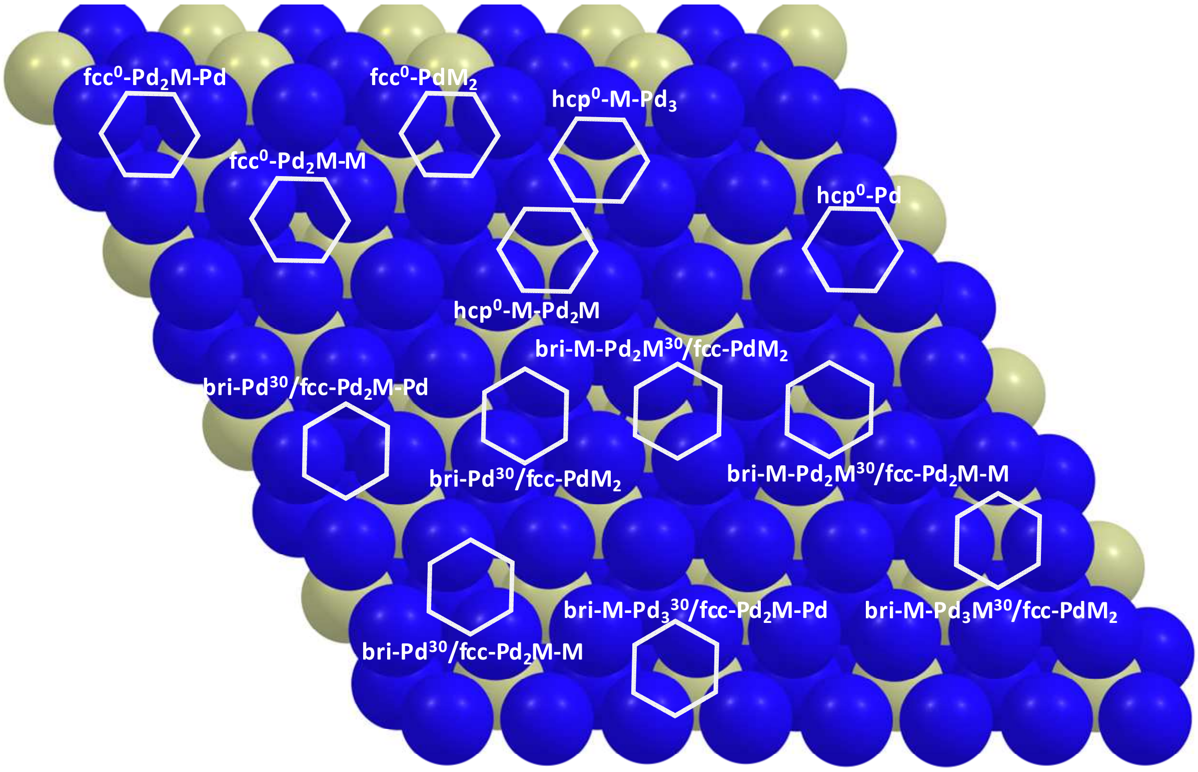

Figure 5-3: Possible adsorption sites for benzene on the surface of antisegregated bulk Pd_3M alloys. Pd and M atoms are indicated in blue and yellow, respectively.

Table 5-2: Adsorption energies (kJ mol^{-1}) for the different adsorption sites of benzene on the antisegregated Pd_3Rh alloy.

	$\Delta E_{ads,B}$ (kJ mol^{-1})
Adsorption sites	**Pd_3Rh**
hcp^0-M-Pd$_3$	–84.9
hcp^0-M-Pd$_2$M	–79.9
hcp^0-Pd	–86.5
fcc^0-Pd$_2$M-M	–84.6
fcc^0-Pd$_2$M-Pd	–76.8
fcc^0-PdM$_2$	–86.2
bri-M-Pd$_2$M^{30}/fcc-PdM$_2$	–91.6
bri-M-Pd$_3$M^{30}/fcc-PdM$_2$	–85.1
bri-M-Pd$_3$^{30}/fcc-Pd$_2$M-Pd	–91.9
bri-M-Pd$_2$M^{30}/fccPd$_2$M-M	–95.8
bri-Pd^{30}/fcc-Pd$_2$M-Pd	–94.9
bri-Pd^{30}/fcc-PdM$_2$	–93.7
bri-Pd^{30}/fcc-Pd$_2$M-M	–94.4

Table 5-3: Adsorption energy (kJ mol^{-1}) of benzene on the surface of several antisegregated catalysts. Values for the bri-M-Pd_2M^{30}/fccPd_2M-M site, which is the most stable site for benzene on Pd_3Rh.

Antisegregated alloys	$\Delta E_{ads,B}$ (kJ mol^{-1}) bri-M-Pd_2M^{30}/fccPd_2M-M
Pd_3V	–51.3
Pd_3Fe	–47.7
Pd_3Co	–59.4
Pd_3Ni	–74.8
Pd_3Nb	–37.9
Pd_3Mo	–44.0
Pd_3Tc	–63.4
Pd_3Ru	–76.7
Pd_3Rh	–95.8
Pd_3Ta	–25.5
Pd_3W	–35.3
Pd_3Re	–56.1
Pd_3Os	–47.7
Pd_3Ir	–93.4

by most of the other bridge^{30} adsorption sites, but the hollow sites are at least 10 kJ mol^{-1} less stable. The adsorption of benzene at the bri-M-Pd_2M^{30}/fcc-Pd_2M-M site on Pd_3Rh also leads to the strongest adsorption energy out of all antisegregated catalysts (see Table 5-3), closely followed by Pd_3Ir with 2.5 kJ mol^{-1} and by the other anti-segregated alloys with at least 20 kJ mol^{-1} weaker adsorption energies.

Segregation in the presence of benzene adsorbed. The most stable segregation state of a clean bimetallic surface has been reported to change upon adsorption of molecules such as O [35-37] or Cl [38]. Therefore, the segregation energy of the covered surfaces has also been calculated comparing the electronic energies of the unit cell with benzene adsorbed at the most stable site of each surfaces. This has only been evaluated for the alloys with segregation energies for the clean (2×2) unit cell surface below ~30 kJ mol^{-1}, namely Pd_3Mn and Pd_3Pt as shown in Table D1 in Appendix D. For the alloys with segregation energies larger than 30 kJ mol^{-1}, changes in the segregation state are not expected upon benzene adsorption. For non-segregated alloys, the adsorption of benzene on the Pd_3Mn further stabilizes this structure, while for Pd_3Pt the antisegregated state is only 3 kJ mol^{-1} more stable than the non-segregated surface with benzene adsorbed. Due to this small difference, the Pd_3Pt non-segregated surface is further considered. For none of the antisegregated alloys the segregation state is inverted upon benzene adsorption, as shown in Table D1 in Appendix D, in line to the results obtained for antisegregated Pt_3M alloys by Sabbe et al.[39]

5.3.3 Benzene adsorption on Ni3M bulk alloys

Antisegregated alloys. Only the bridge^{30} sites are evaluated on Ni_3M antisegregated alloys (M= Cr, Co, Ru, Re, and Os), because they proved to be more stable than the hollow sites on Pd_3M. The whole range of bridge^{30} sites has been evaluated on Ni_3Cr, see Figure 5-3 and Table 5-4. The most stable site is the bri-Pd^{30}/fcc-PdM_2 with an adsorption energy of –94.3 kJ mol^{-1}, different than the antisegregated Pd_3M alloys for which the most stable is the bri-M-Pd_2M^{30}/fcc-Pd_2M-M. On the other Ni_3M antisegregated surfaces, the adsorption energy of benzene at the bri-Pd^{30}/fcc-PdM_2 site is much stronger than on Ni_3Cr, particularly on Ni_3Ru and Ni_3Os, by more than 40 kJ mol^{-1}. Moreover, the adsorption energy on Ni_3Ru (see Table 5-4) is at least 45 kJ mol^{-1} stronger than the values obtained on Pd_3M antisegregated surfaces (see Table 5-2).

Partially segregated alloys. Four Ni_3M alloys show partial segregation of M atoms (Rh, Pd, Ir, and Pt) to the upper surface for the clean surface. Ten different adsorption sites are identified for benzene on this surface with hollow^{0} and bridge^{30} adsorption geometry (see Figure 5-4). The nomenclature of these sites follows that proposed for the previous surfaces. Hollow sites are defined by the three surface metal atoms bound to benzene, followed by the site geometry (hcp^{0} or fcc^{0}). Two fcc sites with the same site characteristics are also identified with the metal atom (M or Ni) in the third layer below the adsorbate. Bridge sites are identified by the two metal atoms bound to carbon atoms in π-type interactions, followed by *bri*, the metal found at the hcp site in the second layer, separated with a slash by *fcc*, and the metal atom below the fcc site in the third layer. The whole range of adsorption sites has been evaluated on Ni_3Pd, as listed in Table 5-5. The most stable adsorbate is the Ni_2-bri-Ni^{30}/fcc-Ni with an adsorption energy of –62.2 kJ mol^{-1}, closely followed by the structurally similar Ni_2-bri-Ni^{30}/fcc-M site, and by the other sites with at least 13 kJ mol^{-1} weaker adsorption energies.

Segregation in the presence of benzene adsorbed. Similarly as for Pd_3M, the antisegregated Ni_3M alloys remain more stable than with the other possible segregation states upon benzene adsorption. For the partially segregated Ni_3Ir and Ni_3Pt surfaces, benzene adsorption reverses the segregation tendency and the non-segregated are more stable than the partially segregated alloys (see the adsorption energy in Table 5-5, and the segregation energies for the clean surface and with benzene adsorbed in Table D1 in Appendix D). The stability is not inverted for the other two segregated surfaces, Ni_3Pd and Ni_3Rh, which can be explained by the stronger adsorption of benzene on Pd and Rh than on Ni. [82, 83]

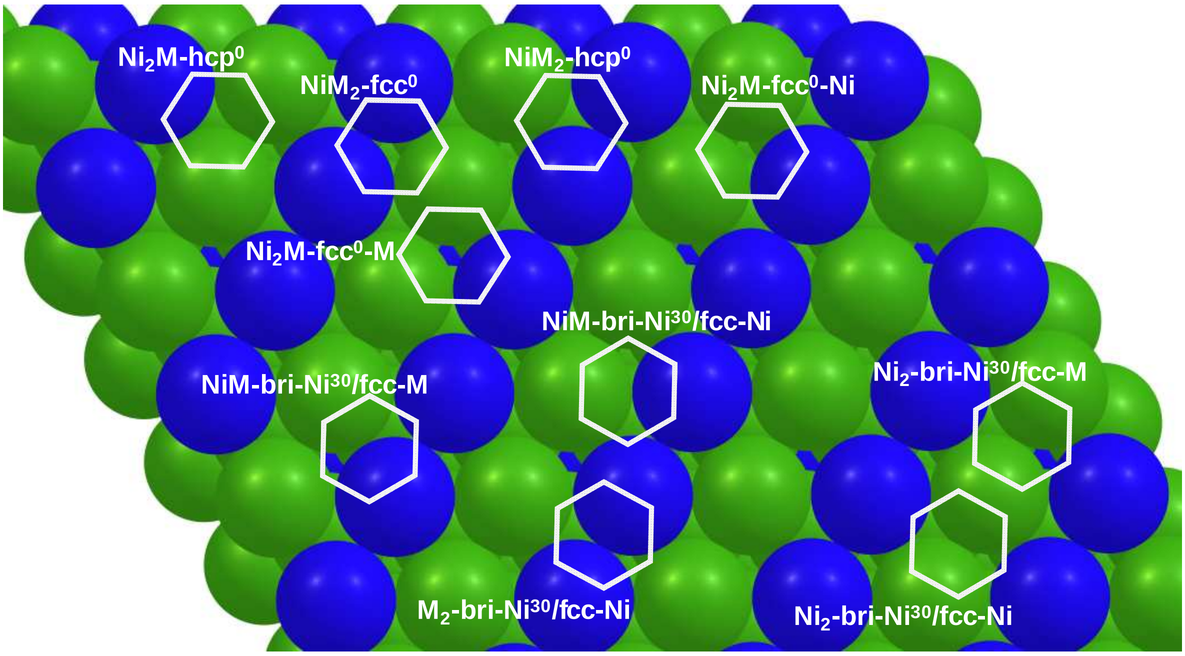

Figure 5-4: Adsorption sites of benzene on the surface of partially segregated Ni_3M alloys. Ni and M atoms are indicated in green and blue colors, respectively.

Table 5-4: Benzene adsorption energies (kJ mol^{-1}) on antisegregated Ni$_3$M alloys.

	ΔE_{ads} (kJ mol^{-1})					
Antisegregated	**Ni$_3$Cr**	**Ni$_3$Cr**	**Ni$_3$Co**	**Ni$_3$Ru**	**Ni$_3$Re**	**Ni$_3$Os**
bri-M-Ni$_2$M^{30}/fcc-NiM$_2$	–87.9	---	---	---	---	---
bri-M-Ni$_3$M^{30}/fcc-NiM$_2$	–81.9	---	---	---	---	---
bri-M-Ni$_3$^{30}/fcc-Ni$_2$M-Ni	–90.6	---	---	---	---	---
bri-M-Ni$_2$M^{30}/fccNi$_2$M-M	–82.4	---	---	---	---	---
bri-Ni^{30}/fcc-Ni$_2$M-Ni	–90.9	---	---	---	---	---
bri-Ni^{30}/fcc-NiM$_2$	–94.3	–94.3	–108.3	–146.0	–120.3	–142.1
bri-Ni^{30}/fcc-Ni$_2$M-M	–77.6	---	---	---	---	---

Table 5-5: Benzene adsorption energies (kJ mol^{-1}) on partially segregated and non-segregated Ni$_3$M alloys.

	ΔE_{ads} (kJ mol^{-1})		
Partially segregated	**Ni$_3$Pd**	**Ni$_3$Rh**	**Ni$_3$Pd**
NiM-bri-Ni^{30}/fcc-M	–47.4	---	---
NiM-bri-Ni/^{30}fcc-Ni	–49.2	---	---
Ni$_2$-bri-Ni^{30}/fcc-Ni	–62.2	–91.1	–62.2
Ni$_2$-bri-Ni^{30}/fcc-M	–59.2	---	---
M$_2$-bri-Ni^{30}/fcc-Ni	–18.4	---	---
Ni$_2$M-hcp^0	–42.1	---	---
NiM$_2$-hcp^0	–38.2	---	---
Ni$_2$M-fcc^0-Ni	–38.4	---	---
NiM$_2$-fcc^0	–36.8	---	---
Ni$_2$M-fcc^0-M	–44.6	---	---
Non-segregated*	**Ni$_3$Ir**	**Ni$_3$Pt**	
Ni$_2$-bri^{30}-Ni	–114.8	–104.8	

* Corresponding to alloys that show partial segregation of the clean surface and non-segregation in the presence of benzene adsorbed. Only the adsorption on the most stable adsorption site obtained for Pd$_3$M non-segregated alloys has been studied (Ni$_2$-bri^{30}-Ni)

5.3.4 Catalysts descriptors for benzene adsorption

The study of benzene adsorption on X$_3$Y bimetallic surfaces is computationally very expensive, due to the large number of possible adsorption sites and the size of the (4×4) four-layered unit cell (64 atoms) that is required to model benzene adsorption below saturation coverage on a surface with X$_3$Y stoichiometric composition. Therefore, catalysts properties that correlate with benzene adsorption energy are interesting to evaluate future catalysts.

The computationally less demanding adsorption of atomic carbon has been evaluated on the different alloys, since it can be expected that changes in benzene adsorption can be accompanied by a similar variation in carbon adsorption. The possible adsorption sites on each segregated surface have been studied in a (2×2) unit cell for those alloys also considered for benzene adsorption. The studied adsorption geometries and the calculated adsorption energies are discussed in Appendix D.

The most stable adsorption energy of benzene in every alloy is plotted as a function of the most stable adsorption sites of carbon in Figure 5-5. A good correlation is observed between the two for which, remarkably, not only the values on Pd_3M correlate (blue in Figure 5-5) but also those calculated on Ni_3M alloys (red), and pure Pd(111) and Ni(111) (green). Although some alloys are observed to deviate from the calculated trend, such as those involving the IVb metals (Ti, Zr, and Hf), the largest deviation between the correlation and the actual values is below ~20 kJ mol^{-1}.

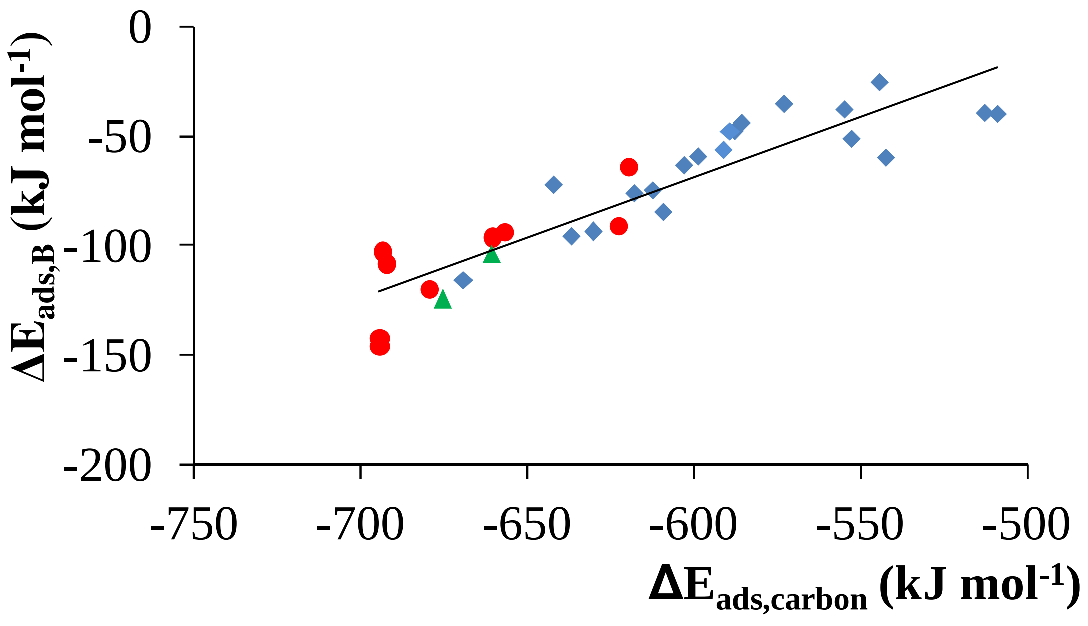

Figure 5-5: Adsorption energy of benzene as a function of that for atomic carbon (kJ mol^{-1}) calculated on Pd_3M (blue), Ni_3M (red), and monometallic catalysts (Ni and Pd in green). The R^2 values for the linear regression is 0.83.

Despite the large decrease in computational cost going from benzene to carbon adsorption, there are still different carbon adsorption sites to be evaluated, and therefore an even more accessible catalyst descriptor that can capture the trend in benzene adsorption is desirable. The binding energy of an adsorbate to a metal surface strongly depends on the molecular valence electrons and the surface band structure.[84] For transition metals, as those investigated in this work, the occupancy of the d-band varies along each series, and differences in reactivity may be related to changes in their d-band structure. [47] Hammer and Nørskov proposed the d-band model,[85, 86] which relies on the relationship between adsorption strength and the center of the d-band (ε_d). This model has been mostly evaluated for the adsorption of simple molecules on metallic [84] and antisegregated (skin) surfaces.[38] However, the applicability of this model may not be straightforward for the adsorption on surfaces consisting of different metals, e.g. non-segregated or partially segregated surfaces,[38] as for certain complex adsorbate–substrate systems.[87]

The d-band center of the occupied d-band projected on all atoms in the surface layer, relative to the Fermi level, is plotted as a function of the adsorption energy at the most stable benzene adsorption site for the whole range of Pd_3M and Ni_3M alloys, together with the value for Pd(111) and Ni(111) (see Figure 5-6). A good correlation is observed for all segregation states, for which the higher the d-band center (the closer to the Fermi level E_{fermi}), the stronger the adsorption. The reason is that higher energy (less populated) antibonding states are created upon adsorption on alloys with a ε_d closer to the E_{fermi}. The error estimating the adsorption energy of benzene from the d-band center is slightly larger than that using carbon adsorption energy. Moreover, both correlations improve if the values are split into antisegregated and non-segregated alloys, including in both correlation the corresponding Pd_3M and Ni_3M results (see Figure D4 in Appendix D).

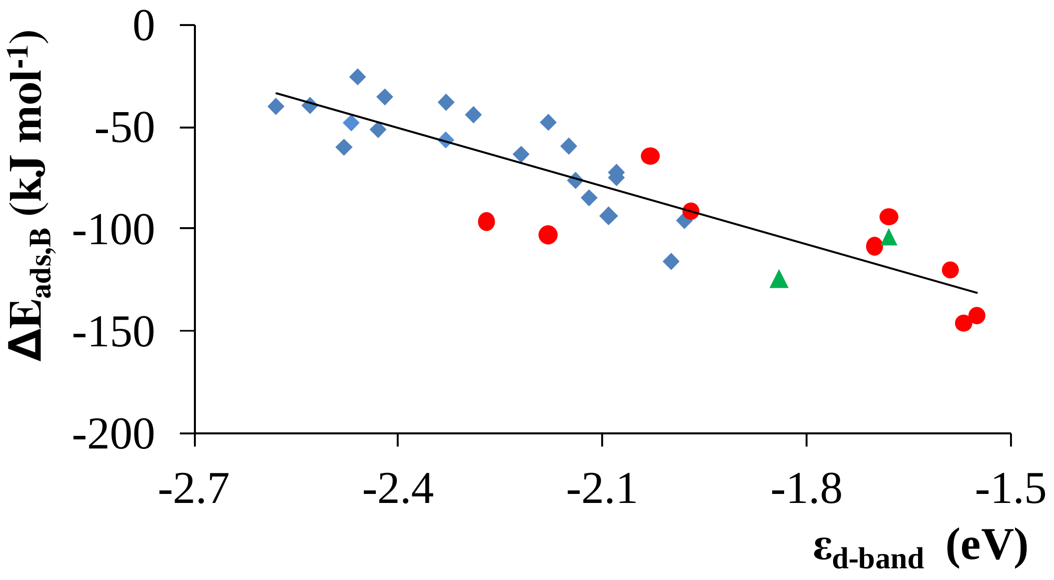

Figure 5-6: Adsorption energy of benzene on the most stable adsorption site (kJ mol^{-1}) as a function of the d-band center of the occupied states projected on all atoms in the surface layer (ε_d in eV) for the most stable site for the whole range of Pd_3M (blue) and Ni_3M alloys (red), Pd(111) and Ni(111) (green). The R^2 values for the linear regression is 0.76.

5.3.5 Screening the reactivity for benzene hydrogenation

If a single benzene adsorption site is considered on each bimetallic surface, the catalytic hydrogenation of benzene consists of six sequential hydrogenation steps via 13 possible reaction paths. The study of this reaction network on several alloys is computationally extremely expensive. Therefore, this work has studied the first hydrogenation step, from benzene to monohydrobenzene, to provide a first estimation of the benzene hydrogenation reactivity of each alloy.

The first hydrogen addition step from benzene to monohydrobenzene has been evaluated on nine Pd_3M alloys (with M = Ti, Cr, Mn, Fe, Co, Ni, Mo, Ir, and Pt), and eight Ni_3M alloys (with M = Cr, Co, Ru, Pd, Re, Os, Ir and Pt). Due to the lower symmetry of benzene adsorbed on bimetallic surfaces as compared to gas-phase benzene and the adsorption on monometallic surfaces, for the first hydrogenation step the H atom can be added to different carbon atoms. As in the Pd(111) case, the hydrogenation of carbon atoms involved in two di-σ-type bonds, i.e., carbon atom bound to a metal atom that is not bound to any other carbon atom, is always more activated, up to 30 kJ mol^{-1}, than the other carbon atoms (those bound to a metal atom that is also bound to another carbon atom). E.g. 14 kJ mol^{-1} more activated in Pd_3Rh, as shown in Table D5 in Appendix D. Secondly, different carbon atoms can be observed in π-type interactions, due to binding to different surface metals, or binding to the same metal but with different neighboring metal atoms. The reported values correspond to the least activated hydrogenation from those evaluated. More details can be found in Appendix D.

To the best of our knowledge, no theoretical study has reported activation barriers for benzene hydrogenation on bimetallic catalysts. As can be observed in Figure 5-7, most bimetallic catalysts are more reactive than Pd(111) for the first hydrogenation step, e.g, Pd_3Ir (106 kJ mol^{-1}), Pd_3Pt (103 kJ mol^{-1}), and Pd_3Cr (112 kJ mol^{-1}) as compared to Pd(111) (122 kJ mol^{-1}), which agrees with the increase in benzene hydrogenation activity experimentally observed for Pt-Ir [88, 89], Pt-Pd [6, 12-14], and Pd-Cr [24] as compared to the Pd.

Three catalysts descriptors are used to describe the reactivity trends from one bimetallic catalysts to the next: (a) the benzene adsorption energy, (b) the carbon adsorption energy, and (c) the d-band center of the occupies states of the surface atoms. The correlation between activation barriers and these three descriptors is shown, respectively, from top to bottom in Figure 5-7. The descriptor that gives the best correlation is the benzene adsorption energy. As expected, the weaker benzene adsorption, the less activated is the reaction. This correlation agrees with those reported for cyclohexene hydrogenation on Pt-based [20] and benzene hydrogenation on Co-based[90] catalysts. The correlation shows that most Pd_3M alloys bind benzene less strong than Ni_3M alloys and have, therefore, lower activation barriers. The geometries of benzene are different for weak and strong adsorption on the surface, as illustrated in Figure 5-8 for (a) Pd_3Ta and (b) Pd_3Pt. Weak adsorption leads benzene to adopt a geometry that resembles that in gas phase, with larger metal-carbon bond length and without

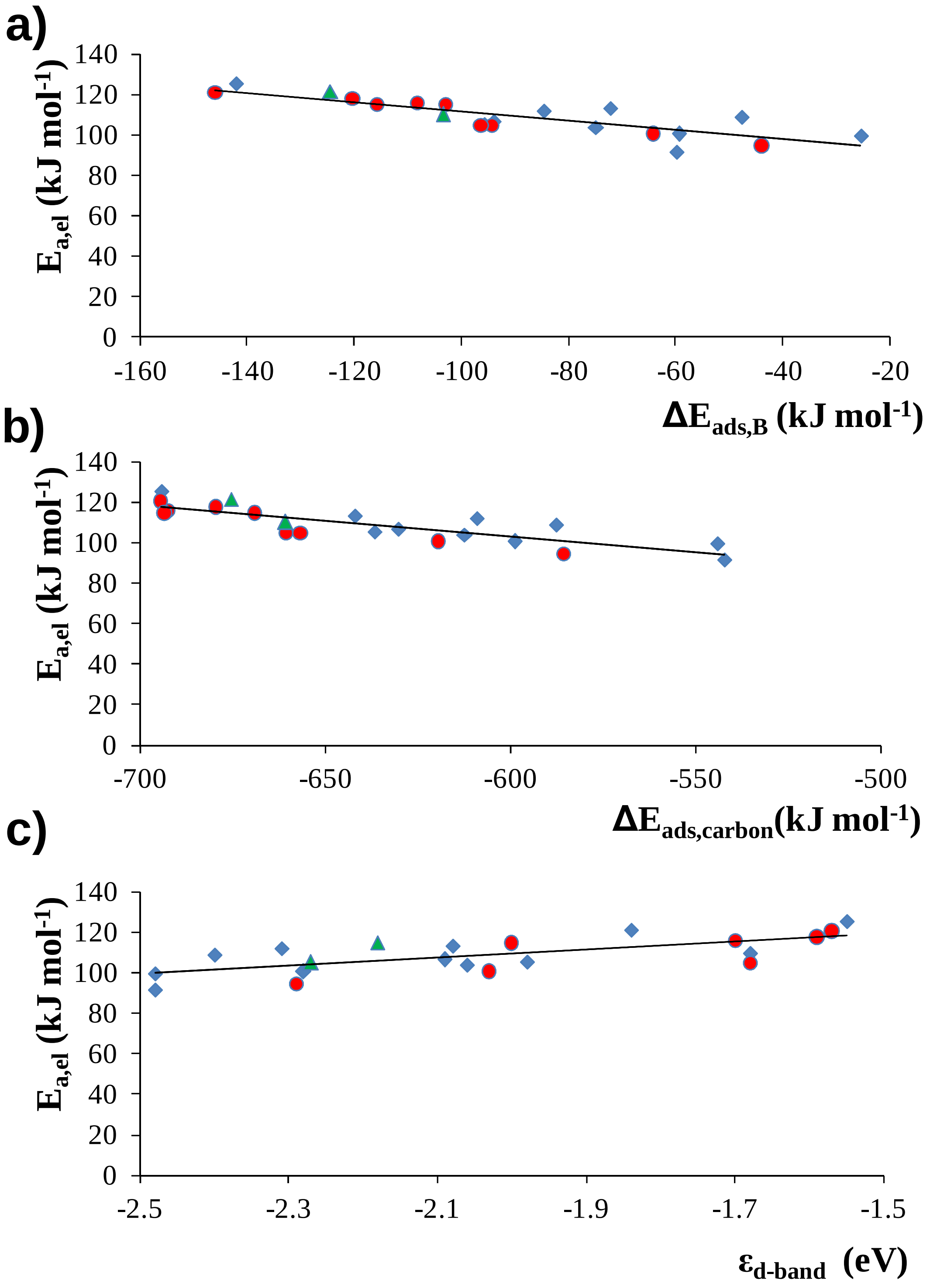

Figure 5-7: Correlation between the electronic activation barrier of the first hydrogenation of benzene to monohydrobenzene and (a) adsorption energy of benzene, (b) adsorption energy of carbon, and (c) d-band center of the occupied states of the surface atoms, for Pd_3M alloys (blue rhombus), Ni_3M alloys (red circles), Pd(111) and Ni(111) (green triangles). R^2 values for the linear regression are, from top to bottom, 0.75, 0.67 and 0.47.

C-H bending out of the ring plane. The correlation indicated that the weaker adsorption leads to a more facile hydrogenation of benzene to monohydrobenzene, e.g. by 15 kJ mol^{-1} for Pd_3Ta as compared to Pd_3Pt as shown in Figure 5-8. However, as it is shown later, the activity does not depend only on activation barriers, and there is an interplay between other factors such as benzene adsorption.

Similar to benzene adsorption, the smaller the carbon adsorption energy the less activated is the first hydrogenation step. For the d-band center of the occupied states of surface atoms, the correlation indicates that that the closer the d-band center to the Fermi level, the higher the electronic activation energy. The slope of the activation energy vs. the occupied d-band center is opposite to the slope observed by Christiansen and Norskov for the adsorption step in ammonia synthesis. [25] but for the activation energy for N_2 dissociation. The two latter catalysts descriptors yield less good correlations compared to benzene adsorption energy.

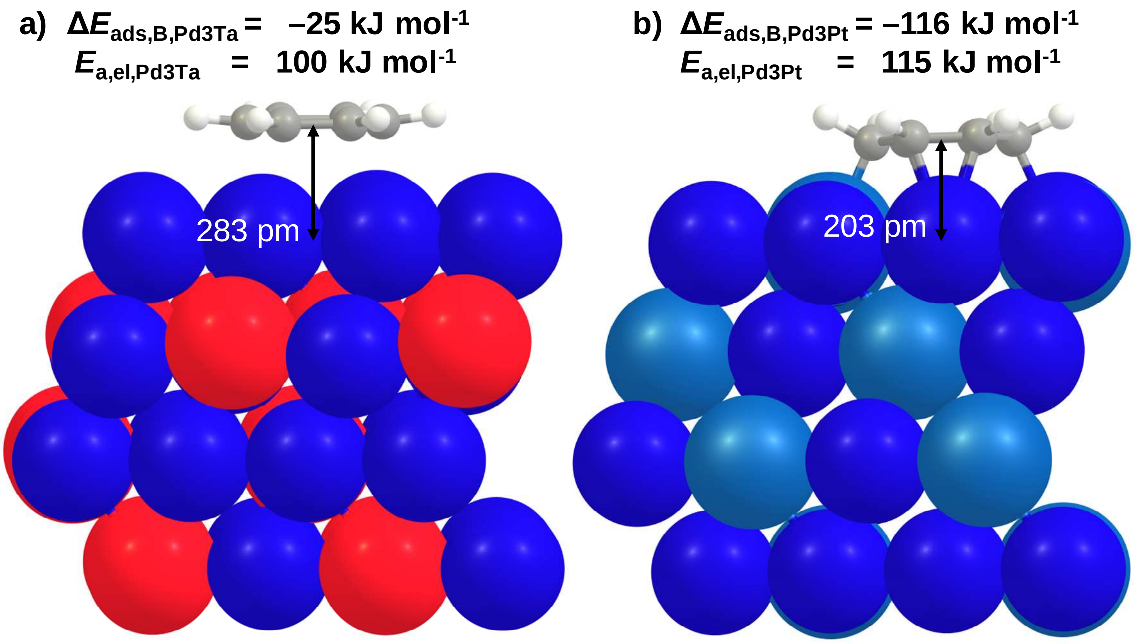

Figure 5-8: Adsorption geometry of benzene on the (a) antisegregated Pd_3Ta and (b) non-segregated Pd_3Pt surfaces, with the corresponding adsorption energy (kJ mol^{-1}), activation barrier for the first hydrogenation (kJ mol^{-1}), and the distance between the center of the carbon ring and the first atomic layer (pm).

Finally, the benzene adsorption energy is used as a catalyst descriptor to assess the activity shown by the virtual candidate catalysts, and establish which values are optimal under given reaction conditions. As explained more in detail in the methodology and in Appendix D, a rate determining step model has been constructed to determine benzene hydrogenation turnover frequencies (TOF in s^{-1}) from the results calculated for different catalysts. In this model, the TOF is calculated as a function of the change in benzene adsorption energy relative to that calculated on Pd(111) ($\Delta\Delta E_{\mathrm{ads,B}} = \Delta E_{\mathrm{ads,B,X3M}} - \Delta E_{\mathrm{ads,Pd(111)}}$). Hydrogen adsorption energy is calculated for the most stable adsorption site calculated for carbon (see correlation as a function of benzene adsorption energies in Figure D7 in Appendix D). The activation barrier for the first hydrogenation relative to the value on Pd(111), $\Delta E_{a,el} = (E_{\mathrm{a,el,X3M}} - E_{\mathrm{a,Pd(111)}})$, is related to the variation in benzene adsorption energy relative to Pd(111) by the relationship $\Delta E_{\mathrm{a,el}} = m\ \Delta\Delta E_{\mathrm{ads,B}}$, shown in Figure D8 in Appendix D and yielding a value of m = -0.3. In a similar way, the variation in hydrogen adsorption is calculated as $\Delta\Delta E_{\mathrm{ads,H2}} = \gamma\ \Delta\Delta E_{\mathrm{ads,B}}$, shown in Figure D8 in Appendix D, with $\gamma = 0.43$. Figure 5-9 shows the TOF calculated at T= 400 (dotted), 450 (dashed), and 500 K (full line) at $p_{\mathrm{B}} = 6.7 \times 10^{-2}$ bar, $p_{H2} = 0.9$, and $p_{\mathrm{CHA}} = 6.6 \times 10^{-4}$ bar. From Figure 5-9 it can be observed that the lower the temperature, the closer the maximum in TOF is to the value for Pd(111), i.e., $\Delta\Delta E_{ads,B} = 0$ kJ mol^{-1}. Increasing the temperature moves the maximum TOF towards stronger benzene adsorption energies ($\Delta\Delta E_{\mathrm{ads,B}}, < 0$), which shows the interplay between adsorption and reaction that is needed to predict catalysts activities. Regarding the reactions conditions that are considered to calculate the TOFs, for temperatures between 400 and 500 K the optimal catalysts are those that bind benzene 10-20 kJ mol^{-1} stronger, e.g. Ni_3Os and Ni_3Ru.

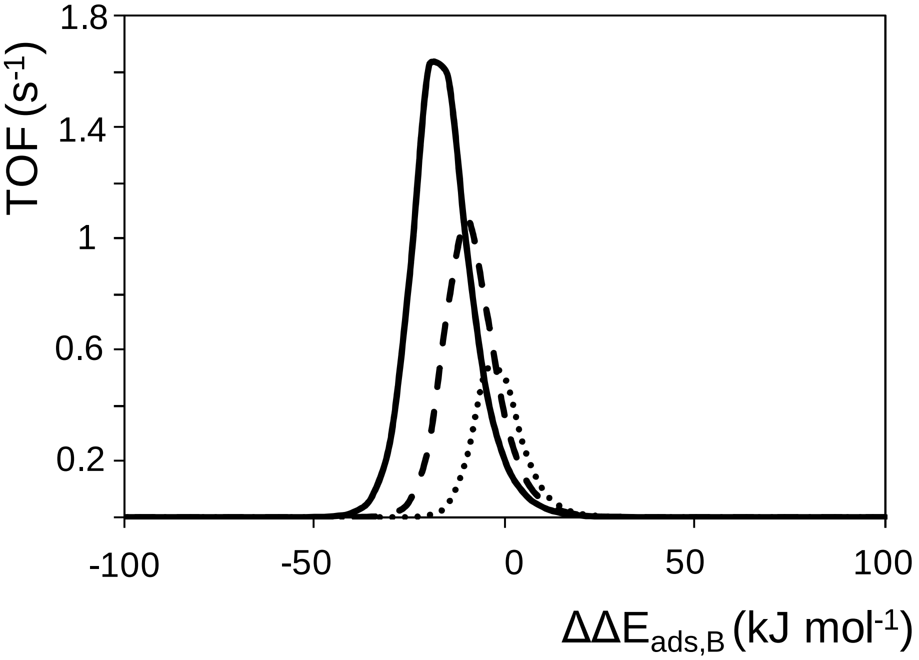

Figure 5-9: Turnover frequency (TOF in s^{-1}) for benzene hydrogenation as a function of benzene adsorption energy. The adsorption energy is shown relative to that on Pd(111). The TOF is calculated assuming a rate determining step model for the second hydrogenation step, using the obtained catalyst descriptor correlation, and kinetic parameters calculated for a coverage-dependent model on Pd(111), as explained in Appendix D. The results correspond to p_B = 6.7 × 10^{-2} bar, p_{H2} = 0.9 bar, and T= 400 (dotted line), 450 (dashed) and 500 K (full).

5.4 Conclusions

Design of catalysts for benzene hydrogenation is performed screening bimetallic $Pd_3M(111)$ and $Ni_3M(111)$ surfaces. Benzene adsorption is evaluated on the most stable segregation state of the bimetallic surfaces. Since benzene adsorption is computationally very demanding, good correlations are obtained with the more accessible carbon adsorption energy and the d-band center of the occupied states of surface atoms. For the latter, benzene adsorption is stronger in those alloys with a d-band center closer to the Fermi level.

The reactivity of different catalysts for benzene hydrogenation is studied for the first hydrogenation step. The electronic barrier correlates well to benzene adsorption energy, which is proposed as a catalyst descriptor. Pd_3M generally bind benzene weaker than Ni_3M alloys, hence the first hydrogenation step is more activated on the latter alloys. Variations in adsorption energies and activation barriers, relative to Pd(111), are implemented in a previously develop microkinetic model on Pd(111) to predict performances as a function of the conditions. At typical hydrogenation conditions, the maximum in turnover frequency is obtained for catalysts that bind benzene stronger than Pd(111), up to 20 kJ mol^{-1} between 400-500 K corresponding e.g. to Ni_3Ru and Ni_3Os antisegregated alloys.

5.5 References

1. F. Cavani and F. Trifiro, *Catal. Today*, 1997, **34**, 269-279.
2. M. Heemeier, A. F. Carlsson, M. Naschitzki, M. Schmal, M. Baumer and H. J. Freund, *Angew Chem Int Edit*, 2002, **41**, 4073-4076.
3. M. P. Latusek, R. M. Heimerl, B. P. Spigarelli and J. H. Holles, *Appl. Catal., A*, 2009, **358**, 79-87.
4. V. R. Stamenkovic, B. Fowler, B. S. Mun, G. F. Wang, et al., *Science*, 2007, **315**, 493-497.
5. J. H. Sinfelt, *Bimetallic catalysts : discoveries, concepts, and applications*, Wiley, New York, 1983.
6. J. G. Chen, C. A. Menning and M. B. Zellner, *Surf Sci Rep*, 2008, **63**, 201-254.
7. B. H. Cooper and B. B. L. Donnis, *Appl. Catal., A*, 1996, **137**, 203-223.
8. A. C. Capleton and L. S. Levy, *Chem. Biol. Interact.*, 2005, **153**, 43-53.
9. W. K. Hall and P. H. Emmett, *J. Phys. Chem.*, 1958, **62**, 816-821.
10. S. I. Reshetnikov, E. A. Ivanov and A. N. Startsev, *Chemical Engineering Journal*, 2007, **134**, 100-105.
11. S. L. Lu, W. W. Lonergan, J. P. Bosco, S. R. Wang, et al., *J. Catal.*, 2008, **259**.
12. B. Pawelec, V. La Parola, S. Thomas and J. L. G. Fierro, *J. Mol. Catal. A: Chem.*, 2006, **253**, 30-43.
13. M. Sanati, B. Harrysson, M. Faghihi, B. Gevert and S. Jaras, in *Catalysis*, ed. J. J. Spivey, Royal Society of Chemistry, Cambridge, Editon edn., 2002, pp. 1-42.
14. R. M. Navarro, B. Pawelec, J. M. Trejo, R. Mariscal and J. L. G. Fierro, *J. Catal.*, 2000, **189**.
15. P. C. LArgentiere and N. S. Figoli, *Ind. Eng. Chem. Res.*, 1997, **36**.

16. H. Yasuda, T. Kameoka, T. Sato, N. Kijima and Y. Yoshimura, *Appl. Catal., A*, 1999, **185**.
17. Y. Yoshimura, H. Yasuda, T. Sato, N. Kijima and T. Kameoka, *Appl. Catal., A*, 2001, **207**.
18. A. M. Venezia, V. La Parola, B. Pawelec and J. L. G. Fierro, *Appl. Catal., A*, 2004, **264**.
19. S. Albonetti, G. Baldi, A. Barzanti, E. R. Castellon, et al., *Catal. Lett.*, 2006, **108**, 197-207.
20. M. P. Humbert and J. G. G. Chen, *J. Catal.*, 2008, **257**, 297-306.
21. L. J. Simon, P. J. Kooyman, J. G. van Ommen and J. A. Lercher, *Appl. Catal., A*, 2003, **252**.
22. Y. M. Chung and H. K. Rhee, *J. Mol. Catal. A: Chem.*, 2003, **206**, 291-298.
23. A. S. Rocha, E. L. Moreno, G. P. M. da Silva, J. L. Zotin and A. C. Faro, *Catal. Today*, 2008, **133**.
24. L. J. Hu, G. F. Xia, L. L. Qu, C. Li, Q. Xin and D. D. Li, *J. Mol. Catal. A: Chem.*, 2001, **171**, 169-179.
25. C. H. Christensen and J. K. Norskov, *J. Chem. Phys.*, 2008, **128**.
26. P. C. Largentiere and N. S. Figoli, *Appl. Catal.*, 1990, **61**, 275-282.
27. N. S. Figoli, P. C. Largentiere, A. Arcoya and X. L. Seoane, *J. Catal.*, 1995, **155**.
28. J. Abe, X. L. Ma and C. S. Song, *Abstr Pap Am Chem S*, 2003, **226**.
29. M. Garcia-Mota, J. Gomez-Diaz, G. Novell-Leruth, C. Vargas-Fuentes, et al., *Theor. Chem. Acc.*, 2011, **128**, 663-673.
30. W. H. Qian, Y. Yoda, Y. Hirai, A. Ishihara and T. Kabe, *Appl. Catal., A*, 1999, **184**, 81-88.
31. L. J. Hu, H. Nie, L. L. Qu, G. F. Xia, Y. H. Shi and D. D. Li, *Abstr Pap Am Chem S*, 1999, **217**, U804-U804.
32. H. Yasuda and Y. Yoshimura, *Catal. Lett.*, 1997, **46**, 43-48.
33. L. O. Paz Borbón, in *Springer theses*, Springer, Berlin ; Heidelberg ; New York, Editon edn., 2011.
34. A. V. Ruban, H. L. Skriver and J. K. Norskov, *Phys. Rev. B: Condens. Matter Mater. Phys.*, 1999, **59**, 15990-16000.
35. C. A. Menning, H. H. Hwu and J. G. G. Chen, *J. Phys. Chem. B*, 2006, **110**, 15471-15477.
36. Y. G. Ma and P. B. Balbuena, *Surf. Sci.*, 2008, **602**, 107-113.
37. C. A. Menning and J. G. Chen, *Top. Catal.*, 2010, **53**, 338-347.
38. I. A. Pasti, N. M. Gavrilov and S. V. Mentus, *Electrochim Acta*, 2014, **130**, 453-463.
39. M. K. Sabbe, L. Lain, M. F. Reyniers and G. B. Marin, *Phys. Chem. Chem. Phys.*, 2013, **15**, 12197-12214.
40. J. M. Caruthers, J. A. Lauterbach, K. T. Thomson, V. Venkatasubramanian, et al., *J. Catal.*, 2003, **216**, 98-109.

41. N. Schweitzer, H. L. Xin, E. Nikolla, J. T. Miller and S. Linic, *Top. Catal.*, 2010, **53**, 348-356.
42. H. Toulhoat and P. Raybaud, *J. Catal.*, 2003, **216**, 63-72.
43. A. A. Peterson and J. K. Norskov, *J. Phys. Chem. Lett.*, 2012, **3**, 251-258.
44. J. Greeley and J. K. Norskov, *Surf. Sci.*, 2007, **601**, 1590-1598.
45. J. Greeley and M. Mavrikakis, *Nat Mater*, 2004, **3**, 810-815.
46. J. K. Norskov, T. Bligaard, J. Rossmeisl and C. H. Christensen, *Nat Chem*, 2009, **1**, 37-46.
47. B. Hammer and J. K. Norskov, *Surf. Sci.*, 1995, **343**, 211-220.
48. V. Pallassana and M. Neurock, *J. Catal.*, 2000, **191**, 301-317.
49. C. Klanner, D. Farrusseng, L. Baumes, M. Lengliz, C. Mirodatos and F. Schuth, *Angew Chem Int Edit*, 2004, **43**, 5347-5349.
50. M. C. Escano, T. Q. Nguyen, H. Nakanishi and H. Kasai, *J. Phys.: Condens. Matter*, 2009, **21**.
51. C. J. H. Jacobsen, S. Dahl, A. Boisen, B. S. Clausen, et al., *J. Catal.*, 2002, **205**, 382-387.
52. G. Kresse and J. Hafner, *Phys. Rev. B: Condens. Matter Mater. Phys.*, 1994, **49**, 14251-14269.
53. G. Kresse, *J. Non-Cryst. Solids*, 1995, **193**, 222-229.
54. G. Kresse and J. Furthmuller, *Comput. Mater. Sci.*, 1996, **6**, 15-50.
55. G. Kresse and J. Furthmuller, *Phys. Rev. B: Condens. Matter Mater. Phys.*, 1996, **54**, 11169-11186.
56. P. E. Blochl, *Phys. Rev. B: Condens. Matter Mater. Phys.*, 1994, **50**, 17953-17979.
57. G. Kresse and D. Joubert, *Phys. Rev. B: Condens. Matter Mater. Phys.*, 1999, **59**, 1758-1775.
58. J. P. Perdew, J. A. Chevary, S. H. Vosko, K. A. Jackson, et al., *Phys. Rev. B: Condens. Matter Mater. Phys.*, 1992, **46**, 6671-6687.
59. J. P. Perdew, J. A. Chevary, S. H. Vosko, K. A. Jackson, et al., *Phys. Rev. B: Condens. Matter Mater. Phys.*, 1993, **48**, 4978-4978.
60. H. J. Monkhorst and J. D. Pack, *Phys. Rev. B: Condens. Matter Mater. Phys.*, 1976, **13**, 5188-5192.
61. G. J. Nieuwenhuys, J. A. Mydosh and E. P. Wohlfarth, *Phys Lett A*, 1978, **66**, 221-222.
62. G. Mills, H. Jonsson and G. K. Schenter, *Surf. Sci.*, 1995, **324**, 305-337.
63. G. Henkelman and H. Jonsson, *J. Chem. Phys.*, 1999, **111**, 7010-7022.
64. T. Jacob and W. A. Goddard, *J. Phys. Chem. B*, 2004, **108**, 8311-8323.
65. F. Delbecq, L. Verite and P. Sautet, *Chem Mater*, 1997, **9**, 3072-3082.
66. C. Konvicka, Y. Jeanvoine, E. Lundgren, G. Kresse, et al., *Surf. Sci.*, 2000, **463**, 199-210.
67. E. Raub, R. Gohle and E. Roschel, *Z Metallkd*, 1967, **58**, 567-&.

68. B. S. Mun, M. Watanabe, M. Rossi, V. Stamenkovic, N. M. Markovic and P. N. Ross, *J. Chem. Phys.*, 2005, **123**.

69. E. J. Lamas, Texas A&M University, 2007.

70. G. Canduela-Rodriguez, M. K. Sabbe, M. F. Reyniers, J. F. Joly and G. B. Marin, *Phys. Chem. Chem. Phys.*, 2014, **16**, 23754.

71. K. H. Hansen, T. Worren, S. Stempel, E. Laegsgaard, et al., *Phys. Rev. Lett.*, 1999, **83**, 4120-4123.

72. L. L. Wang and D. D. Johnson, *J. Am. Chem. Soc.*, 2009, **131**, 14023-14029.

73. P. L. Hansen, A. M. Molenbroek and A. V. Ruban, *J. Phys. Chem. B*, 1997, **101**, 1861-1868.

74. L. C. A. van den Oetelaar, O. W. Nooij, S. Oerlemans, A. W. D. van der Gon, et al., *J. Phys. Chem. B*, 1998, **102**, 3445-3455.

75. J. L. Rousset, A. M. Cadrot, L. Lianos and A. J. Renouprez, *Eur Phys J D*, 1999, **9**, 425-428.

76. N. N. Greenwood and A. Earnshaw, *Chemistry of the elements*, 2nd edn., Butterworth-Heinemann, Oxford ; Boston, 1997.

77. F. R. d. Boer, *Cohesion in metals : transition metal alloys*, North-Holland ;

Sole distributors for the U.S.A. and Canada, Elsevier Scientific Pub. Co., Amsterdam ; New York

New York, N.Y., U.S.A., 1988.

78. M. Ramanathan, V. Ramani and J. Prakash, *Electrochim Acta*, 2012, **75**, 254-261.

79. C. Morin, D. Simon and P. Sautet, *J. Phys. Chem. B*, 2004, **108**, 5653-5665.

80. H. Ohtani, B. E. Bent, C. M. Mate, M. A. Van Hove and G. A. Somorjai, *Appl. Surf. Sci.*, 1988, **33-4**, 254-260.

81. M. Saeys, M. F. Reyniers, G. B. Marin and M. Neurock, *J. Phys. Chem. B*, 2002, **106**, 7489-7498.

82. F. Mittendorfer and J. Hafner, *Surf. Sci.*, 2001, **472**, 133-153.

83. H. Yildirim, T. Greber and A. Kara, *J. Phys. Chem. C*, 2013, **117**, 20572-20583.

84. R. Hoffmann, *Solids and surfaces : a chemist's view of bonding in extended structures*, VCH Publishers, New York, 1988.

85. B. Hammer and J. K. Norskov, *Nature*, 1995, **376**, 238-240.

86. B. Hammer and J. K. Norskov, *Adv. Catal.*, 2000, **45**, 71-129.

87. H. L. Xin and S. Linic, *J. Chem. Phys.*, 2010, **132**.

88. G. Leclercq, H. Charcosset, R. Maurel, C. Bertizeau, et al., *B Soc Chim Belg*, 1979, **88**, 577-597.

89. C. Betizeau, G. Leclercq, R. Maurel, C. Bolivar, et al., *J. Catal.*, 1976, **45**, 179-188.

90. S. L. Lu, C. A. Menning, Y. X. Zhu and J. G. Chen, *ChemPhysChem*, 2009, **10**, 1763-1765.

Chapter 6

Conclusions and perspectives

6.1 Conclusions

In order to optimize the efficiency of its processes, the chemical industry always strives to improve existing catalysts and develop new materials with novel catalytic properties. The present work applies periodic density functional theory (DFT) to search for optimal catalysts for the hydrogenation of benzene. In this respect, a detailed molecular level description of this reaction is first obtained on Pd, which is a commonly used catalyst for the hydrotreatment of oil fractions. Special attention is devoted to understand and quantify the effects of surface coverage on equilibrium coefficients for adsorption and rate coefficients for surface reaction steps, allowing to predict the activity of this reaction at actual conditions. In a second step, DFT is used to calculate the reactivity trends for benzene hydrogenation from one catalysts to the next. These trends are related to a catalyst descriptors, catalysts properties that describes the essential characteristics of a catalyst. The activity of virtual candidate catalysts can be predicted by implementing the catalysts descriptor into the constructed kinetic model for hydrogenation on Pd(111). This methodology results in an efficient, knowledge-based predictive model to design optimal catalysts as a function of the conditions.

Regarding the study of hydrogen coverage effects on benzene and hydrogen coadsorption on Pd(111), several conclusions can be drawn. Thermodynamic phase diagrams are constructed using DFT-based surface Gibbs free energies. These diagrams can predict the most stable surface coverage of a catalysts under reaction conditions. Theoretical studies often, if not always, neglect vibrational contributions to the surface Gibbs free energy and, hence, essentially approximate the Gibbs free energy to the electronic energy calculated from DFT. Furthermore, these studies are typically performed using gradient-corrected functionals, such as PW91, but these functional may not properly describe the van der Waals interactions (vdW), which have a major contribution to the catalyst-adsorbate bond. The present work has shown that, first, inclusion of vibrational contributions to the surface Gibbs free energy and, second, the use of proper functionals to describe vdW interactions, such as optPBE-vdW, is recommended to predict the most stable catalyst surface coverage as a function of conditions. Moreover, the constructed diagrams show that, in contrast to the zero-to-low coverage assumptions usually considered in theoretical studies of catalytic reactions, high hydrogen coverages of about $\theta_H = 0.89$ can be expected to coadsorbed with benzene coverages of $\theta_B = 0.11$ at typical hydrogenation conditions.

The high hydrogen surface coverages predicted by the thermodynamic phase diagrams enforces to study the kinetics for benzene hydrogenation on Pd(111) at increased coverage. Coverage effects are modeled by varying hydrogen coverage on the surface. This allows to represent a wide range of lateral interaction strength with a computationally efficient approach, and to mimic the lateral effects by the actual species present on the surface. Regardless of the surface coverage, the same dominant path is identified in the reaction network of benzene hydrogenation. Simplification of this complex network, consisting of 13 reaction paths per benzene adsorption site, to a single dominant path allows to study coverage effects on the rate coefficients, which would be computationally too expensive for the whole network. The results clearly show that the hydrogen surface coverage affects the adsorption and surface reactions to a large extent. On the one hand, adsorption equilibrium coefficients decrease due to the decrease in adsorption enthalpy with increasing surface coverage. On the other hand, the rate coefficients for hydrogenation on the catalyst surface increase as a function of coverage due to the lower destabilization of transition states as compared to reactants with increasing surface coverage. The coverage-dependent microkinetic model that accounts for the kinetics of every elementary step, calculated with the optPBE-vdW functional, predicts turnover frequencies that are in the same order of magnitude as experimental observations. This is in contrast to the results obtained using low-coverage kinetics or using coverage-dependent PW91 kinetics. In addition, the reactions on which the turnover frequency is most sensitive differ from those identified from the reaction rates with the coverage-dependent model, or from those proposed using low-coverage kinetics.

Surfaces of industrial catalyst are generally non-uniform. The detailed study of the reaction is performed on Pd(111) because it is the most abundant surface of Pd nanoparticles. However, other common surfaces, such as the (100) and (110), have a large influence on the catalytic activity. In a first step, the adsorption of benzene on Pd(100) and Pd(110) is studied as a function of coverage. At the experimental saturation coverage, the adsorption on both surfaces is much weaker than at medium coverage, particularly on Pd(110). In combination with experimental observations, the results allow to propose the preferred adsorption sites for benzene on both surfaces, reducing the number of possible adsorption sites to a large extent.

Based on the obtained microkinetic model on Pd with DFT calculations, in this work a predictive model is developed that can be used to search for optimal bimetallic catalysts for benzene hydrogenation. Periodic DFT calculations are extremely useful to determine trends in stability and reactivity from one bimetallic catalyst to the next. For the first, the adsorption energy of the most stable adsorption site of benzene on Pd_3M and Ni_3M alloys correlates well with that for carbon adsorption, and also with the more accessible d-band center of the occupied states of surface atoms. Secondly, the reactivity for the first hydrogenation step shows a good correlation with benzene adsorption energy. The variations in reactivity and benzene adsorption on the different bimetallic surfaces, relative to those on Pd(111), are implemented in a coverage-dependent microkinetic model on Pd(111) with some approximations, e.g. the second hydrogenation is the rate-determining step. A maximum in activity is exhibited between 400 and 500 K for catalysts that adsorb benzene more strongly than Pd(111), by some 10 – 20 kJ mol^{-1}, e.g. Ni_3Ru and Ni_3Os.

6.2 Perspectives

The present work has proven that periodic DFT calculations can accurately describe the activity and reaction mechanism for the catalytic hydrogenation of benzene on Pd(111). Furthermore, DFT can develop efficient, knowledge-based predictive models to search for optimal catalysts. The applied methodology can be extended to investigate also other industrially important catalytic reactions.

The construction of thermodynamic phase diagrams can predict the Pd(111) surface coverage of a catalyst as a function of the conditions. The coverages that are expected to populate the surface at hydrogenation conditions largely differ from those usually considered in theoretical studies. In this respect, inclusion of vibrational contributions to the surface Gibbs free energy, and the use of a non-local functional that can better describe van der Waals interactions (e.g. using optPBE-vdW) are strongly recommended. This work has only in an extrapolative way included both effects due to computational limitations. Therefore, the approach that accounts for both effects should be investigated, and compared to the applied methodology.

Implementation of coverage effects on adsorption and reactions kinetics in a kinetic model, using the optPBE-vdW functional, allows to predict catalytic activities in the order of magnitude of experimental observations. This could not be achieved using the kinetics calculated at low coverages, either from the results calculated with the gradient-corrected functional. Additional studies regarding hydrogenation reactions, or other industrially important reactions, should therefore incorporate coverage effects and use functionals that properly describe van der Waals interactions.

In this work, however, the effect of surface coverage has been assessed varying hydrogen coverage on the surface only. This approach is much more straightforward than varying benzene coverage and can provide a very good estimation of the effect of lateral interactions on kinetics. However, the coverage-dependent microkinetic modeling indicates that benzene is the one of the most abundant surface species on Pd(111) at reaction conditions. At higher benzene coverage, it is also possible that the reaction follows a different reaction mechanism. Therefore, the effect of benzene coverage on adsorption and reactions kinetics should also be addressed, leading to the full picture of coverage effects. The implementation in DFT can be computationally challenging because of the size of benzene that requires the use of unit cells with different size to study various coverages, on the contrary to hydrogen coverage that can be evaluated with a fixed unit cell. As a first step, the hydrogenation of benzene could be studied at saturation coverage, which requires a small unit cell, and an estimation of benzene coverage effects can be extracted by comparison to the results that are shown in this work at medium coverage.

Aiming to develop a coverage-dependent microkinetic model for benzene hydrogenation on Pd multifaceted particles, the adsorption of benzene has been evaluated on Pd(100) and

Pd(110). The results allow to identify the preferred sites as a function of benzene coverage. Future DFT calculations could evaluate the reaction mechanism and kinetics for benzene hydrogenation on Pd(100) and Pd(110), together with steps and terraces. This evaluation can shed light on the structure sensitivity of this reaction, for which there is no consensus in literature studies.

The combination of constructed microkinetic model for benzene hydrogenation on Pd(111) with stability and reactivity trends on bimetallic catalysts is an efficient tool to construct predictive models to search for optimal bimetallic catalysts. Variations in reactivity from one catalysts to the next have been extrapolated based on the calculated activation barriers for the first hydrogenation step only. These can be further improved by evaluating e.g. the reactions that conform the dominant path identified on Pd(111).

Most metal catalysts are often unstable and vulnerable to sintering, hence they are supported on solid materials such as alumina, silica and carbon to increase their stability. Furthermore, supports may also affect the catalysts activity; they can be a source of active sites and participate in the reaction via hydrogen spill-over processes, or they can also modify the activity of the metal phase (metal-support interactions). This work has not considered supported catalysts to reduce the complexity of the calculations, therefore, future DFT calculations can try to assess the contribution of acid sites for Pd deposited on acidic zeolites, which is relevant for hydrogenation reactions.

Overall, this work has shown that accurate hydrogenation activities can be obtained with periodic density functional theory if important factors, such as coverage effects, are efficiently included. Although gradient-corrected functional can be used to predict trends that capture the difference between various catalysts, comparison of actual values, e.g. adsorption energies, require a proper description of van der Waals interactions with functionals such as optPBE-vdW.

Appendix A

Supporting information for Chapter 2

Contents. Appendix A includes the supporting information for the methodology followed to construct thermodynamic phase diagrams, together with explanation of the procedure to evaluate coadsorption geometries as a function of coverage, adsorption geometry features and energies, corresponding to Chapter 2.

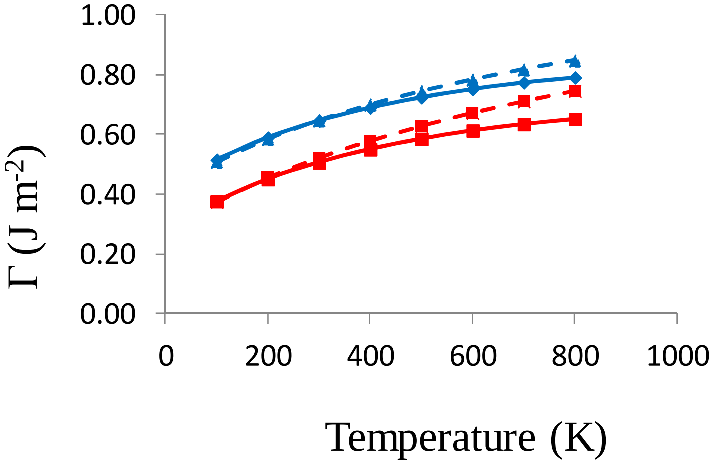

Figure A 1: Surface Gibbs free energies as a function of temperature for the two consecutive systems with benzene and θ_H= 0.67 or 0.78 hydrogen coverage (blue and red lines, respectively). The values are obtained by applying a frequency cutoff of 25 or 50 cm^{-1} (full and dotted lines, respectively).

Table A 1: Geometries in which spurious imaginary (or positive but < 25 cm^{-1}) frequencies are replaced and number of these frequencies that are replaced.

Geometry with spurious frequencies	Number of frequencies replaced
Benzene + θ_H = 0.78	2
Benzene + θ_H = 0.89	2
Benzene + θ_H = 1	3
Benzene + θ_H = 1.11	2
Benzene + θ_H = 1.22	3
Benzene + θ_H = 1.33	3
Benzene + θ_H = 1.44	4
Benzene + θ_H = 1.56	5
Benzene + θ_H = 1.67	4
Benzene + θ_H = 1.78	4
Benzene + θ_H = 1.89	5

Thermodynamic calculations:

The surface Gibbs free energy is calculated as shown in eq. (A1).

$$\Gamma(T, p_i) = \left(\frac{G_{ads}(T) - n_{Pd} \cdot G_{bulk}(T) - \sum_i n_i \cdot G_{m,gas,i}(T, p_i)}{2 \cdot A} \right) \tag{A1}$$

With G_{ads} and G_{bulk} the Gibbs free energy of respectively the adsorbate complex and bulk Pd atom, and $G_{m,gas}$ the molar Gibbs free energy of the gas phase species. n_{Pd} and ni represent respectively the number of Pd atoms in the unit cell and the number of adsorbed molecules at the corresponding evaluated coverage. A is the surface area of the unit cell, which is multiplied by two because of the two surfaces that the slab has in the periodic DFT calculations.

The Gibbs free energy of the adsorbed complex and the bulk is calculated from the enthalpy and entropy values, as shown in eq. (A2) and eq. (A3).

$$G_{ads} = (H - T \cdot S) = \left(E_{el} + ZPVE + U^{vib}(T)\right) - T \cdot S_{vib}(T) \tag{A2}$$

$$G_{bulk} = (H - T \cdot S) = \left(E_{el} + ZPVE + U^{vib}(T)\right) - T \cdot S_{vib}(T) \tag{A3}$$

With E_{el} the electronic energy of the relaxed slab, ZPVE the zero point vibrational contributions, U_{vib} the thermal correction to the enthalpy, T the temperature, and S_{vib} the vibrational entropy. The molar gas phase Gibbs free energy, G_{gas}, accounts for the same terms as the ones in eq. (A2) and eq. (A3), and considers also the free energy contributions from the translational and rotational gas phase modes, $U^{trans+rot}$ and $S^{trans+rot}$, which are also calculated from statistical thermodynamics. Additionally, the molar gas phase Gibbs free energy includes the term that accounts for the gas phase pressure, in which k_B is the Boltzmann constant, T the temperature (K), p_i the pressure of the gas phase species i (bar), and p^o the standard pressure of 1 bar, as shown in eq. (A4).

$$G_{m,gas} = (H - T \cdot S) = [(E_{el} + ZPVE + U^{vib} + R \cdot T + U^{trans+rot})] - T \cdot (S^{vib} + S^{trans+rot}) + R \cdot T \cdot \ln \frac{p}{p^o} \qquad \text{(A4)}$$

The unit cell used in the calculation has two surfaces because a vacuum layer is included between periodic images to avoid interactions in the direction perpendicular to the slab. The Pd atoms in the upper surface are relaxed during the geometry optimization ("top surface"), on which the corresponding coverage of species *i* is adsorbed. However, the Pd atoms that compose the lower ("bottom") surface are constrained to the bulk geometry, and on this surface no species are adsorbed (i.e. *mixed slab* in Fig. S1). The electronic energy obtained from the periodic DFT calculations corresponds to the whole slab, which includes these two surfaces. Therefore, the surface free energy that can be derived from this electronic energy corresponds to an average value of these two surfaces, while only the upper one is of interest. In order to calculate an approximate value for a completely optimized single surface ($\Gamma_{el,relaxed}$), the procedure proposed by Chizallet et al. [1] was followed. The average surface energy of the mixed-surface unit cell is counted twice (*mixed slab*), and the surface energy of a completely non-optimized unit cell (*fixed slab*) is subtracted, i.e. the energy of the unit cell with all atoms in the bulk structure and without adsorbate (see eq. (A2) and Fig. A2). The result is divided by two to obtain the value for one surface, since the frequency analysis to calculate entropies and enthalpies is performed only for the relaxed surface.

$$\Gamma_{el,relaxed}(0K) = \frac{2 \cdot \left(\dfrac{E_{el,ads} - n_{Pd} \cdot E_{el,bulk} - \sum_i n_i \cdot E_{el,gas,i}}{2 \cdot A} \right)_{mixed} - \left(\dfrac{E_{el,ads} - n_{Pd} \cdot E_{el,bulk}}{2 \cdot A} \right)_{fixed}}{2} \qquad \text{(A5)}$$

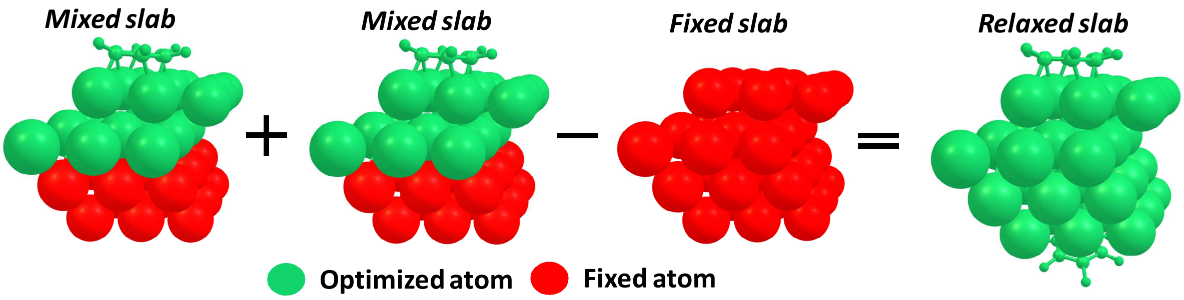

Figure A 2: Scheme illustrating the calculation of the surface free energy of a fully optimized surface, obtained from the mixed and fixed slabs. To avoid the use of an average surface free energy between an optimized and non-optimized surface, the electronic energy of the regular unit cell (with one optimized and another non-optimized surface) is counted two times, and the electronic energy of a non-optimized unit cell is subtracted.

Four different approaches have been considered to calculate surface Gibbs free energies. The first approach, i.e. *PW91-*E_{el}, assumes that the vibrational frequencies have only a small contribution to the surface Gibbs free energy. This is usually done because obtaining vibrational frequencies for adsorbed species is computationally very demanding and not always straightforward. Gibbs free energies for adsorbate and bulk are approximated by the electronic energy from the PW91 functional, neglecting all vibrational contributions and retaining only rotational and translational contributions for gas phase molecules, as shown in eq. (A6).

$$\Gamma^{PW91-E_{el}} = \Gamma_{el,relaxed} - n_i \left(\frac{\sum_i \left(U^{trans+rot} - T \cdot S^{rot+trans} + R \cdot T \cdot \ln\left(\frac{p_i}{p^o} \right) \right)_{gas,i}}{A} \right) \tag{A6}$$

The second approach, i.e. *PW91-G*, calculates the Gibbs free energy including vibrational contributions for the *ads*, *bulk* and *gas* terms, because entropy contributions to the surface Gibbs free energies may play an important role in the thermodynamic phase diagram, particularly for larger molecules such as benzene. Adsorbates are considered immobile[2] for the whole range of coverages and, therefore, Gibbs free energy contributions from translational and rotational modes are only included for gas phase species, see eq. (A7).

$$\begin{aligned}\Gamma^{PW91-G} &= \Gamma_{el,relaxed} + \frac{\left(\left(ZPVE + U^{vib}\right) - T \cdot S^{vib}\right)_{ads}}{2 \cdot A} - \frac{n_{Pd} \cdot \left(\left(ZPVE + U^{vib}\right) - T \cdot S^{vib}\right)_{bulk}}{2 \cdot A} - \\ &- n_i \left(\frac{\sum_i \left(\left(ZPVE + U^{vib} + R \cdot T + U^{trans+rot}\right) - T \cdot (S^{vib} + S^{trans+rot}) + R \cdot T \cdot \ln\left(\frac{p_i}{p^o}\right)\right)_{gas,i}}{2 \cdot A} \right)\end{aligned} \tag{A7}$$

The third *vdW-DF-E*$_{el}$ approach uses the electronic energies with the opt-PBE vdW-DF and neglects vibrational contributions, as shown in eq. (A8).

$$\Gamma^{vdW-DF-E_{el}} = \Gamma_{el,relaxed,vdW-DF} - n_i \left(\frac{\sum_i \left(U^{trans+rot} - T \cdot S^{rot+trans} + R \cdot T \cdot \ln\left(\frac{p_i}{p^o}\right)\right)_{gas,i}}{A} \right) \tag{A8}$$

The final approach gives a rough picture of the results that would be obtained if vdW-DF vibrational contributions are included and the vdW-DF method is used to calculate electronic energies. This is done by adding the PW91 vibrational contributions to the vdW-DF electronic energy term, since the vibrational contributions using the vdW-DF has not been calculated due to computational constrains. This approach is defined as *vdW-DF-G*$_{PW91}$, as is shown in eq. (A9).

$$\begin{aligned}\Gamma^{PW91-G_{PW91}} &= \Gamma_{el,relaxed,vdW-DF} + \frac{\left(\left(ZPVE + U^{vib}\right) - T \cdot S^{vib}\right)_{ads,PW91}}{2 \cdot A} - \\ &- \frac{n_{Pd} \cdot \left(\left(ZPVE + U^{vib}\right) - T \cdot S^{vib}\right)_{bulk,PW91}}{2 \cdot A} - \\ &- n_i \left(\frac{\sum_i \left(\left(ZPVE + U^{vib} + R \cdot T + U^{trans+rot}\right) - T \cdot (S^{vib} + S^{trans+rot}) + R \cdot T \cdot \ln\left(\frac{p_i}{p^o}\right)\right)_{gas,i,PW91}}{2 \cdot A} \right)\end{aligned} \tag{A9}$$

To compare the results obtained between the two first *PW91-E_{el}* and *PW91-G* approaches, surface Gibbs free energies are broken into it constituent terms, i.e. enthalpy, entropy and pressure terms, as shown in eq. (A10).

$$\Gamma = \Gamma_H + \Gamma_S - n_i \left(\frac{R \cdot T \cdot \ln\left(\frac{p_i}{p^o}\right)}{2 \cdot A} \right) \tag{A10}$$

The enthalpy and entropy terms used in *PW91-E_{el}* are respectively shown in eq. (S11) and eq. (S12), i.e. $\Gamma_H^{PW91-E_{el}}$ and $\Gamma_S^{PW91-E_{el}}$, and they are compared to the corresponding ones used in the *PW91-G* approach, see eq. (S13) and eq. (S14).

$$\Gamma_H^{PW91-E_{el}} = \Gamma_{el,relaxed}^{PW91-E_{el}} - \frac{n_i \cdot \sum_i U_{m,gas,i}^{trans+rot}}{2 \cdot A} \tag{A11}$$

$$\Gamma_S^{PW91-E_{el}} = \frac{-n_i \cdot \sum_i - T \cdot S_{m,gas,i}^{trans+rot}}{2 \cdot A} \tag{A12}$$

$$\Gamma_{\mathrm{H}}^{\mathrm{PW91-G}} = \Gamma_{\mathrm{el,relaxed}}^{\mathrm{PW91-G}} + \frac{\left(\mathrm{ZPVE} + \mathrm{U}^{\mathrm{vib}}\right)_{\mathrm{ads}} - \mathrm{n}_{\mathrm{Pd}} \cdot \left(\mathrm{ZPVE} + \mathrm{U}^{\mathrm{vib}}\right)_{\mathrm{bulk}} - \mathrm{n}_{\mathrm{i}} \cdot \sum_{\mathrm{i}} \left(\mathrm{ZPVE} + \mathrm{U}_{\mathrm{m}}^{\mathrm{vib}} + \mathrm{U}_{\mathrm{m}}^{\mathrm{trans+rot}} + \mathrm{RT}\right)_{\mathrm{gas}}}{2 \cdot \mathrm{A}} \tag{A13}$$

$$\Gamma_S^{PW91-G} = \frac{\left(-T \cdot S^{vib}\right)_{ads} - n_{Pd} \cdot \left(-T \cdot S^{vib}\right)_{bulk} - n_i \cdot \sum_i \left(-T \cdot \left(S_m^{vib} - \cdot S_m^{trans+rot}\right)\right)_{gas,i}}{2 \cdot A} \tag{A14}$$

Calculations of benzene pressure as a function of hydrogen pressure for the coadsorption of a fixed benzene coverage with increasing hydrogen coverages:

For benzene and hydrogen coadsorption, the benzene coverage has been fixed in the periodic DFT calculations, however, each condition (T,p_{H2}) requires a different benzene pressure in order to fix the benzene coverage at $\theta_B = 0.11$.

The benzene pressure has been calculated from a Langmuir model for coadsorption, as shown in eq. (S15), given a hydrogen pressure and a fixed benzene coverage, and the equilibrium coefficients at a certain temperature from the periodic DFT calculation.

$$p_B = \frac{\theta_B \cdot \sqrt{(p_{H_2} \cdot K_{H_2})} + \theta_B}{K_B - \theta_B \cdot K_B} \tag{A15}$$

The values of surface Gibbs free energies depend on both hydrogen and benzene gas-phase pressures. However, the transition line in the thermodynamic phase diagram between two consecutive coverages, which are obtained in the same unit cell and at the same benzene coverage, is not affected by benzene pressure, as it is shown in Fig. A3.

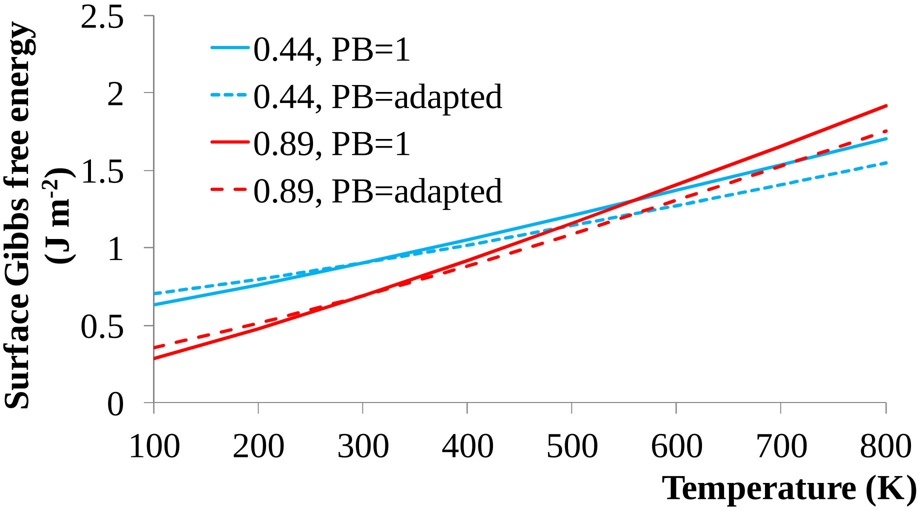

Figure A 3: Surface Gibbs free energies as a function of temperature for the coadsorption systems with benzene and $\theta_H = 0.44$ (blue) and benzene with $\theta_H = 0.89$ (red) using a benzene pressure of 1 bar (full lines) or the one obtained from a Langmuir model for benzene and hydrogen coadsorption

Calculation of the temperature for the transition between clean surface and adsorbed benzene, for the coadsorption of benzene and increasing hydrogen coverages:

The transition line from $\theta_B = 0.11$ / $\theta_H = 0$ to $\theta_B = \theta_H = 0$ is included in the thermodynamic phase diagrams for coadsorption, a transition that is clearly dependent on the pressure of benzene. This line is obtained as follows: first, for every point in the transition from benzene adsorbed (B_{ads}) to the first thermodynamic most stable coadsorbed system, T_1 temperatures in Table A 2, the pressures of benzene required to obtain $\theta_B = 0.11$ at a given temperature and hydrogen pressure are calculated using a simple Langmuir model for coadsorption, as shown in eq. (S15) and the values listed in Table A 2. The adsorption equilibrium coefficients are obtained from the DFT calculations with the corresponding functional. Assuming that for a given hydrogen pressure the obtained benzene pressures remains constant with increasing temperatures, the same Langmuir model is then used to find the temperatures at which the benzene coverage decreases to $\theta_B = 0.05$, T_2 in Table A 2, which can be used to represent the transition from the clean surface to the benzene covered surface.

Geometries evaluated for hydrogen adsorption:

For the adsorption of hydrogen up to $\theta_H = 1$, the following cases were evaluated:

a) Adsorption up to $\theta_H = 1$ on a single type of surface site (most stable case, on fcc sites)
b) Adsorption up to $\theta_H = 1$ on a single type of subsurface site
c) Every combination of two types of surface sites up to $\theta_H = 1$
d) Every combination of two types of subsurface sites up to $\theta_H = 1$
e) Every combination of surface and subsurface sites up to $\theta_H = 1$

For the adsorption of hydrogen from $\theta_H > 1$ to $\theta_H = 2$, the following cases were evaluated:

a) Combination of $\theta_H = 1$ surface hydrogen with up to $\theta_H = 1$ subsurface hydrogen (most stable)
b) Combination of $\theta_H = 1$ subsurface hydrogen with up to $\theta_H = 1$ surface hydrogen.
c) Combination of $\theta_H = 1$ surface hydrogen with up to $\theta_H = 1$ surface hydrogen on a different site.
d) Combination of $\theta_H = 1$ subsurface hydrogen with up to $\theta_H = 1$ subsurface hydrogen on a different site.

Geometries evaluated for hydrogen and benzene coadsorption:

A lesser amount of combinations were evaluated for the coadsorption with benzene due to the large number of possible cases. Conclusions from the adsorption of hydrogen alone, such as that the bridge sites are not stable at higher coverage and diffuse to hollow sites, were incorporated in the rationale what the most possible surface configuration of all the hydrogen atoms could be.

For the coadsorption up to the surface-layer saturation, i.e., $\theta_H = 0.89$, combinations of the two most stable sites (fcc and hcp) were evaluated. As an example, at $\theta_H = 0.44$ these following cases were studied:

a) Benzene + all atoms in fcc sites
b) Benzene + all atoms in hcp sites
c) Benzene + $\theta_H = 0.33$ fcc + $\theta_H = 0.11$ hcp
d) Benzene + $\theta_H = 0.11$ fcc + $\theta_H = 0.33$ hcp

e) Benzene + θ_H = 0.22 fcc + θ_H = 0.22 hcp

A similar approach was used to evaluate absorption up to the subsurface-layer saturation, but now considering combination of the three, octasubsurface, tetrasub13, and tetrasub31, sites.

For coverages above θ_H > 0.89, and up to 1.33, every combination of benzene + θ_H = 0.89 fcc + subsurface hydrogen atoms was investigated.

Above θ_H > 1.33, there are combinations that were not studied because the experience at lower coverage, the experience with hydrogen adsorption and the logic indicated that were, most possible, not the most stable. Additionally, this was evaluated in some cases to verify it, e.g. for the coadsorption of benzene + θ_H = 1.55, a case was studied in which one of the subsurface atoms was absorbed on other subsurface sites rather than the tetrasub13 site, however, the absorption of all atoms on the tetrasub13 site led always (above $\theta_H \geq 1.22$) to the most stable case. From those studied, over 100 possible geometries, the most stable ones are shown in the manuscript.

Table A 2: For each hydrogen pressure, p_{H2} in bar, temperature at which the first coadsorbed system is observed, T_1 in K, and corresponding pressure of benzene at a fixed 0.11 benzene coverage that is calculated from a Langmuir model for coadsorption using the values in the PW91-G approach. T_2 represents the temperature at which a lower benzene coverage of 0.05 is expected assuming the same benzene and hydrogen pressure.

p_{H2} (bar)	T_1		p_B (bar)		T_2	
	PW91-G	vdW-DF-E_{el}	PW91-G	vdW-DF-E_{el}	PW91-G	vdW-DF-E_{el}
10^2	979	832	1.37	$1.19\ 10^{-3}$	1069	870
10	857	724	$2.73\ 10^{-1}$	$4.65\ 10^{-5}$	951	754
1	759	639	$5.24\ 10^{-2}$	$1.74\ 10^{-6}$	850	664
10^{-1}	680	571	$9.72\ 10^{-3}$	$6.21\ 10^{-8}$	763	592
10^{-2}	615	515	$1.75\ 10^{-3}$	$2.12\ 10^{-9}$	689	533
10^{-3}	560	468	$3.05\ 10^{-4}$	$6.98\ 10^{-11}$	626	484
10^{-4}	514	428	$5.21\ 10^{-5}$	$2.22\ 10^{-12}$	571	442
10^{-5}	475	395	$8.72\ 10^{-6}$	$6.93\ 10^{-14}$	524	407
10^{-6}	441	366	$1.43\ 10^{-6}$	$2.12\ 10^{-15}$	483	377
10^{-7}	411	340	$2.29\ 10^{-7}$	$6.40\ 10^{-17}$	447	351
10^{-8}	384	318	$3.61\ 10^{-8}$	$1.89\ 10^{-18}$	416	328
10^{-9}	361	299	$5.59\ 10^{-9}$	$5.48\ 10^{-20}$	387	307
10^{-10}	341	281	$8.55\ 10^{-10}$	$1.55\ 10^{-21}$	363	289

Table A 3: Adsorption energies in kJ mol^{-1} of hydrogen adsorbed at different coverages and sites up to saturation coverage. The values obtained with the vdW-DF functional for the hollow fcc site are shown between brackets.

Site	ΔE_{ads} (kJ mol_H^{-1})			
	0.25 ML	0.5 ML	0.75 ML	1 ML
fcc	–54.2 (–43.4)	–51.5 (–40.6)	–49.5 (–38.3)	–47.9 (–36.6)
hcp	–49.3	–46.6	–44.5	–42.9
bridge	–39.2	–35.9	–32.6	–29.1
top	–1.6	1.1	3.5	7.0
octasub	–17.0	–15.6	–15.2	–14.5
tetrasub31	–17.6	–17.6	–18.4	–19.6
tetrasub13	–13.5	–13.6	–13.8	–14.4

Table A 4: Adsorption energy (kJ mol^{-1}) per mol of hydrogen for the adsorption of $0.25 \leq \Theta_H \leq 1$ hydrogen coverage on a H-covered surface with $\Theta_{H,initial} = 1$, for different combinations. The values obtained with the vdW-DF functional for the combination of $\Theta_H = 1$ hydrogen fcc and addition of $0.25 \leq \Theta_H \leq 1$ tetrasub13 hydrogen is shown between brackets.

$\Theta_{H,initial} = 1$	$0.25 \leq \Theta_H \leq 1$	ΔE_{ads} (kJ mol_H^{-1})			
		$\Theta_{H,total} = 1.25$	$\Theta_{H,total} = 1.5$	$\Theta_{H,total} = 1.75$	$\Theta_{H,total} = 2$
fcc	tetrasub31	–38.6	–32.5	–27.6	–24.2
	octasub	–38.9	–32.7	–28.0	–23.3
	tetrasub13	–39.8 (–28.3)	–34.3 (–22.6)	–30.1 (–18.4)	–26.8 (–15.1)
	hcp	–33.1	–20.0	–0.3	19.1
hcp	octasub	–36.3	–31.7	–28.0	–24.2
	tetrasub31	–30.5	–23.2	–18.0	–14.9
	tetrasub13	–36.1	–31.5	–27.9	–25.2
	fcc	–30.3	–20.0	0.0	19.1
top	octasub	5.0	3.2	1.6	0.4
	tetrasub31	7.3	6.4	4.7	2.5
	tetrasub13	5.9	4.5	2.7	1.1
octasub	fcc	–18.3	–20.8	–22.8	–23.3
	hcp	–18.4	–21.6	–23.7	–24.2
	top	–8.4	–4.4	–1.0	0.4
	tetrasub31	–5.0	–2.1	0.9	1.3
	tetrasub13	–6.7	–3.2	–1.8	–0.6
tetrasub31	fcc	–23.2	–25.3	–25.7	–24.2
	hcp	–18.9	–18.5	–17.1	–14.9
	top	–12.8	–7.6	–2.4	2.7
	octasub	–12.7	–7.3	–1.7	1.3
	tetrasub13	–14.5	–10.4	–6.8	–2.5
tetrasub13	fcc	–20.1	–23.6	–25.8	–26.8
	hcp	–19.6	–22.6	–24.4	–25.2
	top	–10.1	–5.9	–2.2	1.1

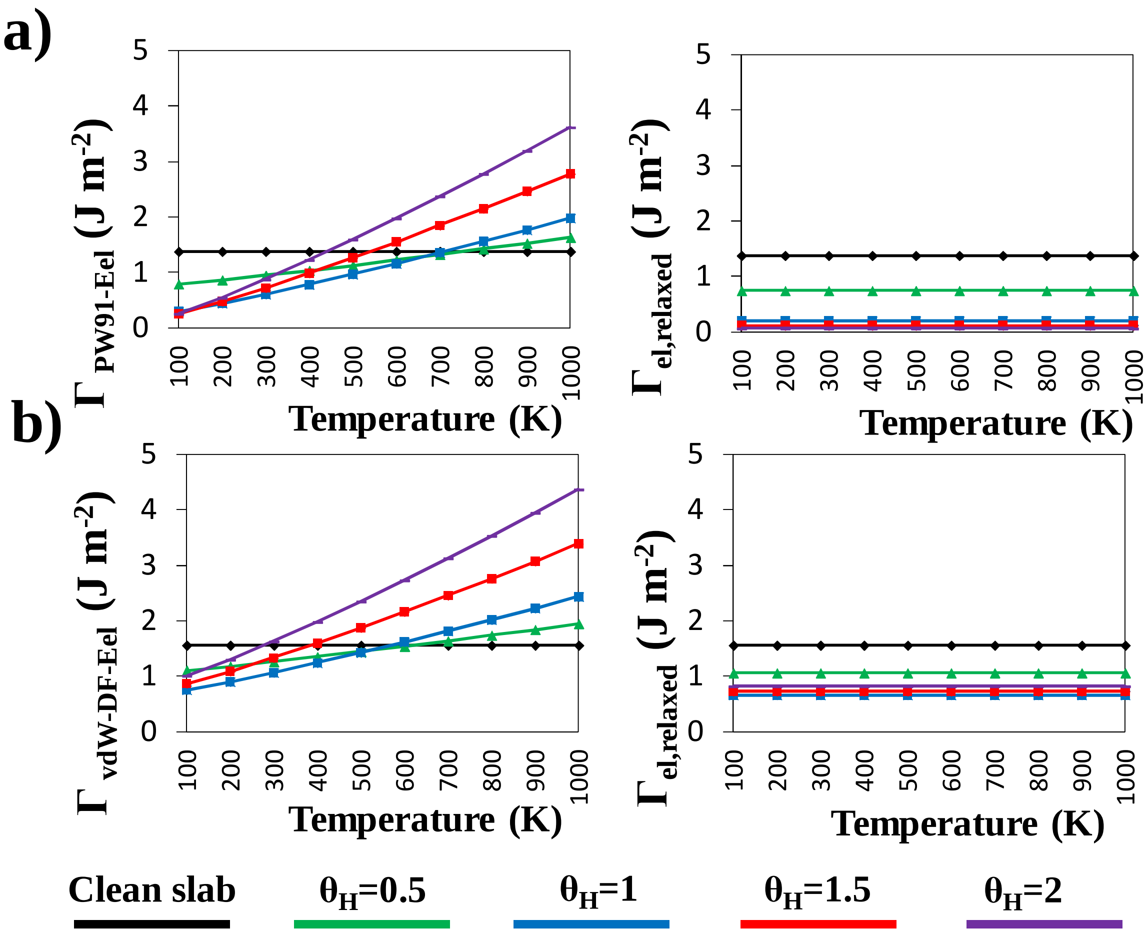

Figure A 4: Surface Gibbs free energies and electronic energy term as a function of the temperature calculated for hydrogen adsorption on Pd(111) with the (a) *PW91-E_{el}* and (b) *vdW-DF-E_{el}* approaches. The enthalpy and entropy terms in the surface Gibbs free energy are the same in both approaches, because they involve only translational and rotational modes for gas phase molecules, therefore, these are not shown.

Table A 5: Geometrical features of benzene adsorbed on different sites at θ_B=0.11. Bond distances are shown in picometer while bond angles in °.

	$d_{C\text{-}C}$	$d_{C\text{-}Pd}$	$d_{C\text{-}H}$	$d_{Benzene\text{-}1stPd}$	C-C-C	C-C-H
	pm	pm	pm	pm	(°)	(°)
bridge(0)	143	245, 217	109	220	120	118
bridge(30)	144	224, 221	109	214	117, 121	118
hollow-hcp(0)	144	225	109	220	120	118
hollow-fcc(0)	144	230	109	227	120	118
hollow-hcp(30)	143	219	109	218	120	118
hollow-fcc(30)	143	220	109	228	120	118
top(0)	147	226	110	191	120	116
top(30)	140	280	109	274	120	120

Table A 6: Geometrical features of benzene adsorbed on hollow-hcp(0) sites at increasing coverage. Bond distances are shown in picometer while bond angles in °.

	$d_{C\text{-}C}$	$d_{C\text{-}Pd}$	$d_{C\text{-}H}$	$d_{Benzene\text{-}1stPd}$	C-C-C	C-C-H
θ	pm	pm	pm	pm	(°)	(°)
$6.25\ 10^{-2}$	144	224	109	212	120	118
0.11	144	225	109	220	120	118
0.17	142	227	109	216	120	120
0.25 (tilted)	140	330	109	431	120	120

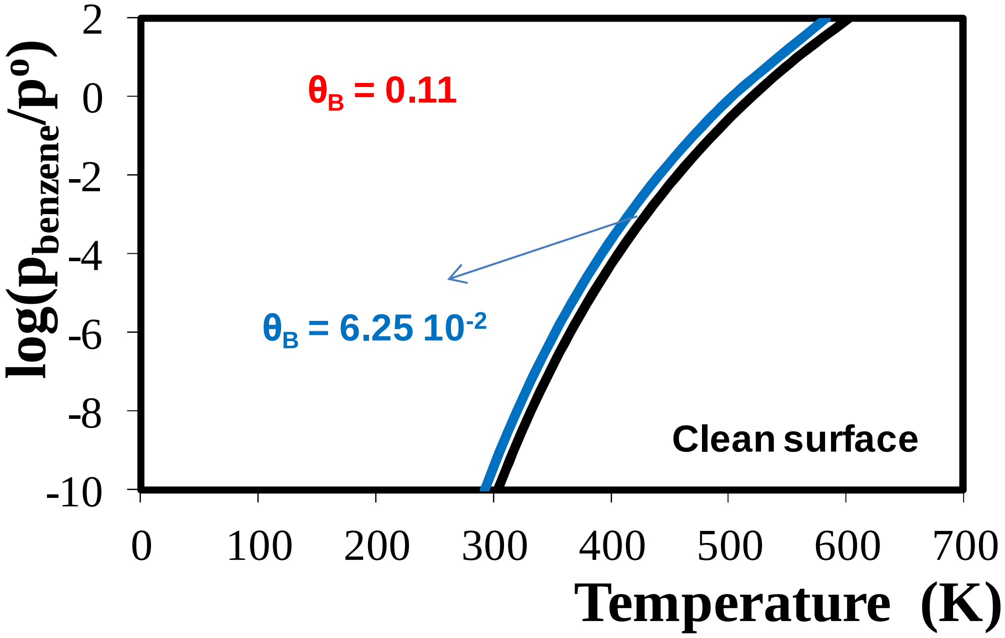

Figure A 5: Thermodynamic phase diagram of benzene adsorption at the bridge(30) site on Pd(111) as a function of temperature (K) and benzene pressure (bar) for standard pressure of p^o = 1 bar using the *PW91-E_{el}* approach.

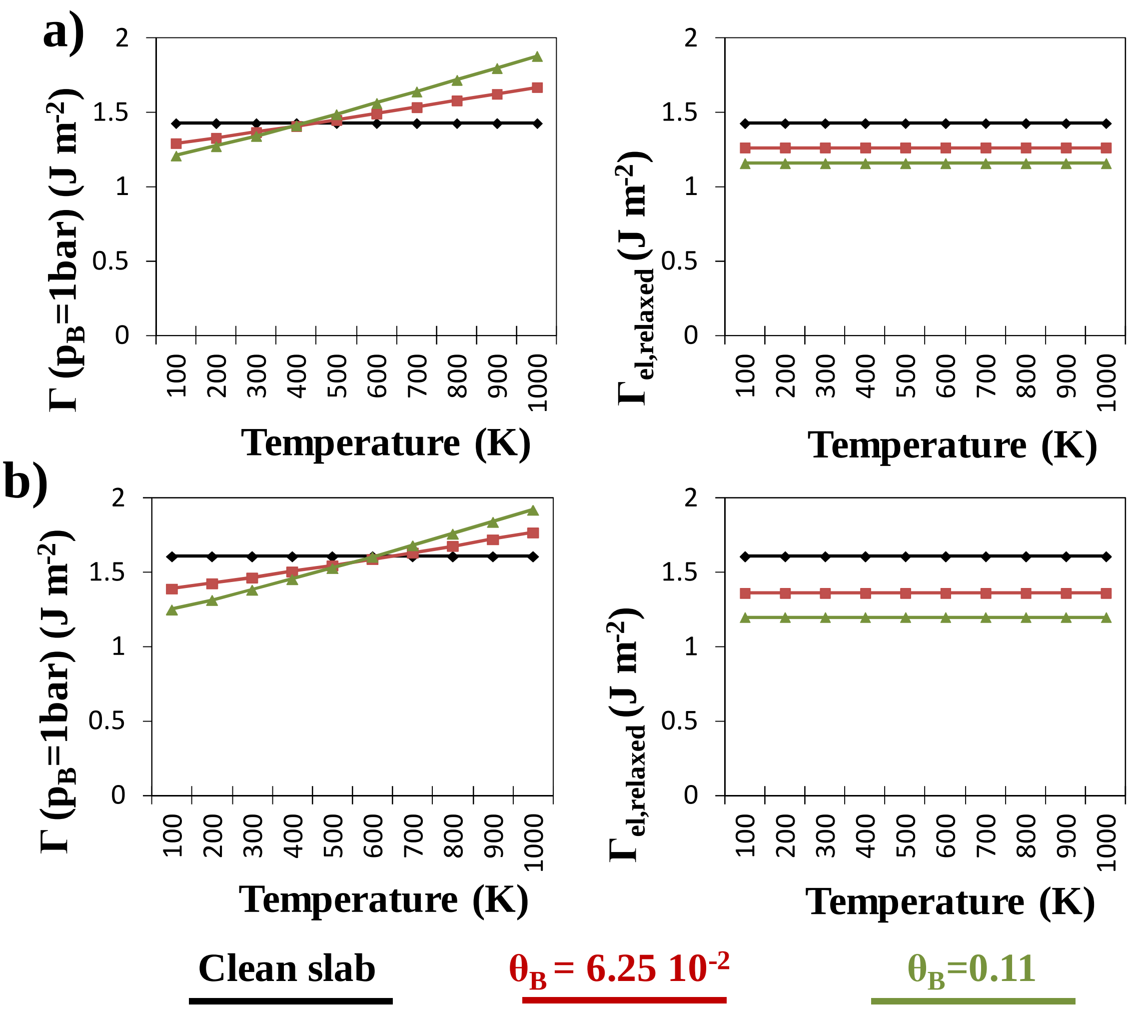

Figure A 6: Surface Gibbs free energies and electronic term for benzene adsorption on Pd(111) with the (a) *PW91-E$_{el}$* and (b) *vdW-DF-E$_{el}$* approaches. The enthalpy and entropy terms in the surface Gibbs free energy are the same in both approaches, because they involve only translational and rotational modes for gas phase molecules, therefore, these are not shown.

Table A 7: Benzene adsorption energies in kJ mol^{-1} on a pre-covered surface with hydrogen at surface and/or subsurface sites, and benzene adsorbing on bridge(30) or hollow-hcp(0) sites.

$E_{ads,benzene}$ (kJ/mol)					
Benzene + Surface hydrogen			Benzene + Subsurface hydrogen		
Hydrogen coverage	*Bridge(30)*	*Hollow–hcp(0)*	Hydrogen coverage	*Bridge(30)*	*Hollow–hcp(0)*
0	–114.9	–100.0	——	–114.9	–100.0
0.11 fcc	–106.0	–89.9	0.11 octasub	–105.7	–91.8
0.11 fcc + 0.11 hcp	–91.9	–78.8	0.22 tetrasub	–100.1	–83.7
0.22 fcc + 0.11 hcp	–77.0	–70.8	0.22 octasub + 0.11 tetrasub31	–88.9	–76.6
0.33 fcc + 0.11 hcp	–62.8	–64.4	0.44 tetrasub31	–87.1	–71.1
0.56 fcc	–42.5	–58.1	0.56 tetrasub31	–71.0	–59.3
0.67 fcc	–11.5	–27.5	0.67 tetrasub31	–70.7	–56.9
0.78 fcc	29.9	–15.1	0.78 tetrasub31	–62.1	–54.4
0.89 fcc	36.4	–13.3	0.89 tetrasub31	–62.0	–51.0
0.89 fcc+ 0.11 tetrasub31	35.0	–12.5	1 tetrasub31	–61.2	–60.8

Benzene + Surface ($\theta_{surface} = 0.89$) + Subsurface ($0.22 \leq \theta_{subsurface} \leq 1$)		
Hydrogen coverage ($\theta_{surface} + \theta_{subsurface}$)	*Bridge(30)*	*Hollow–hcp(0)*
0.89 fcc + 0.22 tetrasub13	33.7	–14.0
0.89 fcc + 0.33 tetrasub13	34.5	–15.7
0.89 fcc + 0.44 tetrasub13	27.6	–13.4
0.89 fcc + 0.56 tetrasub13	30.5	–13.3
0.89 fcc + 0.67 tetrasub13	32.8	–11.3
0.89 fcc + 0.78 tetrasub13	22.7	–10.3
0.89 fcc + 0.89 tetrasub13	24.6	–10.0
0.89 fcc + 1 tetrasub13	23.8	–11.5

Table A 8: Geometrical parameters of benzene hollow–hcp(0) and hydrogen coadsorbed on Pd(111) for hydrogen coverages between 0 (clean surface) and θ_H = 1.89. Average C-C bond length (pm), angle of C-H bond relative to the C atom at the opposite side of the ring (º), distance between the benzene centre of mass and the Pd top layer (pm), between the two first Pd layers (pm), and finally average bond distance (pm) between all hydrogen atoms, considering that fcc sites form three bonds with the Pd atoms.

θ_H	C-C (pm)	C-C-H* (º)	B-Pd (pm)	Pd1-Pd2 (pm)	H-Pd (pm)
0	143.5	164.8	209	230	––
0.11	143.4	165.1	221	231	180.7
0.22	143.2	165.5	220	232	180.9
0.33	143.1	165.7	220	232	180.4
0.44	143.0	165.8	221	233	180.2
0.56	142.7	166.8	226	234	178.0
0.67	142.2	168.8	239	235	179.2
0.78	139.8	179.5	346	233	180.5
0.89	139.7	179.8	386	233	---
1	139.7	179.8	387	235	---
1.11	139.7	179.8	398	238	---
1.22	139.7	179.8	389	243	---
1.33	139.7	179.8	385	247	---
1.44	139.7	179.8	382	251	---
1.56	139.7	179.8	379	255	---
1.67	139.7	179.8	380	259	---
1.78	139.7	179.8	383	263	---
1.89	139.7	179.8	383	268	---
Benzene gas phase	140.0	180.0	––	––	––

* Corresponding to the carbon atoms at the opposite side of the aromatic ring.

References

1. C. Chizallet, G. Bonnard, E. Krebs, L. Bisson, C. Thomazeau and P. Raybaud, *J. Phys. Chem. C*, 2011, **115**, 12135-12149.
2. B. A. De Moor, M. F. Reyniers and G. B. Marin, *Phys. Chem. Chem. Phys.*, 2009, **11**, 2939-2958.

Appendix B

Supporting information for Chapter 3

Contents. Appendix B provides the equations of the statistical thermodynamics that have been used to calculate thermodynamic properties, and those used to calculate reaction rate coefficients for Chapter 3. Furthermore, adsorption geometries, kinetics and thermodynamic parameters are shown, together with catalytic performances.

Statistical thermodynamics

Quantum mechanics consider that oscillators have a residual motion even at the absolute zero temperature, *i.e.*, the zero-point vibrational energy (ZPVE).obtained as:

$$ZPVE = \frac{1}{2} \sum_{i-1}^{3N-6} h\nu_i \tag{B1}$$

with N being the number of atoms in the system, ν_i the vibrational frequency, h the Planck constant, and $3N$–6 the degrees of vibrational freedom. The partition function Q is calculated as the product of the electronic, vibrational, translational, and rotational contributions.

$$Q = \sum_{i}^{\infty} e^{\frac{-Ei}{k_B T}} = q_{el} \cdot q_{vib} \cdot q_{trans} \cdot q_{rot} \tag{B2}$$

For gas-phase molecules, the electronic partition function q_{elec} is usually the simplest to compute, see eq. (B3), involving a sum over the electronic states from the lowest ground state up to the possible excited states. [1] For typical singlet molecules, the degeneracy (g_k) of the ground state is unity, and at temperatures below 1000 K the excited states are usually neglected because they are very high in energy as compared to the ground state.

$$q_{\mathrm{el}} = \sum_{k}^{levels} g_k \cdot e^{\frac{-E_{el}}{k_B T}} \tag{B3}$$

By convention, the ground state energy is defined to have an energy of zero,[1] therefore, the electronic partition functions is equal to one (q_{elec} = 1) and the electronic contribution is obtained by adding the electronic energy to the U(0 K), as already discussed above.

The vibrational partition function q_{vib} of a polyatomic molecule is obtained assuming that the sum of all individual energies associated with each vibrational mode of the molecule results in the total vibrational energy. To obtain this sum, the harmonic oscillator approach is considered to calculate the different modes. [2] This can be obtained by expanding the energy as function of the nuclear coordinates in a Taylor series around the equilibrium geometry. The vibrational partition function of each of the 3N–6 modes is calculated as:

$$q_{vib} = \prod_{i=1}^{3N-6} \left(\frac{1}{1 - \exp\left(\frac{-h\nu_i}{k_B T} \right)} \right) \tag{B4}$$

The contributions to the molar internal energy and molar entropy are obtained from:

$$U_{vib} = RT^2 \left(\frac{\delta \ln q_{vib}}{\delta T} \right)_V = \sum_{i=1}^{3N-6} \left(\frac{h\nu_i}{k_B \cdot \left[\exp\left(\frac{h\nu_i}{k_B T} \right) - 1 \right]} \right) \tag{B5}$$

$$S_{vib} = RT \left(\frac{\delta \ln q_{vib}}{\delta T} \right)_V + R \ln q_{vib} = R \sum_{i=1}^{3N-6} \left(\frac{h\nu_i}{k_B T \cdot \left[\exp\left(\frac{h\nu_i}{k_B T} \right) - 1 \right] - \ln\left(1 - \exp\left(\frac{-h\nu_i}{k_B T} \right) \right)} \right) \tag{B6}$$

For the molecular translational partition function of a gas-phase molecule, q_{trans}, it is assumed that the molecule moves as a particle in a three dimensional cubic box, [2] see eq. (B7).

$$q_{\text{trans}} = \left(\frac{2\pi m k_B T}{h^2}\right)^{3/2} V \tag{B7}$$

With m being the molecular mass and q_{trans} the partition function evaluated at p = 1 atm for gas-phase species. This function depends on the volume because particle in a box wave functions cannot be normalized without choice of a volume. [2] The resulting contribution to the internal energy and the molar entropy is according to the following eq. (B8) and eq. (B9), respectively.

$$U_{trans} = \frac{3}{2} RT \tag{B8}$$

$$S_{trans} = R \cdot \left(\ln q_{trans} + \frac{5}{2}\right) \tag{B9}$$

The molecular rotational partition function for gas phase molecules is calculated from eq. (B10), where I_x, I_y and I_z are the principal moments of inertia of the three principal axes, and σ is the external symmetry number, *i.e.,* the number of pure rotations that yield indistinguishable geometries.

$$q_{rot} = \frac{\sqrt{\pi I_X I_Y I_Z}}{\sigma}\left(\frac{8\pi^2 k_B T}{h^2}\right)^{3/2} \tag{B10}$$

Evaluation of the rotational components of the internal energy and entropy using the partition function gives:

$$U_{rot} = \frac{3}{2} RT \tag{B11}$$

$$S_{rot} = R\left(\ln q_{rot} + \frac{3}{2}\right) \tag{B12}$$

Rate equations

The **adsorption** of hydrocarbon molecules (BH_i) is considered to be molecular (non-dissociate adsorption), and non-activated. The adsorption rate is expressed as

$$r_{ads,BHi} = k_{ads} p_i \theta^* \tag{B13}$$

The adsorption of dihydrogen ($H_{2(g)} + 2^* \rightarrow 2H^*$) is considered to be dissociative and also non-activated. A similar expression as for the hydrocarbon molecules is used:

$$r_{ads,diss} = 2k_{ads,diss} p_i \theta^{*2} \tag{B14}$$

With p_i the pressure of the adsorbate in gas phase and θ^* the fraction free sites at the surface. Adsorption rate coefficients k_{ads} are described with the Hertz-Knudsen flux as a product of the incident molecular flux, F, and the sticking probability s, which is approximated by the initial sticking coefficient without activation, as shown in eq. (B15).

$$k_{ads} = \frac{s \cdot F}{p} = \frac{s_0}{n_t\sqrt{2\pi \cdot m \cdot k_B \cdot T}} \tag{B15}$$

With s_0 being the sticking coefficient, , p the pressure in bar, n_t the number of active sites per m^2, m the molecular mass, k_B the Boltzmann constant and T the temperature. Desorption rate coefficients are obtained using the thermodynamic equilibrium coefficient, which is calculated from the DFT adsorption enthalpies and entropies, as shown in eq. (B16).

$$k_{des} = \frac{k_{ads}}{K_{eq}} = \frac{k_{ads}}{\exp^{\left(\frac{-\Delta H_{ads}}{RT}\right)} \cdot \exp^{\left(\frac{-\Delta S_{ads}}{R}\right)}} \tag{B16}$$

With R the universal gas constant, and ΔH_{ads} and ΔS_{ads} the adsorption enthalpies and entropies in kJ mol^{-1} and J mol^{-1} K^{-1}, respectively, defined as the difference between the adsorbed complex minus the (clean or covered) surface and gas-phase species.

For the **surface** reaction: $BH_i + H \leftrightarrow BH_{i+1} + *$, the net rate is defined as the difference between the forward and the reverse rate:

$$r_{net} = r_{for} - r_{rev} = k_{for}\theta_{BHi}\theta_H - k_{rev}\theta_{BHi+1}\theta^* \tag{B17}$$

According to the Arrhenius equations, the rate coefficient has been calculated as:

$$k = A\exp\left(\frac{-E_a}{RT}\right) \tag{B18}$$

Where the pre-exponential factor A is defined as:

$$A = \frac{k_B T}{h} e \exp\left(\frac{\Delta^{\ddagger} S}{R}\right) \tag{B19}$$

And the Arrhenius activation energy for hydrogenation reactions E_a is calculated as:

$$E_a(T) = RT^2 \frac{\partial \ln k}{\partial T} = \Delta H^{\ddagger} + RT \tag{B20}$$

The standard reaction enthalpy and entropy as a function of the temperature, ΔH_r and ΔS_r, is obtained as:

$$\Delta H_r(T) = \sum_{i=1}^{prod} \nu_i H_i - \sum_{i=1}^{react} \nu_i H_i \tag{B21}$$

$$\Delta S_r(T) = \sum_{i=1}^{prod} \nu_i S_i - \sum_{i=1}^{react} \nu_i S_i \tag{B22}$$

Reverse rate coefficients are calculated from the ratio of forward and the equilibrium coefficient:

$$k_{rev} = \frac{k_{for}}{K_{eq}} \tag{B23}$$

Results for the full reaction network at low hydrogen coverage

Table B 1: Kinetic and thermodynamic parameters of each elementary hydrogenation step in the full reaction network with the PW91 functional at 450 K. Benzene adsorbs and reacts on a hollow-hcp(0) site, and the values are relative to θ_H=0.11 and θ_{BHi}=0.11 adsorbed in different unit cells.

Reaction	label	E_a (kJ mol^{-1})		A (s^{-1})		k (s^{-1})		$\Delta_r H$ (kJ mol^{-1})	$\Delta_r S$ (J mol^{-1}K^{-1})	K_{eq}
		forward	reverse	forward	reverse	forward	reverse			
B + * → B*	a							-96	-182	4.2 E+1
B*+H*→BH*	b	111	39	5.3E+14	5.46E+12	7.8E+01	1.7E+08	71.8	38.0	4.5 E-07
BH*+H*→13CHD*	c-1	85	28	6.4E+13	2.20E+12	8.8E+03	1.3E+09	57.3	28.1	6.5 E-06
BH*+H*→13DHB*	c-2	113	49	3.6E+14	1.30E+14	2.8E+01	2.5E+08	63.7	8.5	1.1 E-07
BH*+H*→14CHD*	c-3	118	41	8.7E+13	1.54E+13	1.8E+00	2.5E+08	76.6	14.4	7.2 E-09
13CHD*+H*→123THB*	d-1	94	67	3.6E+14	2.71E+12	4.4E+03	5.0E+04	27.3	40.7	8.9 E-02
13CHD*+H*→124THB*	d-2	107	40	4.2E+14	2.06E+13	1.7E+02	4.4E+08	66.4	25.0	3.9 E-07
13DHB*+H*→123THB*	d-3	90	69	1.6E+15	1.13E+12	5.9E+04	1.2E+04	21.0	60.2	5.1 E+00
13DHB *+H*→124THB*	d-4	94	34	7.8E+14	3.69E+12	8.7E+03	3.8E+08	60.0	44.5	2.3 E-05
13DHB *+H*→135THB	d-5	126	46	7.2E+14	3.60E+13	1.6E+00	1.8E+08	80.6	24.9	8.9 E-09
14CHD *+H*→124THB	d-6	83	36	5.5E+14	5.28E+12	1.1E+05	3.2E+08	47.1	38.6	3.6 E-04
123THB*+H*→CHE*	e-1	82	22	1.7E+14	6.24E+11	4.8E+04	1.6E+09	59.9	46.8	3.1 E-05
123THB*+H*→1235THB *	e-2	132	45	1.1E+14	8.34E+12	6.0E-02	4.6E+07	86.2	21.6	1.3 E-09
124THB*+H*→CHE*	e-3	86	65	7.9E+14	4.33E+11	7.6E+04	1.1E+04	20.8	62.5	7.0 E+00
124THB*+H*→1235THB *	e-4	102	55	1.1E+15	1.29E+13	1.5E+03	4.9E+06	47.1	37.3	3.0 E-04
123THB*+H*→1245THB*	e-5	100	40	1.2E+15	9.40E+12	3.1E+03	2.3E+08	60.2	40.5	1.3 E-05
135THB*+H*→1235THB *	e-6	97	74	3.4E+14	3.57E+11	1.7E+03	1.0E+03	23.9	56.9	1.6 E+00
CHE*+H*→C-hexyl*	f-1	78	47	1.8E+14	2.34E+13	1.8E+05	9.0E+07	31.0	17.1	2.0 E-03
1235THB *+H*→C-hexyl*	f-2	83	79	6.4E+14	3.92E+12	1.4E+05	3.0E+03	4.6	42.3	4.7 E+01
1245THB *+H*→C-hexyl*	f-3	96	102	1.0E+15	2.23E+13	7.9E+03	3.7E+01	-5.7	32.0	2.2 E+02
C-hexyl*+H*→CHA*	g	70	61	2.2E+16	1.36E+12	1.7E+08	1.2E+05	9.1	80.6	1.4 E+03
CHA + * → CHA*	h							-13	-117	2.7 E-05

Table B 2: Kinetic and thermodynamic parameters of each elementary hydrogenation step in the full reaction network with the PW91 functional at 450 K. Benzene adsorbs and reacts on a bridge(30) site, and the values are relative to θ_{H}=0.11 and θ_{BHi}=0.11 adsorbed in different unit cells.

Reaction	label	E_a (kJ mol^{-1})		A (s^{-1})		k (s^{-1})		$\Delta_r H$ (kJ mol^{-1})	$\Delta_r S$ (J mol^{-1}K^{-1})	K_{eq}
		forward	reverse	forward	reverse	forward	reverse			
B + * → B*	a							-113	-194	9.6 E+02
$B^{*}+H^{*} \rightarrow BH^{*}$	b	119	34	7.7E+14	3.7E+13	1.1E+01	4.2E+09	85.4	25.3	2.6 E-09
$BH^{*}+H^{*} \rightarrow 13CHD^{*}$	c-1	100	48	2.0E+15	4.7E+12	4.6E+03	1.4E+07	52.6	50.4	3.4 E-04
$BH^{*}+H^{*} \rightarrow 13DHB^{*}$	c-2	115	46	3.0E+15	1.2E+13	1.2E+02	5.8E+07	69.6	45.9	2.1 E-06
$BH^{*}+H^{*} \rightarrow 14CHD^{*}$	c-3	123	41	1.7E+15	3.0E+13	9.9E+00	4.9E+08	81.3	33.4	2.0 E-08
$13CHD^{*}+H^{*} \rightarrow 123THB^{*}$	d-1	117	82	1.3E+14	1.4E+12	3.1E+00	4.0E+02	35.4	38.2	7.6 E-03
$13CHD^{*}+H^{*} \rightarrow 124THB^{*}$	d-2	146	33	4.0E+14	6.1E+12	5.0E-03	9.8E+08	113.0	34.8	5.1 E-12
$13DHB^{*}+H^{*} \rightarrow 123THB^{*}$	d-3	87	69	5.3E+14	3.1E+12	4.0E+04	3.2E+04	18.4	42.7	1.2 E+00
$13DHB^{*}+H^{*} \rightarrow 124THB^{*}$	d-4	92	-4	2.3E+14	2.1E+12	5.2E+03	6.3E+12	95.9	39.3	8.3 E-10
$13DHB^{*}+H^{*} \rightarrow 135THB$	d-5	123	43	7.7E+13	5.6E+13	4.3E-01	6.1E+08	80.1	2.6	6.9 E-10
$14CHD^{*}+H^{*} \rightarrow 124THB$	d-6	101	17	1.8E+15	3.6E+12	3.1E+03	3.7E+10	84.2	51.8	8.5 E-08
$123THB^{*}+H^{*} \rightarrow CHE^{*}$	e-1	82	32	1.4E+14	1.1E+12	4.0E+04	2.0E+08	50.1	40.4	2.0 E-04
$123THB^{*}+H^{*} \rightarrow 1235THB^{*}$	e-2	131	43	2.7E+14	1.5E+13	1.5E-01	1.3E+08	88.1	24.2	1.1 E-09
$124THB^{*}+H^{*} \rightarrow CHE^{*}$	e-3	63	91	7.3E+14	3.8E+12	3.3E+07	1.1E+02	-27.4	43.7	2.9 E+05
$124THB^{*}+H^{*} \rightarrow 1235THB^{*}$	e-4	56	45	1.3E+15	4.6E+13	4.1E+08	2.5E+08	10.6	27.6	1.6 E+00
$123THB^{*}+H^{*} \rightarrow 1245THB^{*}$	e-5	63	41	1.3E+15	2.5E+13	6.5E+07	4.2E+08	21.7	32.7	1.5 E-01
$135THB^{*}+H^{*} \rightarrow 1235THB^{*}$	e-6	90	53	6.7E+15	1.6E+12	2.3E+05	1.3E+06	37.6	69.4	1.8 E-01
$CHE^{*}+H^{*} \rightarrow C\text{-}hexyl^{*}$	f-1	87	45	2.0E+15	3.1E+14	1.4E+05	2.0E+09	42.6	15.3	7.1 E-05
$1235THB^{*}+H^{*} \rightarrow C\text{-}hexyl^{*}$	f-2	79	74	5.8E+14	6.6E+12	3.7E+05	1.8E+04	5.4	37.1	2.0 E+01
$1245THB^{*}+H^{*} \rightarrow C\text{-}hexyl^{*}$	f-3	96	102	1.0E+15	2.2E+13	7.9E+03	3.7E+01	-5.7	32.0	2.2 E+02
$C\text{-}hexyl^{*}+H^{*} \rightarrow CHA^{*}$	g	64	62	1.0E+15	1.8E+12	4.1E+07	1.3E+05	2.2	52.7	3.1 E+02
CHA + * → CHA*	h							-18	-157	8.1 E-07

Table B 3: Rate of production coefficient for the reactions in the dominant path at different temperatures, and using the values relative to θ_H=0.11 and θ_{BHi}=0.11 adsorbed in different unit cells.

Reaction	X_{ROP}			
	350 K	**400 K**	**450 K**	**500 K**
b	1.00	1.00	1.00	1.00
c1	0.86	0.83	0.81	0.80
c2	0.14	0.17	0.19	0.20
d1	0.86	0.83	0.81	0.80
d3	0.14	0.17	0.19	0.20
e1	1.00	1.00	1.00	1.00
f1	1.00	1.00	1.00	1.00
g	1.00	1.00	1.00	1.00

Table B 4: Sensitivity coefficients for the reactions in the dominant path at different temperatures, and using the values relative to θ_H=0.11 and θ_{BHi}=0.11 adsorbed in different unit cells.

Reaction	X_{SA}		
	350 K	**450 K**	**550 K**
b	0.0	0.0	0.0
c1	0.0	0.0	0.0
d1	0.99	0.77	0.19
e1	0.0	0.0	0.0
f1	0.01	0.23	0.79
g	0.0	0.0	0.02

Table B 5: Electronic barriers (kJ mol^{-1}) for the reactions in the dominant path (b1,c1, and d1) and for the alternative reactions, with the difference as compared to the corresponding reaction in the dominant path in the right column.

	θ_H=0.11 and θ_{BHi}=0.11				θ_H=0.44 and θ_{BHi}=0.11	
	PW91		**optPBE-vdW**		**optPBE-vdW**	
Reaction	$E_{el,a}$	$\Delta E_{el,a}$	$E_{el,a}$	$\Delta E_{el,a}$	$E_{el,a}$	$\Delta E_{el,a}$
	kJ mol^{-1}		**kJ mol^{-1}**		**kJ mol^{-1}**	
c1	85	0	97	0	62	0
c2	113	28	115	18	92	30
c3	117	32	120	23	93	31
d1	94	0	95	0	81	0
d2	110	16	110	15	106	25
e1	82	0	82	0	69	0
e2	131	49	131	49	103	34

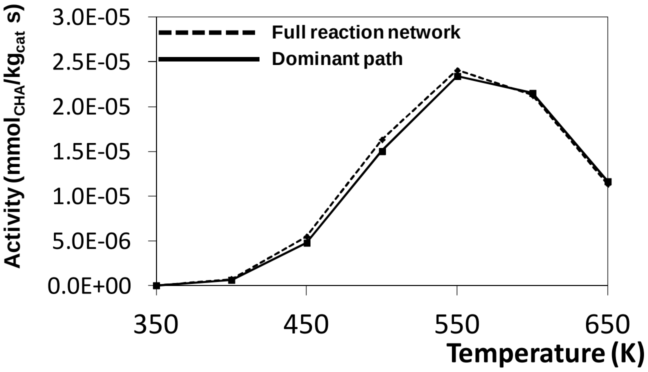

Figure B 1: Catalytic activity (mmol$_{CHA}$ kg$_{cat}^{-1}$ s^{-1}) as a function of the temperature for the full reaction network and the dominant path (dotted and full line, respectively) (W/F_B^0 = 62.5 kg s mol^{-1}; F_B^0 = 0.074 mol h^{-1}; F_{H2}^0 = 1.0 mol h^{-1}, p_B^0 = 6.7 × 10^{-2} bar; p_{H2}^0 = 0.9 bar), using the values relative to θ_H=0.11 and θ_{BHi}=0.11 adsorbed in different unit cells.

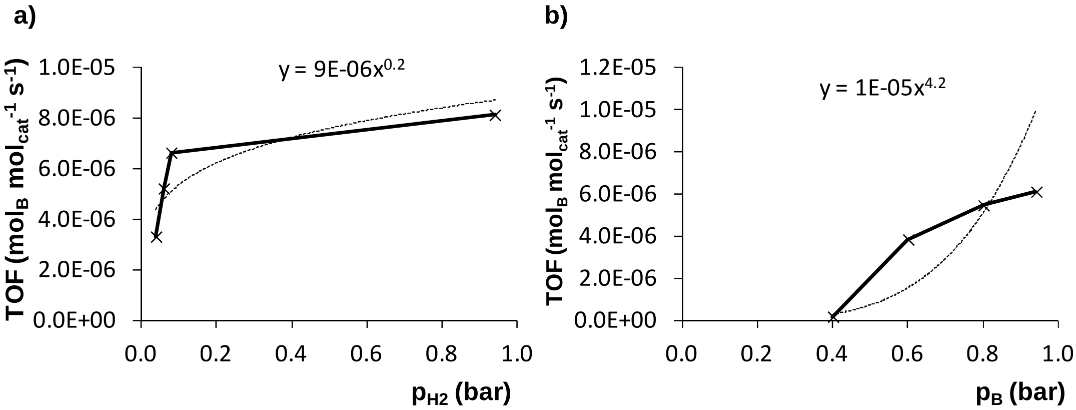

Figure B 2: Turnover frequency as a function of (a) hydrogen and (b) benzene partial pressure, at T = 450 K, and for a fixed (a) p_B^0 = 6.7 × 10^{-2} bar and (b) p_{H2}^0 = 0.9 bar, and using the values relative to θ_H=0.11 and θ_{BHi}=0.11 adsorbed in different unit cells.

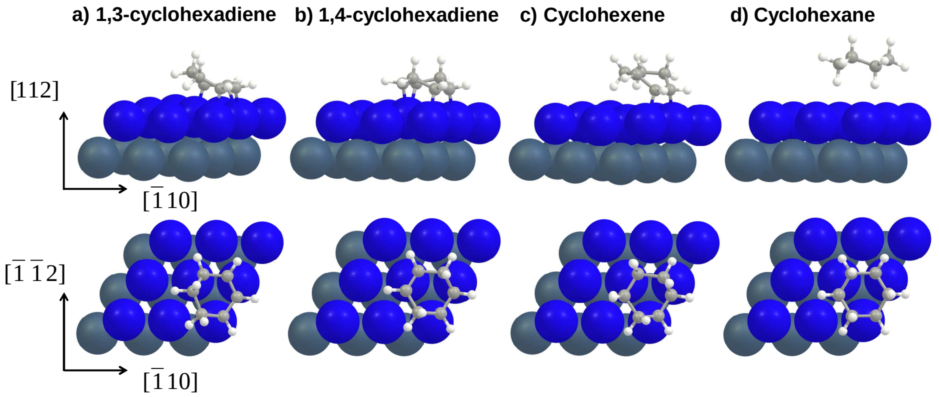

Figure B 3: Side and top view of the adsorption geometry of (a) 1,3-cyclohexadiene, (b) 1,4-cyclohexadiene, (c) cyclohexene and (d) cyclohexane on a clean surface. Pd atoms in the second layer are colored in grey for easier visualization

DFT results for the dominant path at increasing θ_H

Table B 6: Benzene, 1,3-cyclohexadiene, cyclohexene and cyclohexane adsorption enthalpies and entropies for the adsorption on a clean Pd(111) surface, and pre-covered with 0.11, 0.44 and 0.67 hydrogen, calculated with DFT calculations using the optPBE-vdW functional, and the corresponding values calculated with the PW91 functional are shown between brackets.

	ΔH_{ads} (kJ mol^{-1})				ΔS_{ads}(J mol^{-1} K^{-1})			
	Hydrogen coverage covering the surface				Hydrogen coverage pre-covering the surface			
	θ_H=0	θ_H=0.11	θ_H=0.44	θ_H=0.67	θ_H=0	θ_H=0.11	θ_H=0.44	θ_H=0.67
Dihydrogen	(–125) –102	(–112) –102	(–88) –91	(–57) –90	(–191) –137	(–191) –137	(–138) –132	(–134) –135
Benzene	(–96) –163	(–86) –155	(–66) –136	(–1) –78	(–182) –180	(–163) –178	(–188) –179	(–178) –145
1,3-cyclohexadiene	(–117) –173	(–110) –169	(–91) –152	(–35) –100	(–197) –192	(–170) –198	(–191) –203	(–195) –191
Cyclohexene	(–69) –109	(–62) –104	(–54) –97	(–18) –66	(–169) –170	(–144) –174	(–175) –175	(–183) –175
Cyclohexane	(–15) –81	(–11) –81	(–13) –84	(–1) –78	(–116) –126	(–97) –114	(–120) –112	(–120) –122

Table B 7: Activation energy and pre-exponential factor (kJ mol^{-1} and s^{-1}, respectively) for the forward reactions of the dominant path as a function of the hydrogen coverage coadsorbed with the hydrocarbon reactant, calculated with the PW91 functional.

	E_a (kJ mol^{-1})				A (s^{-1})			
	θ_H=0	θ_H=0.11	θ_H=0.44	θ_H=0.67	θ_H=0	θ_H=0.11	θ_H=0.44	θ_H=0.67
B* + H* ↔ BH* + *	109	99	96	73	$8.9\ 10^{15}$	$8.2\ 10^{14}$	$1.1\ 10^{14}$	$1.5\ 10^{14}$
BH* + H* ↔ 1,3CHD* + *	85	76	58	54	$6.4\ 10^{13}$	$1.1\ 10^{13}$	$1.8\ 10^{13}$	$1.1\ 10^{13}$
1,3CHD * + H* ↔ 1,2,3-THB* + *	94	87	81	84	$3.6\ 10^{14}$	$7.9\ 10^{13}$	$3.5\ 10^{13}$	$1.6\ 10^{14}$
1,2,3-THB* + H* ↔ CHE* + *	82	73	66	49	$1.7\ 10^{14}$	$8.6\ 10^{12}$	$1.6\ 10^{13}$	$2.3\ 10^{13}$
CHE* + H* ↔ C-hexyl* + *	78	71	64	46	$1.8\ 10^{14}$	$8.7\ 10^{12}$	$5.4\ 10^{13}$	$6.8\ 10^{13}$
C-hexyl* + H* ↔CHA* + *	70	62	52	22	$2.2\ 10^{16}$	$4.0\ 10^{16}$	$2.6\ 10^{14}$	$2.3\ 10^{13}$

Table B 8: Reaction enthalpy, reaction entropy (kJ mol^{-1} , kJ mol^{-1}K^{-1}) and equilibrium coefficient for the forward reactions of the dominant path as a function of the hydrogen coverage coadsorbed with the hydrocarbon reactant, calculated with the PW91 functional.

	ΔH_r (kJ mol^{-1})				ΔS_r (J mol^{-1} K^{-1})				K_{eq}			
	θ_H=0	θ_H=0.11	θ_H=0.44	θ_H=0.67	θ_H=0	θ_H=0.11	θ_H=0.44	θ_H=0.67	θ_H=0	θ_H=0.11	θ_H=0.44	θ_H=0.67
B* + H* ↔ BH* + *	72	62	52	31	38	18	17	1	$4.4\ 10^{-7}$	$6.1\ 10^{-7}$	$7.7\ 10^{-6}$	$2.8\ 10^{-4}$
BH* + H* ↔ 1,3CHD* + *	57	48	17	6	28	14	18	2	$6.5\ 10^{-6}$	$1.4\ 10^{-5}$	$1.0\ 10^{-1}$	$2.7\ 10^{-1}$
1,3CHD * + H* ↔ 1,2,3-THB* + *	27	21	8	-14	41	28	18	6	$8.9\ 10^{-2}$	$1.2\ 10^{-1}$	$9.7\ 10^{-1}$	$9.5\ 10^{1}$
1,2,3-THB* + H* ↔ CHE* + *	60	50	39	6	47	22	25	12	$3.1\ 10^{-5}$	$2.1\ 10^{-5}$	$6.2\ 10^{-4}$	$9.7\ 10^{-1}$
CHE* + H* ↔ C-hexyl* + *	28	21	23	-1	56	31	6	10	$5.3\ 10^{-1}$	$1.6\ 10^{-1}$	$5.0\ 10^{-3}$	4.6
C-hexyl* + H* ↔CHA* + *	12	4	-21	-58	41	46	79	59	5.3	78	$3.5\ 10^{6}$	$6.3\ 10^{9}$

Table B 9: Activation energy and pre-exponential factor (kJ mol^{-1} and s^{-1}, respectively) for the forward reactions of the dominant path as a function of the hydrogen coverage coadsorbed with the hydrocarbon reactant, calculated with the optPBE-vdW functional.

	E_a (kJ mol^{-1})				A (s^{-1})			
	θ_H=0	θ_H=0.11	θ_H=0.44	θ_H=0.67	θ_H=0	θ_H=0.11	θ_H=0.44	θ_H=0.67
B* + H* ↔ BH* + *	110	103	98	70	$7.6\ 10^{13}$	$6.9\ 10^{13}$	$3.4\ 10^{13}$	$1.0\ 10^{13}$
BH* + H* ↔ 1,3CHD* + *	97	91	60	54	$1.4\ 10^{13}$	$1.3\ 10^{13}$	$1.2\ 10^{13}$	$2.1\ 10^{13}$
1,3CHD * + H* ↔ 1,2,3-THB* + *	95	91	84	54	$2.5\ 10^{13}$	$4.8\ 10^{13}$	$1.3\ 10^{14}$	$1.7\ 10^{14}$
1,2,3-THB* + H* ↔ CHE* + *	81	75	67	47	$2.1\ 10^{13}$	$6.4\ 10^{12}$	$1.5\ 10^{13}$	$1.1\ 10^{13}$
CHE* + H* ↔ C-hexyl* + *	81	77	70	51	$2.4\ 10^{13}$	$3.6\ 10^{13}$	$3.5\ 10^{13}$	$7.8\ 10^{13}$
C-hexyl* + H* ↔CHA* + *	71	69	57	25	$4.8\ 10^{13}$	$3.7\ 10^{13}$	$3.8\ 10^{13}$	$1.5\ 10^{13}$

Table B 10: Reaction enthalpy, reaction entropy (kJ mol^{-1} , kJ mol^{-1}K^{-1}) and equilibrium coefficient for the forward reactions of the dominant path as a function of the hydrogen coverage coadsorbed with the hydrocarbon reactant, calculated with the optPBE-vdW functional.

	ΔH_r (kJ mol^{-1})				ΔS_r (J mol^{-1} K^{-1})				K_{eq}			
	θ_H=0	θ_H=0.11	θ_H=0.44	θ_H=0.67	θ_H=0	θ_H=0.11	θ_H=0.44	θ_H=0.67	θ_H=0	θ_H=0.11	θ_H=0.44	θ_H=0.67
B* + H* ↔ BH* + *	62	55	45	27	0	–1	–2	–26	$9.0\ 10^{-7}$	$6.3\ 10^{-6}$	$4.8\ 10^{-6}$	$3.5\ 10^{-5}$
BH* + H* ↔ 1,3CHD* + *	49	43	9	–2	14	14	0	14	$6.8\ 10^{-7}$	$5.8\ 10^{-5}$	$9.0\ 10^{-2}$	10.0
1,3CHD * + H* ↔ 1,2,3-THB* + *	21	17	4	–19	6	12	22	13	$7.4\ 10^{-3}$	$4.3\ 10^{-2}$	4.6	786
1,2,3-THB* + H* ↔ CHE* + *	50	43	32	–3	22	12	19	4	$2.2\ 10^{-5}$	$3.9\ 10^{-5}$	$1.9\ 10^{-3}$	4.0
CHE* + H* ↔ C-hexyl* + *	23	19	16	–8	0	4	–1	10	$2.3\ 10^{-3}$	$1.1\ 10^{-2}$	$1.2\ 10^{-2}$	29.5
C-hexyl* + H* ↔CHA* + *	2	0	–20	–58	34	32	48	29	33	51	$6.2\ 10^{4}$	$2.1\ 10^{8}$

Values used to construct the microkinetic model

Table B 11: 1,3-cyclohexadiene, cyclohexene and cyclohexane adsorption enthalpies and entropies on a clean Pd(111) surface, and pre-covered with 0.11, 0.44 and 0.67 hydrogen calculated used in the coverage-dependent microkinetic model. The values have been calculated with the optPBE-vdW functional, and adapted to match experimental equilibrium coefficient from NIST coefficients.

	ΔH_{ads} (kJ mol^{-1})				ΔS_{ads}(J mol^{-1} K^{-1})			
	Hydrogen coverage covering the surface				Hydrogen coverage pre-covering the surface			
	θ_H=0	θ_H=0.11	θ_H=0.44	θ_H=0.67	θ_H=0	θ_H=0.11	θ_H=0.44	θ_H=0.67
1,3-cyclohexadiene	-189	-185	-168	-116	-200	-205	-211	-198
Cyclohexene	-125	-121	-113	-83	-177	-180	-182	-182
Cyclohexane	-95	-95	-98	-92	-126	-114	-112	-122

Table B 12: Adsorption enthalpies and entropies (kJ mol^{-1} and J mol^{-1} K^{-1}, respectively) for θ_H=0.11 hydrogen adsorption on a covered surface with the product of each elementary reaction step in the dominant path ($BH_i + \theta_{H,final} + \theta_H \leftrightarrow BH_i + \theta_{H,initial}$).

	$\Delta H_{ads,H}$ (kJ mol^{-1})			$\Delta S_{ads,H}$ (J mol^{-1}K^{-1})		
	$\theta_{H,initial}$ = 0.11	$\theta_{H,initial}$ = 0.44	$\theta_{H,initial}$ = 0.67	$\theta_{H,initial}$ = 0.11	$\theta_{H,initial}$ = 0.44	$\theta_{H,initial}$ = 0.67
$BH_1 + \theta_{H,final} + \theta_H \leftrightarrow BH_1 + \theta_{H,initial}$	-54	-23	-19	-68	-61	-73
$BH_2 + \theta_{H,final} + \theta_H \leftrightarrow BH_2 + \theta_{H,initial}$	-56	-44	-26	-74	-71	-70
$BH_3 + \theta_{H,final} + \theta_H \leftrightarrow BH_3 + \theta_{H,initial}$	-53	-48	-24	-58	-76	-71
$BH_4 + \theta_{H,final} + \theta_H \leftrightarrow BH_4 + \theta_{H,initial}$	-56	-47	-34	-72	-68	-62
$BH_5 + \theta_{H,final} + \theta_H \leftrightarrow BH_5 + \theta_{H,initial}$	-57	-54	-22	-66	-73	-65
$BH_6 + \theta_{H,final} + \theta_H \leftrightarrow BH_6 + \theta_{H,initial}$	-60	-53	-45	-56	-58	-68
Average value used for H_2 adsorption	-112	-90	-57	-131	-136	137

Table B 13: Coefficients used in the coverage-dependent model to perform regression of the adsorption enthalpy and entropy of the different species to a third-order polynomial as a function of the total coverage $\theta_{total.}$

	$E_{ads} = a\theta_{total}^3+b\theta_{total}^2+c\theta_{total}+d$				$S_{ads}= a\theta_{total}^3+b\theta_{total}^2+c\theta_{total}+d$			
	a	b	c	d	a	b	c	d
Hydrogen	219	-204	121	-131	240	-358	150	-150
Benzene	559	-517	193	-165	431	-399	103	-187
1,3-cyclohexadiene	401	-319	109	-198	77	8	-59	-193
Cyclohexene	352	-350	125	-135	-77	126	-65	-171
Cyclohexane	126	-128	30	-97	237	-456	244	-148

Table B 14: Coefficients used in the coverage-dependent model to perform regression of the activation energy and entropy for the six forward hydrogenation steps to a third-order polynomial as a function of the total coverage $\theta_{total.}$

	$E_{a,f} = a\theta_{total}^3+b\theta_{total}^2+c\theta_{total}+d$				$\Delta^{\ddagger}S_f= a\theta_{total}^3+b\theta_{total}^2+c\theta_{total}+d$			
	a	b	c	d	a	b	c	d
B* + H* ↔ BH* + *	-465	532	-205	127	-44	18	-10	10
BH* + H* ↔ 1,3CHD* + *	308	-354	32	98	52	-34	-2	-4
1,3CHD * + H* ↔ 1,2,3-THB* + *	-358	357	-125	105	47	-98	78	-8
1,2,3-THB* + H* ↔ CHE* + *	-298	347	-150	94	-473	675	-274	21
CHE* + H* ↔ C-hexyl* + *	-231	246	-101	90	184	-231	91	-8
C-hexyl* + H* ↔CHA* + *	-238	184	-64	76	-165	193	-71	11

Table B 15: Coefficients used in the coverage-dependent model to perform regression of the activation energy and entropy for the six reverse hydrogenation steps to a third-order polynomial as a function of the total coverage θ_{total}

	$E_{a,r} = a\theta_{total}^3+b\theta_{total}^2+c\theta_{total}+d$				$\Delta^{\ddagger}S_r= a\theta_{total}^3+b\theta_{total}^2+c\theta_{total}+d$			
	a	b	c	d	a	b	c	d
B* + H* ↔ BH* + *	-199	208	-52	51	248	-251	62	5
BH* + H* ↔ 1,3CHD* + *	21	-2	-1	48	-328	374	-96	-13
1,3CHD * + H* ↔ 1,2,3-THB* + *	-196	217	-55	78	170	-165	40	-9
1,2,3-THB* + H* ↔ CHE* + *	109	-72	14	31	140	-123	29	-25
CHE* + H* ↔ C-hexyl* + *	142	-156	39	56	-128	143	-36	2
C-hexyl* + H* ↔CHA* + *	-69	114	-32	71	412	-473	121	-37

References

1. F. Jensen, *Introduction to computational chemistry,* 2nd edn., John Wiley & Sons, Chichester, England ; Hoboken, NJ, 2007.
2. C. J. Cramer, *Essentials of computational chemistry: theories and models,* 2nd edn., Wiley, Chichester, West Sussex, England ; Hoboken, NJ, 2004.

Appendix C

Supporting information for Chapter 4

Contents. Appendix C includes adsorption geometries for benzene on both Pd(100) and Pd(110) surfaces, together with vibrational frequencies and density of states. All figures and tables correspond to Chapter 4.

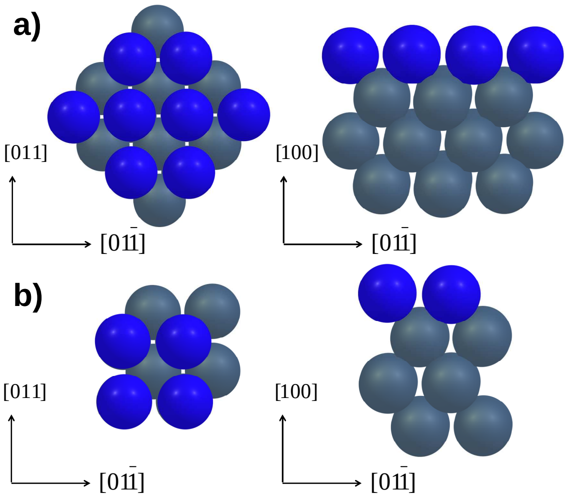

Figure C 1: Top (left) and side (right) views of the unit cells used to investigate medium and saturation coverage of benzene on Pd(100), *i.e.* the a) (2√2×2√2)R45° and b) (2×2). Only Pd atoms in the top layer are colored blue for easier visualization.

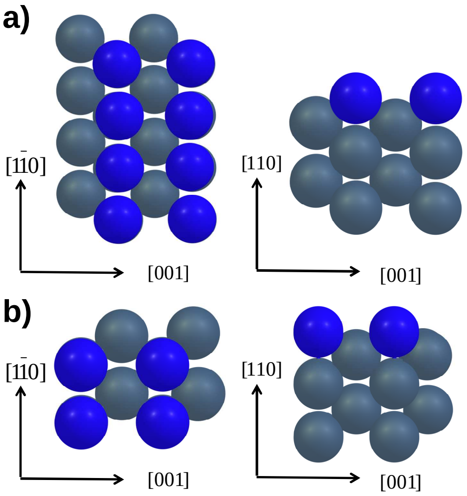

Figure C 2: Top (left) and side (right) views of the unit cells used to investigate medium and saturation coverage of benzene on Pd(110), *i.e.* the (a) p(4×2) and (b) c(4×2) surface overlayers. Only Pd atoms in the top layer are colored blue for easier visualization.

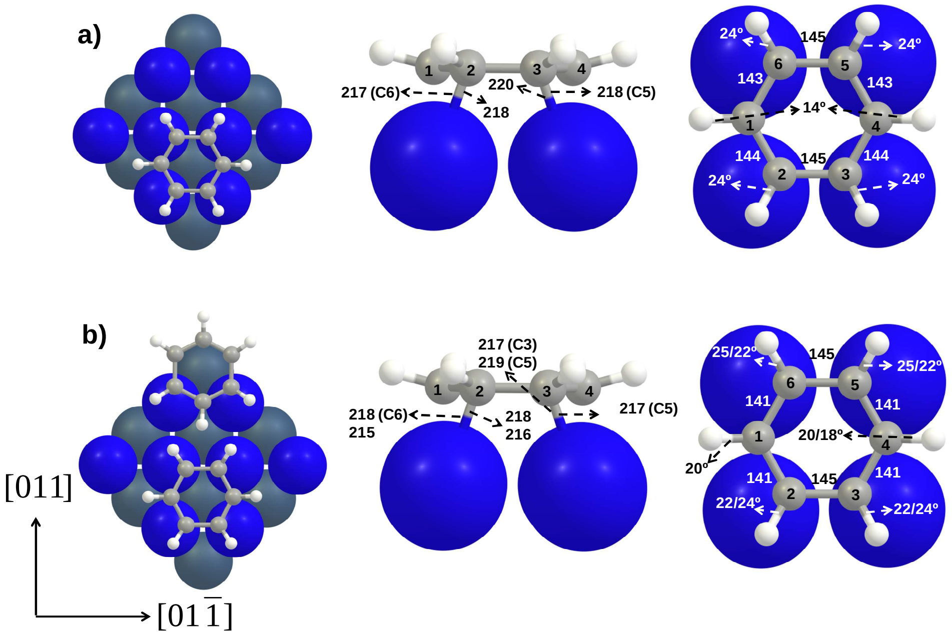

Figure C 3: Geometrical characteristics of benzene adsorbed at the hollowA site on Pd(100) at (a) medium and (b) saturation coverages. The left panels show the top view of the unit cell used. Middle panels depict the front view of benzene adsorbed on the active site, and C-Pd bonds are indicated in pm. Right panels show the top view of the benzene adsorbed on the active site with the C-C bond lengths (pm) and C-H angles (°). At saturation coverage (bottom panels) there are two benzene molecules on the same unit cell, therefore, distances and angles for the second benzene molecule are given in case they differ from those for the molecule shown.

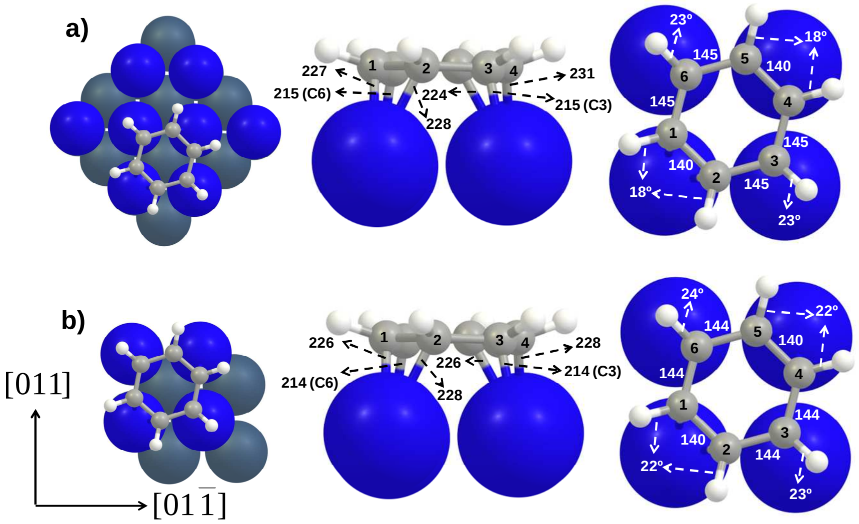

Figure C 4: Geometrical characteristics of benzene adsorbed at the hollowB site on Pd(100) at a) medium and b) saturation coverage. The left panels show the top view of the unit cell used. Middle panels depict the front view of benzene adsorbed on the active site, and C-Pd bonds are indicated in pm. Right panels show the top view of the benzene adsorbed on the active site with the C-C bond lengths (pm) and C-H angles (°).

Table C 1: Vibrational modes, with the corresponding frequency in cm^{-1}, identified for the hollowA and hollowB adsorption sites of benzene on Pd(100) at medium and saturation coverage, and compared to the experimental HREELS values for saturation coverage at 300 K reported by Waddill et al. [1]

Vibrational mode	Vibrational frequency, cm^{-1}				
	HollowA		HollowB		
	Medium	Saturation	Medium	Saturation	Exp. [1]
νCM	303, 327	290	337	254, 370	280 and 435
δCC	472, 557	448, 589	460, 563	448, 587	---
γCH, out-of-plane	709, 860	721, 927	720, 927	715, 837	720 and 870
δCH, in-plane	1109	1176	1118	1157	1115
νCC	1418	1442	1454	1320, 1520	1320 (νCC) and 1425 (δCC)
νCH	3096	3079, 3371	3096	3002, 3220	3010

Table C 2: Bond lengths (pm) and angles (º) for the different adsorption sites of benzene on Pd(100) at medium coverage.

	d_{C-C}	$d\pi_{C-Pd}$	$d\sigma_{C-Pd}$	d_{C-H}	$d_{Benzene-1stPd}$	$d_{1st–2nd-Pdlayer}$	C-C-C	C-C-H
	pm	pm	pm	pm	pm	pm	(º)	(º)
HollowA	143/145	217-220		109	213	199	119-121	14-24
HollowB	142/145	227-231	215	108-109	212	201	119-121	18-23
BridgeA	143	221-242		109	229	198	120	9-13
BridgeB	142-143	222-265		109-110	215	198	120	9-15
BridgeC	142-144	222-244		109-110	215	198	120-121	11-13
Top	142-145	264-279		109-110	208	198	119-122	12-17

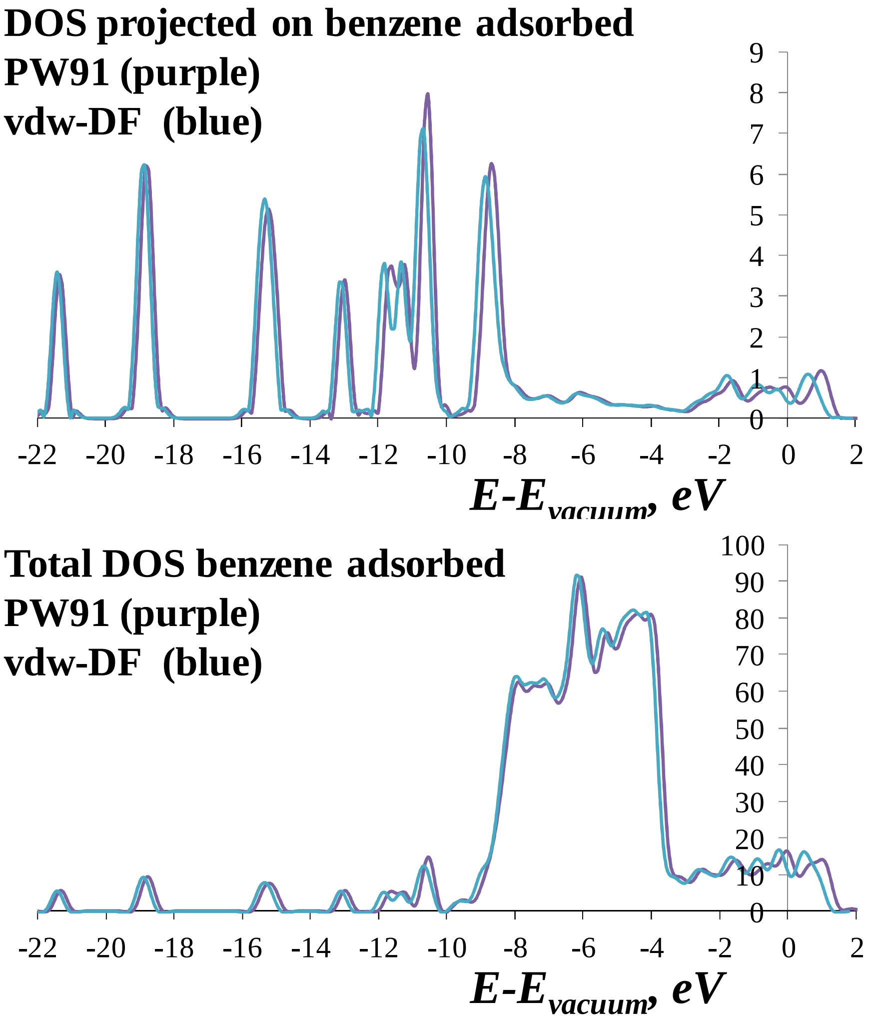

Figure C 5: Comparison of the DOS projected on benzene adsorbed and total DOS (top and bottom resp.) between the results from PW91 and vdw-DF approaches (purple and blue lines).

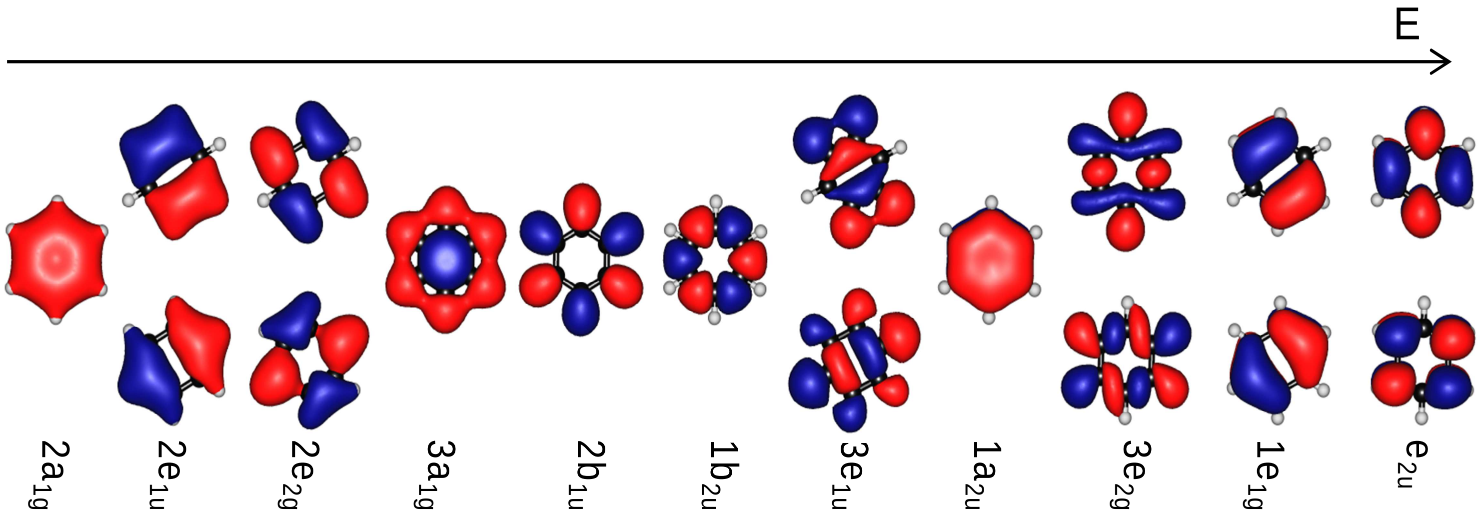

Figure C 6: Molecular orbitals of gas phase benzene.

Table C 3: Calculated energies of molecular eigenstates of benzene in gas phase, adsorbed at the hollowA and hollowB sites on Pd(100) at medium and saturation coverage. Energies are related to the vacuum level.

		Medium coverage		Saturation coverage	
Orbital	Benzene gas	hollowA	hollowB	hollowA’	hollowB
$1e_{1g}$ (π)	– 6.0	–8.8	–8.9	–8.8	–8.7
$3e_{2g}$	– 8.0	–9.0	–9.0	– 9.0	– 8.9
$1a_{2u}$ (π)	– 8.8	–10.7	–11.0	– 10.7	– 10.4
$3e_{1u}$	– 10.0	–11.5	–10.9	– 10.6	– 10.8
$1b_{2u}$	– 10.6	–11.7	–11.5	– 11.2	– 11.6
$2b_{1u}$	– 11.0	–12.4	–12.0	– 11.7	– 12.2
$3a_{1g}$	– 12.6	–13.8	–13.3	– 13.0	– 13.4
$2e_{2g}$	– 14.6	–16.1	–16.3	– 15.6	– 15.8
$3e_{1u}$	– 18.3	–19.2	–19.4	– 19.2	– 19.2
$2a_{1g}$	– 21.1	–22.4	–22.2	– 21.9	– 22.0

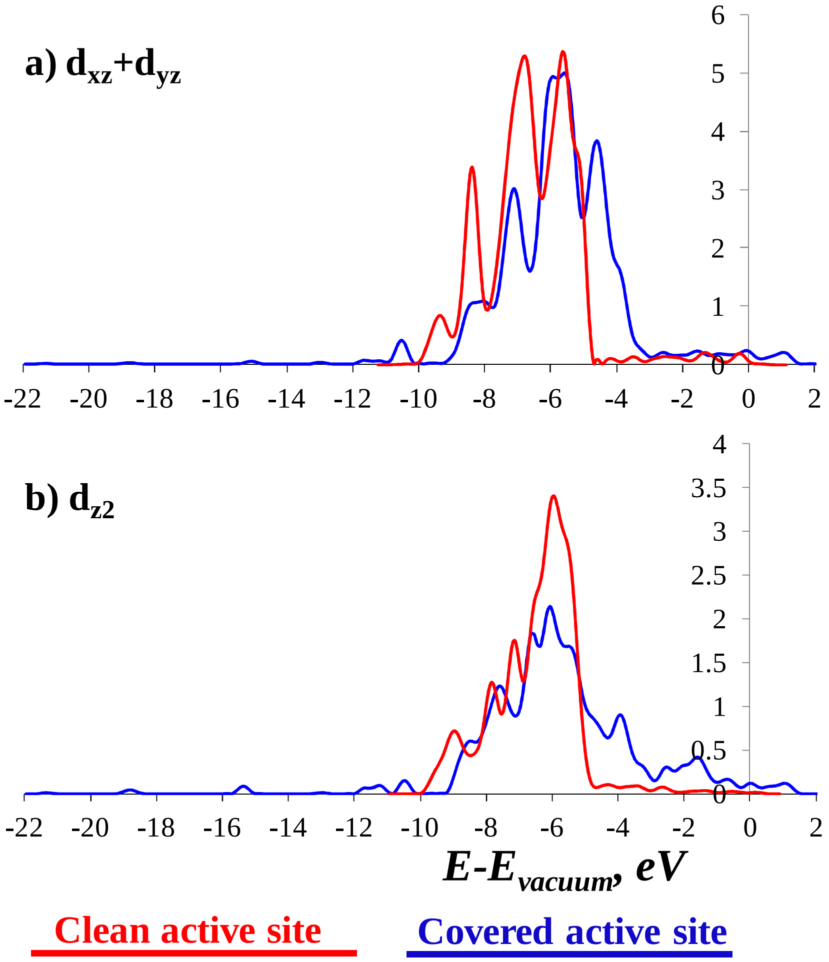

Figure C 7: DOS projected on the d_{xz}+d_{yz} (a window) and on the d_{z2} (b window) of the Pd(100) atoms at the bare and hollowA covered active site (red and blue lines resp.).

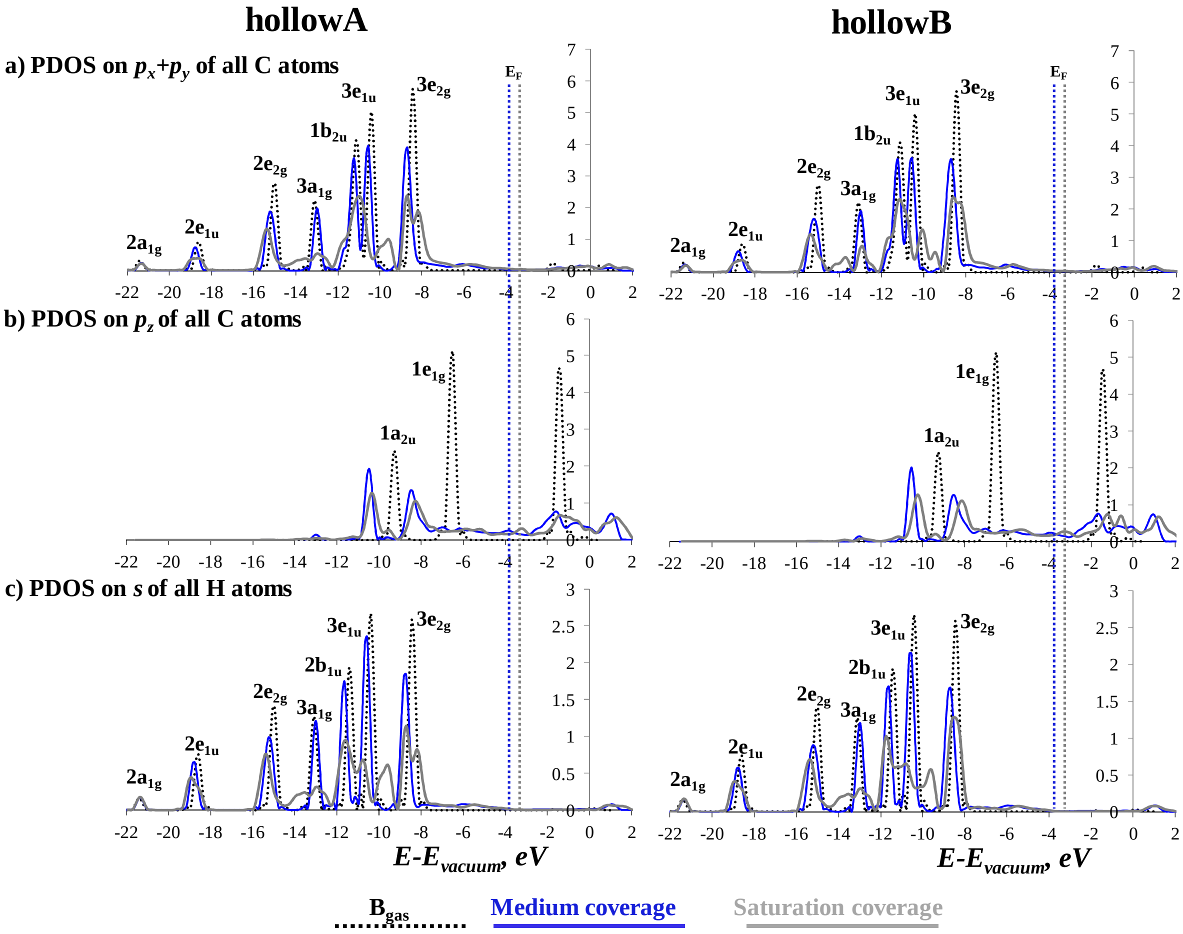

Figure C 8: a) DOS projected on the p_x+p_y orbitals of all carbon atoms of benzene. b) DOS projected on the p_z orbitals of all carbon atoms of benzene. c) DOS projected on the s orbitals of all hydrogen atoms of benzene. All energies are related to the vacuum level and the Fermi level is indicated in dotted lines for the three plots. The dotted black lines represent the gas phase orbitals, while the full blue and grey lines correspond to the medium and saturation coverage on Pd(100).

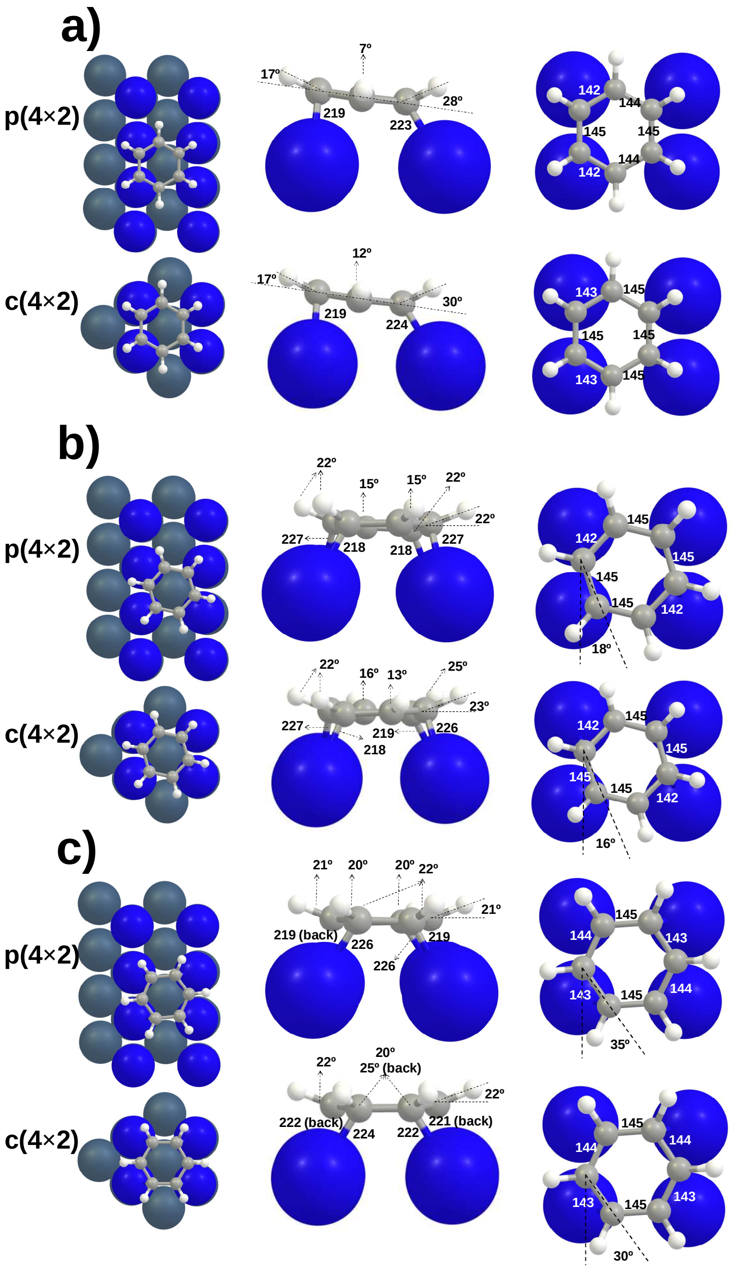

Figure C 9: Adsorption geometries of the a) hollow(0), b) hollow(15) and c) hollow(30) adsorbates on Pd(110) at medium and saturation coverage (resp. p(4×2) and c(4×2) overlayers). From left to right: top view of benzene adsorbed on the corresponding unit cell, side view of the adsorption on the active site with indication of C-Pd bond lengths (pm) and C-H bonds angles relative to the C-plane (°), and top view of the active site with C-C bond lengths indicated (pm). Only Pd atoms in the top layer are colored blue for easier interpretation.

Table C 4: Vibrational modes, with the corresponding frequency in cm^{-1}, identified for the adsorption sites of benzene on Pd(110) compared to the experimental specular HREELS values at 300 K reported by Fujisawa et al.[2].

Vibrational mode	Vibrational frequency, cm^{-1}						
	Hollow(0)		Hollow(15)		Hollow(30)		
	Medium	Saturation	Medium	Saturation	Medium	Saturation	Exp. [2]
νCM	324, 418	327, 412	317, 414	412	403	400	350, ~460
δCC	562	---	558	557	562	563	---
γCH, out-of-plane	637, 746, 861*	618, 734, 873*	647, 740, 818*	673, 806, 890*	681, 832*	684, 873*	705 (flat), 745 (tilted), 890
δCH, in-plane	1124, 1319	1097, 1321	1117, 1293	1109, 1295	1113, 1297	1109	~1150
νCC	1423	1412	1455	1466	1448	1400	1340, 1460, ~1580
νCH	3102	3097	3091	3090	3095	3096	3050

* Mixure of γCH (out-of-plane) and νCC (ring deformation) from the visualization of the mode, in agreement with [2]

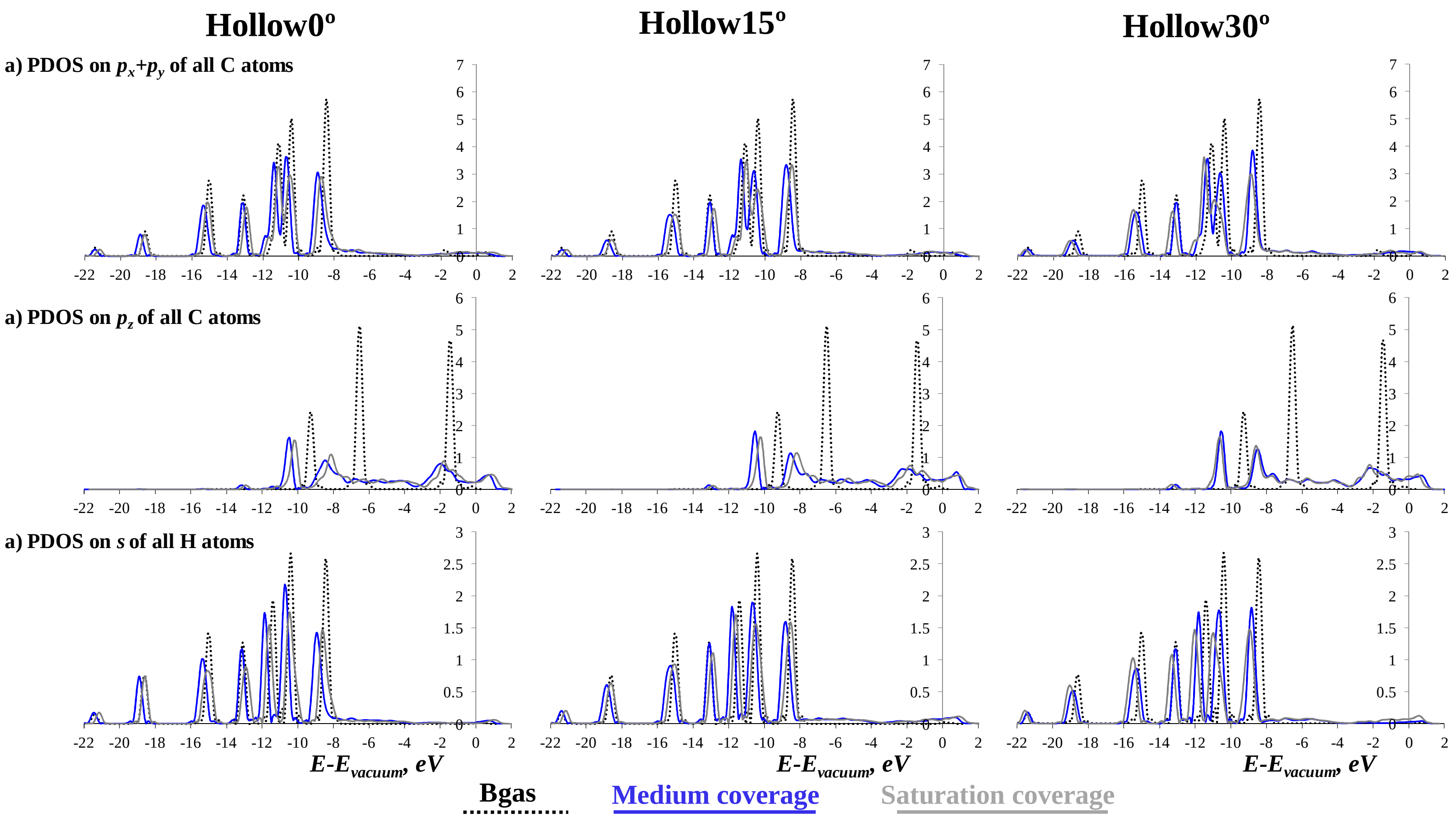

Figure C 10: a) DOS projected on the p_x+p_y orbitals of all carbon atoms of benzene. b) DOS projected on the p_z orbitals of all carbon atoms of benzene. c) DOS projected on the s orbitals of all hydrogen atoms of benzene, for the hollow0º, hollow15º and hollow30º adsorption sites from left to right. All energies are related to the vacuum level. The dotted black lines represent the gas phase orbitals, while the full blue and grey lines correspond to the medium and saturation coverage of benzene on Pd(110).

Table C 5: Calculated energies of molecular eigenstates of benzene in gas phase, adsorbed at the hollow(0) site on Pd(110) at medium and saturation coverage, *i.e.* p(4×2) and c(4×2) surface overlayers. Energies are related to the vacuum level.

		Hollow(0)	
Orbital	Benzene gas	p(4×2)	c(4×2)
$1e_{1g}$ (π)	– 6.0	-8.6	-8.3
$3e_{2g}$	– 8.0	-8.9	-8.7
$1a_{2u}$ (π)	– 8.8	-10.5	-10.3
$3e_{1u}$	– 10.0	-10.7	-10.6
$1b_{2u}$	– 10.6	-11.4	-11.3
$2b_{1u}$	– 11.0	-12.0	-11.9
$3a_{1g}$	– 12.6	-13.2	-13.1
$2e_{2g}$	– 14.6	-15.6	-15.4
$2e_{1u}$	– 18.3	-19.1	-18.9
$2a_{1g}$	– 21.1	-21.6	-21.4

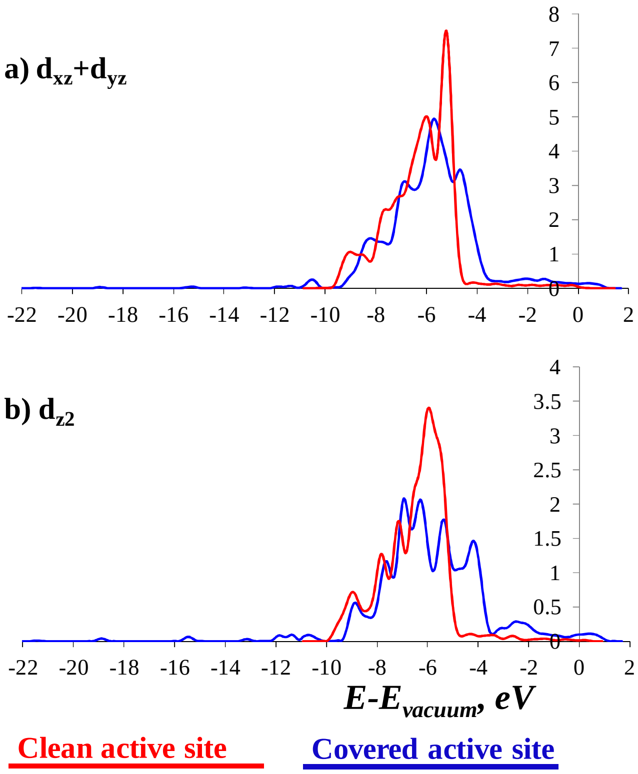

Figure C 11: DOS projected on the d_{xz}+d_{yz} (a window) and on the d_{z2} (b window) of the Pd(110) atoms at the bare and hollow(0) covered active site (red and blue lines resp.)

References

1. G. D. Waddill and L. L. Kesmodel, *Phys. Rev. B: Condens. Matter Mater. Phys.*, 1985, **31**, 4940-4946.
2. M. Fujisawa, T. Sekitani, Y. Morikawa and M. Nishijima, *J. Phys. Chem.*, 1991, **95**, 7415-7422.

Appendix D

Supporting information for Chapter 5

Contents. Appendix D includes segregation energies for the evaluated bimetallic catalysts, together with a description of the adsorption of carbon, correlations between benzene and carbon adsorption energies, the methodology applied to study the reactivity of the different catalysts, and finally the approach to implement the observed trends in a microkinetic model.

Segregation energies

Table D 1: (Anti)segregation energies for the different bimetallic bulk alloys evaluated for the clean surface and covered with benzene. Initially the most stable state is shown for the clean surface in the left column, with the corresponding segregation energy. The segregation energy with benzene adsorbed is also listed, indicating if a change in the segregation state is expected.

Pd_3M, non-segregated	ΔE^{clean}_{anti} (kJ mol^{-1})	$\Delta E^{ads}_{antiseg}$ (kJ mol^{-1})	Restructured with B_{ads}
Pd_3Ti	72.8	---	No
Pd_3Cr	167.5	---	No
Pd_3Mn	13.3	90	No
Pd_3Zr	191.2	---	No
Pd_3Hf	207.6	---	No
Pd_3Pt	-0.4	-3	No
Pd_3M, antisegregated	$\Delta E_{antiseg}$ (kJ mol^{-1})	$\Delta E^{ads}_{antiseg}$ (kJ mol^{-1})	Restructured with B_{ads}
Pd_3V	-31.0	---	No
Pd_3Fe	-22.5	-70.2	No
Pd_3Co	-53.4	---	No
Pd_3Ni	-25.7	-80.2	No
Pd_3Nb	-35.9	---	No
Pd_3Mo	-142.5	---	No
Pd_3Tc	-149.5	---	No
Pd_3Ru	-113.7	---	No
Pd_3Rh	-42.4	---	No
Pd_3Ta	-32.9	---	No
Pd_3W	-213.0	---	No
Pd_3Re	-239.7	---	No
Pd_3Os	-151.0	---	No
Pd_3Ir	-73.0	---	No
Ni_3M, antisegregated	$\Delta E_{antiseg}$ (kJ mol^{-1})	$\Delta E^{ads}_{antiseg}$ (kJ mol^{-1})	Restructured with B_{ads}
Ni_3Cr	-75.9	---	No
Ni_3Co	-23.2	-100.2	No
Ni_3Ru	-11.9	-198.2	No
Ni_3Re	-147.5	---	No
Ni_3Os	-101.2	---	No
Ni_3M, partially segregated	ΔE_{seg} (kJ mol^{-1})	ΔE^{ads}_{seg} (kJ mol^{-1})	Restructured with B_{ads}
Ni_3Rh	-11.9	-17.2	No
Ni_3Pd	-30.2	-65.5	No
Ni_3Ir	-0.2	+25.5	Yes, non-segregated
Ni_3Pt	-16.0	+4.5	Yes, non-segregated

Carbon adsorption on the different alloys

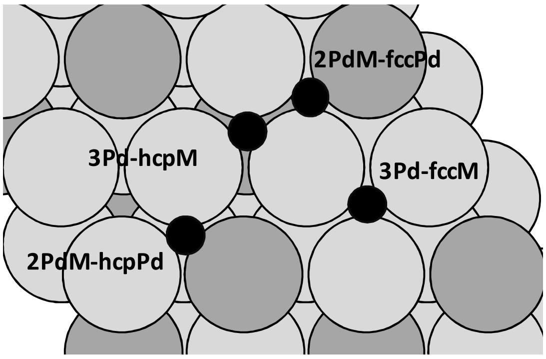

Figure D 1: Adsorption sites for carbon on non-segregated bimetallic alloys.

Table D 2: Adsorption energies (kJ mol^{-1}) of carbon on different adsorption sites on Pd_3Pt and Pd_3Cr non-segregated catalysts, and the values for the two most stable sites on other non-segregated alloys. The adsorption sites are represented in Figure D 1.

Sites	ΔE_{ads} (kJ mol^{-1})				
	Pd_3Pt	Pd_3Cr		3Pd-fccM	2PdM-fccPd
3Pd-hcpM	-627.8	-328.3	Pd_3Ti	-493.6	-542.3
2PdM-hcpPd	-669.0	-581.9	Pd_3Cr	-609.1	-609.0
3Pd-fccM	-635.3	-609.1	Pd_3Mn	-642.5	-388.9
2PdM-fccPd	-666.1	-609.0	Pd_3Zr	-462.5	-512.6
			Pd_3Hf	-457.2	-508.7
			Pd_3Pt	-609.1	-609.0

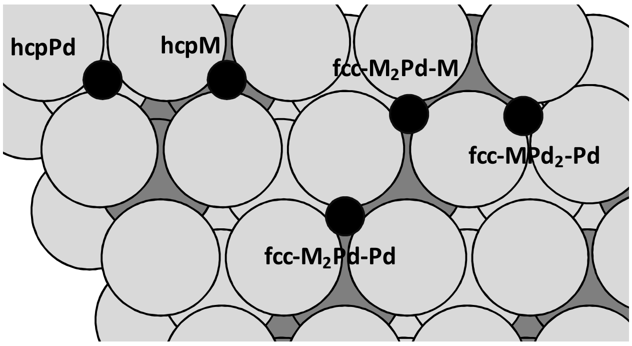

Figure D 2: Adsorption sites for carbon on antisegregated bimetallic alloys

Table D 3: Adsorption energies (kJ mol^{-1}) of carbon on different adsorption sites on Pd$_3$Rh antisegregated catalyst, and the values for the most stable site on other antisegregated alloys. The adsorption sites are represented in Figure D 2.

Sites	ΔE_{ads} (kJ mol^{-1})			
	Pd$_3$Rh	Antisegregated alloys	hcpM	hcpPd
hcpM	-636.7	Pd$_3$V	-547.1	-552.6
hcpPd	-632.1	Pd$_3$Fe	-585.8	-587.7
fcc-M$_2$Pd-M	-625.6	Pd$_3$Co	-598.7	-597.7
fcc-MPd$_2$-Pd	-622.4	Pd$_3$Ni	-612.2	-610.6
fcc-M$_2$Pd-Pd	-629.3	Pd$_3$Nb	-546.7	-554.7
		Pd$_3$Mo	-561.4	-585.5
		Pd$_3$Tc	-582.6	-602.8
		Pd$_3$Ru	-606.9	-617.8
		Pd$_3$Rh	-636.7	-632.1
		Pd$_3$Ta	-527.9	-544.1
		Pd$_3$W	-542.5	-572.8
		Pd$_3$Re	-555.9	-591.0
		Pd$_3$Os	-567.8	-589.0
		Pd$_3$Ir	-614.5	-630.1

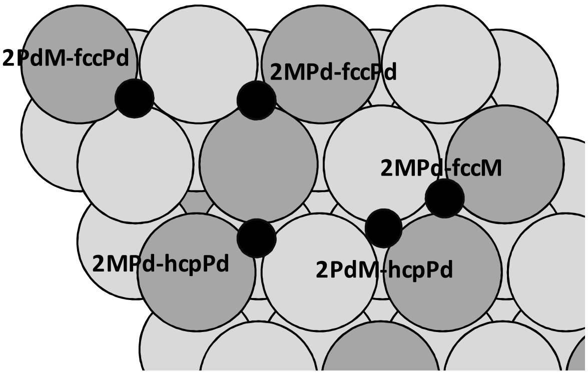

Figure D 3: Adsorption sites for carbon on partially segregated bimetallic alloys.

Table D 4: Adsorption energies (kJ mol^{-1}) of carbon on different adsorption sites on Pd$_3$Rh antisegregated catalyst, and the values for the most stable site on other antisegregated alloys. The adsorption sites are represented in Figure D 3.

Partially segregated	ΔE_{ads} (kJ mol^{-1}) Ni$_3$Pd	Alloys	ΔE_{ads} (kJ mol^{-1}) 2MNi-fccM
2NiM-fccNi	-619.3	Ni$_3$Rh	-622.6
2MNi-fccNi	-586.8	Ni$_3$Pd	-606.8
2MNi-fccM	-620.6		
2NiM-hcpNi	-606.8		
2MNi-hcpNi	-560.7		
Antisegregated	ΔE_{ads} (kJ mol^{-1}) Ni$_3$Cr	Alloys	ΔE_{ads} (kJ mol^{-1}) hcpNi
hcpM	-609.6	Ni$_3$Cr	-656.7
hcpNi	-656.7	Ni$_3$Co	-692.3
fcc-M$_2$Ni-M	-645.7	Ni$_3$Ru	-694.2
fcc-MNi$_2$-Ni	-631.5	Ni$_3$Re	-679.5
fcc-M$_2$Ni-Ni	-645.2	Ni$_3$Os	-694.2
Non-segregated*	---	Alloys	ΔE_{ads} (kJ mol^{-1}) 2NiM-fccNi
		Ni$_3$Ir	-693.4
		Ni$_3$Pt	-660.4
* Corresponding to alloys that show partial segregation of the clean surface and non-segregation with benzene adsorbed. Only the adsorption on the most stable adsorption site obtained for Pd$_3$M non-segregated alloys has been studied.			

Correlation between benzene and carbon adsorption

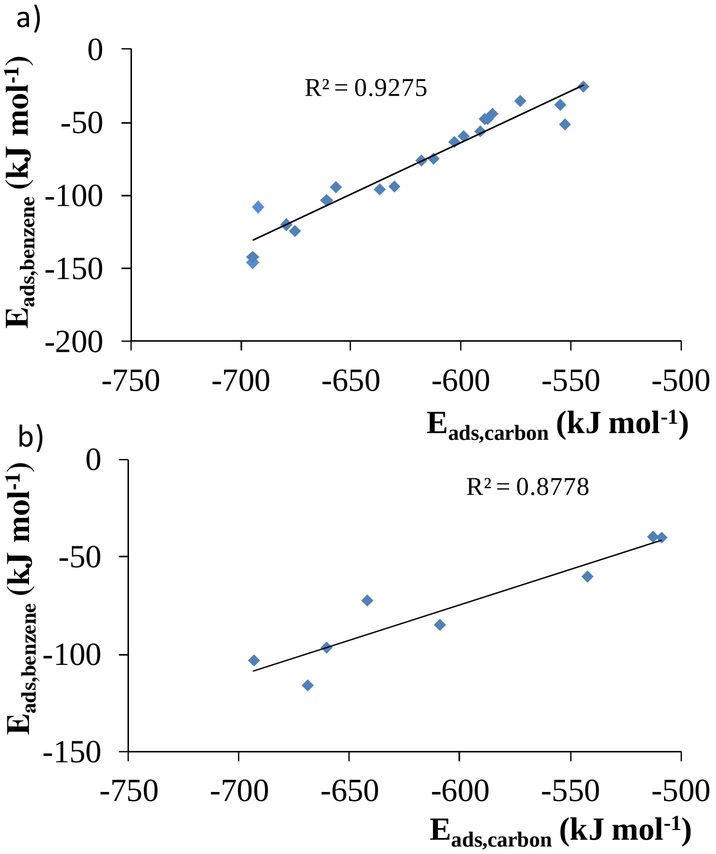

Figure D 4: Correlation for benzene and carbon adsorption energy considering Pd_3M and Ni_3M (a) antisegregated and (b) non-segregated alloys separately.

Reactivity of the different catalysts for benzene hydrogenation

Due to the large number of adsorption sites and bimetallic catalyst, the reactivity of the different alloys is evaluated only for the first hydrogenation step. In turn, various carbon atoms of benzene can be, most of the times, hydrogenated on each adsorption site. The barriers for different carbon atoms cannot be evaluated for every bimetallic catalysts. On antisegregated alloys, four types of carbon atoms are found in the most stable bri[30]/hcp-M-Pd_2M/fcc-Pd_2M-M site. Two are bound to the same surface metal atoms through a π-type interaction; the first closer to an fcc site below the adsorbate (c1 in Figure D 5), and the second closer to the hcp site (c2). The other two types of carbon are involved in a σ-type interaction with a single metal surface atom: the first is closer to the fcc site (c3), and the second closer to the hcp site (c3). The barriers obtained for hydrogenation of each carbon atoms on Pd_3Rh are listed in Figure D 5. For the other antisegregated catalysts, only hydrogenation of the c1 carbon type is studied.

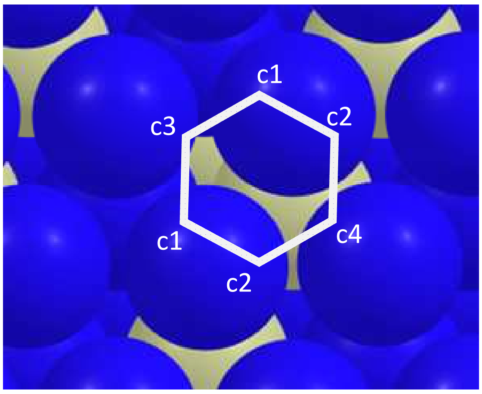

Figure D 5: Different types of carbon atoms in benzene adsorbed at the bri[30]/hcp-M-

Table D 5: Activation barrier for hydrogenation of the different carbon atoms in benzene adsorbed at the bri[30]/hcp-M-Pd_2M/fcc-Pd_2M-M site of the Pd_3Rh antisegregated catalyst.

Pd_3M, non-segregated	**$E_{a,el}$ (kJ mol^{-1}) for Pd_3Rh**
c1	106
c2	110
c3	120
c4	115

For partially segregated catalysts, the most stable adsorption site is the Ni_2-bri[30]/hcp-Ni/fcc-Ni, which has four carbon atoms bound to Ni with a π-type interactions, and two carbon atoms in σ-type interactions with M. For Ni_3Pd, hydrogenation of the first type of carbon atoms yields lower barriers than hydrogenation of those on σ-type interactions by 24 kJ mol^{-1}. On non-segregated catalysts, only the hydrogenation of the carbon atoms in π-type interactions have been studied, and two type of carbon atoms are found: the first one is bound to Pd for Pd_3M and Ni for Ni_3M alloys, while the second is bound to M atoms. Hydrogenation of the atoms bound to M atoms resulted in barriers lower by ~ 12 kJ mol^{-1}, e.g. for Pd_3Cr the hydrogenation of the first type yields a barrier of 125 kJ mol^{-1} and hydrogenation of the carbon atom in a C-M bond yields 112 kJ mol^{-1}.

Table D 6: Activation barriers (kJ mol^{-1}) for the first hydrogenation of benzene to monohydrobenzene on the most stable adsorption site of benzene on the different bimetallic surfaces.

Pd_3M, non-segregated	$E_{a,el}$ **(kJ mol^{-1})**
Pd_3Ti	92
Pd_3Cr	112
Pd_3Mn	114
Pd_3Pt	115
Pd_3M, antisegregated	
Pd_3Fe	109
Pd_3Co	100
Pd_3Ni	106
Pd_3Mo	95
Pd_3Rh	106
Pd_3Ta	100
Pd_3Ir	106
Ni_3M, anti-segregated	
Ni_3Cr	105
Ni_3Co	116
Ni_3Ru	121
Ni_3Re	118
Ni_3Os	126
Ni_3M, segregated	
Ni_3Pd	101
Ni_3Ir	115
Ni_3Pt	105

Implementation of catalyst descriptors on a kinetic model

In a previous study, a coverage-dependent microkinetic model has been constructed for the dominant path of benzene hydrogenation on Pd(111). The kinetic and thermodynamic parameters obtained solving the model on Pd(111) at T = 450 K, W/F_B^0 = 62.5 kg_{cat} s mol^{-1}, F_B^0=2.1 × 10^{-5} mol s^{-1}, F_{H2}^0 = 2.8 × 10^{-4} mol s^{-1}, p_B^0 = 6.7 × 10^{-2} bar, p_{H2}^0 = 0.9 bar, are listed in Table D 7, and correspond to the values for a coverage of occupied sites of $\theta_{occ} = 1 - \theta_{free}$ = 0.82.

Table D 7: Coverage-dependent parameters on Pd(111) obtained at $\theta_{occ} = 1 - \theta_{free} = 0.82$ calculated at T = 450 K, W/F_B^0 = 62.5 kg_{cat} s mol^{-1}, $F_B^0 = 2.1 \times 10^{-5}$ mol s^{-1}, $F_{H2}^0 = 2.8 \times 10^{-4}$ mol s^{-1}, $p_B^0 = 6.7 \times 10^{-2}$ bar, p_{H2}^0 = 0.9 bar.

Coverage-dependent parameters	Value on Pd(111) at θ_{occ} = 0.82
$A_{1,forward}$ (s^{-1})	7.2×10^{12}
$A_{1,reverse}$ (s^{-1})	4.8×10^{14}
$A_{2,forward}$ (s^{-1})	2.7×10^{13}
$E_{a1,forward}$ (kJ mol^{-1})	58.6
$E_{a1,reverse}$ (kJ mol^{-1})	38.3
$E_{a2,forward}$ (kJ mol^{-1})	56.4
$\Delta H_{ads,Benzene}$ (kJ mol^{-1})	–57.9
$\Delta S_{ads,Benzene}$ (J mol^{-1} K^{-1})	–132.4
$\Delta H_{ads,H2}$ (kJ mol^{-1})	–47.0
$\Delta S_{ads,H2}$ (J mol^{-1} K^{-1})	–134.8

For bimetallic catalysts, a rate determining step model for the second hydrogenation step has been considered to calculate turnover frequencies for benzene hydrogenation (TOF in s^{-1}):

$$TOF = \frac{k_{2,\,forward} \cdot K_1 \cdot K_B \cdot p_B \cdot K_{H2} \cdot p_{H2}}{\left(1 + K_B \cdot p_B \cdot \sqrt{K_{H2} \cdot p_{H2}}\right)^2} \cdot \left(1 - \frac{p_{CHA}}{p_B \cdot p_{H2}^3}\right) \tag{1}$$

The catalyst descriptor is implemented in this model to predict catalyst performances for a broad range of catalyst descriptor values and reaction conditions. The catalyst descriptor is the adsorption energy of benzene on a bimetallic alloy relative to that on Pd(111).

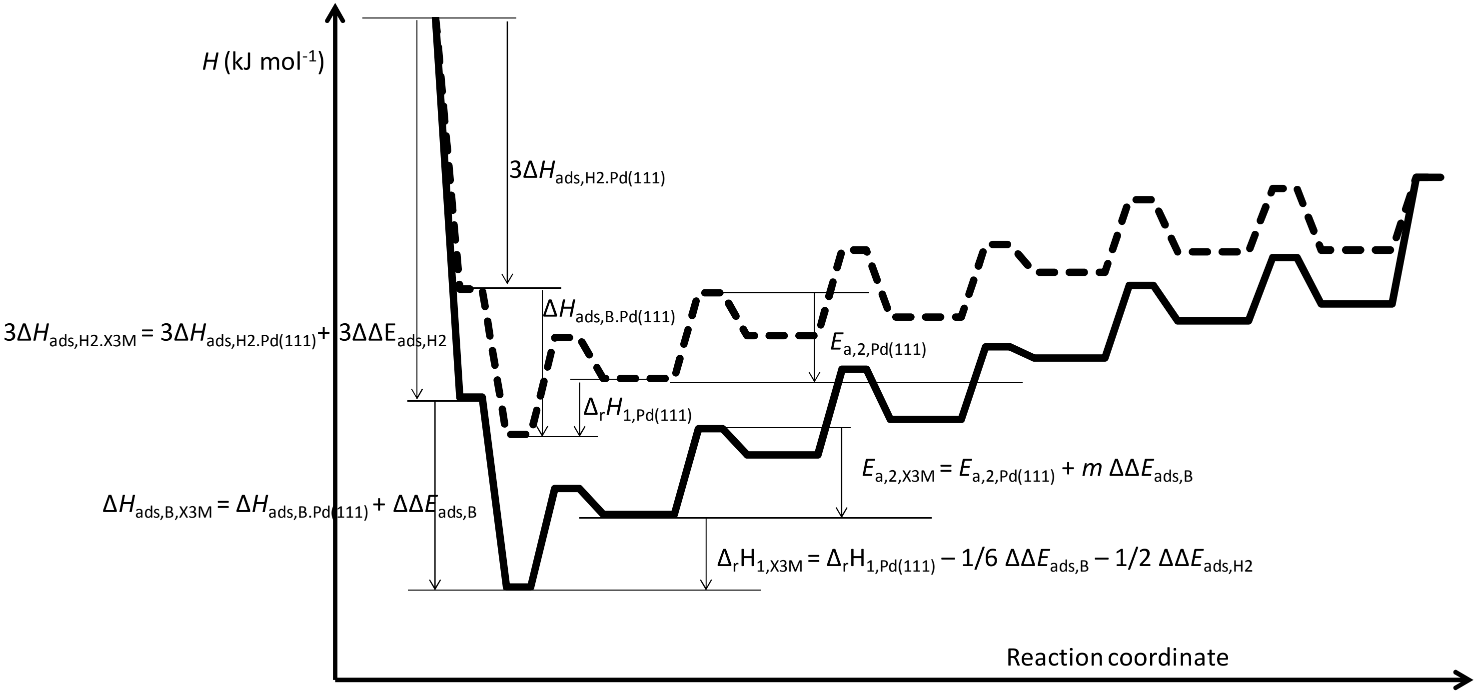

Figure D 6 Enthalpy diagram for the dominant path of benzene hydrogenation on Pd(111) (dotted line) and on a bimetallic catalyst (full line). Variation of the adsorption of benzene and (three) dihydrogen molecules from Pd(111) to another catalysts is corrected adapting the equilibrium coefficients of the hydrogenation steps.

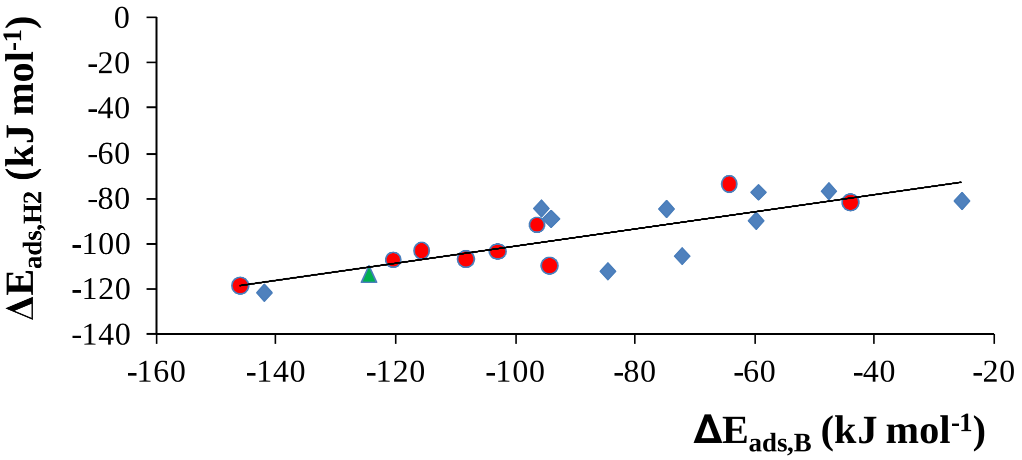

Figure D 7 Adsorption energy of dihydrogen as a function of benzene adsorption energy (kJ mol^{-1}).

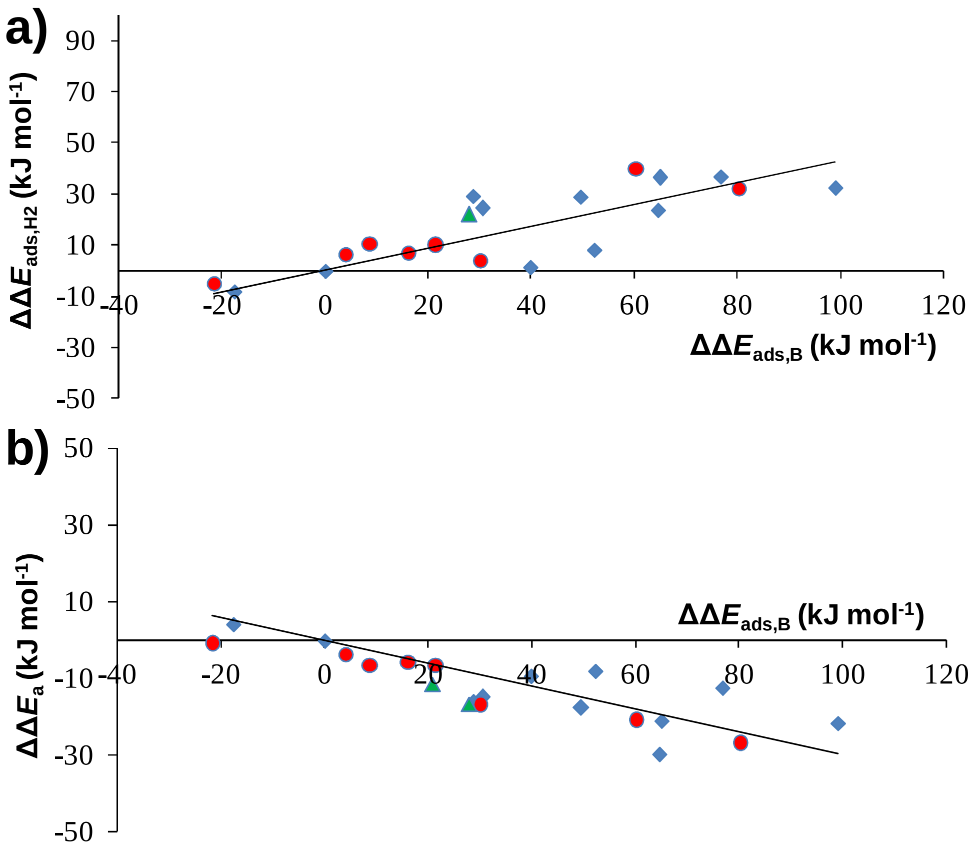

Figure D 8: Variation of the (a) adsorption energy of hydrogen and (b) activation barrier for the first hydrogenation step, relative to those on Pd(111), as a function of the variation of benzene adsorption energy, relative to that on Pd(111).

List of publications

Journal papers

1. G. Canduela-Rodriguez, M. K. Sabbe, M.–F. Reyniers, J.–F. Joly and G. B. Marin, Thermodynamic study of benzene and hydrogen coadsorption on Pd(111), Physical Chemistry Chemical Physics **16** (2014) 23754 – 23768.
2. G. Canduela-Rodriguez, M. K. Sabbe, M.–F. Reyniers, J.–F. Joly and G. B. Marin, Periodic DFT study of benzene adsorption on Pd(100) and Pd(110) as a function of coverage The Journal of Physical Chemistry C **118** (37) (2014) 21483 – 21499.

Oral presentations

1. **G. Canduela-Rodriguez**, M. K. Sabbe, M.–F. Reyniers, J.–F. Joly and G. B. Marin, *Ab initio based micro-kinetic modeling of benzene hydrogenation on Pd(111) as a function of hydrogen coverage*, **The 15th NCCC**, Noordwijkerhout, Netherlands, 2013.
2. **G. Canduela-Rodriguez**, M. K. Sabbe, M.–F. Reyniers, J.–F. Joly and G. B. Marin, *Ab initio reaction path and coverage effects analysis of benzene hydrogenation on Pd(111)*, **AIChE Annual Meeting**, San Francisco, USA, 2014.

Poster presentations

1. **G. Canduela-Rodriguez**, M. K. Sabbe, M.–F. Reyniers, J.–F. Joly and G. B. Marin, *Multi-scale modeling of benzene hydrogenation on Pd-based bimetallic catalysts*, **5th IDECAT/ERIC-JCAT Conference on Catalysis,** Bertinoro, Italy, 2011.
2. **G. Canduela-Rodriguez**, M. K. Sabbe, M.–F. Reyniers, J.–F. Joly and G. B. Marin, *Micro-kinetic modeling of benzene hydrogenation on Pd(111),* **XIth European Congress on Catalysis EUROPACAT**, Lyon, France, 2013.
3. **G. Canduela-Rodriguez**, M. K. Sabbe, M.–F. Reyniers, J.–F. Joly and G. B. Marin, *Micro-kinetic modeling of benzene hydrogenation on Pd(111),* **XIV Congrès de la Société Française de Génie des Procédés (SFGP 2013)**, Lyon, France, 2013.

Glossary

Ab initio	Latin term for “from first principles”. In this work, it is referred to those theoretical methods based on quantum chemistry that determine the energy of a systems, consisting of electrons and nuclei, based on the Schrödinger equation. Strictly speaking, no parameters other than the fundamental constant, e.g. Planck’s constant, are used by ab initio methods.
Active site	Ensemble of (catalyst) atoms where molecules bind and where these effectively combine to form the reaction product of a particular heterogeneous catalytic reaction.
Adsorption	An increase in the concentration of a gas or dissolved substance at the interface of a condensed and a liquid phase due to the operation of surface forces.
Arrhenius activation energy	The parameter E_a characterizing the exponential temperature dependence of the rate coefficient $k = A \exp(-E_a/\mathrm{RT})$.
Arrhenius equation	See Arrhenius activation energy.
Arrhenius pre-exponential factor	Coefficient A in front of the exponential term of the rate constant $k = A\,\mathrm{e}^{-Ea/\mathrm{RT}}$.
Bond dissociation energy	The bond dissociation energy (BDE) is the enthalpy change when cleaving a bond by homolysis.
Catalysis	The action of a catalyst.
Catalyst	Substance that changes the rate of a reaction, without modifying the overall standard Gibbs energy change. This substance is regenerated in the course of a catalytic reaction.
Catalyst descriptor	Property of a catalysts that correlates with the difference in activity from one catalyst to the next.

Chemical reaction	A process that results in the interconversion of chemical species.
Coverage dependence	Relation between the rate coefficient of an elementary reaction step and the surface coverage of the catalyst.
Density functional theory	Electronic structure theory that considers the energy to be a functional of the three–dimensional many–electron density.
Elementary reaction step	A chemical reaction in which one or more species react to products in a single step, passing through a single transition state, consisting of forward and reverse elementary reactions.
Enthalpy	Thermodynamic quantity that is calculated from the internal energy U as $H = U + pV$, in which p is the pressure and V is the volume.
Entropy	Thermodynamic quantity that measures the disorder of a system.
Gibbs free energy	Thermodynamic quantity that is calculated as $G = H – TS$ with H the enthalpy, T the temperature and S the entropy.
Hydrogenation	To chemically combine an unsaturated compound with hydrogen.
Langmuir-Hinshelwood mechanism	A mechanism for surface catalysis in which the reaction occurs between species that are adsorbed on the surface.
Mechanism	Step by step sequence of elementary reactions by which an overall reaction occurs.
Microkinetic analysis	Examination of a catalytic reaction in terms of the elementary reaction steps that occur on the catalyst surface and their relation with each other during a catalytic cycle.
Periodic boundary conditions	A set of boundary conditions which are often chosen for approximating a large (infinite) system by using a small part called a unit cell.
Quasi-steady-state approximation (QSSA)	Model simplification in which the rate of production of an intermediate is approximately equal to the rate of its generation.
Rate-determining step	If, in a reaction consisting of n steps, $(n – 1)$ steps

	have fast rate parameters and the n-th step has rate parameters that are much smaller than the others, the observed kinetic dependence is governed by the small parameters of the n-th step.
Rate of production analysis	Method to determine the paths through which a reaction, with multiple paths, proceeds. This method compares the net rate of the elementary reaction steps with that of the global reaction.
Reactant	A substance that is consumed in the course of a chemical reaction.
Reaction barrier	The energy barrier to chemical reaction.
Sensitivity analysis	Method to quantify the importance of elementary reaction steps on the global catalytic turnover frequency. It gives an estimation of the reactions with the a large influence on the global rate.
Standard state	State chosen for reference as convection. For a gas phase, it is the (hypothetical) state of the pure substance in the gaseous phase at the standard pressure $p = p^{\circ}$, assuming ideal behavior.
Surface coverage	Number of adsorbed molecules or atoms on a catalytic surface divided by the number of active sites.
Surface Gibbs free energy	Reversible work required to create a surface from the bulk and the adsorbate in gas phase.
Thermodynamic phase diagram	Graphical representation of the most stable (lowest surface Gibbs free energy) coverage of the catalysts surface catalysts surface in thermodynamic equilibrium with a surrounding gas phase reservoir as a function of temperature and pressure.
Transition state	The configuration of highest potential energy along the path of lowest energy between reactants and products.
Transition state theory	A theory of the rates of elementary reactions which assumes a special type of equilibrium, having an equilibrium constant $K^{\ddagger}$, to exist between reactants and activated complexes.
Turnover frequency	Number of molecules reacting per active site per unit time.
Van der Waals interactions	Dispersion forces between temporally polarized

	species, resulting in a stabilizing interaction.
Zero-point vibrational energy	Energy of the ground vibrational state. All quantum mechanical systems undergo fluctuations even in their ground state and have an associated zero-point vibrational energy.